ISBN 978-82-326-1822-4 (printed ver.)
ISBN 978-82-326-1823-1 (electronic ver.)
ISSN 1503-8181

NTNU
Norwegian University of
Science and Technology

Doctoral theses at NTNU, 2016:242

Dinh Thuc Duong

Doctoral thesis

NTNU
Norwegian University of
Science and Technology
Thesis for the Degree of
Philosophiae Doctor
Faculty of Information Technology, Mathematics
and Electrical Engineering
Department of Electric Power Engineering

NTNU

Doctoral theses at NTNU, 2016:242

Dinh Thuc Duong

Online Voltage Stability Monitoring and Coordinated Secondary Voltage Control

NTNU
Norwegian University of
Science and Technology

Dinh Thuc Duong

Online Voltage Stability Monitoring and Coordinated Secondary Voltage Control

Thesis for the Degree of Philosophiae Doctor

Trondheim, September 2016

Norwegian University of Science and Technology
Faculty of Information Technology, Mathematics
and Electrical Engineering
Department of Electric Power Engineering

NTNU
Norwegian University of
Science and Technology

NTNU
Norwegian University of Science and Technology

Thesis for the Degree of Philosophiae Doctor

Faculty of Information Technology, Mathematics and Electrical Engineering
Department of Electric Power Engineering

© Dinh Thuc Duong

ISBN 978-82-326-1822-4 (printed ver.)
ISBN 978-82-326-1823-1 (electronic ver.)
ISSN 1503-8181

Doctoral theses at NTNU, 2016:242

Printed by NTNU Grafisk senter

To my parents

Preface

This thesis is submitted to the Norwegian University of Science and Technology (NTNU) for partial fulfillment of the requirements for the degree of philosophiae doctor (PhD).

The research is carried out at the Department of Electric Power Engineering, Faculty of Information Technology, Mathematics and Electrical Engineering, NTNU. The PhD work is financed by the research project "Smart transmission grid operation and control" ($STRONg^2rid$), which is funded by Nordic Energy Research.

Trondheim, August 2016
Dinh Thuc Duong

Acknowledgments

First and foremost, I would like to express my sincere gratitude to my main supervisor, Prof. Kjetil Uhlen, for the great opportunity he has given me to carry out this work and his invaluable support for my PhD project. I really appreciate his constructive advice and guidance during the research. The fruitful discussions with him intrigued new ideas for the PhD work.

I also thank Prof. Olav B. Fosso, my co-supervisor, for his support. The PhD course on power systems stability he offered is really helpful for my research.

My thanks further go to my colleagues and friends at the Department of Electric Power Engineering. I will remember the cosy atmosphere at the weekly mini-seminars and social events we had. I am grateful to Inger, Åshild, Eva, Anders and Kurt, who have given me valuable help for practical matters since the first day I came to NTNU. Moreover, Vladimir receives my thanks for his help in setting up the first PMU in the smart grid lab.

I am also indebted to Lester, a colleague and a good friend of mine. Thanks for his great help to improve my English in this thesis. It is really time-consuming to read a draft of the dissertation and suggest corrections for grammatical errors, but he has got this tedious task very well done.

Last but not least, I give my heartfelt thanks to my parents and especially my wife for their wholehearted support for my PhD project. For me, pursuing a PhD is similar to running the marathon, I would not have finished this challenging, but fascinating, job without their continuing and tremendous support and encouragement. Moreover, it is impossible not to mention my beloved daughter, Ngoc. She gave me more motivation and energy to accomplish the PhD project.

Abstract

The development towards increasing use of renewable energy sources and smart grid applications represent a paradigm shift in power system operation. Due to the large share of variable generation and more dynamic load patterns, operation conditions in the future grid will change faster than today's situation. This will render the grid less predictable and consequently affect system operation, and voltage stability will undoubtedly remain one of the major concerns. In this scenario, it is necessary to have new real-time monitoring tools to timely identify operational limits in order to devise preventive and corrective schemes to maintain security of operation.

Aiming at developing new online monitoring tools for power systems, the PhD project has produced two methods to assess voltage stability in real time. Both are based on estimation of the Thevenin impedance and consequently the maximum power transfer. The first one estimates the Thevenin impedance by only local phasor measurements; meanwhile, the second approach obtains the Thevenin impedance by combination of system topology and measurements from phasor measurement units (PMUs). Although the second method takes the system topology into its calculation, it requires only information of the studied area, which is quite small since it is limited by boundary nodes. Therefore, both proposed methods are suitable for online implementation. Through simulations of the dynamic model of the Norwegian transmission system, the two algorithms result in comparable estimations of the Thevenin impedance, and both successfully detect the margin to voltage instability. In addition, with the topology-based method, it is able to estimate the post-contingency Thevenin impedance in real time. Thanks to this capability, it is possible to issue early warning of impact of critical disturbances on voltage stability, which is vital for the secure and reliable operation of power systems.

Apart from the estimation of the Thevenin impedance, the PhD work also introduces a new indicator called S-Z sensitivity indicator (S-ZI) for online voltage stability monitoring. The algorithm for the new indicator is simple and requires only PMU measurements of voltage and current of the considered load. Since the S-ZI is computed directly from the local phasor measurements, the method works robustly; it does not face any problems with divergence as often experienced in other approaches. The proposed indicator also shows a good performance in detecting the margin to the voltage stability limit, with both simulation and real PMU data. In addition, the S-ZI also functions as a calibrating tool to verify accuracy of the online estimated Thevenin impedance. Based on this new indicator and the proposed algorithm for estimation of the Thevenin impedance, a prototype of online voltage stability monitoring has been built and tested with live stream of PMU data obtained from the Norwegian transmission system. The results from the tests at two locations in the 420kV and 130kV networks have shown that the proposed methods have performed very well with real measurements in power systems.

Additionally, a scheme for coordinated secondary voltage control for systems with

multiple VAr reserves has been introduced in the PhD project. The proposed scheme is inspired by the concept of multi-agent system. Like an agent, the local controller takes on the assigned tasks itself and contacts its neighbors for support when needed. The control structure incorporates not only controllable VAr sources but also mechanically switched capacitor banks and reactors, resulting in increased online reactive power reserves for critical contingencies. The approach is suitable for areas with high penetration of FACTS devices, distributed generation connected to power systems through voltage source converters (VSCs), or VSC-HVDC systems. Moreover, the proposed scheme is also simple and flexible in terms of coordination, implementation and expansion. Through simulations, the control scheme has shown a good performance in coordinating reactive power sources to obtain a flat voltage profile and sufficient reactive power reserves, not only in normal operation but also under disturbance conditions.

Table of Contents

Preface **i**

Acknowledgments **iii**

Abstract **v**

Table of Contents **vii**

List of Tables **xi**

List of Figures **xiii**

Abbreviations and nomenclature **xvii**

1 Introduction **1**
1.1 Motivation . . . 1
1.2 Main contributions . . . 3
1.3 List of publications . . . 4
1.4 Thesis outline . . . 4

2 Review of voltage stability **7**
2.1 Power system stability . . . 7
2.1.1 Rotor angle stability . . . 8
2.1.2 Frequency stability . . . 9
2.1.3 Voltage stability . . . 9
2.2 Voltage stability phenomenon . . . 9
2.2.1 Definitions . . . 9
2.2.2 Classification and time scale of voltage stability . . . 10
2.3 Key features in voltage stability . . . 11
2.3.1 Generator . . . 11
2.3.2 Network . . . 14
2.3.3 Load dynamics . . . 18
2.4 Countermeasures against voltage collapse . . . 20
2.4.1 Switching of reactive power compensation . . . 21
2.4.2 Blocking OLTC operation . . . 21
2.4.3 Actions on generation . . . 21
2.4.4 Undervoltage protection . . . 22
2.5 Voltage stability analysis . . . 23
2.5.1 Continuation power flow . . . 23

2.5.2 Steady state analysis 26
2.6 Online voltage stability assessment 28
2.6.1 Principle of Thevenin equivalent-based methods for online voltage stability assessment 28
2.6.2 Voltage instability predictor (VIP) 29
2.6.3 The CT method 31
2.7 Discussion on methods for voltage stability assessment in the literature and online voltage stability monitoring 34
2.8 Major blackouts in power systems and the role of load curtailment based on voltage instability indicators 35
2.8.1 Major blackouts in power systems 35
2.8.2 Role of load shedding based on voltage stability indicators 37

3 Online voltage stability monitoring and protection based on local PMU measurements 39
3.1 Estimation of the Thevenin impedance based on S-Z sensitivity: the S-Z method 39
3.1.1 Estimation of the Thevenin impedance 39
3.1.2 Impact of the ratio X_{Th}/R_{Th} 41
3.1.3 Impact of abrupt variations of the load current 42
3.2 S-Z sensitivity used as a new indicator for online voltage stability monitoring 42
3.2.1 S-Z sensitivity indicator (S-ZI) 42
3.2.2 Early warning of voltage instability 45
3.3 Online voltage stability monitoring based on the Thevenin impedance and S-ZI 46
3.3.1 Indicator based on the Thevenin impedance 46
3.3.2 Applications of the S-ZI 46
3.3.3 S-ZI as an indicator for online voltage stability monitoring 48
3.3.4 S-ZI as a validation tool 48
3.4 Voltage instability protection and load shedding 49
3.5 Signal filtering 51

4 Online voltage stability monitoring based on system topology and phasor measurements 55
4.1 The Thevenin impedance in power systems with large generation 55
4.1.1 Estimation of the Thevenin impedance 55
4.1.2 Treatment of shunt compensation 59
4.2 Effect of active power dispatch on the Thevenin impedance 60
4.2.1 Impact of small generators on the Thevenin impedance 60
4.2.2 Active power injection modeled as a reactance 62
4.3 Topology- and PMU-based approach 65
4.3.1 Introduction 65
4.3.2 Description of the topology- and PMU-based approach 65
4.4 Real time estimation of the post-contingency Thevenin impedance 68
4.5 Summary of the topology-based method 70
4.6 Remarks on impacts of shunt compensation 72
4.6.1 Effect of shunt compensation on the Thevenin impedance 72

4.6.2 Relation between the maximum power transfer and the peak load power in highly overcompensated systems 72

5 Case study for online voltage stability monitoring 79
5.1 Case study on a 130 kV subsystem in the northern Norway 79
5.2 Case study at the Hasle corridor 84
5.2.1 Load increase 84
5.2.2 Load recovery after a line outage 89
5.3 Prototype of online voltage stability monitoring - V_{app} 93
5.3.1 Results from the Hasle corridor 95
5.3.2 Results from the Alta substation 108
5.4 Case study on the modified CIGRE Nordic32 test system 112
5.5 Load curtailment based on online voltage stability indicators 118

6 Coordinated secondary voltage control 121
6.1 Review of the secondary voltage control 121
6.1.1 Voltage control structure in power systems 121
6.1.2 Secondary voltage control 123
6.1.3 Coordinated secondary voltage control 125
6.2 A new scheme for coordinated secondary voltage control for systems with multiple VAr reserves 127
6.2.1 Motivation for the proposed control scheme 127
6.2.2 Overview of the proposed control scheme 128
6.2.3 Detail of controller design for controllable VAr sources 130
6.2.4 Detail of controller design for mechanically switched shunt capacitor/reactor 134
6.2.5 Simulation results 135

7 Conclusions and future work 143
7.1 Conclusions 143
7.2 Future work 145

References 147

Appendix A Dynamic models of the modified CIGRE Nordic32 test system 155

List of Tables

1.1 Some voltage instability incidents with collapse in the past [1]. 2

2.1 An example of fractional load exponents [14] 20

4.1 Maximum loadability and corresponding load impedance. 61
4.2 Load impedance and the Thevenin impedance at the nose point. 63

List of Figures

2.1 Classification of power system stability [12]. 8
2.2 Voltage stability phenomena and time scale [1]. 11
2.3 Schematic diagram of AVR. 12
2.4 Simplified generator capacity curve [14, 19, 20]. 13
2.5 Thermal limit of the field and armature windings [17]. 14
2.6 A two-bus system. 15
2.7 The well-known normalized PV curves. 16
2.8 The QV curves. 18
2.9 Illustration of impact of OLTC on voltage instability [14]. 19
2.10 Adjustment of generator's output power to mitigate voltage instability. . . 22
2.11 Description of the continuation power flow method. 24
2.12 Thevenin equivalent of power system seen at a load bus. 28
2.13 Voltage instability monitoring based on the Thevenin impedance [45]. . . . 30
2.14 Illustration of maloperation of undervoltage protection [45]. 31
2.15 Phasor diagram of voltages and current in Fig. 2.12 [47]. 32
2.16 Example of power system structure. 37

3.1 The Thevenin equivalent circuit. 40
3.2 Impact of the ratio X_{Th}/R_{Th} on the estimated Thevenin impedance. 42
3.3 Impact of deviation of load current on the estimated Thevenin impedance. 43
3.4 Sketch of another shape of the PV curve [50]. 43
3.5 Trajectories of the S-ZI with different Thevenin impedance. 45
3.6 Trajectories of the S-ZI when load is approaching the voltage stability limit. 46
3.7 Magnitudes of the load impedance and the Thevenin impedance estimated in real time; white curve: the load impedance; red curve: the Thevenin impedance; 47
3.8 Apparent power of the load and the maximum loadability estimated in real time; white curve: load; red curve: the estimated loadability. 47
3.9 Performance of the S-Z sensitivity at a 420 kV bus; x-axis is magnitude of load impedance, y-axis is the S-ZI (MVA/Ω); the red point is the S-ZI computed from phasor measurements and the thick blue curve is the trajectory of the currently estimated Thevenin impedance. 48
3.10 Estimated Thevenin impedances obtained from different algorithms. 49
3.11 Illustration of inaccurate estimation of the Thevenin impedance, verified by the S-Z sensitivity. 50
3.12 Schematic diagram of voltage instability protection deployed at a substation. 51

3.13 Voltage instability protection based on the S-ZI and Thevenin impedance; $\bar{Z}_{Th}$ is the Thevenin impedance, $\bar{Z}_L$ is the load impedance and $\bar{Z}_f$ is the load impedance of feeders. 52
3.14 The S-Z sensitivity computed from raw data. 53
3.15 Variations of the load impedance and apparent power during a period of four seconds obtained from real PMU measurements; reporting frequency is 50 data frames per second. 53
3.16 The S-Z sensitivity ($\zeta = dS_L/dZ_L$) after filtering. 53

4.1 A 3-bus system to illustrate the Thevenin impedance in systems with large generation. 56
4.2 Equivalent circuit of the 3-bus system. 56
4.3 The Thevenin equivalent circuit. 57
4.4 A 130 kV subsystem of the Norwegian transmission system. 58
4.5 Graphical illustration of the Thevenin impedance estimation. 59
4.6 A simple system to analyze the influence of dispatch of active power on the Thevenin impedance. 60
4.7 The PV curves under different scenarios of active power injection at bus 2. 61
4.8 Model of active power limitation by an reactance. 62
4.9 The equivalent grid after applying the modeling reactance concept. 63
4.10 The estimated Thevenin impedance after applying the modeling reactance for active power injection; the blue curve is load impedance, the red and dashed curve is the Thevenin impedance and the green curve is load power. 64
4.11 The Nordic32 test system [60]. 68
4.12 Direct connection between A-P nodes and the considered load bus after the simplification of the studied area. 69
4.13 Illustration of the Thevenin impedance estimation under contingency. . . . 69
4.14 A small system to demonstrate the post-contingency Thevenin impedance. 70
4.15 Performance of the post-contingency Thevenin impedance estimation. . . . 71
4.16 Flow chart of the proposed approach to online voltage stability monitoring based on system topology and PMU measurements. 71
4.17 A simple system with shunt capacitor. 73
4.18 A 2-bus system with static VAr compensator. 73
4.19 The Thevenin impedance and load power when rated power of the SVC is 56 MVAr. 74
4.20 The Thevenin impedance and load power when rated power of the SVC is 169 MVAr. 75
4.21 Load voltage and reactive output power when rated power of the SVC is 169 MVAr. 75
4.22 PV curves to illustrate the trajectory of the operation point when the system is highly overcompensated by the 169 MVAr SVC. 76
4.23 Load power versus R and X_c. 77
4.24 Load trajectory on the R-X_c plane under SVC's constant voltage control. . 77
4.25 Maximum power transfer condition curve and load trajectory under constant voltage control. 78

5.1 Simplified single line diagram of the studied 130 kV subsystem. 81
5.2 Voltage and the PV curve at bus 21 during the load increase period. 82

5.3 The Thevenin impedance seen at bus 21. 82
5.4 Estimated maximum loadability at bus 21. 83
5.5 Trajectory of the S-ZI during the load increase period. 83
5.6 The transmission system in the southern Norway [63]. 85
5.7 Voltage and the PV curve at the Hasle corridor when power transfer on the corridor is increased until it crosses the maximum loadability. 86
5.8 Thevenin impedance at the Hasle corridor when power transfer on the corridor is increased until it crosses the maximum loadability. 87
5.9 Estimated maximum loadability at the Hasle corridor when power transfer on the corridor is increased until it crosses the maximum loadability. 88
5.10 Trajectory of S-ZI during load increase period at the Hasle corridor. 88
5.11 Estimation of the Thevenin impedance under contingency at the Hasle corridor, obtained from the topology-based method. 89
5.12 The Thevenin impedance at the Hasle corridor obtained from the S-Z and CT methods during the load recovery period. 90
5.13 Estimated maximum loadability at the Hasle corridor obtained from the topology-based, S-Z and CT methods in the load recovery case study. . . . 91
5.14 Trajectory of the S-ZI during the load recovery at the Hasle corridor. . . . 91
5.15 Variations of the apparent power between two consecutive measurements at the Hasle corridor. 92
5.16 Online voltage stability monitoring application V_{app} at the Hasle corridor. . 93
5.17 The PMU Recorder Light (PRL) developed for the STRONg^2rid project. . 94
5.18 Prototype of the online voltage stability monitoring V_{app} at the Hasle corridor 96
5.19 Snapshot of V_{app} at the Hasle corridor on Feb. 18, 2014. 97
5.20 Snapshot of V_{app} at the Hasle corridor on Mar. 19, 2014. 98
5.21 Snapshot of V_{app} at the Hasle corridor on Mar. 28, 2014. 98
5.22 Snapshot of V_{app} at the Hasle corridor on Mar. 31, 2014. 99
5.23 Snapshot of V_{app} at the Hasle corridor on Dec. 10, 2014. 99
5.24 Snapshot of V_{app} at the Hasle corridor on Dec. 15, 2014. 100
5.25 Snapshot of V_{app} at the Hasle corridor on Dec. 15, 2014. 100
5.26 Snapshot of V_{app} at the Hasle corridor on Feb. 11, 2014. 101
5.27 Snapshot of V_{app} at the Hasle corridor on Feb. 11, 2014. 102
5.28 Snapshot of V_{app} at the Hasle corridor on May 2, 2014; the red curve is from the S-Z method, the green curve is from the CT method. 103
5.29 Snapshot of V_{app} at the Hasle corridor on May 21, 2014; the red curve is from the S-Z method, the green curve is from the CT method. 104
5.30 Snapshot of V_{app} at the Hasle corridor on Dec. 15, 2014; the red curve is from the S-Z method, the green curve is from the CT method. 104
5.31 Snapshot of V_{app} at the Hasle corridor on Dec. 15, 2014; the red curve is from the S-Z method, the green curve is from the CT method. 105
5.32 Snapshot of V_{app} at the Hasle corridor on Apr. 28, 2014; the red curve is from the S-Z method, the green curve is from the CT method. 105
5.33 Snapshot of V_{app} at the Hasle corridor on Apr 29, 2014; the red curve is from the S-Z method, the green curve is from the CT method. 106
5.34 Online voltage stability monitoring at the 130 kV substation Alta 109
5.35 Snapshot of V_{app} at the 130 kV substation Alta on Dec. 18, 2014; the red curve in graph 1 is the result from the S-Z method. 110

5.36 Estimated Thevenin impedance from the CT method at Alta substation. . 111
5.37 Single line diagram of the Nordic32 test system [60]. 113
5.38 Load recovery in the central area. 114
5.39 S-ZI of all the loads in the central area. 115
5.40 Thevenin impedance from the topology-based method as seen at bus 1041. 116
5.41 Thevenin impedances from the S-Z and CT methods seen at bus 1041. . . 116
5.42 Load power at bus 1041 when there is only load recovery at the monitored bus. 117
5.43 The Thevenin impedance and the load impedance at bus 1041 when there is only load recovery at the monitored bus. 117
5.44 System performance when load 1 and 3 are curtailed. 118
5.45 System performance when load 4 is curtailed. 119
5.46 System performance when load 5 is curtailed. 119
5.47 System performance when load 43 is curtailed. 119

6.1 Structure of voltage control in power systems. 122
6.2 Sketch of block diagram of secondary voltage control. 124
6.3 Structure of coordinated secondary voltage control in power systems. . . . 126
6.4 Example of a subsystem with shunt compensators. 129
6.5 One of possible control schemes for the system in Fig. 6.4. 130
6.6 A simplified primary controller of SVC. 130
6.7 Control structure for controllable VAr reserves. 132
6.8 Logic to obtain support from the neighboring controllers. 133
6.9 Logic to lower support from the neighboring controllers. 133
6.10 Criterion to decide the state of lack or surplus of reactive power reserve. . . 134
6.11 Algorithm of the Incoming Support Handler block (ISH). 134
6.12 Control logic for capacitor bank. 135
6.13 A 5-bus system and the coordinated control scheme. 136
6.14 Five-bus system's performance during load variation. 137
6.15 Voltage and SVC's susceptance in the five-bus system without coordinated control. 138
6.16 The simplified 420 kV system in the southern part of Norway and its coordinated control scheme. 139
6.17 The 420 kV system performance during the test. 140
6.18 Voltage and SVC susceptance without the coordinated control. 141

Abbreviations and nomenclature

Abbreviations

AGC	Automatic generation control
A-P	A bus type with positive net active power injection
AVR	Automatic voltage regulator
CT	The name of a method to estimate the Thevenin impedance [47]
EHV	Extra-high voltage
FACTS	Flexible AC transmission system
HVDC	High voltage direct current
IED	Intelligent electronic device
ISI	Impedance stability index
LTC	Load tap changer
MSC	Mechanically switched capacitor
OLTC	Onload tap changer
OXL	Overexcitation limiter
PDC	Phasor data concentrator
PMU	Phasor measurement unit
PRL	PMU Recorder Light
S-ZI	S-Z sensitivity indicator
STATCOM	Static synchronous compensator
SVC	Static VAr compensator
TCR	Thyristor-controlled reactor
TSC	Thyristor-switched capacitor
V_{app}	The prototype of online voltage stability monitoring
VIP	Voltage instability predictor
VSC	Voltage source converter

Symbols

$\vec{E}_{Th}$	Thevenin voltage, $\vec{E}_{Th} = E_{Thr} + jE_{Thi}$
$\vec{I}$	Current, $\vec{I} = I_r + jI_i$
p	Normalized active power
P	Active power
q	Normalized reactive power
q_{crit}	Normalized reactive power at the critical point of the QV curve
Q	Reactive power
S	Apparent power, $S = \sqrt{P^2 + Q^2}$
$\bar{S}$	Apparent power as a complex number, $\bar{S} = P + jQ$
v	Normalized voltage, $v = V/E_{Th}$
v_{crit}	Normalized voltage at the critical point of the QV curve
$\vec{V}$	Voltage, $\vec{V} = V\angle\delta = V_r + jV_i$
$\vec{V}_\Delta$	Voltage drop on the Thevenin impedance
$\bar{Z}_f$	Load impedance of feeder(s)
$\bar{Z}_L$	Load impedance, $\bar{Z}_L = Z_L\angle\phi = R_L + jX_L$
$\bar{Z}_{Th}$	Thevenin impedance, $\bar{Z}_{Th} = Z_{Th}\angle\alpha = R_{Th} + jX_{Th}$
α	Phase angle of the Thevenin impedance
β	Angle between the Thevenin voltage and load current
δ	Voltage angle
ζ	S-Z sensitivity, $\zeta = dS/dZ$
θ	Angle between $\bar{Z}_{Th}$ and $\bar{Z}_L$
κ	Load parameter in the continuation power flow method
ϕ	Power factor angle
η	Left eigenvector matrix
λ	Eigenvalue
ξ	Right eigenvector matrix
Λ	Diagonal eigenvalue matrix

Chapter 1

Introduction

This chapter starts with the need for online voltage stability monitoring in power systems at the present time and in the foreseeable future. That is also the main motivation for the PhD work. In the next section, main contributions of the PhD project are presented. It is then followed by a list of publications, which have been produced during the period of the PhD project. Finally, the chapter is closed with an outline of the thesis.

1.1 Motivation

Among other stability problems in power systems, voltage stability remains one of the major concerns. Depending on a particular operation condition, load characteristics and other factors, voltage instability can lead to a system collapse or blackout, which can affect millions of customers. Indeed, several voltage collapse incidents around the world have been observed as listed in Table 1.1 [1]. An early incident took place in France in 1965, but most of the events occurred in the 1980s. In addition, voltage collapse has been experienced in USA [2,3] and southern Sweden and eastern Denmark [4] in 2003. In the same year, it was also observed that voltage instability contributed to the blackout in the Italian power system [3, 5–7]. Although significant investments have been made to strengthen the power networks and many measures have been taken in both planning and operation stage, the grid is still vulnerable to stability problems. Recent blackouts in India in 2012 [8] and Turkey in 2015 [9] indicate that more work needs to be done to secure reliable operation of power systems.

Although operation of power systems was very well planned, unexpected disturbances and other factors have pushed the system out of their limits and finally led to interruption of power supply. Under condition of high penetration of renewable energy sources, concern about stability problems of power systems is growing. Due to its variable characteristics, the renewable generation can cause fast changes of operation condition, which can go beyond the worst scenarios identified in the planning stage. Under these circumstances, it is necessary to have good monitoring tools, which are able to properly detect operational limits in real time. These tools are needed for timely remedial actions to maintain secure and reliable operation of the grid.

Recently, the smart grid has attracted huge attention from researchers and stakeholders in the power industry. It is widely acknowledged that in the future smart grid, the distribution network is no longer passive; it will become more and more active. This shift requires better coordination between the transmission and distribution networks in order

Table 1.1: Some voltage instability incidents with collapse in the past [1].

Date	Location	Time frame
13 April 1986	Winnipeg, Canada. Nelson River HVDC link	Transient, 1 sec.
30 Nov. 1986	SE Brazil, Paraguay. Itaipu HVDC link	Transient, 2 sec.
17 May 1985	South Florida, USA	Transient, 4 sec.
22 Aug. 1987	Western Tennessee, USA	Transient, 10 sec.
27 Dec. 1983	Sweden	Longer term, 55 sec.
02 Sept. 1982	Florida, USA	Longer term, 1-3 min.
26 Nov. 1982	Florida, USA	Longer term, 1-3 min.
28 Dec. 1982	Florida, USA	Longer term, 1-3 min.
30 Dec. 1982	Florida, USA	Longer term, 1-3 min.
22 Sept. 1977	Jacksonville, Florida	Longer term, few min.
04 Aug. 1982	Belgium	Longer term, 4.5 min.
12 Jan. 1987	Western France	Longer term, 6-7 min.
09 Dec. 1965	Brittany, France	Longer term
10 Nov. 1976	Brittany, France	Longer term
23 July 1987	Tokyo, Japan	Longer term, 20 min.
19 Dec. 1978	France	Longer term, 26 min.
22 Aug. 1970	Japan	Longer term, 30 min.

to secure operation of the power system as a whole. In this context, remedial actions can be taken at the distribution level to alleviate critical operation conditions in the transmission system. To achieve this goal, there is a need for online indicators that can detect the margin to operational limits in the transmission network. These indicators are then used to determine effective and timely countermeasures in the distribution grid. Regarding this issue, real-time indicator for voltage stability monitoring is one of the indispensable tools, not only for the present but also for the foreseeable future.

Additionally, in order to meet the growing demand, especially potentially massive influx of electric vehicles in the years to come, the grid needs to be expanded and upgraded. To reduce the cost, resources of power systems are expected to be better utilized. Hence, it is expected that power systems are about to be operated closer to their limits, in which voltage stability is one of the active constraints. In order to obtain higher utilization of the grid, system operators need good awareness of the system's operational limits in real time. This requirement encourages researchers to develop new monitoring tools for online applications. In response to this, the project "Smart transmission grid operation and control" (STRONg^2rid) funded by Nordic Energy Research was launched in 2011. Among other objectives, "this project seeks to develop better tools for addressing the increasing need to move electricity across national borders" and "develop a solid interdisciplinary theoretical foundation supporting development of better tools for planning, operation and control of power grids interconnected across traditional national boundaries and at various voltage levels" [10].

Motivated by the need for online monitoring tools for power systems as mentioned above and in combination of pursuing the objectives of the STRONg^2rid project, the PhD work focuses on developing new online indicators for voltage stability monitoring, which

utilizes PMU measurements to properly detect voltage stability limit in both transmission and sub-transmission systems. In addition, the PhD study also aims at developing a scheme for coordinated secondary voltage control, which is able to keep voltage in the controlled area within the permissible band and to maintain a sufficient dynamic VAr reserves for fast remedial actions against voltage collapse.

1.2 Main contributions

The main contributions of the PhD work are as follows:

- Development of two new methods to estimate, in real time, the Thevenin impedance in power systems seen at a load bus. This impedance is the key parameter for the online voltage stability assessment.
  - The first algorithm is model-free; it requires only phasor measurements of voltage and current of the considered load.
  - Unlike the first one, the second approach utilizes both information of system topology and phasor measurements.
- Proposition to a novel indicator for online voltage stability monitoring. The indicator is computed directly from phasor measurements of voltage and current of the considered load and works properly in any loading condition.
- Estimation of the Thevenin impedance under contingency in real time. This post-contingency impedance reflects impacts of disturbances on voltage stability at the current operating point.
- Introduction of a new tool to verify the online estimated Thevenin impedance. Thanks to a significant amount of research on voltage stability, several methods to estimate the Thevenin impedance in real time have been proposed. However, accuracy and performance of these algorithms can vary. In normal operation, all the estimated values can be claimed reasonable as long as they are smaller than the load impedance. However, at one instant of time, the Thevenin impedance seen at the same observation location in the grid is unique. Addressing this issue, an approach has been proposed in the PhD project; it functions as an online calibrating instrument to validate the Thevenin impedance estimated by different algorithms.
- Formation of a load curtailment scheme to prevent voltage instability. The methodology secures selectivity of the load shedding. In addition, it also avoids excessive load curtailment with respect to voltage instability.
- Development of a new scheme for coordinated secondary voltage control for systems with multiple VAr reserves. Objectives of the control scheme are to avoid voltage violation, both in normal operation and after disturbances, to keep sufficient reactive power reserve of fast-acting compensators available for other functions, and to improve voltage stability in critical contingencies.
- Enhanced understanding of the Thevenin impedance in power systems and the relationship between the Thevenin impedance, the maximum power transfer theorem and the peak power of the load when the system is highly overcompensated.

1.3 List of publications

The main contributions in this thesis are presented in the following publications:

Publication A. Dinh Thuc Duong and Kjetil Uhlen, "S-Z Sensitivity: an Indicator and a Tool for Online Voltage Stability Monitoring," submitted to the *IEEE Transactions on Power Systems*.

Publication B. Dinh Thuc Duong, Kjetil Uhlen, Glauco Nery Taranto and Stig Løvlund, "A comparative case study of online voltage instability monitoring," in *Proc. Conf. PowerTech 2015*, Eindhoven, Netherlands, 2015.

Publication C. Dinh Thuc Duong, Lester Kalemba, Kjetil Uhlen and Stig Løvlund, "A Scheme for coordinated secondary voltage control for systems with multiple VAr reserves," in *Proc. Conf. Innovative smart grid technologies North Amarica ISGT 2015*, Washington D.C., USA, 2015.

Publication D. Dinh Thuc Duong, Kjetil Uhlen and Stig Løvlund, "A method for real time voltage stability monitoring in sub-transmission networks," in *Proc. Conf. Power Systems Computation PSCC2014*, Wroclaw, Poland, 2014.

Publication E. Dinh Thuc Duong and Kjetil Uhlen, "Analysis of impacts of SVC on voltage collapse mechanism and maximum loadability," in *Proc. Conf. International Conference and Utility Exhibition on Green Energy for Sustainable Development ICUE 2014* , Pattaya, Thailand, 2014.

Publication F. Dinh Thuc Duong and Kjetil Uhlen, "Online voltage stability monitoring based on PMU measurements and system topology," in *Proc. the third International Conf. Electric Power and Energy Conversion Systems*, Istanbul, Turkey, 2013.

In addition, the PhD project has produced another publication, which is not included in the thesis:

Publication G. Dinh Thuc Duong, Kjetil Uhlen and Erik Alexander Jansson, "Estimation of Hydro Turbine-Governor System Transfer Function from PMU Measurements," presented at the *PES General Meeting 2016*, Boston, USA, 2016.

1.4 Thesis outline

The first chapter of the thesis, Chapter 1, presents the motivation for the PhD work. It is followed by the summary of the main contributions of the research carried out during the PhD project period. The chapter ends with the list of publications and the outline of the thesis.

Chapter 2 reviews the literature on voltage stability phenomenon in power systems. First, an overview of power system stability is presented. Then, the voltage stability phenomenon is described in the next section. It is followed by the next two sections, addressing key factors involved in voltage instability and countermeasures against voltage

collapse. Next, the continuation power flow method and steady state analysis of voltage stability are presented. The chapter continues with the review of some well-known methods, which have been proposed for online voltage stability assessment before a brief summary of major blackouts in power systems is made and the role of load shedding based on voltage stability indicators is discussed at the end of the chapter.

Chapter 3 starts with a new method to estimate the Thevenin impedance based on local PMU measurements. In the next section, a new indicator for voltage stability assessment is presented. Based on these tools, applications for online voltage stability monitoring scheme are introduced, followed by a scheme for voltage instability protection based on load curtailment. The chapter ends with a brief description of signal filtering.

Chapter 4 introduces another approach to estimate the Thevenin impedance in power systems. First, systems with only large generation is considered. Then, the analysis is carried out to explore the impact of small generators on the Thevenin impedance. Based on this, a concept of modeling active power injection by a reactance is proposed. It paves the way for development of a method for online voltage stability monitoring based on system topology and PMU measurements. Finally, remarks on the impact of shunt compensation on the Thevenin impedance and maximum power transfer are presented.

Chapter 5 shows a performance of all of the proposed approaches in the case study, which includes the studies on a 130 kV sub-system in the northern Norway, the main 420 kV corridor between Norway and Sweden, and the Nordic32 test system.

Apart from the topic on online voltage stability monitoring, Chapter 6 concentrates on the coordinated secondary voltage control. The chapter starts with a review of literature on the secondary voltage control before it introduces a new scheme for coordinated secondary voltage control. Finally, the simulation results are presented.

After all of the research work is presented, conclusions are drawn in Chapter 7, where a discussion about the entire thesis and future work are also presented.

Chapter 2

Review of voltage stability

This chapter presents the background to voltage stability in power systems, which is the main research area of the PhD project. First, a definition of stability in power systems is presented. It is followed by an in-depth analysis of voltage stability phenomenon. Then the chapter continues with key features in voltage stability. In the next section, countermeasures against voltage collapse are presented, followed by well-known methods for steady-state voltage stability analysis. The chapter goes on with state-of-the-art approaches for online voltage stability monitoring and ends with a summary of major blackouts in power systems and a discussion of the role of load shedding based on real-time voltage stability indicators.

2.1 Power system stability

Since operation of the first complete electric power system in September 1882 [11], power systems have expanded significantly and become highly complex electrical networks, consisting of an enormous number of electrical components. Along with interconnections among power systems and penetration of renewable generation, the rapidly growing number of applications based on power electronics in the modern grid, like HVDC and FACTS devices, has contributed to the increase in system complexity. In order to supply energy to loads continuously and reliably, power systems must be stable under various operating conditions and subject to a range of disturbances. This requirement poses huge challenges. Therefore, power system stability continues to be of high interest. To analyze this issue, it is necessary to have a practical definition of stability in the grid. According to [12], power system stability is defined as:

> "*Power system stability is the ability of an electric power system, for a given initial operating condition, to regain a state of operating equilibrium after being subjected to a physical disturbance, with most system variables bounded so that practically the entire system remains intact.*"

Although the main subject of this section is voltage stability, this phenomenon is interrelated to other stability problems. Therefore, it is necessary to have an overview of all stability issues in power systems. Mathematically, stability has a single precise definition,

but from a practical point of view, power system stability can be classified into different categories as shown in Fig. 2.1. This classification [12] is based on the following aspects:

- The physical nature of the phenomenon that leads to instability, as indicated by the main system variable in which instability can be observed.
- The size of the disturbance considered, which influences the preferred method for analyzing the problem.
- The time span and modeling details that must be taken into consideration in order to assess stability.

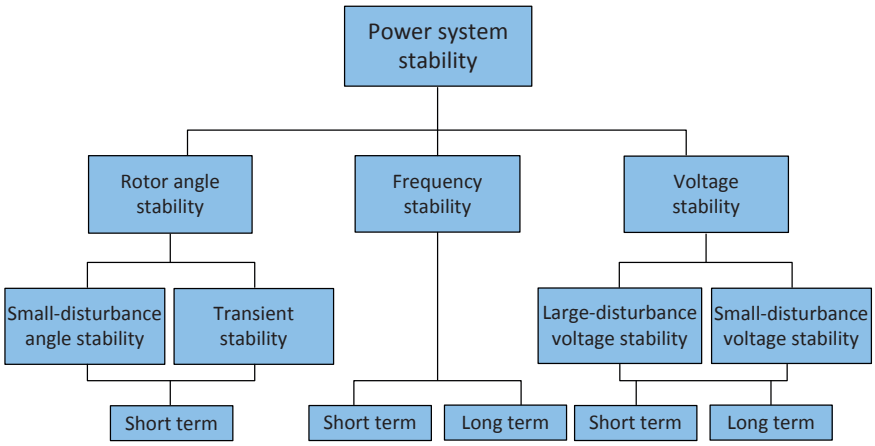

Figure 2.1: Classification of power system stability [12].

2.1.1 Rotor angle stability

In Fig. 2.1, the first stability category is rotor angle stability. This issue is related to the synchronism of generators in interconnected systems. In normal operation, the generator is synchronous to the grid; but the synchronism can be lost after the machine is subjected to a disturbance. To carry out in-depth analysis of the nature of rotor angle stability, it is convenient to divide the phenomenon into two categories: small-disturbance angle stability and transient stability. A disturbance is considered as small if it allows linearized system models to be used in the analysis with permissible errors. Regarding this kind of stability, the main concern in modern power systems is low damped or un-damped power oscillations. The oscillation can be local, where local generators oscillate against the system or against each other, or inter-area, where one group of generators oscillates against other distant groups. In contrast to the small disturbance stability, transient stability is associated with large disturbances like short circuits, which can lead to loss of synchronism. Both small disturbance and transient stability are considered as short term stability since they have the time spans ranging from 10 to 20 seconds and 3 to 5 seconds (maybe up to 10 to 20 seconds for very large systems with dominant inter-area swings [12]), respectively.

2.1.2 Frequency stability

Frequency is an indicator for continuous active power balance in the grid. The frequency is unchanged if generation is equal to consumption (including losses); it will go up when the dispatched generation is larger than the consumption and it will go down if the relation between generation and consumption is opposite.

Short-term frequency instability is related to the deficiency of active power of an island system with insufficient underfrequency load shedding such that frequency decays rapidly and leads to blackout within a few seconds. On the other hand, more complex situations, in which frequency instability is caused by steam turbine overspeed controls or boiler/reactor protection and controls, are longer-term phenomena with the time frame of interest ranging from tens of seconds to several minutes [12].

2.1.3 Voltage stability

Voltage stability is the main focus of the PhD work. This issue is presented in detail in the next section.

2.2 Voltage stability phenomenon

2.2.1 Definitions

Voltage stability is a complex phenomenon, which involves dynamic characteristics of power system components. Depending on the point of view, voltage stability can be interpreted by different definitions. In [14], voltage stability is not defined, but a definition of voltage instability is given instead, as:

> *Voltage instability stems from the attempt of load dynamics to restore power consumption beyond the capability of the combined transmission and generation system.*

This definition encompasses key factors involved in voltage instability. Here, the main actors in the phenomenon are load dynamics, capacity of the transmission network and generation. The definition is further elaborated as [14]:

- *Voltage*: the phenomenon is manifested in the form of large uncontrollable voltage drops at a number of network buses.
- *Instability*: having crossed the maximum deliverable power limit, the mechanism of load power restoration becomes unstable, reducing instead of increasing the power consumed. This mechanism is the heart of voltage instability.
- *Dynamics*: any stability problem involves dynamics. These can be modelled with either differential equations (continuous dynamics), or with difference equations (discrete dynamics).
- *Loads* are the driving force of voltage instability. Note, however, that loads are not the only players in this game.

- *Transmission* systems have a limited capacity for power transfer, as well known from circuit theory. This limit (as affected also by the generation system) marks the onset of voltage instability.

- *Generation*: generators are not ideal voltage sources. Their accurate modelling (including controllers) is important for correctly assessing voltage stability.

Alternatively, the Cigre Task Force 38-02-10 [15] considers the power system as a dynamic system and embraces definitions of stability for dynamic systems. From this point of view, several aspects of voltage stability are defined as follows:

- ***Small-disturbance voltage stability:***

  > *A power system at a given operating state is small-disturbance voltage stable if, following any small disturbance, voltages near loads are identical or close to the pre-disturbance values. (Small-disturbance voltage stability corresponds to a related linearized dynamic model with eigenvalues having negative real parts. For analysis, discontinuous models for tap changers may have to be replaced with equivalent continuous models.)*

- ***Voltage stability***

  > *A power system at a given operating state and subject to a given disturbance is voltage stable if voltages near loads approach post-disturbance equilibrium values. The disturbed state is within the region of attraction of the stable post-disturbance equilibrium.*

- ***Voltage instability***

  > *Voltage instability is the absence of voltage stability, and results in progressive voltage decrease (or increase). Destabilizing controls reaching limits, or other control actions (e.g., load disconnection), however, may estalish global stability.*

- ***Voltage collapse***

  > *Following voltage instability, a power system undergoes voltage collapse if the post-disturbance equilibrium voltages near loads are below acceptable limits. Voltage collapse may be total (blackout) or partial.*

2.2.2 Classification and time scale of voltage stability

As shown in Fig. 2.1, voltage stability is categorized as a large- and small-disturbance phenomenon. The large-disturbance stability considers the effect of large disturbances such as outage of generators, faults and changes of network topology on voltage stability of power systems. On the other hand, small-disturbance stability is related to impact

of small perturbations, like load increase, on the system's capability to maintain voltage stability.

Regarding the time scale, voltage stability may be divided into two categories: transient or short term and long-term stability as illustrated in Fig. 2.2. The former has the time response about several seconds, and the latter can vary from several seconds to many minutes, typically two to three minutes [1].

Transient voltage stability involves fast acting components, such as induction machines, generator excitation, SVCs, HVDC substations and protective relays, which may cause a sudden increase or loss in reactive power. The long-term instability on the other hand is influenced by several factors. After the system survives the transient voltage stability, slow load recovery and operation of OLTCs can cause more stress on the network. During this period, the system operation goes through critical phases under condition of highly complex reactions and interactions among electrical components, intervention of system operators and other factors.

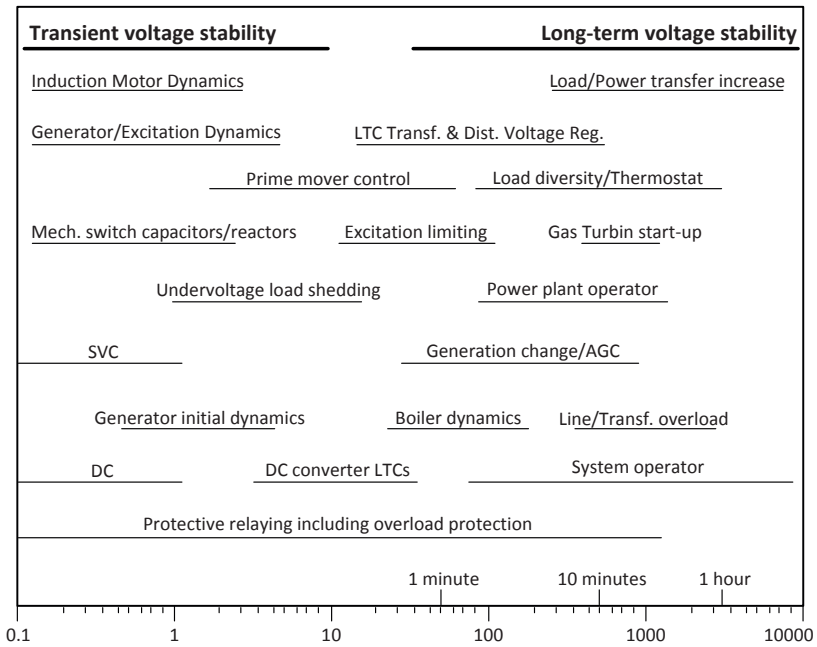

Figure 2.2: Voltage stability phenomena and time scale [1].

2.3 Key features in voltage stability

2.3.1 Generator

Synchronous generators are the main reactive power sources used to control voltage in power systems. The machine is able to inject or absorb reactive power smoothly to regulate its terminal voltage as desired. As observed from many voltage collapse incidents in the past [2–5], lack of reactive power support from generators or disconnection of the

machine was one of the main causes of voltage instability. Reactive power is controlled by means of adjusting the field current, which is carried out by the automatic voltage regulator (AVR) as shown in Fig. 2.3. As operated in voltage control mode, the AVR senses the generator terminal voltage and compares this value with the reference voltage. If mismatch between the two quantities appears, the AVR will adjust the field current to eliminate the error. The time response of AVR is from 100ms to some seconds [16].

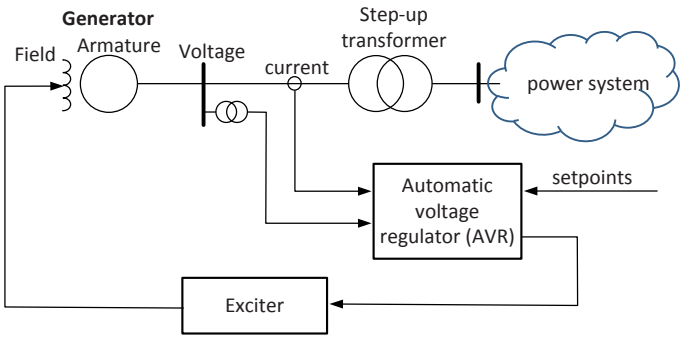

Figure 2.3: Schematic diagram of AVR.

Although synchronous machines are a powerful tool to control voltage, they also have certain physical limits. Therefore, the machine is equipped with protective relays or other functions to maintain operating parameters within its constraints. These factors have a large impact on voltage instability; hence they should be taken into consideration. The two protective functions that have influence on voltage control are overexcitation limiter (OXL) and armature current limiter as shown in Fig. 2.4. When terminal voltage is around the nominal value, the maximum limit on reactive power is normally set by the OXL. In case the terminal voltage is low (normally in critical conditions), armature heating is the one that imposes the limit.

- **Overexcitation limiter**: the field winding is designed to work under a certain current limit. The machine is also allowed to operate at higher field current, but within a certain time limit. Otherwise, the winding will be overheated and damaged. The overload capability is defined by the standard IEEE Std C.50.13-2014 [17] as shown in Fig. 2.5a. This curve passes the following four points as listed in the table below.

Time (s)	10	30	60	120
Rotor current (percent)	209	146	125	113

  The OXL continuously measures the field current and compares it to the predefined threshold. If the current has been above the limit for a period of time, which is longer than the predefined time delay, the OXL will act through the voltage regulator to bring the field current back to the limit. The delay time can be fixed time (for old exciters) or inverse time, which is a function of field current. To protect the generator from overheating, the OXL curve must be coordinated with the thermal capability curve of the field winding, ensuring that the field current cannot reach the thermal limit.

The OXL has an important role in voltage instability. When the system is approaching voltage collapse, demand for reactive power rises significantly. Generators consequently increase their reactive power to maintain the terminal voltage until the OXL is activated. After this event, the field voltage (or current) is kept constant at the permissible maximum limit; generators are no longer able to maintain the terminal voltage while the demand is still rising. As a result, voltages in the grid drop more drastically and the pace of voltage collapse is accelerated.

- **Armature current limiter**: similar to the field winding, the armature winding is also protected against overheating. As the limiter detects that the armature current is above the limit, it will act through the voltage regulator to reduce reactive power output by means of decreasing the field current. The thermal overload capability of armature winding is defined in [17]. The capacity curve is illustrated in Fig. 2.5b. This curve also goes through the following points as listed in the table below.

Time (s)	10	30	60	120
Armature current (percent)	218	150	127	115

As seen in Fig. 2.4, the limit on armature current becomes the active constraint when terminal voltage is low, after the generator has reached the excitation limit. When the system is on the brink of voltage instability, the armature current deteriorates the situation further because it decreases the machine's reactive power output, causing further voltage drop and speeding up the voltage stability problem.

Although the armature current limiter is one of the constraints, it can be utilized to mitigate voltage instability. The study in [18] has shown that under the active constraint set by armature current, adapting active and reactive power of the local generator is able to maximize power transfer, hence possibly preventing voltage collapse at the local concerned load.

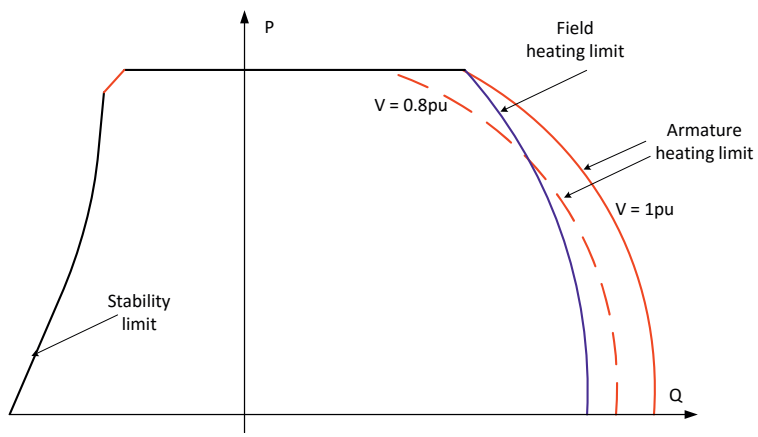

Figure 2.4: Simplified generator capacity curve [14, 19, 20].

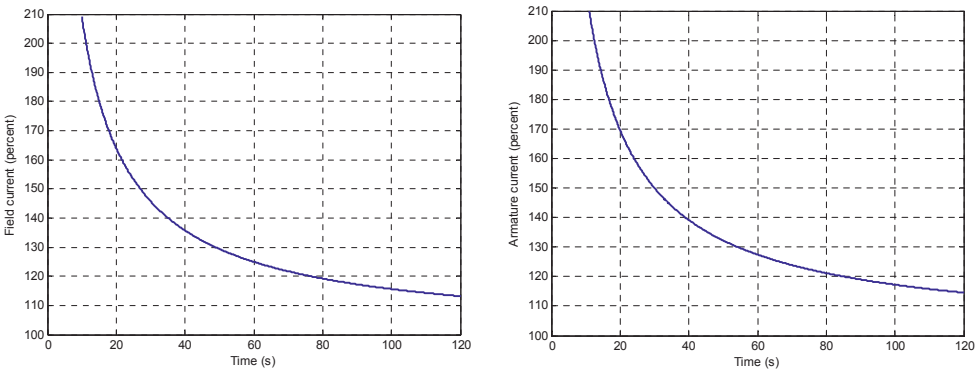

(a) Overexcitation limit. **(b)** Armature current limit.

Figure 2.5: Thermal limit of the field and armature windings [17].

2.3.2 Network

2.3.2.1 The PV curve

In power systems, energy is transported from power plants to loads through a network of power lines. Since the transportation incurs losses due to the line impedances, voltage drop and maximum power transfer are heavily dependent on the strength of the network. Consider a simple system shown in Fig. 2.6, where the load is supplied by the infinite system represented by an ideal voltage source $\vec{E}_{Th} = E_{Th}\angle 0$. The transmission line is considered as lossless and treated as a reactance jX_{Th}. According to the Kirchhoff's law, the load voltage $\vec{V} = V\angle\delta$ is calculated as

$$\vec{V} = \vec{E}_{Th} - jX_{Th}\vec{I} \tag{2.1}$$

and the load power is

$$\begin{aligned} \bar{S} = P + jQ = \vec{V}\vec{I}^* &= \vec{V}\frac{\vec{E}^*_{Th} - \vec{V}^*}{-jX_{Th}} \\ &= \frac{j}{X_{Th}}\left(E_{Th}V\cos\delta + jE_{Th}V\sin\delta - V^2\right) \end{aligned} \tag{2.2}$$

From (2.2), the load active and reactive power are extracted as

$$P = -\frac{E_{Th}V}{X_{Th}}\sin\delta \tag{2.3a}$$

$$Q = -\frac{V^2}{X_{Th}} + \frac{E_{Th}V}{X_{Th}}\cos\delta \tag{2.3b}$$

Using the relation $\sin^2\delta + \cos^2\delta = 1$, one can eliminate δ in (2.3a) and (2.3b) and obtain

$$(V^2)^2 + (2QX_{Th} - E^2_{Th})V^2 + X^2_{Th}(P^2 + Q^2) = 0 \tag{2.4}$$

This equation is a quadratic equation in V^2. To obtain a physically meaningful solution for the voltage magnitude V, one of the conditions, which must be fulfilled, is

$$(2QX_{Th} - E^2_{Th})^2 - 4X^2_{Th}(P^2 + Q^2) \geq 0 \tag{2.5}$$

Then, the solution for (2.4) is found as [14]

$$V = \sqrt{\frac{E_{Th}^2}{2} - QX_{Th} \pm \sqrt{\frac{E_{Th}^4}{4} - X_{Th}^2 P^2 - X_{Th} E_{Th}^2 Q}} \tag{2.6}$$

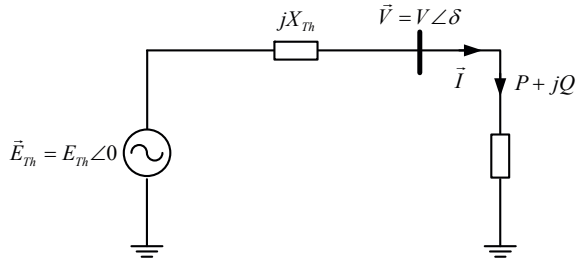

Figure 2.6: A two-bus system.

Assuming that the ideal voltage source $\vec{E}_{Th}$ is known, the load voltage is a function of the load active and reactive power. Let the reactive power be $Q = P \tan\phi$, where ϕ is the power factor angle. Equation (2.6) becomes

$$V = \sqrt{\frac{E_{Th}^2}{2} - PX_{Th} \tan\phi \pm \sqrt{\frac{E_{Th}^4}{4} - X_{Th}^2 P^2 - X_{Th} E_{Th}^2 P \tan\phi}} \tag{2.7}$$

Normalizing (2.7) by $v = V/E_{Th}$ and $p = PX_{Th}/E_{Th}^2$ yields

$$v = \sqrt{\frac{1}{2} - p\ \tan\phi \pm \sqrt{\frac{1}{4} - p^2 - p\ \tan\phi}} \tag{2.8}$$

Based on (2.8), the well-known PV curve is established and presented in Fig. 2.7. The PV curve is a useful tool to obtain insights into voltage stability and provides a good explanation about this phenomenon:

- As the load power increases, the load voltage drops accordingly (if $\tan\phi \geq 0$). The load power can grow until it reaches the limit - the maximum loadability (this point is also called the nose point). Here, the limit is imposed by the network; it is the line impedance jX_{Th}, which results in voltage drop and losses on the transmission network. Consequently, the maximum power transferred to the load is limited.

- After the load has crossed the nose point, the system cannot supply more power to the load. If the demand continues to increase, the load power does not rise. On the contrary, it drops, and so does the load voltage. The instant voltage instability occurs depends on the load dynamic characteristics; it is the time when the operating point no longer exists. For example, an induction motor stalls when it does not provide sufficient torque to meet the mechanical demand under low voltage condition. It is noted that although "permanent operation at the lower solutions is unacceptable" [14], the system can be stably operated in this area under certain circumstances. For instance, there is no voltage instability if the load is an impedance. Therefore, it is not precise to call the lower part of the PV curve the unstable region.

- In case the load is overcompensated ($\tan\phi < 0$), voltage will increase as the load power rises. This results from the assumption that the load has constant power factor. In practice, overcompensation frequently takes place, but not in the manner of constant power factor. Reactive power is increased gradually to keep the voltage (not power factor) within the permissible limit. Nevertheless, it is worth noticing that the voltage instability can arise at nominal voltage when the load is overcompensated. This makes the voltage magnitude a poor indicator for voltage stability assessment.

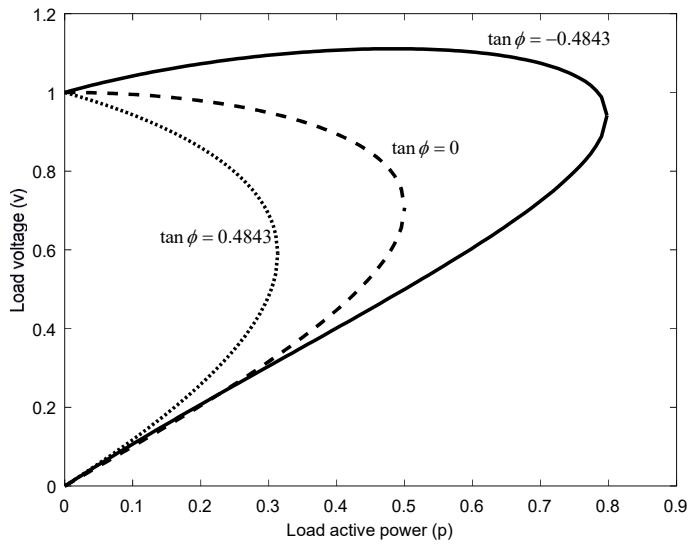

Figure 2.7: The well-known normalized PV curves.

The maximum loadability is the critical point, representing the transfer capacity of the grid. To assess voltage stability at a load bus, it is necessary to identify the maximum power, which the load can draw from the network. As can be seen in Fig. 2.7, at the maximum loadability point, there is only one solution for the voltage V. That means, at this point, the condition (2.5) now becomes

$$(2Q_{max}X_{Th} - E_{Th}^2)^2 - 4X_{Th}^2(P_{max}^2 + Q_{max}^2) = 0 \tag{2.9}$$

where P_{max} and Q_{max} are active and reactive power at the maximum loadability point, respectively.
After the insertion of $Q_{max} = P_{max}\tan\phi$ into (2.9) and rearrangement, it leads to

$$4X_{Th}^2P_{max}^2 + 4X_{Th}E_{Th}^2\tan\phi P_{max} - E_{Th}^4 = 0 \tag{2.10}$$

Once this quadratic equation in P_{max} is solved, P_{max}, which must be a positive number, is identified as:

$$P_{max} = \frac{E_{Th}^2}{2X_{Th}}(-\tan\phi + \sqrt{1+\tan^2\phi}) \tag{2.11}$$

Further simplification gives

$$P_{max} = \frac{E_{Th}^2}{2X_{Th}}(\frac{1-\sin\phi}{\cos\phi}) \tag{2.12}$$

Consequently, the normalized maximum active power of the PV curve is

$$p_{\max} = \frac{1}{2}(\frac{1-\sin\phi}{\cos\phi}) \tag{2.13}$$

2.3.2.2 The QV curve

Reactive power is highly related to voltage; variation of this power at a load bus affects not only the voltage but also the maximum power transfer limit at that bus. The QV curve is a tool to gain the insights into this relation. Based on (2.8), one can establish the relation between load voltage and reactive power as [21]:

$$v^2 = \frac{-(2q-1) \pm \sqrt{(2q-1)^2 - 4(p^2+q^2)}}{2} \tag{2.14}$$

where q is the normalized reactive power defined by $q = QX_{Th}/E_{Th}^2$ and p is the normalized active power as defined in the above section about the PV curve.

To analyze the effect of reactive power on the voltage, let p be assumed unchanged and q be considered negative if the load absorbs reactive power. For each given value of p, the QV curve is computed by (2.14) and plotted in Fig. 2.8. At a given loading condition of active power, the QV curve provides information about the required reactive power to keep the load voltage at the desired value. In normal operation, the operating point is located on the right portion of the curve, where voltage will increase if more reactive power is injected and vice versa. It is noted that the angle of the slope of the curve or the derivative dq/dv is quite large at the current operating point, meaning that variation of reactive power has small impact on the voltage. As reactive power goes down, voltage becomes more and more sensitive to change of reactive power. At the the critical point where $dq/dv = 0$, the maximum loadability limit is reached; the system cannot supply more power as demanded. This point is actually equivalent to the nose point of the PV curve, and the segment on the left of this point is equivalent to the lower part of the PV curve.

Based on the QV curve, the margin of reactive power is easily computed. It is the distance between the reactive power at the current operating point and that at the critical point. The margin indicates the local reserve of reactive power at the considered bus in order to meet the current demand of active power. From (2.14), the critical point is obtained by letting the term in the square root equal to zero, which gives

$$q_{crit} = \frac{1}{4} - p^2 \tag{2.15}$$

and

$$v_{crit} = \sqrt{\frac{1}{2}(1-2q_{crit})} \tag{2.16}$$

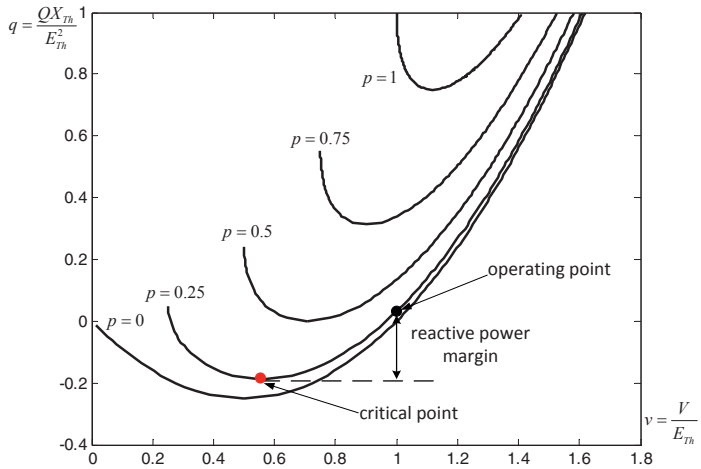

Figure 2.8: The QV curves.

2.3.3 Load dynamics

Load dynamics is a key element in voltage instability. After a severe disturbance like outage of a large generator or tripping of an important line, the system can establish a new stable operating point at lower voltage level. Since most of loads are dependent on the voltage, load power at lower voltage normally becomes smaller. Due to the dynamic characteristics, the demand tends to restore its power to the pre-event level. This causes higher stress on the grid, which has been weakened by the disturbance. As a result, the increasing demand can go beyond the maximum power transfer limit, pushing the operating point to the lower part of the PV curve.

2.3.3.1 Onload tap changer (OLTC)

OLTC is equipment used to regulate voltage at one side of power transformers. OLTC plays an important role in voltage instability; it has large contribution to the load restoration, which is illustrated in Fig. 2.9. This issue has been studied by many works; among these, [23] and [24] provide a deep insight into the matter. Before a disturbance, the system is operating at point O. After a disturbance, the system is characterized by a new PV curve and a new operating point is established at the intersection of the PV curve and the demand curve (point A). At this point, voltage falls below the lower limit of the deadband; load power also drops. However, after a predefined time delay, the OLTC starts tapping to restore the voltage. This action increases the power demand drawn from the system. As a result, voltage in the grid falls further. This in turn triggers further tapping of the OLTC. Consequently, the operating point moves from A to B. The process goes on until voltage instability occurs or the OLTC reaches its limit. With such characteristics, the OLTC speeds up the load restoration process and accelerates the pace of voltage instability. Therefore, under low voltage conditions, OLTC should be blocked to prevent voltage collapse.

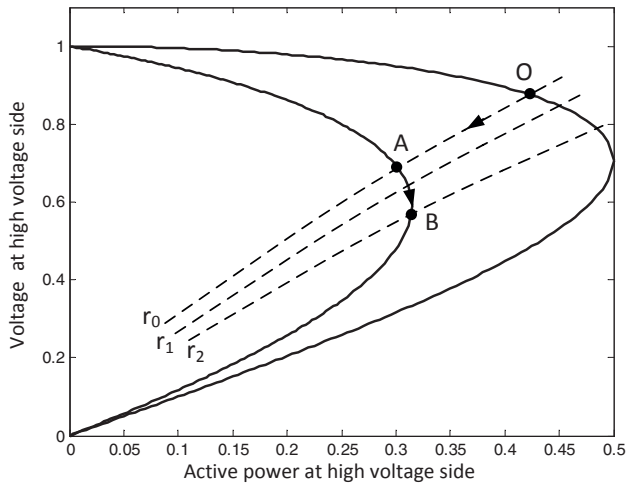

Figure 2.9: Illustration of impact of OLTC on voltage instability [14].

2.3.3.2 Thermostat-controlled load

Thermostat-controlled load is a heating system, which is controlled by a thermostat. This device has the main function to keep temperature at desired value. To maintain the reference temperature, the thermostat switches the heater on during a certain period (t_{on}); in the rest of the cycle, the heater is off. When the grid voltage drops below the nominal value, the load power during the period t_{on} is reduced, not sufficient to maintain the temperature. Consequently, the thermostat increases t_{on} to draw more power from the system. The lower the voltage, the higher t_{on}. From the grid side, thermostat-controlled load acts like a constant power load with large time response, contributing to the whole load recovery process.

2.3.3.3 Static load models

In general, loads are dependent on voltage. As voltage changes, load power also varies accordingly. However, this relationship is very complex. As seen from the system side, loads comprise a very large number of electric devices, such as motors, fridges, washing machines, fluorescent lamps, heaters, computers, compressors, furnaces, etc. Each device has its own characteristics with respect to voltage. In addition, load composition is unknown; it also changes from time to time. These features make it impractical to fully represent all types of loads in voltage stability analysis. Therefore, it is useful to represent the load characteristics by simple static models, in which active and reactive power are separately modeled as functions of voltage.

- ***Exponential model***: this model is a widely used one, in which the relationship between power and voltage is determined by [11]:

$$P = P_0 \left(\frac{V}{V_0}\right)^a \tag{2.17}$$

$$Q = Q_0 \left(\frac{V}{V_0}\right)^b \tag{2.18}$$

where P_0 and Q_0 are active and reactive power at the initial voltage V_0; the exponent a and b determine the load model. For instance, the load is considered as constant power, constant current or constant impedance if a and b are equal to 0, 1 or 2, respectively. In case the load has none of these types, a and b can take other values that match the actual load behaviors, which is illustrated in Table 2.1 [14].

Table 2.1: An example of fractional load exponents [14]

Load component	a	b
Incandescent lamps	1.54	-
Room air conditioner	0.50	2.5
Furnace fan	0.08	1.6
Battery charger	2.59	4.06
Electronic compact fluorescent	0.95-1.03	0.31-0.46
Conventional fluorescent	2.07	3.21

- ***Polynomial model***: this model is commonly known as the ZIP model since active and reactive power consist of the three components of constant impedance, constant current and constant power, which are defined as

$$P = P_0 \left(p_1 \left(\frac{V}{V_0}\right)^2 + p_2 \frac{V}{V_0} + p_3\right) \tag{2.19}$$

$$Q = Q_0 \left(q_1 \left(\frac{V}{V_0}\right)^2 + q_2 \frac{V}{V_0} + q_3\right) \tag{2.20}$$

where p_1, p_2 and p_3 define the percentage of each component in active power; q_1, q_2 and q_3 have the same meaning for reactive power.

2.4 Countermeasures against voltage collapse

In essence, voltage instability is caused by excessive demand that exceeds the system transfer capacity. This leads to disconnection of power system components and finally ends up with a blackout in the affected area. As the system is approaching voltage collapse, countermeasures against voltage collapse are actions that help the grid increase transfer capacity and reduce or slow down load demand during the critical period. This issue has been thoroughly examined and presented in several works [1, 11, 14, 30–36].

2.4.1 Switching of reactive power compensation

- Shunt capacitors are widely used by utilities to increase transfer capacity and improve the voltage profile throughout the network, ranging from the transmission system down to the distribution grid. In normal operation, not all capacitor banks are connected. Depending on the loading condition, a certain number of capacitor banks are selected; some are in service and others can be switched out. Therefore, to mitigate voltage instability, capacitor banks in the affected area should be switched in as soon as possible to increase the network capacity and improve the voltage profile.

- SVC and STATCOM are fast-acting devices. They are effective instruments to prevent short-term voltage instability. To maximize the device effectiveness, their reactive power reserve should be maintained at a certain level. This requirement is not always fulfilled in normal operation. Since the main function of SVC/STATCOM is to regulate the voltage, in some cases, they can run out of reserve of reactive power for emergency control. Moreover, the number of these shunt compensation systems deployed in power systems has been increased in recent years. This opens up possibilities to coordinate VAr resources in order to maintain sufficient dynamic VAr reserve to cope with voltage collapse, especially the short-term instability. This issue is addressed in Chapter 6.

- Shunt reactor is used in the transmission system to absorb reactive power generated by long and lightly loaded transmission lines. In case voltage instability is about to occur, disconnection of this component reduces reactive power demand and improves the voltage profile and power transfer capacity.

2.4.2 Blocking OLTC operation

- Operation of OLTC has been observed as one of the main actors that drive the system to voltage collapse. As mentioned in the above section, OLTC operation, in an effort to restore voltage at the distribution side, increases power demand. This action imposes more stress on the network, further deteriorating the voltage and finally causing cascading tripping and blackout. Blocking OLTC operation suppresses the load recovery process; therefore, system operators have more time to perform other remedial actions to prevent voltage collapse.

2.4.3 Actions on generation

- Start-up of gas turbine of local power plants and synchronous condenser: long-term voltage instability is a slow process. It has the time response up to one hour or even more. This period is long enough to start up local gas turbines and synchronous condensers, which are not in operation. This action is one of the most effective remedial measures against voltage collapse. Once these machines have been in operation, their reactive power output is an important resource to alleviate the critical operation condition in the grid.

- Increase of voltage setpoint: this action is valid for generators that have not reached the capacity limits. Increase of the voltage setpoint will result in a higher reactive

power output from the generator and raise voltages in the network. This in turn helps shunt capacitors inject more reactive power into the grid. However, reactive power can be increased to a certain level, where the OXL starts taking effect and then keeps the field current at the maximum permissible limit. From this time on, the excitation is kept unchanged although reactive power output can increase if voltage in the grid continues dropping.

- Adjustment of generator's output power: those generators, which are located in the area vulnerable to voltage instability, have a certain degree of freedom to mitigate voltage collapse. They can, within the capacity curve, adjust both active and reactive power to increase maximum loadability of the network. This aspect has been studied by [18]. Illustration of this idea is presented in Fig. 2.10. Assume that point 1 is the current operating point. If the generator delivers maximum active power at point 2, active power transmitted from remote areas is reduced. This might increase loadability. But at the same time the generator must reduce its reactive power output. This leads to voltage drop in the load area and consequently lowers the transfer capacity. At point 3, the local generator injects more reactive power, but less active power. Both operating points 2 and 3 have impact on the network's maximum loadability. To conclude which action is more effective, it depends on other factors, for example: output power of other generators in the concerned area, location of the most vulnerable load bus, load dynamics, network topology, etc. To solve the problem, one might need optimization approaches. Here, the challenges are the robustness of the optimization algorithms, reliability of data management to obtain full observability and limited time to find solutions while the system is changing quickly and approaching the critical point of voltage collapse.

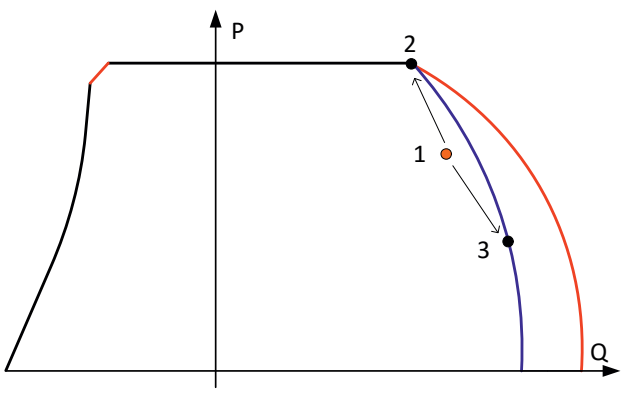

Figure 2.10: Adjustment of generator's output power to mitigate voltage instability.

2.4.4 Undervoltage protection

It has been observed in the past that voltage collapse occurred at low voltage level. Hence, it is reasonable to use voltage magnitude as a criterion to shed loads in order to prevent voltage instability. If voltage drops below the threshold and remains low

continuously during the predefined time delay, the undervoltage protection will operate and shed a certain amount of load, which has been determined in advance. Since the demand falls, the voltages will be restored and the system comes back to normal operation. This is the main idea of the approach. However, the challenge is how to determine properly the threshold for voltage magnitude; this quantity is a poor indicator for voltage stability assessment. Voltage magnitude at the maximum power transfer condition varies under different operating conditions; it can be low, but also can be high if the system is overcompensated. Using voltage magnitude to shed loads could lead to unnecessary or untimely load shedding. The next challenge is related to how to identify minimum amount of loads that needs to be shed. These challenges have been addressed and presented in several works [31, 32, 34–36]. In addition, selectivity is also another challenge while using undervoltage protection as a countermeasure against voltage instability. Voltages in the affected area can be low, but it does not mean that all the loads have crossed the maximum loadability.

2.5 Voltage stability analysis

2.5.1 Continuation power flow

As presented in Section 2.3.2, the maximum loadability point (the nose point) is the critical point; operation beyond this point can lead to voltage instability. Estimating the margin between the current operating point and the maximum power transfer gives an indication of voltage stability at the considered load bus. This task cannot however be done by conventional power flow methods. The challenge is that power flow calculation has convergence problems when load is approaching the maximum loadability. It is because the Jacobian becomes singular at the nose point. Continuation power flow is a well-known method, which can overcome this challenge [11, 21, 37]. Recently, another power flow based method has been proposed. To tackle the singularity problem, this new approach introduces a new type of bus called AQ bus, whose voltage phase angle and reactive power must be specified. Details of the algorithm are presented in [38].

The main idea behind the continuation power flow method is to reformulate the power flow equations by adding a new variable called the load parameter and a new row into the Jacobian matrix. With this modification, the Jacobian matrix is not singular at the maximum power transfer condition. The approach is an iterative process as illustrated in Fig. 2.11. First, the tangent vector at the current operating point (point A) is computed by the predictor. In this step, loads are increased by a small predefined amount, and then variation of the state variables caused by the load increase are detected (point B). In the next step, the corrector finds a new operating point (point C), assuming that one state variable or the loading level is fixed to the value found by the predictor. The approach to obtain state variables in this step is the conventional power flow algorithm with minor modification of the Jacobian matrix. After the new operating point is determined, the process advances with a repetitive cycle of prediction and correction until the PV curve is complete.

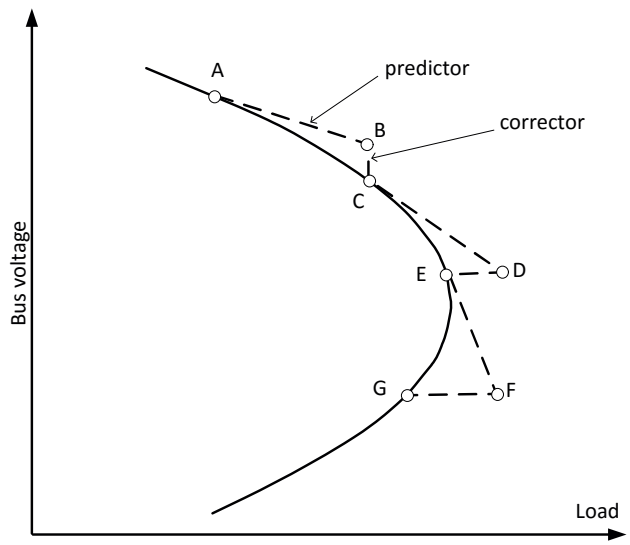

Figure 2.11: Description of the continuation power flow method.

2.5.1.1 Mathematical formulation

One of the principles used in conventional power flow is that the sum of all power injection into each node in the network must be equal to zero, which is mathematically expressed as [37]

$$P_{G_i} - P_{L_i} - P_{T_i} = 0, P_{T_i} = \sum_{j=1}^{n} V_i V_j y_{ij} \cos(\delta_i - \delta_j - \nu_{ij}) \tag{2.21}$$

$$Q_{G_i} - Q_{L_i} - Q_{T_i} = 0, Q_{T_i} = \sum_{j=1}^{n} V_i V_j y_{ij} \sin(\delta_i - \delta_j - \nu_{ij}) \tag{2.22}$$

for each bus i of a n-bus system, where P is active power, Q is reactive power, and the subscripts L, G and T denote load, generation and flow, respectively. Meanwhile, voltages at bus i and j are $V_i\angle\delta_i$ and $V_j\angle\delta_j$, and $y_{ij}\angle\nu_{ij}$ is the admittance of the line connecting bus i and bus j.
Considering the whole system, power flow equations can take a general expression as

$$\mathrm{F}(\delta, V) = 0 \tag{2.23}$$

Let κ represent the load parameter in the way that

$$0 \leq \kappa \leq \kappa_{critical} \tag{2.24}$$

where $\kappa = 0$ corresponds to the base case and $\kappa = \kappa_{critical}$ represents the maximum power transfer condition.

One of the reasons to introduce κ is to involve the increase of load and generation in the power flow equation as expressed in the following formulation:

$$P_{Li}(\kappa) = P_{Li0}\left[1 + \kappa K_{Li}\right] \tag{2.25}$$
$$Q_{Li}(\kappa) = P_{Li0}\tan\phi_i\left[1 + \kappa K_{Li}\right] \tag{2.26}$$
$$P_{Gi}(\kappa) = P_{Gi0}\left[1 + \kappa K_{Gi}\right] \tag{2.27}$$

where P_{Li0} and Q_{Li0} are active and reactive power of the load, ϕ_i is the power factor angle of load change at bus i, and P_{Gi0} is generation active power at bus i in the base case. The constant K_{Li} and K_{Gi} are used to specify the rate of change of load and generation power at bus i, respectively. It is noted that the number of buses involved in the variation of the load and generation power is not limited; one can select as many buses as desired. Now, the modified power flow equations can be expressed in the form of

$$\mathrm{F}(\delta, V, \kappa) = 0 \tag{2.28}$$

Predictor

The main purpose of this step is to find deviation of the state variables in response to the small variation of either loading condition (the load parameter κ) or a state variable (V or δ). Taking the derivatives of two sides of (2.28) with respect to the state variables and κ gives

$$F_\delta d\delta + F_V dV + F_\kappa d\kappa = 0 \tag{2.29}$$

or

$$\left[F_\delta \; F_V \; F_\kappa\right] \begin{bmatrix} d\delta \\ dV \\ d\kappa \end{bmatrix} = 0 \tag{2.30}$$

The vector $[d\delta \; dV \; d\kappa]^T$ is called the tangent vector, which is to be sought in the predictor step. In (2.30), κ is an additional unknown. Therefore, to solve this equation, one more equation is needed. This challenge is overcome by setting one element in the tangent vector equal to +1 or -1. This element is called the contiuation parameter. Inserting the new equation into (2.30) yields

$$\begin{bmatrix} F_\delta & F_V & F_\kappa \\ & e_k & \end{bmatrix} \begin{bmatrix} d\delta \\ dV \\ d\kappa \end{bmatrix} = \begin{bmatrix} 0 \\ \pm 1 \end{bmatrix} \tag{2.31}$$

where e_k is a row vector, which has the kth element equal to 1 (this element corresponds to the continuation parameter) and all other elements are equal to zero. After this modification, (2.31) is solvable, consequently giving solution to the tangent vector $[d\delta \; dV \; d\kappa]^T$. Based on this information, all the state variables and κ are advanced by

$$\begin{bmatrix} \delta \\ V \\ \kappa \end{bmatrix} = \begin{bmatrix} \delta_0 \\ V_0 \\ \kappa_0 \end{bmatrix} + \sigma \begin{bmatrix} d\delta \\ dV \\ d\kappa \end{bmatrix} \tag{2.32}$$

where the subscript "$_0$" denotes the operating point at the beginning of the predictor step (point A or C or E, etc. in Fig. 2.11), and σ is a constant that decides the step size. The result obtained from this step is point B (or D or F, etc). It is then used for the next corrector step.

Corrector

In this step, the continuation parameter is kept equal to the value determined in the previous step. The objective here is to identify the values of the other variables. This task is done by solving the following equation:

$$\begin{bmatrix} F(\delta, V, \kappa) \\ x_k - \mu \end{bmatrix} = \begin{bmatrix} 0 \end{bmatrix} \tag{2.33}$$

where x_k is the continuation parameter and μ is its value obtained in the predictor step. Compared to the set of equations in the conventional power flow methods, (2.33) has only one difference; it has one additional equation and one more variable. Applying the Newton-Raphson method, the problem can be formulated as

$$\begin{bmatrix} J_V & J_\delta & J_\kappa \\ & e_k & \end{bmatrix} \begin{bmatrix} d\delta \\ dV \\ d\kappa \end{bmatrix} = \begin{bmatrix} \Delta P \\ \Delta Q \\ 0 \end{bmatrix} \tag{2.34}$$

where J_V, J_δ and J_κ constitute the Jacobian matrix with respect to the state variables and κ; e_k is the row vector mentioned in (2.31). This problem is solved as it is done in the conventional power flow method. Once all the state variables and κ are identified, the continuation process continues with a new sequence of the predictor and corrector steps until the maximum loadability point is reached. Details of the continuation power flow method are thoroughly presented in [21, 37].

2.5.2 Steady state analysis

2.5.2.1 V-Q sensitivity analysis

As observed from the QV curve shown in Fig. 2.8, the variation of voltage magnitude at a bus with respect to that of the reactive power injection at that bus indicates the degree of voltage stability. In normal operation, this sensitivity ($\Delta V/\Delta Q$) is small, meaning that the load power is far from the maximum loadability. As the load approaches the voltage stability limit, the sensitivity increases significantly; this value is going to infinite at the nose point, after that it will become negative.

At a particular operating point, the linear relation between power and voltage can be described as:

$$\begin{bmatrix} \Delta P \\ \Delta Q \end{bmatrix} = \begin{bmatrix} J_{P\delta} & J_{PV} \\ J_{Q\delta} & J_{QV} \end{bmatrix} \begin{bmatrix} \Delta\delta \\ \Delta V \end{bmatrix} \tag{2.35}$$

where

ΔP = incremental change of active power
ΔQ = incremental change reactive power
$\Delta\delta$ = incremental change of voltage angle
ΔV = incremental change of voltage magnitude

To obtain the V-Q sensitivity, let $\Delta P = 0$. This results in [11]

$$\Delta Q = J_R \Delta V \tag{2.36}$$

where the reduced Jacobian matrix J_R is defined as

$$J_R = \left[J_{QV} - J_{Q\delta} J_{P\delta}^{-1} J_{PV} \right] \tag{2.37}$$

From (2.36), the V-Q sensitivity is found as

$$\Delta V = J_R^{-1} \Delta Q \tag{2.38}$$

The diagonal of the matrix J_R^{-1} contains the information about the sensitivity $\Delta V / \Delta Q$ at all the buses in the network. The sensitivity at bus i is indeed the (i^{th}, i^{th}) element on the diagonal of the matrix.

2.5.2.2 V-Q modal analysis

The reduced Jacobian matrix J_R contains information about correlations between voltages and reactive power injection throughout the network. Hence, its eigenvalues and eigenvectors indicate the degree of voltage stability at load buses in the grid. This matrix can be expressed as [39]

$$J_R = \xi \Lambda \eta \tag{2.39}$$

where
ξ is the right eigenvector matrix of J_R
η is the left eigenvector matrix of J_R
Λ is the diagonal eigenvalue matrix of J_R

From (2.39), the matrix J_R^{-1} is computed by

$$J_R^{-1} = \xi \Lambda^{-1} \eta \tag{2.40}$$

Replacing J_R^{-1} in (2.36) results in

$$\Delta V = \xi \Lambda^{-1} \eta \Delta Q \tag{2.41}$$

or

$$\Delta V = \sum_i \frac{\xi_i \eta_i}{\lambda_i} \Delta Q \tag{2.42}$$

where ξ_i is the ith column right eigenvector and η the ith row left eigenvector of J_R

Inserting $\xi^{-1} = \eta$ into (2.41) gives

$$\eta \Delta V = \Lambda^{-1} \eta \Delta Q \tag{2.43}$$

or

$$v = \Lambda^{-1} q \tag{2.44}$$

where
$v = \eta \Delta V$ is the vector of modal voltage variations
$q = \eta \Delta Q$ is the vector of modal reactive power variations

Since Λ^{-1} is the diagonal matrix, from (2.44) the following relation for the ith mode holds

$$v_i = \frac{1}{\lambda_i} q_i \tag{2.45}$$

where λ is the ith eigenvalue.

In this equation, the sign of λ_i can be used to evaluate voltage instability of the grid. If $\lambda_i > 0$, variations of reactive power and voltage are in the same direction. This means the system is stable. On the contrary, $\lambda_i < 0$ indicates that the system is unstable. In addition, the magnitude of λ_i reflects the degree of stability of the ith modal voltage. In normal operation, λ is positive. As the system is approaching voltage instability, the magnitude of λ becomes smaller and smaller until it it reaches zero, which is the limit of voltage instability.

2.6 Online voltage stability assessment

2.6.1 Principle of Thevenin equivalent-based methods for online voltage stability assessment

The idea of using the Thevenin impedance to establish an indicator for online voltage stability assessment based on phasor measurements was proposed by [40]. The notion has initiated several works from researchers in the field, including this PhD project. Consider a particular load bus in the grid. The rest of the system can be represented by a Thevenin voltage source $\vec{E}_{Th}$ behind the Thevenin impedance $\bar{Z}_{Th}$ as illustrated in Fig. 2.12. According to the maximum power transfer theorem [41], when the load power reaches the the maximum loadability, the magnitude of load impedance is equal to that of the Thevenin impedance:

$$Z_L = Z_{Th} \tag{2.46}$$

Therefore, by comparing the magnitude of the two impedances, one can establish an indicator for voltage stability. This indicator [42] is called the Impedance Stability Index (ISI) and defined by

$$\text{ISI} = \frac{Z_{Th}}{Z_L} \tag{2.47}$$

With this indicator, ISI = 1 is the limit when the load is located at the nose point. In normal operation, ISI < 1.

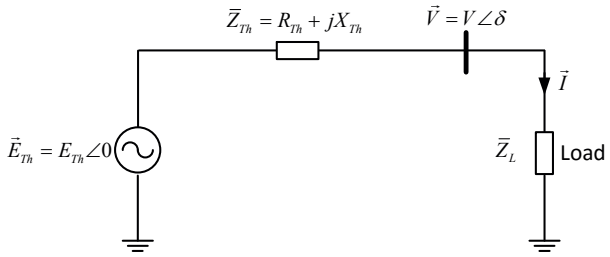

Figure 2.12: Thevenin equivalent of power system seen at a load bus.

Furthermore, when the $\bar{Z}_{Th}$ is known, the Thevenin voltage source can be identified by

$$\vec{E}_{Th} = \vec{V} + \vec{I}\bar{Z}_{Th} \tag{2.48}$$

where $\vec{V}$ and $\vec{I}$ are voltage and current of the load, respectively.
Given the Thevenin equivalent, it is possible to estimate the maximum loadability by assuming that the magnitude of the load is equal to that of the Thevenin impedance. This results in [43]

$$S_{max} = \frac{E_{Th}^2 \left[Z_{Th} - (\text{imag}(\bar{Z}_{Th}) \sin\phi + \text{real}(\bar{Z}_{Th}) \cos\phi\right]}{2 \left[\text{imag}(\bar{Z}_{Th}) \cos\phi - \text{real}(\bar{Z}_{Th}) \sin\phi\right]^2} \tag{2.49}$$

where S_{max} is the estimated maximum loadability, ϕ is the power factor angle. After crossing the maximum loadability, voltage collapse can occur at a certain instant of time, depending on the load characteristics. Different load models may exhibit different voltage collapse scenarios. Nonetheless, operation beyond the limit is not expected. From the voltage stability monitoring point of view, it is reasonable to consider the maximum power transfer as the limit for voltage stability. Thus, the distance from the current operating point to voltage stability limit is the power margin to the estimated maximum loadability determined by [43]

$$Power\ margin = \frac{S_{max} - S_L}{S_L} \times 100\% \tag{2.50}$$

where S_L is the current apparent power of the load.

Alternatively, [44] computes the power margin by

$$Power\ margin = \frac{(V - Z_{Th} I)^2}{4 Z_{Th}} \tag{2.51}$$

In summary, the main task of online voltage stability assessment based on the Thevenin equivalent is to estimate properly the Thevenin impedance of the rest of the system. Then, assisted by local phasor measurements of voltage and current of the load, the maximum power transfer is computed. Finally, the indicator for real time voltage stability monitoring is established either by comparing the magnitude of load impedance to that of the Thevenin impedance by (2.47) or by identifying power margin by (2.49) and (2.50) or (2.51). Overall, the essence of the method is to estimate appropriately in real time the Thevenin impedance seen at a load bus.

2.6.2 Voltage instability predictor (VIP)

2.6.2.1 Description of the VIP method

The VIP method evaluates voltage instability in real time by continuously tracking the Thevenin impedance and comparing its magnitude with that of the load impedance [40, 44–46]. The idea is illustrated in Fig. 2.13. In normal operation, the magnitude of load impedance stays outside the circle, whose radius is the magnitude of the estimated Thevenin impedance. The maximum power transfer condition occurs when the load reaches the edge of the circle.
Denoting $\vec{E}_{Th} = E_{Thr} + jE_{Thi}$, $\vec{V} = V_r + jV_i$ and $\vec{I} = I_r + jI_i$, (2.48) can be expressed as

$$\begin{bmatrix} 1 & 0 & -I_r & I_i \\ 0 & 1 & -I_i & -I_r \end{bmatrix} \times \begin{bmatrix} E_{Thr} \\ E_{Thi} \\ R_{Th} \\ X_{Th} \end{bmatrix} = \begin{bmatrix} V_r \\ V_i \end{bmatrix} \tag{2.52}$$

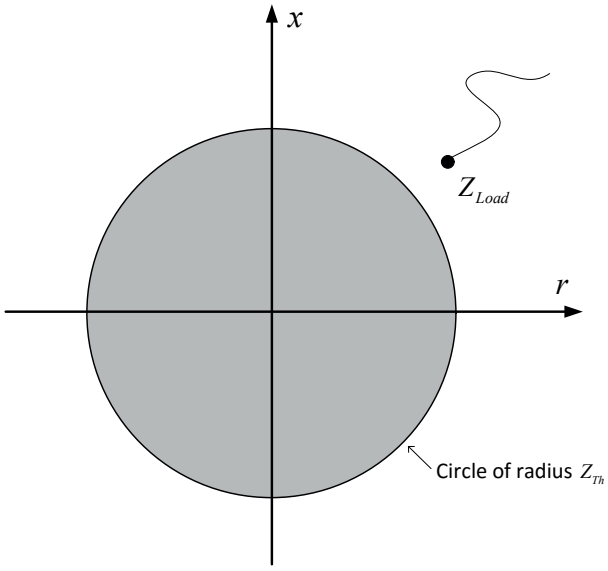

Figure 2.13: Voltage instability monitoring based on the Thevenin impedance [45].

In this equation, V_r, V_i, I_r and I_i are directly obtained from local phasor measurements of the load current and voltage. Here, the unknowns are E_{Thr}, E_{Thi}, R_{Th} and X_{Th}. To find the solution for (2.52), at least two measurements at different time instants are needed. However, to minimize errors caused by measurement accuracy, noise, system's transients, etc., several measurements over an observation window time are needed to form an overdetermined set of equations. Then, it is possible to apply the least-squares method to estimate the unknowns.

2.6.2.2 Comparison of the VIP and undervoltage load shedding

Undervoltage load shedding is often used to prevent voltage collapse. The principle is that the relay compares the measured voltage with the fixed threshold. If the voltage drops and stays continuously below the threshold during a certain period (time delay), the relay will shed a predefined block of load as a remedial action to prevent voltage instability. However, as discussed in Section 2.4, voltage magnitude is a poor indicator for voltage instability. Voltage collapse can occur at different voltage levels, depending on the operating conditions and reactive power reserve in the grid. In some cases, voltage instability can even take place at nominal voltage when the system is overcompensated by capacitors. To demonstrate this issue, let the operation of undervoltage protection be mapped into the impedance plane.

From Fig. 2.12, this relation holds

$$\frac{E_{Th}}{V} = \frac{E_{Th}/I}{V/I} = \frac{\left|\bar{Z}_L + \bar{Z}_{Th}\right|}{Z_L} \tag{2.53}$$

Assume that the setpoint for the undervoltage protection is 0.95 pu and the magnitude of the Thevenin voltage is 1.05 pu. The protection will operate when $V < 0.95$. In other

words, when

$$\frac{\left|\bar{Z}_L + \bar{Z}_{Th}\right|}{Z_L} > \frac{1.05}{0.95} = 1.105 \tag{2.54}$$

This condition is represented by the undervoltage protection circle, whose radius is 1.105, in the impedance plane. Fig. 2.14 shows the relative position of this circle and the Thevenin one. As can be seen, in case of load trajectory 1, the relay does not work properly; it operates and sheds load when the maximum loadability has not been reached yet. But in case 2, the relay cannot recognize the risk of voltage collapse when maximum power transfer limit has been crossed.

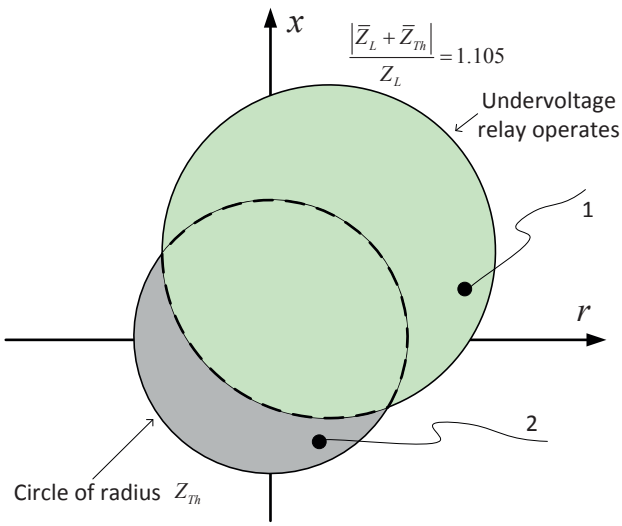

Figure 2.14: Illustration of maloperation of undervoltage protection [45].

2.6.3 The CT method

The CT method [47] is an approach to estimate the Thevenin impedance used to form an indicator for online voltage instability monitoring. This algorithm assumes that the Thevenin impedance is a pure reactance. Hence, it is suitable for networks, where the Thevenin impedance has a high X_{Th}/R_{Th} ratio (ratio of reactance to resistance). Detail of this issue is presented in [48].

The CT method is based on an adaptive estimation process, in which E_{Th} and X_{Th} are consecutively corrected based on previous estimation and present measurements of current and voltage. Consider Fig. 2.12, where the Thevenin voltage in this section is expressed as $\vec{E} = E_{Th}\angle\beta$, the load voltage is $\vec{V} = V\angle\phi$ and the load current is $\vec{I} = I\angle 0^0$. The relation between voltages and current in (2.48) can be described by the phasor diagram shown in Fig. 2.15, where

$$\vec{V}_\Delta = \bar{Z}_{Th}\vec{I} = R_{Th}I + jX_{Th}I \tag{2.55}$$

$$\vec{E}_{Th} = \vec{V} + \vec{V}_\Delta \tag{2.56}$$

Splitting (2.55) into the real and imaginary part results in

$$E_{Th}\cos\beta = R_{Th}I + V\cos\phi \tag{2.57}$$

$$E_{Th}\sin\beta = X_{Th}I + V\sin\phi \tag{2.58}$$

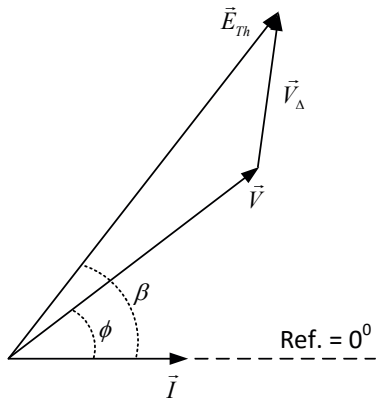

Figure 2.15: Phasor diagram of voltages and current in Fig. 2.12 [47].

To estimate X_{Th}, β and E_{Th} need to be identified. In transmission systems, it is normally true that $X_{Th} \gg R_{Th}$. Therefore, it is reasonable to assume $R_{Th} = 0$. Consequently, initial estimation of β is obtained from (2.57) as

$$\beta = \arccos\left(\frac{V\cos\phi}{E_{Th}}\right) \tag{2.59}$$

Although E_{Th} is initially unknown, it must follow electric circuit laws. In other words, this value is bounded by E_{min} and E_{max}, which correspond to the following conditions:

- E_{min}: the Thevenin voltage must be higher than the load voltage. Therefore, it is reasonable to let

$$E_{\min} = V \tag{2.60}$$

- $E_{\max}$: assume that the current operating point is the nose point, where

$$X_{Th} = Z_L$$

Consequently, $E_{\max}$ can be computed as

$$E_{\max} = \frac{V\cos\phi}{\cos\beta} \tag{2.61}$$

where β is obtained from

$$\tan\beta = \frac{Z_L I + V\sin\phi}{V\cos\phi} \tag{2.62}$$

The Thevenin voltage at the current operating point must be within the range from E_{min} to E_{max}. Thus, it is reasonable to estimate the initial value of this quantity as the average of the two limits:

$$E_{Th}^0 = \frac{E_{max} - E_{min}}{2} \tag{2.63}$$

After E_{Th}^0 is estimated, the initial value of β^0 can be computed by (2.59) and then X_{Th}^0 by (2.58). When a new set of measurements is available (say i^{th} measurements), E_{Th}^0 and β^0, along with the new measurements, are used to compute intermediate estimation of the Thevenin impedance X_{Th}^{i*}. As proven in [47], given two consecutive measurements ($(i-1)^{th}$ and $(i)^{th}$), comparison of the variations of magnitude of load impedance ($Z_L^i - Z_L^{i-1}$) and that of the Thevenin impedance ($X_{Th}^{i*} - X_{Th}^{i-1}$) determines how the magnitude of the Thevenin voltage of the previous step is adjusted:

$$E_{Th}^i = E_{Th}^{i-1} \pm \varepsilon_E \tag{2.64}$$

where ε_E is defined as

$$\varepsilon_E = \min(\varepsilon_{inf}, \varepsilon_{sup}, \varepsilon_{lim}) \tag{2.65}$$

with

$$\varepsilon_{inf} = \left|E_{Th}^{i-1} - V^i\right| \tag{2.66}$$
$$\varepsilon_{sup} = \left|E_{Th}^{i-1} - E_{max}^i\right| \tag{2.67}$$
$$\varepsilon_{lim} = \left|E_{Th}^{i-1} \times k\right| \tag{2.68}$$

It is noted that the coefficient k in (2.68) is a setting parameter, which is used to bound the identification error within a narrow band. This parameter has a decisive role in the performance of the algorithm. A large value of k reduces the initialization period and helps the method converge, but it results in more oscillatory estimation. A small k, however, prolongs the initialization time, but produces smoother estimation. But in many cases, the result cannot converge to the actual Thevenin impedance if k is too small. Therefore, the setting of k is vital to obtaining an appropriate estimation of the Thevenin equivalent; it depends on specific location of the considered load, where the algorithm is deployed. Normally, k is in the range of 0.01% to 0.1% [47].

In summary, detailed implementation of the CT method includes the following steps [47]:

1. **Step 1:** Compute initial estimation of E_{Th}^0 by (2.63) and β^0 by (2.59).
2. **Step 2:** Identify X_{Th}^0 by (2.58).
3. **Step 3:** Compute E_{Th}^i based on the conditions:
   - If $(Z_L^i - Z_L^{i-1}) < 0$
     - If $(X_{Th}^{i*} - X_{Th}^{i-1}) < 0$ then $E_{Th}^i = E_{Th}^{i-1} - \varepsilon_E$
     - If $(X_{Th}^{i*} - X_{Th}^{i-1}) > 0$ then $E_{Th}^i = E_{Th}^{i-1} + \varepsilon_E$
   - If $(Z_{Load}^i - Z_{Load}^{i-1}) > 0$
     - If $(X_{Th}^{i*} - X_{Th}^{i-1}) < 0$ then $E_{Th}^i = E_{Th}^{i-1} + \varepsilon_E$
     - If $(X_{Th}^{i*} - X_{Th}^{i-1}) > 0$ then $E_{Th}^i = E_{Th}^{i-1} - \varepsilon_E$
   - If $(Z_L^i - Z_L^{i-1}) = 0$
     - $E_{Th}^i = E_{Th}^{i-1}$

4. **Step 4:** Compute β^i and X_{Th}^i by (2.59) and (2.58) with the updated Thevenin voltage E_{Th}^i, respectively.

5. **Step 5:** As new phasor measurements of load voltage and current are available, go back to Step 3 to obtain a new estimation.

It is noted that X_{Th}^{i*} is intermediate identification of X_{Th}. It is derived from (2.58) as

$$X_{Th}^{i*} = \frac{E_{Th}^{i-1} \sin \beta^{i-1} - V^i \sin \phi^i}{I^i} \tag{2.69}$$

where E_{Th}^{i-1} and β^{i-1} are from the previous stage, but voltage and current are obtained from the current measurements.

2.7 Discussion on methods for voltage stability assessment in the literature and online voltage stability monitoring

Online monitoring is an important tool for secure operation of power systems. For practical implementations of online voltage stability assessment, one of the constraints is the computation time. To be used online, the monitoring scheme must be fast enough to evaluate the current operation state of the system. In addition, the application should be able not only to assess stability of the present operating condition, but also to determine the distance between the current operating point and the limits. Regarding these issues, there are some challenges related to the implementation of the methods in the literature as tools for online voltage stability assessment:

- In the continuation power flow method, in order to detect the nose point at a load bus, power flow calculation must be conducted several times. The computational burden increases if there are more load buses needed to be monitored. Furthermore, power systems nowadays are large and normally interconnected. Implementation of the continuation power flow method in such systems incurs enormous computational cost. This might make the method not fast enough for online applications.

- The V-Q sensitivity analysis detects voltage stability limit by computing incremental change of voltage and reactive power of the considered load, assuming that the active power in the system is unchanged. As the load is approaching the voltage stability limit, the sensitivity increases significantly before it becomes negative after the load has crossed the nose point. One limitation of the method is that it cannot determine the operational margin of the current operating point. For system operators, such indication of the margin, e.g. power margin, is really helpful. In addition, a challenge in this approach is that the sensitivity is computed from the Jacobian matrix of the entire system. Errors in data management in the SCADA/EMS system can make the matrix incorrect, and consequently lead to wrong assessment of voltage stability. Besides, how to determine the threshold for the sensitivity is also another challenge. In order to detect voltage stability timely, the threshold should be set appropriately, depending on location of the monitored bus. Moreover, one can also notice that inverting a large matrix is time-consuming. This task increases computation time

of the method and might make the approach implausible for online implementation. Compared to the V-Q sensitivity analysis, the V-Q modal analysis method shares similar philosophy; therefore, it has similar limitations as the other.

- In the VIP method, the Thevenin impedance is used for online voltage stability monitoring in power systems. The VIP algorithm is simple to implement and requires only local phasor measurements of the load current and voltage. The essence of this method is using consecutive phasor measurements to build an over-determined set of equations and then obtaining the best solution by the least squares method. However, in normal operation, variation of the load current and voltage is quite small; it is also distorted by disturbances in the grid, noise, and errors of measurement instruments, etc. As a result, the variation of the local measurements do not always reflect the true response of the system. Using these local measurements to find the Thevenin parameters by the least squares method, therefore, has some problems. Probably, considerable disturbances are prerequisites for good performance. This is also the major challenge for methods based on local phasors.

- The CT method also utilizes local phasor measurements to estimate the Thevenin equivalent by an adaptive process. Its performance has been well demonstrated by simulation of the Italian transmission grid [47]. The algorithm is also tested with real PMU data in the Brazilian power system [49], showing practical possibility for online implementation in power systems. However, similar to other methods based on only local PMU measurements, disturbances in the grid, noise, and errors of measurement instruments, etc. might affect the performance of the algorithm. More test cases with real PMU data are needed to validate the effectiveness of this methodology.

2.8 Major blackouts in power systems and the role of load curtailment based on voltage instability indicators

2.8.1 Major blackouts in power systems

Blackouts in power systems are a result of a complex process, which normally involves many factors and phenomena. In this section, recent blackouts are briefly described, just to demonstrate the role of voltage instability in these extraordinary events. Details of these incidents are presented in [1–5].

2.8.1.1 The blackout in southern Sweden and eastern Denmark in 2003

The blackout in southern Sweden and eastern Denmark occurred on September 23, 2003 [4]. The Swedish power system was in the operating condition, where large generation was mainly in the north, but the main load area was located in the south. Therefore, large amount of energy was transported over long transmission lines. The blackout took place in the southern part due to critical disturbances. The initial event was the loss of a 1200 MW generation unit at the load center at 12:30. After this incident, the grid went through a transient period of less than one minute and became stable; voltage profile

and frequency were still within limits. However, at 12:35, a double busbar fault occurred and caused another loss of two generation units with total power of 1750 MW. This event pushed the system into critical operating condition: underfrequency and very low voltage. When the frequency went down to slightly over 49 Hz, underfrequency protection started operating and shed loads. However, the grid was still heavily overloaded. The voltage in the affected area in south-east and south-central remained very low. This triggered operation of numerous number of OLTCs to restore the voltage at the load side. Action of OLTCs and load recovery deteriorated the critical situation further; voltages in the affected area became lower and lower. It is noted that in the load area, there were no large generators, which could be used to mitigate the problem.
Due to low voltage and high current, distance relays tripped circuit breakers and therefore lines were disconnected. As a result, the network was split into two areas. One of them did not have enough capacity to meet the demand. As a result, voltage and frequency plummeted, leading to the blackout.

2.8.1.2 The blackout in North America in 2003

This incident occurred on August 14, 2003 and affected large areas in the US and Canada [2, 3]. The initial disturbances were the loss of a generator at 13:31 due to high reactive power output and the tripping of several lines due to tree contact. Disconnection of these lines weakened the strength of the network and worsened the operating condition. After theses events, the grid no longer tolerated more disturbances and became vulnerable.
After the initial disturbances, loss of the a 345 kV line (Sammis-Star) triggered cascading tripping in the network. This line was tripped at 16:05:57 by Zone 3 of the distance relay due to overload current and depressed voltage although there was no fault on the line. “Prior to the Sammis-Star tripping, the blackout could have been prevented by load shedding in northeast Ohio” [3].

Following this event, several lines were also tripped by the same type of relay. As a result, direction of power flow of 3700 MW was reversed; the new long transfer path resulted in voltage collapse and consequently cascading tripping of several hundred lines and generators and led to the blackout in the region.

2.8.1.3 The blackout in Italy in 2003

The blackout in Italy occurred on September 28, 2003 [3, 5–7]. Before the incident, the Italian power system had large import of 6651 MW from Switzerland, France, Austria and Slovenia. Therefore, tripping of tie lines and lack of management initiated cascading tripping of all the other tie lines. This led to large imbalance of active power and consequently underfrequency problems and others.

At 3:01, a 380 kV tie line between Italy and Switzerland was tripped and could not be reclosed due to large angle difference between voltages at the to ends. Shortly later, all the tie lines between Italy and Switzerland were also tripped due to overload. The loss of imported power from Switzerland resulted in an increase of power transfer on the tie lines between Italy and France. This led to voltage stability problem on these corridors; voltage fell sharply to 300 kV at some 380 kV buses in the French network [7]. As a result, the tie line between France and Italy was tripped at 3:25:32 by the distance relay. This event was followed by cascading tripping of the rest of the tie lines between Italy

and neighboring countries, which finished at 3:25. From this moment the Italian network was isolated from the UCTE grid.

After separation from the European system, there was a deficit of 6646 MW in the Italian grid. Although underfrequency protection and other defense schemes had shed the loads, the deficit still remained. It led to tripping of many generators due to underfrequency, undervoltage and other protection functions. This finally led to the blackout.

2.8.2 Role of load shedding based on voltage stability indicators

As presented in the previous section, the blackouts in Sweden and North America are typical examples of voltage instability phenomenon in power systems. After disturbances, transfer capacity of the network is reduced and voltage is at low level. Then the load restoration aggravates the problem by the increasing demand. As a result, voltage becomes lower and lower. This can cause maloperation of the Zone 3 function of the distance relay. Several lines are tripped although there are no faults on the lines. The maloperation of protective relays is the critical factor. The disconnection of lines weakens the strength of the network and consequently speeds up voltage instability.

Although the blackout in Italy was mainly driven by the underfrequency problem due to a deficit of active power, voltage instability was also involved. Tripping of the tie lines between France and Italy was one of the important events, which contributed to the separation of the Italian network from the UCTE interconnected system. This line was also tripped by the distance relay due to high current and low voltage.

Generally, power systems can be decomposed into generation, loads, network (power lines) and interconnections with external grid as illustrated in Fig. 2.16. Blackout in an affected area is the situation where the area is isolated from the rest of the system and all local generators and many lines are disconnected. These components are tripped automatically by protective relays. Therefore, to prevent blackout when the system is in the emergency state, generators and lines should stay connected (except they are faulty or being damaged). If remedial measures are not sufficient to bring the system back to normal condition, load shedding is an effective measure to prevent the collapse.

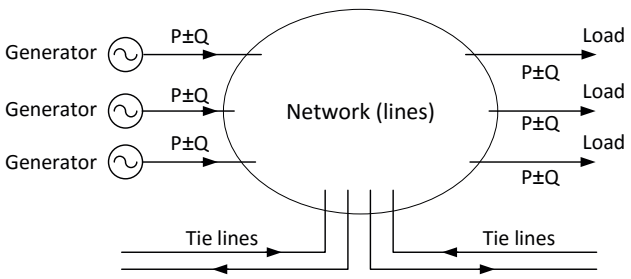

Figure 2.16: Example of power system structure.

As observed from previous blackouts, apart from the overloading issue, the disturbances finally led to the lack of active or reactive power or both, which was the main cause of stability problems. Generators were tripped by underfrequency and undervoltage protection; lines were commonly tripped by the distance relay due to low voltage and high current. The underfrequency issue is related to the imbalance of active power. This

problem can be solved by load shedding based on underfrequency protection, assuming that the setting is appropriate.

On the other hand, lack of reactive power results in low voltage condition, which can lead to malfunction of protective relays and overloading problems. As presented in Section 2.3.2, loads that have crossed the maximum loadability have lower power but cause very high losses in the network due to high current. The excessive portion of these loads should be shed to alleviate the critical situation the grid is facing. Fast load shedding based on voltage stability indicators is one of effective countermeasures to prevent blackouts by containing the excessive load recovery and avoiding wrong tripping of lines and generators.

As discussed in Section 2.4.4, load shedding based on undervoltage protection is one of the remedial measures to prevent voltage instability. But voltage magnitude is a poor indicator for voltage instability; it cannot distinguish whether or not loads have crossed the maximum loadability. Hence, undervoltage protection is not selective with regard to voltage stability limit. In addition, this protection cannot detect the excessive amount of loads that need to be shed. As the operating condition continuously changes, fixed setting of load shedding is not always an optimum approach; the amount of load going to be shed could be less than the required or more than needed. Therefore, it is necessary to have an online indicator, which is able to: i) assess properly voltage stability at each load bus; and ii) quantify maximum loadability and excessive load demand. This tool is definitely a useful measure for load shedding to prevent voltage collapse or blackout in power systems.

Conventionally, the distribution grid is treated as a load when the analysis of stability in transmission system is conducted. However, in the smart grid context, this notion no longer holds true because load is no longer passive. The distribution grid, to some extent, has the possibility to adjust the power exchange with the transmission grid thanks to presence of energy storage, distributed generation and large number of electric vehicles. To secure operation of the entire system, it could be impractical to take both transmission and distribution grids into calculation, especially when the system becomes more and more complex. To simplify security assessment of the two networks, it is useful to have a tool that can assess critical operating conditions in the transmission system. The assessment is then used as a criterion for corrective actions taken in the distribution grid. In this scenario, online voltage stability indicator is a necessary tool. The indicator provides information about the transfer capacity of the transmission system, which can be used to control the charging and discharging of batteries and other types of energy storage. By properly coordinated actions from both sides (transmission and distribution), voltage collapse and load shedding could be prevented. This could contribute to building resilient and complex power systems in the future.

Chapter 3

Online voltage stability monitoring and protection based on local PMU measurements

In the PhD project, an approach to estimate, in real time, the Thevenin impedance seen at a load bus and a new indicator for online voltage stability monitoring have been developed. With the proposed algorithm, the Thevenin impedance can be estimated properly and robustly in real time, and the new indicator is formed based on computation of the derivative of apparent power of the load with respect to the magnitude of its impedance. This indicator can detect properly an occurrence of the maximum power transfer condition, which is widely acknowledged as the limit for voltage stability. Additionally, it is able to identify and illustrate graphically a trajectory of the current operating point with respect to the maximum loadability. The method shows a good performance with simulation data as well as with real PMU measurements in the Norwegian transmission system. The proposed algorithm is simple and requires only phasor measurements of the load current and voltage. Therefore, it is easily implemented in a wide area monitoring and protection system or used as a protective function for voltage instability protection within an intelligent electronic device (IED).

The chapter begins with a detailed description of the method to estimate the Thevenin impedance in real time. Then, the indicator for online voltage stability assessment is described. In the next section, applications of the new indicator are presented. The chapter continues with a load curtailment scheme for voltage instability protection and ends with a short description of signal filtering.

3.1 Estimation of the Thevenin impedance based on S-Z sensitivity: the S-Z method

3.1.1 Estimation of the Thevenin impedance

To model an equivalent circuit of the grid seen at a particular load bus, the rest of the system is normally represented by a voltage source $\vec{E}_{Th}$ behind the Thevenin inpedance $\bar{Z}_{Th}$ as shown in Fig. 3.1, where the load is considered as the impedance $\bar{Z}_L$. Here, the voltage source $\vec{E}_{Th}$ is treated as the reference phasor, and hence its phase angle is equal

to zero, $\vec{E}_{Th} = E_{Th}\angle 0$.

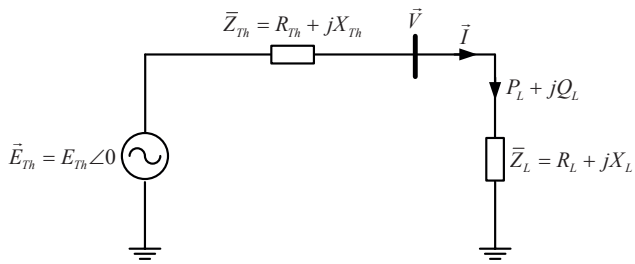

Figure 3.1: The Thevenin equivalent circuit.

Based on the circuit, the magnitude of the load current is

$$I = \frac{E_{Th}}{\sqrt{(R_L + R_{Th})^2 + (X_L + X_{Th})^2}}, \tag{3.1}$$

or

$$I = \frac{E_{Th}}{\sqrt{Z_{Th}^2 + Z_L^2 + 2\left(R_L R_{Th} + X_L X_{Th}\right)}}, \tag{3.2}$$

where Z_L and Z_{Th} are the magnitudes of $\bar{Z}_L$ and $\bar{Z}_{Th}$, respectively. It is noted that $R_L R_{Th} + X_L X_{Th}$ is the scalar product of $\bar{Z}_{Th}$ and $\bar{Z}_L$. Therefore, this relation holds:

$$R_L R_{Th} + X_L X_{Th} = Z_L Z_{Th} \cos\theta, \tag{3.3}$$

where θ is the angle between $\bar{Z}_{Th}$ and $\bar{Z}_L$. Inserting (3.3) into (3.2) yields

$$I = \frac{E_{Th}}{\sqrt{Z_{Th}^2 + Z_L^2 + 2Z_L Z_{Th}\cos\theta}}. \tag{3.4}$$

Consequently, apparent power of the load is formulated as

$$S_L = I^2 Z_L = \frac{E_{Th}^2 Z_L}{Z_{Th}^2 + Z_L^2 + 2Z_L Z_{Th}\cos\theta}. \tag{3.5}$$

Since $\vec{E}_{Th}$ and $\bar{Z}_{Th}$ are the Thevenin voltage and impedance seen at the load bus, during a short period of time, it is reasonable to assume that $\vec{E}_{Th}$ and $\bar{Z}_{Th}$ are constant. In addition, $\cos\theta$ is also assumed unchanged. From (3.5), the derivative of the apparent power with respect to magnitude of the load impedance is

$$\frac{dS_L}{dZ_L} = \frac{E_{Th}^2\left(Z_{Th}^2 - Z_L^2\right)}{\left(Z_L^2 + Z_{Th}^2 + 2Z_L Z_{Th}\cos\theta\right)^2}. \tag{3.6}$$

Substituting E_{Th} in (3.6) by (3.2) leads to

$$\frac{dS_L}{dZ_L} = \frac{I^2\left(Z_{Th}^2 - Z_L^2\right)}{Z_L^2 + Z_{Th}^2 + 2Z_L Z_{Th}\cos\theta} \tag{3.7}$$

Define $\zeta = \dfrac{dS_L}{dZ_L}$, which is also called S-Z sensitivity. Rearranging (3.7) yields

$$\left(I^2 - \zeta\right) Z_{Th}^2 - 2\zeta \cos\theta Z_L Z_{Th} - Z_L^2 \left(I^2 + \zeta^2\right) = 0. \tag{3.8}$$

In (3.8), Z_{Th} is considered as an unknown. If the other parameters are known, solving (3.8) will give the magnitude of the Thevenin impedance seen at the load bus. Indeed, this solution is viable thanks to the following features:

- Magnitudes of the load current I and impedance Z_L are easily obtained from phasor measurements of the load current and voltage.
- Variations of the apparent power dS_L and impedance dZ_L are obtainable by using consecutive phasor measurements of the load current and voltage. Consequently, ζ (the S-Z sensitivity) is identified.
- As previously defined, θ is the angle between $\bar{Z}_L$ and $\bar{Z}_{Th}$. Based on local phasor measurements, the phase angle of the load impedance is easily computed. The angle θ is obtainable if the phase angle of the Thevenin impedance is known. As it will be analyzed in Chapter 4, the Thevenin impedance seen at a load bus is mainly determined by impedance of power lines in the studied area, where the load is connected. Therefore, it is reasonable to use a typical ratio X/R of the lines in that area to determine, in advance, the phase angle of the Thevenin impedance. This ratio is mainly dependent on the voltage level of the studied area although other factors (configuration of the lines, towers, cross-section of conductors, adjacent lines, etc.) have a certain impact.

After all the parameters are identified, (3.8) is solved to find the magnitude of the Thevenin impedance Z_{Th}, which must be a real and positive number.

3.1.2 Impact of the ratio X_{Th}/R_{Th}

As presented, the phase angle (or the ratio X_{Th}/R_{Th}) of the Thevenin impedance must be identified before this impedance can be estimated. Determination of this ratio has a certain influence on the estimated value. For illustration, the Thevenin impedance of the Norwegian transmission system seen at the Halse corridor between Norway and Sweden is estimated, using PMU measurements on the 420 kV tie lines. First, the ratio $X_{Th}/R_{Th} = 15$ is selected, which results in $Z_{Th} = 33.18\ \Omega$. For comparison, this value is considered as the reference magnitude of the Thevenin impedance. After that, the ratio X_{Th}/R_{Th} is adjusted to analyze its impact on the Thevenin impedance. As shown in Fig. 3.2, when X_{Th}/R_{Th} varies from 10 to 30, there is a rather small variation of the estimated Thevenin impedance, just less than 5% of the reference. However, the deviation increases sharply when the ratio becomes smaller than 10.

In summary, the ratio X_{Th}/R_{Th} is a setting parameter in the proposed algorithm. An incorrect ratio can lead to a large error in the estimation. Although this ratio of the Thevenin impedance seen at a particular load bus is unknown, it can be identified. First, this parameter can take a typical ratio X/R of the power lines in the studied area. Then, the ratio will be adjusted appropriately by comparing the trajectory of the S-Z sensitivity obtained from the estimated Thevenin impedance with the actual value of the S-Z sensitivity computed from measurements of the load current and voltage, which will be presented in Section 3.2.

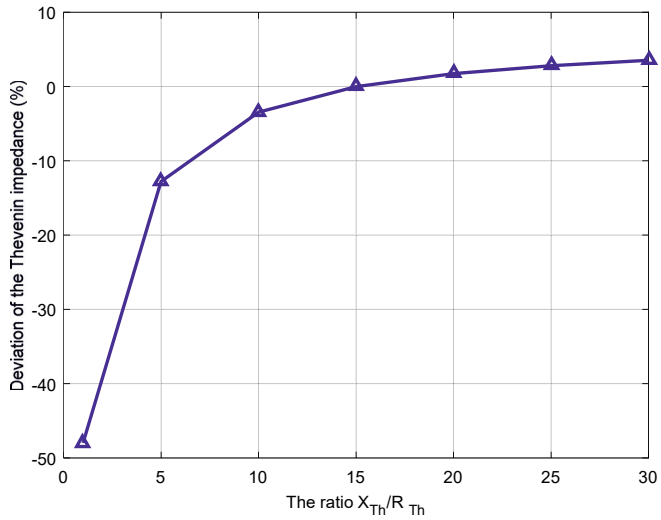

Figure 3.2: Impact of the ratio X_{Th}/R_{Th} on the estimated Thevenin impedance.

3.1.3 Impact of abrupt variations of the load current

Under transient conditions, the roots of (3.8) can be complex numbers, which do not have a physical meaning. These values are not correct and should be, therefore, neglected. This case might occur during the time the system is experiencing large disturbances like short circuits or switchings, which result in abrupt variations of the load current. Fig. 3.3 shows how the estimated Thevenin impedance varies when magnitude of the load current in (3.8) are altered from the actual measured value while the other parameters are kept unchanged. As can be seen, the load current has a very large impact on the estimated value. Especially, when the current is smaller than 90% of the actual value, (3.8) does not have meaningful solutions; its roots become complex.

3.2 S-Z sensitivity used as a new indicator for online voltage stability monitoring

3.2.1 S-Z sensitivity indicator (S-ZI)

In Fig. 2.7, the well-known PV curve reflects a relationship between the load voltage and active power. In the upper section of the curve, the power can increase, but the voltage will drop accordingly. However, due to losses on the line impedance represented by Z_{Th}, the power can grow until it reaches the maximum loadability (the "nose" point). Beyond this point, the system cannot supply more power, and the active power, therefore, starts to decrease despite the rising demand (lower load impedance).

It is noted that, in power systems, the PV curve is not as ideal as shown in Fig. 2.7. Reference [50] presents different shapes of the PV curve when dynamic behaviors of electric equipment in the grid (load characteristics, operation of OLTCs, overexcitation limiters, etc.) are considered. However, in spite of the differences among the PV curves, the maximum power transfer point is still the critical point. In [51], it is pointed out that

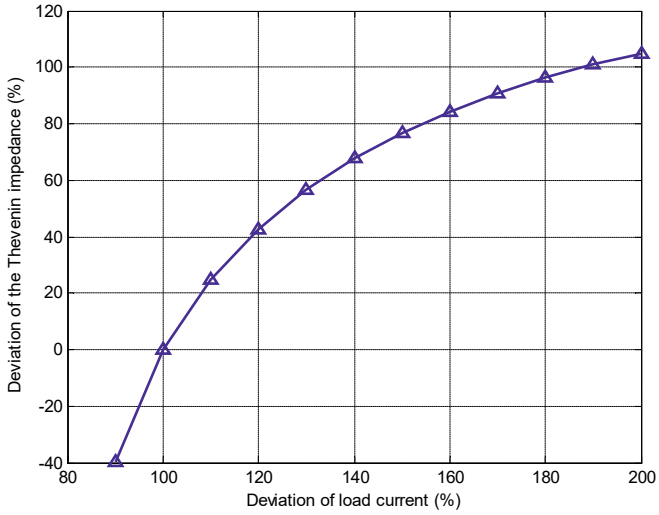

Figure 3.3: Impact of deviation of load current on the estimated Thevenin impedance.

voltage collapse can occur at this point or at a particular point on the lower part of the curve, depending on the load characteristics. These features pose challenges for methods using the PV curve to detect the voltage stability limit. From a viewpoint of long-term voltage stability monitoring, it is reasonable to consider the maximum loadability point as the limit for voltage stability. Operation beyond this limit has lower power, lower voltage and causes more losses. Eventually, it is very likely that this operation condition will lead to voltage instability.

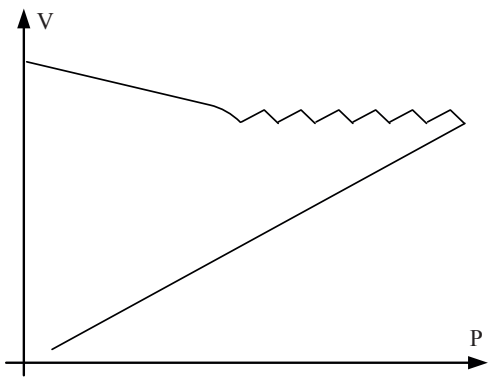

Figure 3.4: Sketch of another shape of the PV curve [50].

As observed in Fig. 2.7, in the upper section of the PV curve, when the load requires more power from the grid, this demand will be met. But in the lower section of the curve, the response from the grid is opposite. Here, the maximum power transfer point is the border of these two operation conditions. This feature forms an idea for a new indicator for voltage stability monitoring. Let a deviation of the magnitude of the load impedance (dZ_L) represent the demand and a corresponding deviation of apparent power of the load

(dS_L) account for the response of the grid. Consider the S-Z sensitivity as a new indicator called S-ZI:

$$\text{S-ZI} = \frac{dS_L}{dZ_L}$$

When the demand increases ($dZ_L < 0$), the S-ZI will fall into one of these three cases:

- S-ZI < 0 : the power increases, $dS_L > 0$. The grid meets the demand; it is equivalent to the upper section of the PV curve. The load does not reach the maximum loadability.
- S-ZI > 0 : the power decreases, $dS_L < 0$. The grid does not meet the demand; it is equivalent to the lower section of the PV curve. The load has passed the maximum loadability.
- S-ZI $= 0$: the power is unchanged, $dS_L = 0$. The current operating point is located at the nose point of the PV curve; the maximum loadability is reached.

Evidently, the S-ZI can distinguish the upper and lower sections of the PV curve. This S-Z sensitivity can be a suitable indicator for voltage stability assessment. This notion is mathematically underpinned by the following analysis. As presented in Section 3.1, (3.7) describes the relationship among the S-Z sensitivity, magnitude of the Thevenin impedance and that of the load. It is obvious that the term ($Z_{Th}^2 - Z_L^2$) determines the sign of the S-ZI as follows:

- $Z_L > Z_{Th}$ $\rightarrow$ S-ZI < 0 Magnitude of the load impedance is larger than that of the Thevenin impedance. Therefore, the load does dot reach the maximum loadability limit.
- $Z_L < Z_{Th}$ $\rightarrow$ S-ZI > 0 Magnitude of the load impedance is smaller than that of the Thevenin impedance. Therefore, the load has crossed the maximum loadability limit.
- $Z_L = Z_{Th}$ $\rightarrow$ S-ZI $= 0$ Magnitude of load impedance is equal to that of the Thevenin impedance. Therefore, the load is reaching the maximum loadability limit.

This mathematical analysis substantiates the above examination of the S-ZI. Convincingly, this is an appropriate indicator for online voltage stability in power systems.

Besides, it is possible to compute and draw a trajectory of the S-ZI with respect to magnitude of the load impedance, showing a clear curve from the current operating point to the voltage stability limit. Based on (3.6), it is possible to plot the S-ZI versus magnitude of the load impedance. Take a specific 420 kV grid in the Norwegian transmission system as an example. The transmission lines in this network have typical ratio X/R around 15.71. This value can be assigned to the Thevenin impedance. Assuming that the load is purely resistive, so the angle between the Thevenin and load impedance is then 86.36^0. Further, the Thevenin voltage is given as $E_{Th} = 254$ kV (this has been observed in the studied 420 kV grid). Based on these parameters, trajectories of the S-ZI (MVA/Ohm) with respect to magnitude of load impedance are plotted and shown in

Fig. 3.5. Each curve corresponds to a given magnitude of the Thevenin impedance (20 Ω, 30 Ω, 40 Ω, 50 Ω and 60 Ω). These magnitudes are selected since they have been observed at a load bus in the Norwegian transmission system.

As can be seen, each Thevenin impedance has a distinctive trajectory. When the load is light (load impedance is high), the S-ZI is almost the same for all trajectories. As the load is approaching the maximum loadability, the trajectories drift away from each other, showing a clear difference among the S-ZI curves. Fig. 3.6 magnifies the area around the instant when the voltage stability limit is crossed. As expected, the S-ZIs are equal to zero when magnitude of the load impedance is equal to that of the Thevenin impedance.

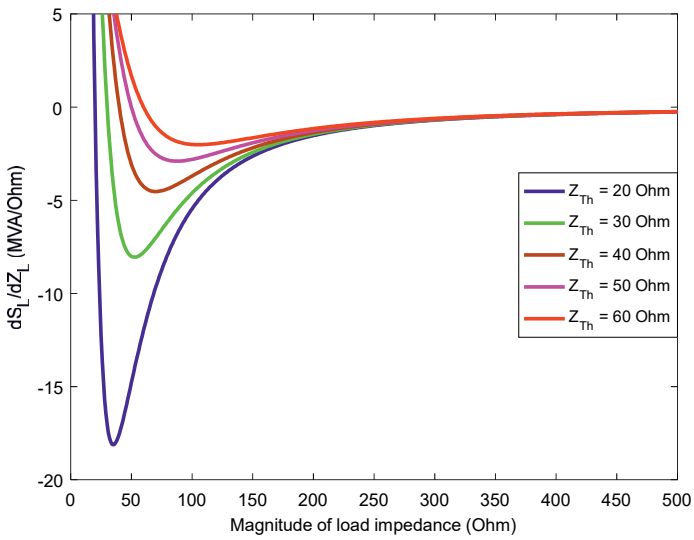

Figure 3.5: Trajectories of the S-ZI with different Thevenin impedance.

3.2.2 Early warning of voltage instability

As seen in Fig. 3.5, the S-Z sensitivity curves have a minimum when magnitude of the load impedance is approaching that of the Thevenin impedance. At this extremum, the operating point is quite close to the voltage stability limit. Therefore, this minimum point can be used as the threshold to issue an early warning for voltage instability. Base on (3.5), the second derivative of S_L with respect to the Z_L is

$$\frac{d^2 S_L}{dZ_L^2} = \frac{2E_{Th}^2 \left(Z_L^2 + 2Z_{Th}\cos\theta Z_L + Z_{Th}^2\right)\left(Z_L^3 - 3Z_{Th}^2 Z_L - 2Z_{Th}^3\cos\theta\right)}{\left(Z_L^2 + Z_{Th}^2 + 2Z_L Z_{Th}\cos\theta\right)^4} \tag{3.9}$$

Consequently, the minimum point is one of the roots of the following equations:

$$Z_L^2 + 2Z_{Th}\cos\theta Z_L + Z_{Th}^2 = 0 \tag{3.10}$$

$$Z_L^3 - 3Z_{Th}^2 Z_L - 2Z_{Th}^3\cos\theta = 0 \tag{3.11}$$

The discriminant of (3.10) is

$$\Delta = 4Z_{Th}^2\left(\cos^2\theta - Z_L^2\right) \tag{3.12}$$

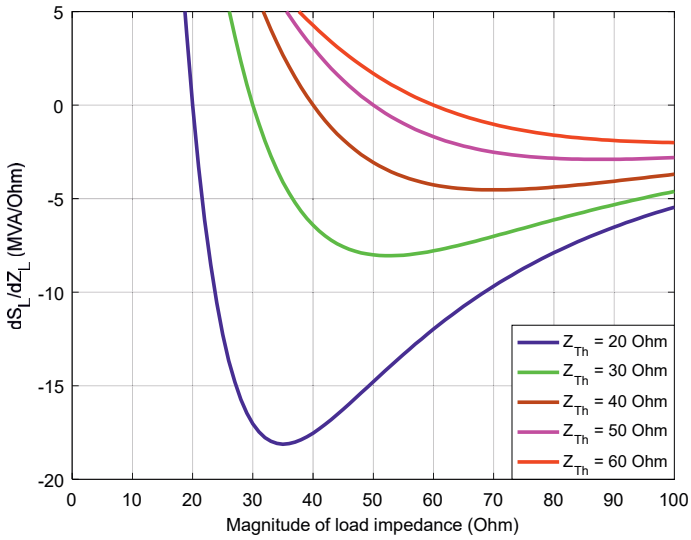

Figure 3.6: Trajectories of the S-ZI when load is approaching the voltage stability limit.

In power systems, Z_L is normally much larger than 1 Ω, so $\Delta < 0$. This means the roots of (3.10) are complex numbers, which are obviously not a physically valid solution. Therefore, magnitude of the load impedance at the extremun is one of the roots of (3.11). This root is slightly higher than Z_{Th}. It is noted that (3.11) is a polynomial equation, which can be easily solved by several numerical methods [52, 53].

3.3 Online voltage stability monitoring based on the Thevenin impedance and S-ZI

3.3.1 Indicator based on the Thevenin impedance

As presented in Section 3.1, the Thevenin impedance seen at a load bus in power systems can be estimated in real time by local phasor measurements of the load current and voltage. The magnitude of the estimated Thevenin impedance in comparison with that of the load establishes an indicator for online voltage stability monitoring, which has been presented in Chapter 2. Moreover, after the Thevenin impedance is estimated, the maximum loadability is obtainable by (2.49). The indicator based on the Thevenin impedance and the power margin display a clear picture of the current operating point and the distance to the voltage stability limit as can be seen in Fig. 3.7 and 3.8, which illustrate a performance of the proposed method at a 420 kV node in the Norwegian transmission system. More details are presented in Chapter 5.

3.3.2 Applications of the S-ZI

The proposed indicator S-ZI in Section 3.2 requires only PMU measurements of the load current and voltage to detect the system behavior in response to variations of the concerned load. Thus, it is suitable for online implementation. Basically, the S-ZI has two

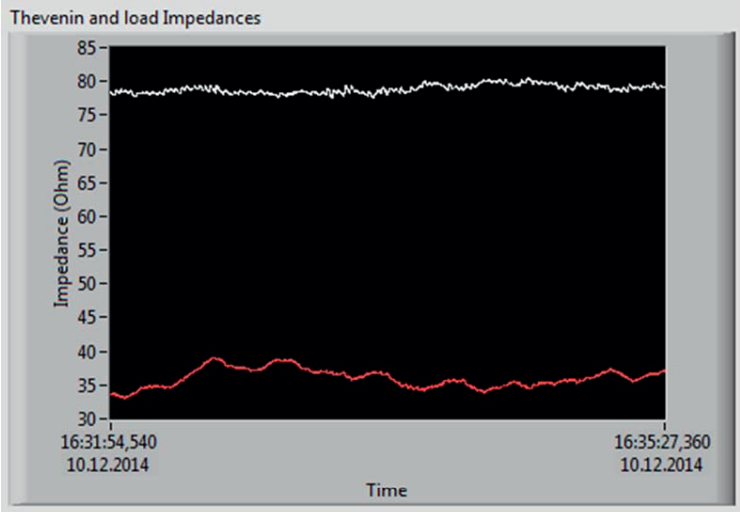

Figure 3.7: Magnitudes of the load impedance and the Thevenin impedance estimated in real time; white curve: the load impedance; red curve: the Thevenin impedance;

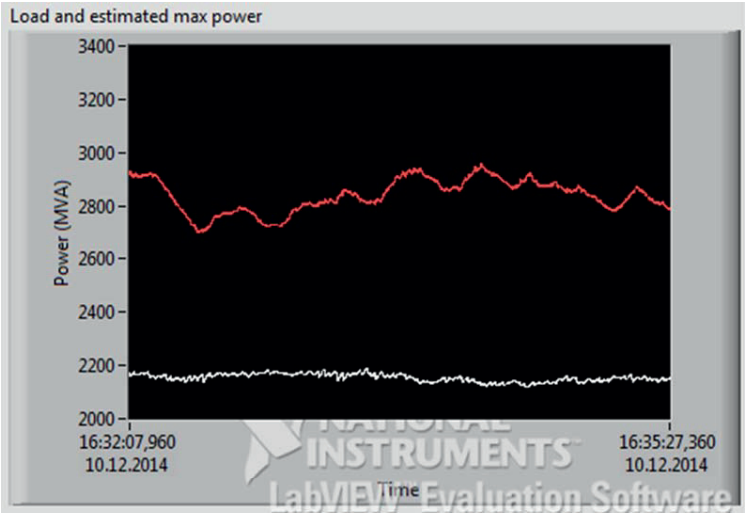

Figure 3.8: Apparent power of the load and the maximum loadability estimated in real time; white curve: load; red curve: the estimated loadability.

applications. The first one is an indicator for online voltage stability monitoring, and the second one is a tool to validate accuracy of the estimated Thevenin impedance in real time.

3.3.3 S-ZI as an indicator for online voltage stability monitoring

As presented in Section 3.2, the S-ZI is a new indicator for online voltage stability monitoring. With this indicator, the voltage stability limit is the point where the S-ZI is equal to zero. This threshold is unchanged; it does not depend on operation conditions in the grid. Based on local phasor mearements of the load current and voltage, the S-ZI of the concerned load is computed directly. There are not any problems related to divergence or other issues. Moreover, assuming that the range of the Thevenin impedance's magnitude seen at the considered load bus is known (based on the proposed method to estimate the Thevenin impedance in this chapter, for example), one can draw pre-defined trajectories of the S-ZI with respect to the magnitude of the load impedance. By this way, the distance between the operating point and the voltage stability limit can be showed very clearly as illustrated in Fig. 3.9. In addition, based on the online estimated Thevenin impedance which is presented in Section 3.1, the current trajectory is able to be plotted.

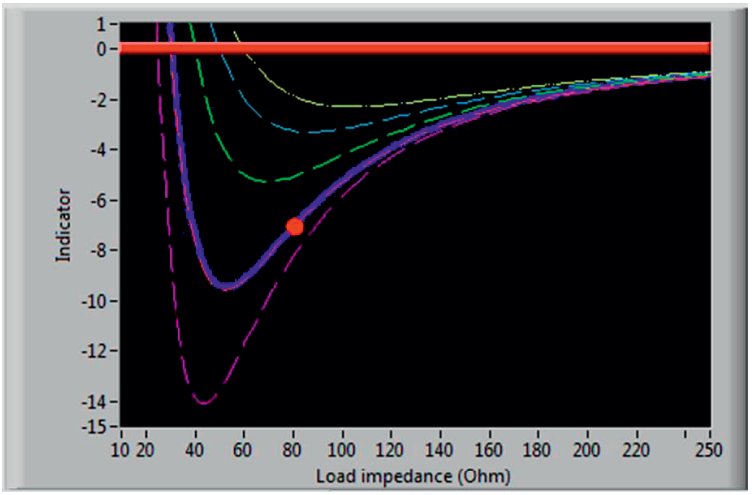

Figure 3.9: Performance of the S-Z sensitivity at a 420 kV bus; x-axis is magnitude of load impedance, y-axis is the S-ZI (MVA/Ω); the red point is the S-ZI computed from phasor measurements and the thick blue curve is the trajectory of the currently estimated Thevenin impedance.

3.3.4 S-ZI as a validation tool

3.3.4.1 Correction of the ratio X_{Th}/R_{Th}

As previously presented in Section 3.1, the ratio X_{Th}/R_{Th} of the Thevenin impedance must be known before the estimation of the Thevenin impedance can be conducted. Since this parameter is initially unknown, a typical value of X/R of power lines in the studied area can be assigned to the Thevenin impedance, and then the magnitude of the Thevenin impedance is estimated. If the assigned value is incorrect, the S-ZI trajectory, which is drawn based on the estimated Thevenin impedance, will not cross the S-ZI computed from the local phasor measurements. In this case, the ratio X_{Th}/R_{Th} should be adjusted until the S-ZI is located on the trajectory.

3.3.4.2 Validation of the Thevenin impedance

Estimation of the Thevenin impedance in real time has been studied in several works [45, 47, 54–56]. At the same load bus, magnitudes of the estimated impedances can be different from algorithm to algorithm. This issue is illustrated in Fig. 3.10, in which the blue curve is the Thevenin impedance obtained from [47] and the red one results from [57]. As can been seen, the mismatch between the two impedances varies from 35 Ω to 67 Ω. To evaluate accuracy of the estimated Thevenin impedances, an occurrence of the maximum power transfer condition is needed. It is because, at this special instant, the magnitude of the Thevenin impedance must be equal to that of the load impedance. However, in normal operation, there are not any tools that can verify the Thevenin impedance estimated by different algorithms. This problem can be tackled by comparing the S-ZI obtained from measurements with the trajectory drawn from the online estimated Thevenin impedance. As shown in Fig. 3.9, the red point is the S-ZI directly computed from the current phasor measurements. The thick blue curve is the trajectory of the S-ZI. This curve is drawn based on the currently estimated Thevenin impedance. If the estimation is accurate, the red point must be located on the trajectory as seen in Fig. 3.9. Otherwise, this point will drift away from the curve as illustrated in Fig. 3.11.

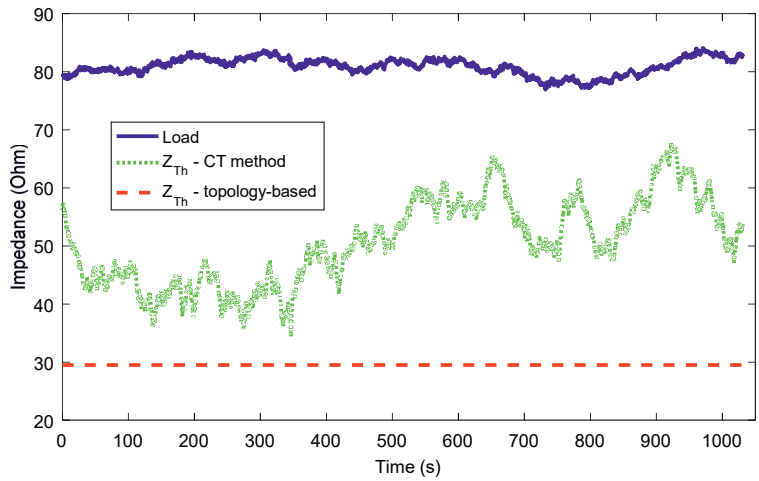

Figure 3.10: Estimated Thevenin impedances obtained from different algorithms.

3.4 Voltage instability protection and load shedding

As discussed in Chapter 2, voltage instability occurs only if the maximum loadability has been passed. In this case, the excessive demand causes lower load power, lower voltage and higher losses in the network. In order to prevent voltage instability, load shedding is considered as an effective countermeasure. The challenges related to this measure are: i) how to detect load that has crossed the maximum loadability; and ii) how to determine an adequate amount of load, which is going to be shed. Little load shedding would not be sufficient to prevent the collapse, but excessive load shedding should be avoided since it has adverse effects on customers. It is favorable that only a portion of the load that exceeds

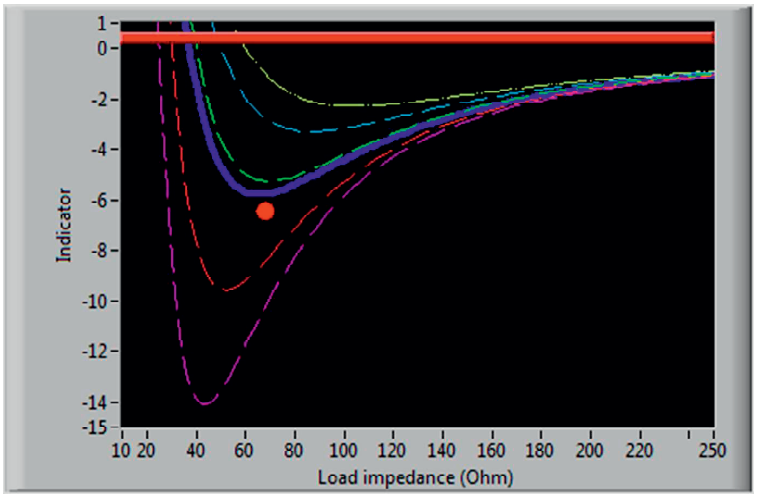

Figure 3.11: Illustration of inaccurate estimation of the Thevenin impedance, verified by the S-Z sensitivity.

the maximum loadability should be shed in order to bring the operating point back to the upper section of the PV curve. In addition, it is noted that the maximum loadability is different from bus to bus. When the system is on the brink of voltage collapse, there is a certain number of nodes where the load is still lower than the maximum loadability. Shedding these loads is not necessary with respect to preventing voltage instability. To improve reliability of power supply, load shedding should be selective.

Regarding the requirements for an adequate and selective load shedding scheme, the proposed methods to estimate the Thevenin impedance in real time and the S-ZI indicator in Section 3.1 and 3.2 are suitable tools. These approaches have a low computational cost; hence, they can be implemented in processor-based devices (intelligent electronic devices, for example) or integrated into the wide area monitoring and protection system as a protective function against voltage instability. Fig. 3.12 and 3.13 depict a schematic diagram and a flowchart of the load shedding scheme used as a protective function against voltage instability. Here, the power drawn from the transmission or subtransmission systems is considered as the power demand, and the feeders connected to the busbar at the secondary side of the transformer are treated as a portion of the load. Based on the inputs, which are the voltage $\vec{V}_L$ and current $\vec{I}_L$ at the high voltage side, the protection block estimates the Thevenin impedance and computes the S-ZI and the load impedance. If the load has crossed the maximum loadability, a timer will start counting. After a certain time delay, if the load is still beyond the limit, the protective function will disconnect a feeder or some feeders, which have load impedance's magnitude larger than the difference between magnitudes of the total load impedance and the Thevenin impedance. This ensures that only the excessive portion of load is shed and the rest remain connected. By this way, the load shedding is minimized, without any intensive computational cost. After the first round of load shedding, if the transfer capacity of the system is reduced and the remaining loads exceed the limit again, a new load shedding command will be released. The voltage instability protection works continuously to keep the load within the voltage stability limit. If this protection is deployed at all load buses,

voltage collapse can be averted, assuming that problems related to malfunction of the protection system and overloading have been avoided.

In the context of smart grid, the output of the voltage instability protection can be used to adjust the demand in the distribution grid, instead of shedding load, to prevent voltage collapse. A large number of electric vehicles, distributed generation and energy storage allow remedial actions to be taken in the distribution level to alleviate voltage stability problem in the transmission network.

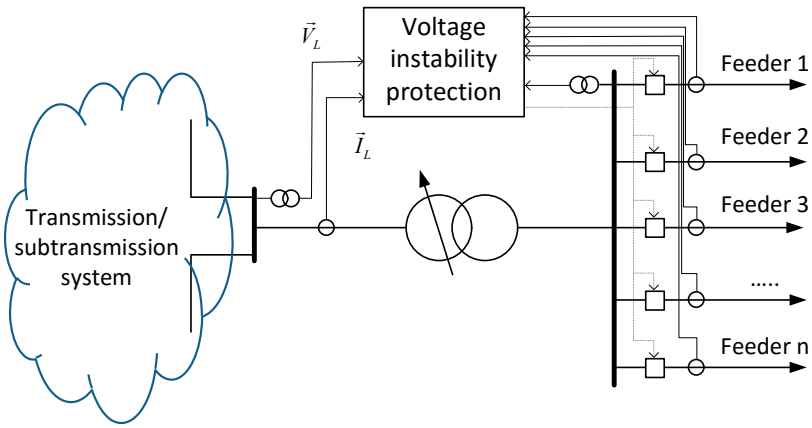

Figure 3.12: Schematic diagram of voltage instability protection deployed at a substation.

3.5 Signal filtering

The proposed algorithm estimates the Thevenin impedance based on variations of the load impedance and apparent power, which are computed from the load current and voltage. In normal operation, variations of the load current and voltage are quite small, and they are also distorted by transients in the grid, noise, and errors of measurement instruments, etc. As a result, these variations obtained from raw measurements do not reveal the true reaction of the system in response to variations of the load, which is measured by the S-Z sensitivity (ζ) in the proposed algorithm. This is generally the main challenge for many methods based on local phasor measurements. In (3.8), ζ has a large impact on the unknown Z_{Th}. In order to obtain a good estimation of the Thevenin impedance, this parameter should be computed appropriately from the raw measurements. Fig. 3.14 shows the S-Z sensitivity at the Hasle corridor. In this case, ζ is computed directly from the raw data, without any filtering. As can be seen, the S-Z sensitivity is highly distorted and not usable; it does not reflect the true characteristic of the system when the load varies. Fig. 3.15 shows variations of the apparent power and load impedance computed from two consecutive PMU measurements, which are taken every 20ms at the same location. During the observation time, both dS_L and dZ_L change randomly and can be negative or positive. From these figures, one can recognize that it is necessary to filter these signals to obtain a better response of the system.

To obtain a good estimate of the S-Z sensitivity, one can take the following steps:

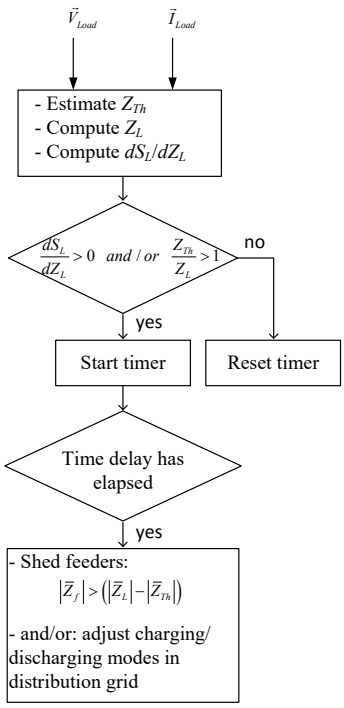

Figure 3.13: Voltage instability protection based on the S-ZI and Thevenin impedance; $\bar{Z}_{Th}$ is the Thevenin impedance, $\bar{Z}_L$ is the load impedance and $\bar{Z}_f$ is the load impedance of feeders.

- Take into account only two consecutive measurements, which result in $dZ_L < 0$. As discussed in Chapter 2, voltage collapse is mainly driven by the load recovery; therefore, $dZ_L < 0$ is more critical than $dZ_L > 0$.
- To reduce the impact of noise, only large dZ_Ls are considered. How a large dZ_L is defined depends on specific load.
- Compute the S-Z sensitivity ζ from dS_L and dZ_L. Since ζ varies very slightly at a certain loading level, it is suitable to filter this signal by the moving average filter, which is mathematically expressed by:

$$y[i] = \frac{1}{N}\sum_{j=0}^{N-1} x[i-j] \tag{3.13}$$

  where x is a series of samples of the input, y is the corresponding output and N is the number of samples used in the moving average.

Fig. 3.16 depicts the trend curve of the S-Z sensitivity after it has been filtered. Compared to the curve in Fig. 3.14, this curve is now much smoother and truly represents the system response.

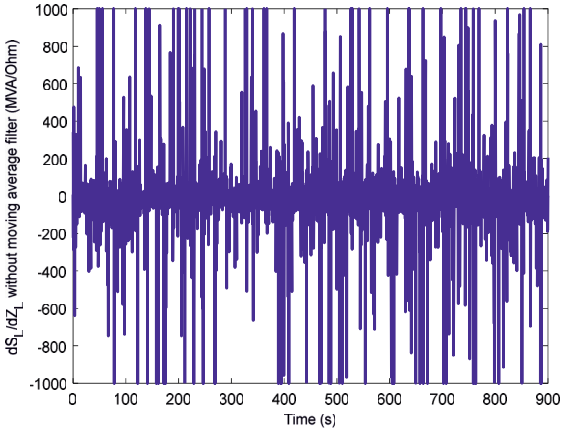

Figure 3.14: The S-Z sensitivity computed from raw data.

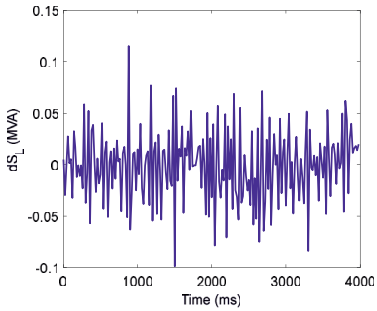

(a) Variations of dS_L, computed from two consecutive measurements.

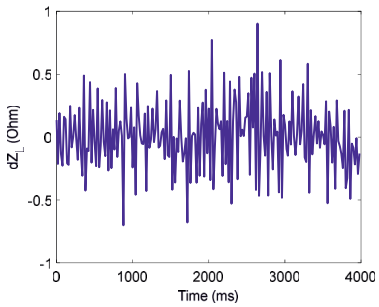

(b) Variations of dZ_L, computed from two consecutive measurements.

Figure 3.15: Variations of the load impedance and apparent power during a period of four seconds obtained from real PMU measurements; reporting frequency is 50 data frames per second.

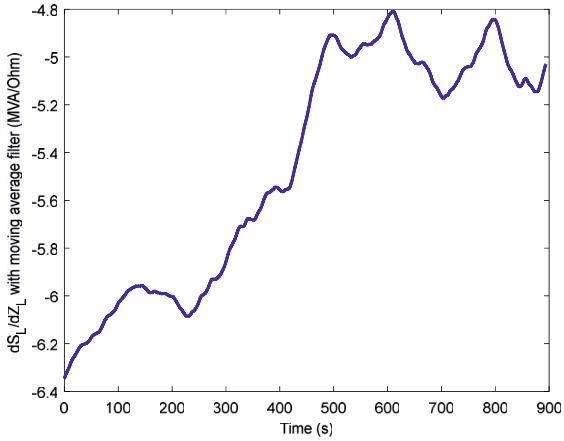

Figure 3.16: The S-Z sensitivity ($\zeta = dS_L/dZ_L$) after filtering.

Chapter 4

Online voltage stability monitoring based on system topology and phasor measurements

Estimation of the Thevenin equivalent based on information of system topology and PMU measurements is one of the main contributions of this PhD project. The method utilizes PMU measurements at boundary nodes to limit the size of the subsystem, which is vulnerable to voltage instability. Therefore, it is not necessary to take the entire power system into calculation. This solution reduces computation time and paves the way for online implementation. The approach computes directly the Thevenin impedance from system topology and PMU measurements; it does not have any problem of divergence and hence can work reliably and robustly. Moreover, not only the Thevenin impedance of the current operation state is estimated but also the Thevenin impedance under different contingencies can be predicted in real time. This helps the system operators to have better awareness of operational margins with respect to voltage stability.

The chapter starts with the estimation of the Thevenin impedance in systems dominated by large generation. It is followed by the analysis of the Thevenin impedance in power systems under the impact of small generation and active power dispatch. Based on this study, a technique to model active power injection by a reactance is presented, which contributes to the comprehensive approach to online voltage stability monitoring based on system topology and PMU measurements presented in the next section. After that, estimation of the online post-contingency Thevenin impedance is presented. It is followed by a summary of the proposed approach before the chapter is finally closed by some remarks on impacts of shunt compensation on the Thevenin impedance and the maximum loadability.

4.1 The Thevenin impedance in power systems with large generation

4.1.1 Estimation of the Thevenin impedance

In power systems, generation and loads are generally connected by a meshed network of power lines. The length and parameters of the lines, topology and voltage level de-

termine the transfer capacity of the network. Therefore, it has significant influence on the maximum loadability allocated to each load bus in the grid. Regarding this feature, this section analyses the estimation of the Thevenin equivalent in systems with large generation, where voltage stability limit is imposed only by the network.

Consider Fig. 4.1, where the loads are located at bus 2 and 3. The generator G1 is connected to bus 1, feeding power to the grid through the step-up transformer T1; Line 1 connects bus 2 and 3. Since the focus is on voltage stability, it is, at this stage, reasonable to assume that G1 has unlimited power. This assumption holds for large and electrically distant generators with regard to the monitored load. Assuming that the AVR of generator G1 is able to keep the terminal voltage at bus 1 constant during operation, then the generator behaves like a voltage source connected to bus 1. Hence, from Fig. 4.1, the electric equivalent circuit of this system can be obtained as depicted in Fig. 4.2, where T1, Line 1, L1 and L2 are represented by impedances $\bar{Z}_T$, $\bar{Z}_{Line}$, $\bar{Z}_{L1}$, and $\bar{Z}_{L2}$ respectively. For the sake of illustration, shunt admittances of Line 1 are neglected.

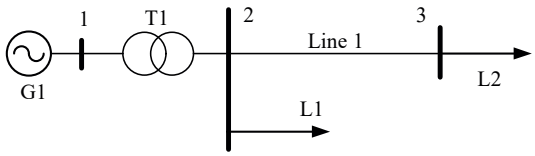

Figure 4.1: A 3-bus system to illustrate the Thevenin impedance in systems with large generation.

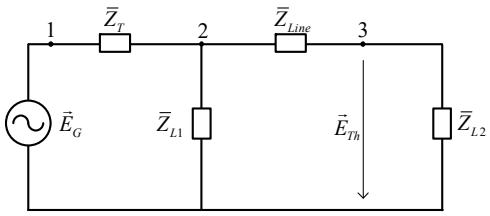

Figure 4.2: Equivalent circuit of the 3-bus system.

According to the Thevenin's theorem, the equivalent impedance of the system seen at bus 3 is

$$\bar{Z}_{Th} = \bar{Z}_{Line} + \frac{\bar{Z}_{L1}\bar{Z}_T}{\bar{Z}_{L1} + \bar{Z}_T} \tag{4.1}$$

Alternatively, from Fig. 4.1, the admittance matrix Y of the grid (not including the load) is formed by:

$$Y = \begin{pmatrix} \frac{1}{\bar{Z}_{Line}} + \frac{1}{\bar{Z}_T} & -\frac{1}{\bar{Z}_{Line}} \\ -\frac{1}{\bar{Z}_{Line}} & \frac{1}{\bar{Z}_{Line}} \end{pmatrix} \tag{4.2}$$

It is noted that bus 1 is treated as the reference node because it is connected to the large generator.

Modifying the diagonal elements of the matrix Y by adding all the load admittances, except the monitored load, to corresponding diagonal elements to establish a new matrix:

$$Y_{eq} = \begin{pmatrix} \frac{1}{\bar{Z}_{Line}} + \frac{1}{\bar{Z}_T} + \frac{1}{\bar{Z}_{L1}} & -\frac{1}{\bar{Z}_{Line}} \\ -\frac{1}{\bar{Z}_{Line}} & \frac{1}{\bar{Z}_{Line}} \end{pmatrix} \tag{4.3}$$

Define the impedance matrix Z_{eq} as the inverse of Y_{eq},

$$Z_{eq} = {Y_{eq}}^{-1}. \tag{4.4}$$

The diagonal element located at the second row and second column of Z_{eq} is

$$Z_{eq}(2,2) = Z_L + \frac{Z_{L1}Z_T}{Z_{L1} + Z_T}, \tag{4.5}$$

which is by definition equal to the Thevenin impedance seen at bus 3 in (4.1) (in general, the diagonal element at i^{th} row and i^{th} column of the impedance matrix is the Thevenin impedance seen at the ith bus in the grid [58, 59]). The system is now simplified as shown in Fig. 4.3a

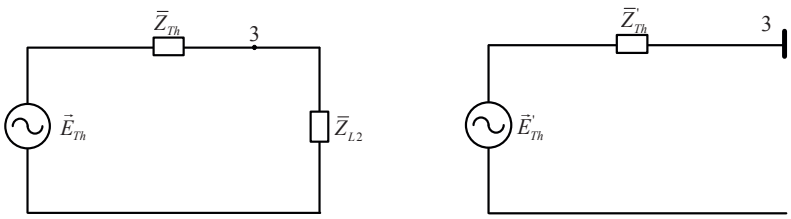

(a) Monitored load admittance is not integrated to the admittance matrix.

(b) All load admittances are integrated to the admittance matrix.

Figure 4.3: The Thevenin equivalent circuit.

It is noted that if the Thevenin impedance at another node needs to be computed, the admittance matrix Y must be modified by other loads and inverted again. If there are n monitored buses in the concerned area, the matrix inversion must be conducted n times. However, this problem can be avoided by simply adding all the load admittances (including the monitored one) into the admittance matrix. In this case, the impedance obtained from the corresponding diagonal element of Z_{eq} ($\bar{Z}'_{Th}$ in Fig. 4.3b) is the equivalent of the actual Thevenin impedance and the load in parallel. Therefore, after computing the impedance matrix Z_{eq}, the actual Thevenin impedance is found by

$$\bar{Z}'_{Th} = \bar{Z}_{Th} \parallel \bar{Z}_{L2} \Rightarrow \bar{Z}_{Th} = \frac{\bar{Z}_{L2}\bar{Z}'_{Th}}{\bar{Z}_{L2} - \bar{Z}'_{Th}} \tag{4.6}$$

where $\bar{Z}'_{Th}$ is the corresponding diagonal element $Z_{eq}(2,2)$. By this technique, matrix inversion must be carried out once to compute the Thevenin impedance seen at all the load buses.

In summary, the concept of this approach can be applied to systems that fulfill the assumption about having only large generators. The estimation process is as follows:

1. Treat all generation buses as the reference node and establish the admittance matrix.
2. Add all the load admittances into the corresponding diagonal elements to modify the admittance matrix.
3. Invert the modified admittance matrix. Extract impedances from the diagonal and compute the Thevenin impedance at the concerned load buses by (4.6).

4.1.1.1 Discussion

- In general, real power systems are large and complex. They comprise many generators with different rated power and often have connections to external systems. The requirement for existence of only large generators in the grid somehow seems unrealistic. However, this condition can be fulfilled in some sub-transmission networks, where there is no generation and loads are fed from the transmission system through transformers. Fig. 4.4 depicts a small part of the Norwegian transmission system as an example. This area consists of only loads and a weak network. The loads are supplied by the 420 kV network through a substation connected to bus 1 and a large power plant connected to bus 2. Voltage collapse sometimes occurs in this subsystem, mainly caused by outage of some important lines in the area. Under this circumstance, limits on the maximum loadability are imposed by the network, rather than by the generation. Consider the voltage at bus 1. Since the transformer has an OLTC, it can keep the voltage constant at a desired value in normal operation while the power is drawn from the 420 kV transmission system to meet the demand in the 130 kV grid. From the 130 kV side, the 420 kV side acts like a large generator or a voltage source, without any power limits. From this point of view, this subsystem fulfills the above assumption; therefore, the method presented in this section can be applied directly without further tactics. It is noted that only the information about the topology of this subsystem is needed to form the admittance matrix; information about topology and loading condition of the rest of the system is not required. Hence, the size of the admittance matrix is reduced significantly. Computation cost on matrix inversion is consequently low. This makes the approach simple and viable for real time implementation.

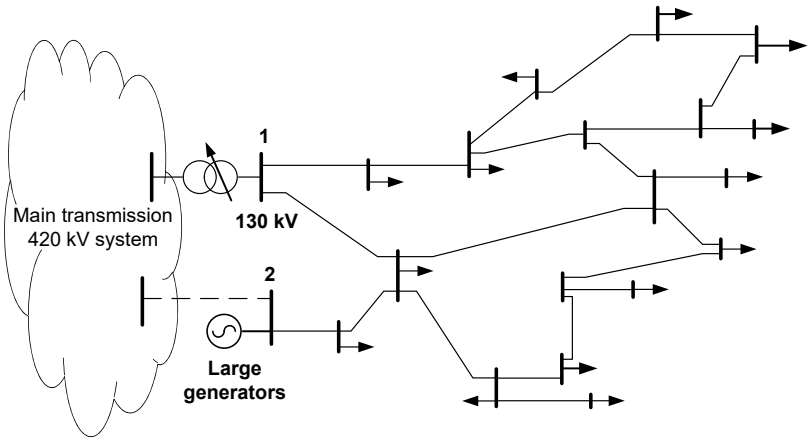

Figure 4.4: A 130 kV subsystem of the Norwegian transmission system.

- The essence of the method is graphically illustrated in Fig. 4.5. There are generally two paths that determine the Thevenin impedance seen at a certain load bus. The first one is the series path. This path comprises line impedances, which connects the load and generation. The second path is constituted by load impedances, which are normally much larger than the line impedances. Hence, the network topology

largely determines the Thevenin impedance and should be well tracked. To obtain this, breaker statuses could be communicated from the SCADA/EMS system at regular intervals or preferrably event-based. The load impedances, however, have small impact on the estimation; it is not necessary to update their values quickly. Information on load impedances obtained from most of existing state estimators is fast enough.

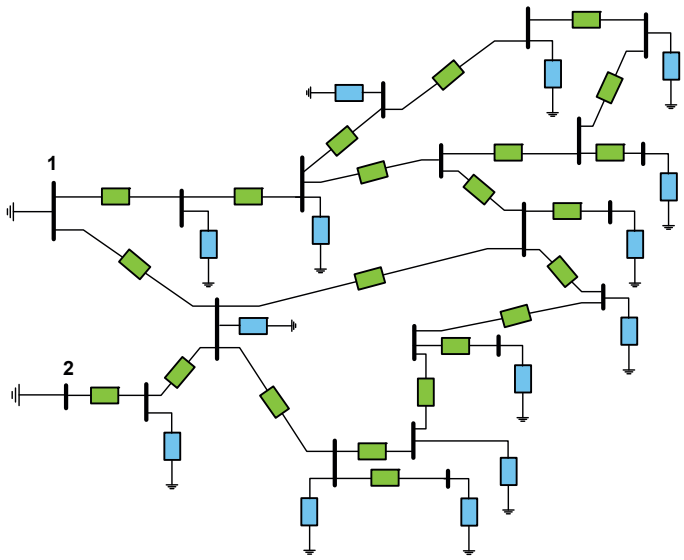

Figure 4.5: Graphical illustration of the Thevenin impedance estimation.

4.1.2 Treatment of shunt compensation

Shunt capacitors are widely used to improve voltage profile in power systems, especially in load areas. For transmission networks, shunt reactors are also deployed to avoid overvoltage during light loading conditions. These components have influence on the maximum loadability and the Thevenin impedance seen at the load bus. Thus, they should be included in the admittance matrix. As known, shunt capacitors and reactors are simply impedances connected to the grid. Therefore, in the admittance matrix, they are treated as a shunt admittance at the node they are connected to.

Synchronous condenser, SVC or STATCOM can inject or absorb reactive power from the grid, acting like a capacitor or reactor. Thus, they are represented as a reactance, whose magnitude is determined by the currently injected reactive power as

$$X = \frac{U^2}{Q} \tag{4.7}$$

where U is the bus voltage and Q is reactive power, which is negative if it is injected into the grid.

4.2 Effect of active power dispatch on the Thevenin impedance

4.2.1 Impact of small generators on the Thevenin impedance

The Thevenin theorem in circuit theory is a useful tool to obtain the equivalent of the rest of a circuit seen at a particular terminal. This theorem is valid for linear circuits or for a certain operating range where the circuit is linear. In nonlinear systems like power systems, estimation of the Thevenin impedance is different from the theorem. As discussed in Chapter 2 regarding online voltage stability monitoring based on the Thevenin equivalent, a good estimate of the Thevenin impedance is the one which is equal the load impedance at the instant of maximum power transfer condition. The challenge is that the maximum power a load can draw from the grid is dependent on specific operation conditions, such as dispatch of active power among generators, limits of VAr reserves, topology, loading condition, load behaviors, etc. These factors, therefore, affect the Thevenin impedance seen at the load. Regarding this issue, this section analyzes how the Thevenin impedance in a simple system varies under different operation conditions, and how to model power limit of small generators in the Thevenin equivalent estimation. The study improves understanding of the Thevenin equivalent in power systems; it forms the basics of a new method for online voltage stability monitoring presented in Section 4.3.

Consider a small 110 kV grid depicted in Fig. 4.6. Generator G1 is located at the bus 1, which is treated as the slack bus. Meanwhile, bus 2 is a PQ bus; the reactive power injection at this bus is fixed at 9 MVAr. To examine how the Thevenin impedance is affected by the dispatch of active power, the continuation power flow method [37] is implemented. The load is increased until it goes beyond the maximum power transfer limit; meanwhile, active power injected into bus 2 is unchanged, and G1 is responsible for keeping the balance of active power. The computation is conducted with different active power (5 MW, 10 MW, 15 MW and 20 MW) injected into bus 2.

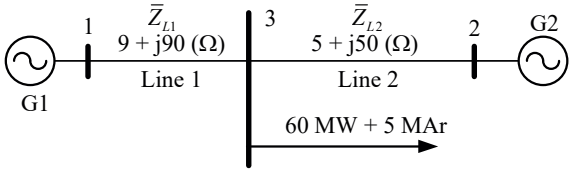

Figure 4.6: A simple system to analyze the influence of dispatch of active power on the Thevenin impedance.

Fig. 4.7 shows the PV curves under 4 scenarios of active power injection at bus 2. As can be seen, the maximum loadability varies as active power dispatch changes. The peak power and the corresponding load impedance are presented in Table 4.1. It is noted that the load impedance in each case is different from the other. It varies from 84.08 Ω to 71.89 Ω when the injected active power at bus 2 changes from 5 MW to 20 MW, respectively. According to [45] and the maximum power transfer theorem, the magnitude of the load impedance at the instant of maximum power transfer is also the magnitude of the Thevenin impedance seen at bus 3. As observed, although the network is unchanged, the Thevenin impedance is not constant; it is affected by the dispatch of active

power. In addition, if the two generators are considered as voltage sources, the Thevenin impedance, according to the Thevenin theorem, is the equivalent impedance of the two parallel impedances Z_{L1} and Z_{L2}, which is 32.3 Ω. This value is not equal to any of the load impedances listed in Table 4.1. Evidently, the method to compute the Thevenin impedance in the circuit theory cannot be applied directly in power systems, which are highly nonlinear and have limited capacity imposed by the physical limits of components installed in the system.

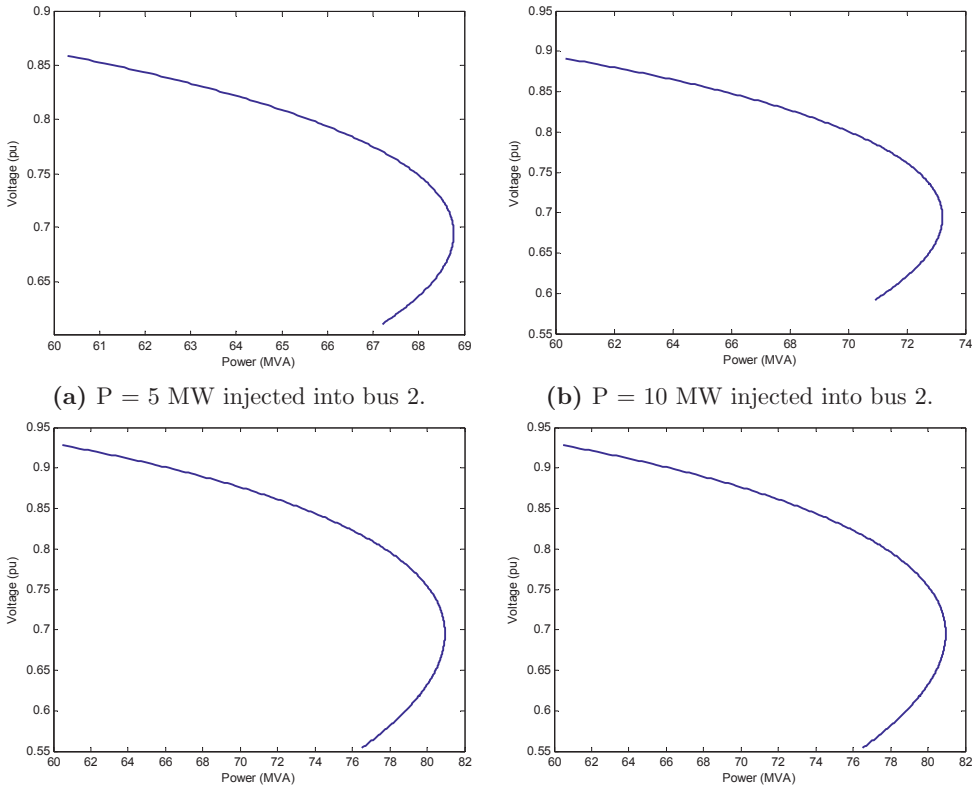

(a) P = 5 MW injected into bus 2.

(b) P = 10 MW injected into bus 2.

(c) P = 15 MW injected into bus 2.

(d) P = 20 MW injected into bus 2.

Figure 4.7: The PV curves under different scenarios of active power injection at bus 2.

Table 4.1: Maximum loadability and corresponding load impedance.

G2 active power (MW)	Load Impedance (Ω)	Max. Loadability (MVA)
5	84.08	69.18
10	79.16	73.60
15	75.07	77.65
20	71.89	81.30

Based on this analysis, the following comments can be drawn:

- Generator G1 represents a large system, which functions as a voltage source and does not set the limit on the power transferred from bus 1 to 3. It is indeed the

line impedance between these two buses, which imposes the limit on the maximum power transfer. This impedance should be taken into account when estimating the Thevenin impedance seen at bus 3.

- The maximum power injected into bus 3 from bus 2 is not restricted by Z_{L2}; it is controlled to stay within the rated output of the component. In other words, Line 2 can facilitate higher power transferred from bus 2 to 3, but the machine at bus 2 is not able to provide such high power. Under this circumstance, the impedance of Line 2 does not represent the transfer capacity; hence, it should not be taken into account when the Thevenin impedance is estimated. The line impedance Z_{L2} should be replaced by a new impedance, which can represent the rated output of the generator. The new impedance functions as a virtual line impedance that set the limit of the maximum power injected into the considered load.

4.2.2 Active power injection modeled as a reactance

Consider a resistive load connected to an arbitrary node in the grid as shown in Fig. 4.8. Assume that the voltage level V_n of the grid and the available maximum active power P_{max}, which the grid can supply, are given. It is a common practice to model the system as a voltage source behind an impedance. For simplification, it is reasonable, especially in transmission system, to assume that the impedance is just a pure reactance X_P, called modeling reactance. From Fig. 4.8, the magnitude of load current can be computed as

$$I = \frac{V_n}{\sqrt{R^2 + X_P^2}} \tag{4.8}$$

At the maximum power transfer, this holds true:

$$R = X_P$$

Therefore, the maximum power transfer is

$$P_{max} = I^2 R = \frac{V_n^2}{2X_P} \tag{4.9}$$

Rearranging (4.9) yields

$$X_P = \frac{V_n^2}{2P_{max}} \tag{4.10}$$

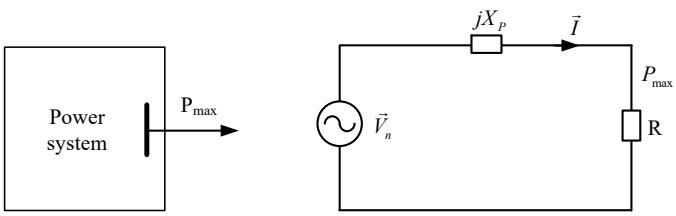

Figure 4.8: Model of active power limitation by an reactance.

In summary, at a particular node in the grid, given that the maximum active power the load can draw is P_{max}, the grid can be modeled as a voltage source behind a reactance

X_P. This modeling technique, together with (4.10), is a tool to represent power injection from small generators and boundary nodes when estimating the Thevenin impedance.

To illustrate the idea, take the grid shown in Fig. 4.6 as an example. The active power currently injected into bus 3 from bus 2 can be considered as the maximum power the load can draw from this branch. Thus, it is modeled by a voltage source behind the reactance X_P, which is computed by (4.10). After this step, the equivalent circuit can be obtained, as shown in Fig. 4.9. Since the load is now supplied by the two voltage sources, the Thevenin impedance is simply the equivalent of the two parallel impedances: jX_P and $\bar{Z}_{L1}$.

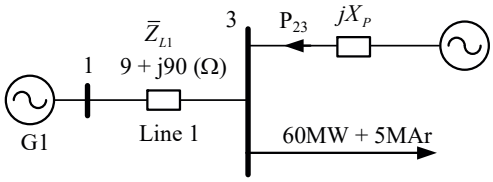

Figure 4.9: The equivalent grid after applying the modeling reactance concept.

Fig. 4.10 shows the performance of the proposed approach under the four scenarios of power injection at bus 2 mentioned in the above section. As expected, there is good agreement between the instant the load reaches the maximum loadability and the time the magnitude of the Thevenin impedance is equal to that of the load impedance. It is noted that the estimated Thevenin impedance is smooth and stable. It is not intermittent as often seen from other methods based on local PMU measurements. In addition, Table 4.2 shows the estimated Thevenin and load impedance at the instant of the maximum power transfer. As can be seen, the error of the estimation is relatively small, just around 2.75%. Obviously, the proposed modeling reactance has improved the Thevenin impedance estimation significantly.

Table 4.2: Load impedance and the Thevenin impedance at the nose point.

G2 active power (MW)	Load Impedance (Ω)	Thevenin impedance (Ω)	Error (%)
5	84.08	84.28	0.24
10	79.16	78.87	0.37
15	75.07	77.14	2.75
20	71.89	69.98	2.67

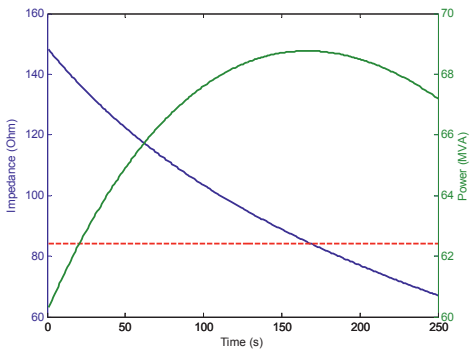

(a) P = 5 MW injected into bus 2.

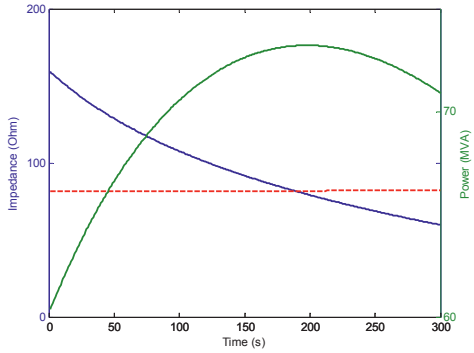

(b) P = 10 MW injected into bus 2.

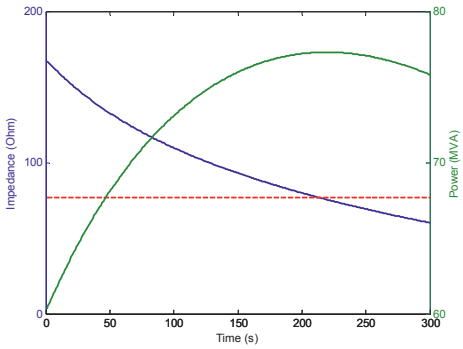

(c) P = 15 MW injected into bus 2.

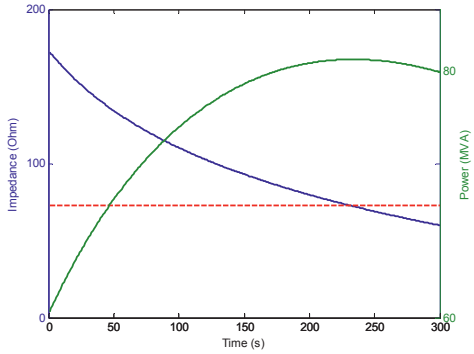

(d) P = 20 MW injected into bus 2.

Figure 4.10: The estimated Thevenin impedance after applying the modeling reactance for active power injection; the blue curve is load impedance, the red and dashed curve is the Thevenin impedance and the green curve is load power.

4.3 Topology- and PMU-based approach

4.3.1 Introduction

Modern power systems are normally large and have connections with external networks. Together with the increasingly high penetration of power electronics devices, the grid becomes more and more complex. This is a challenge for practical implementation of methods for online voltage stability monitoring based on system topology. Taking the entire power system into calculation demands enormous effort in terms of data acquisition and computation; consequently the calculation is not fast enough for online applications, especially during the rapid transition of operation conditions after disturbances. However, information of system topology is valuable; it reflects the strength of the network and highly related to the Thevenin impedance seen at load buses. When used properly, the system topology in estimation of the Thevenin impedance can provide a stable and reliable estimate. In order to achieve this goal, the system should be simplified or the studied area should be bounded.

It is widely acknowledged that voltage stability is rather a local problem, existing in a certain area in the grid. Operation of electrically distant generators, loads and other components does not have a very large impact on the concerned area, which is vulnerable to voltage instability. Therefore, it is not necessary to take the entire system into calculation. Take the Nordic32 test system [60] depicted in Fig. 4.11 as an example. The system is characterized by large generation in the northern part with long transmission lines down to the south to meet the demand in this area, where heavy loads are located. The Nordic32 test system developed by [60] is a variant of the one presented in [61]. In this variant system, the southern part is subjected to long-term voltage instability after the outage of the line between node 4032 and 4044. Since the northern area is not exposed to voltage collapse, it is not necessarily included in the monitoring scheme for voltage instability in the southern part. Obviously, the upper subsystem can be treated as an external grid and represented in real time as virtual voltage sources at the boundary nodes by PMU measurements. With this approach, the size of the monitored area is reduced significantly, especially for large systems. Using system topology to estimate the Thevenin impedance in real time becomes viable for practical implementation. This is the essence of the topology- and PMU-based method for online voltage stability monitoring presented in this section.

4.3.2 Description of the topology- and PMU-based approach

This section presents details of the monitoring scheme, which utilizes the system topology and PMU measurements to estimate the Thevenin impedance at concerned nodes. For the sake of illustration, the Nordic32 test system in Fig. 4.11 is selected for detailed implementation. Overall, the approach consists of the following steps:

STEP 1: Determination of "A-P" nodes for the studied area

To limit the size of the studied area, which is vulnerable to voltage instability, a new type of bus called A-P bus is introduced. This is the bus where the net active power injection is positive. The A-P bus can be a generation or boundary bus, which are defined as follows:

- Generation bus in this algorithm is the bus, where generators are connected and the net active power injection is positive. For instance, bus 4062, G6, G14 and G15 are considered as generation buses because the active power they produce is larger than that of the load located at these buses. On the other hand, bus 1043 and 4051 are not considered as generation buses although they have generators connected. The reason is that the net active power injection is negative; therefore, they are treated as load buses.

- Boundary bus is a bus that has strong connections to the rest of the system. At this bus, the studied area draws active power from the rest of the system. In Fig. 4.11, they are bus 4021 and 4031. These nodes are located at the boundary of the studied area and have strong connections to the rest of the system.

  It is noted that boundary buses, where the studied area exports active power, are not considered as A-P buses, but as load buses.

After the A-P buses are identified, they are then categorized into the weak and strong A-P nodes. As discussed in Section 4.2, small generators have influence on the Thevenin impedance seen at the monitored bus; they need to be treated as weak A-P nodes. At the weak A-P nodes, PMU needs to be installed to obtain the phasor of the bus voltage. On the contrary, the strong A-P node is defined as the bus where large generators (compared to the loading condition in the studied area) are connected. The large generators normally behave like voltage source in terms of having enough output power to meet the demand. As presented in Section 4.1.1, the strong A-P nodes are treated as the reference node in order to compute the Thevenin impedance. Thus, PMU deployment at these buses is not required. Depending on the specific studied area, the strong A-P node can exist or not. For instance, in the subsystem shown in Fig. 4.4, all boundary nodes are treated as strong A-P buses; but in the Nordic32 test system in Fig. 4.11, all the A-P nodes are treated as weak ones. They are marked by the magenta rectangles in the figure.

STEP 2: Simplification of the studied area

In general, after being bounded, the studied area is a small system, but it is still a meshed grid; there are not direct connections from A-P nodes and the monitored load bus. Hence, the technique to model active power injection from the weak A-P nodes by the modeling reactance presented in Section 4.2.2 cannot be directly applied to the studied area. It is necessary to obtain a simplified network, which contains only the monitored bus and the A-P buses. The target is to establish direct connections between each A-P node and the monitored bus.

Based on the topology of the concerned area, one can establish the modified admittance matrix Y_{eq} in form of

$$Y_{eq} = \begin{pmatrix} Y_E & Y_{EB} \\ Y_{EB} & Y_I \end{pmatrix} \tag{4.11}$$

where Y_I is a submatrix, which includes only buses being retained after the simplification, i.e. A-P nodes and the monitored bus; Y_E contains buses of the rest of the studied area, and Y_{EB} is a coupling submatrix between the two. It is noted that all load admittances in the studied area must be added into the corresponding diagonal element of the modified admittance matrix. Assume that bus 1041 in Fig. 4.11 is the monitored bus, Y_I will have the size of 7x7 (6 A-P nodes and 1 concerned load bus).

Gaussian elimination on Y_{eq} is then applied to eliminate elements below the diagonal until the submatrix Y_I is reached. In other words, elements of Y_{eq} below the diagonal are retained; they are not eliminated. As a result, the matrix has the final form as

$$Y_{eq} = \begin{pmatrix} \ddots & & & & \\ 0 & \ddots & & & \\ 0 & 0 & \ddots & & \\ 0 & 0 & 0 & \ddots & \\ 0 & 0 & 0 & 0 & \\ 0 & 0 & 0 & 0 & \boxed{Y_{Ieq}} \end{pmatrix}$$

After the transformation, the submatrix Y_I in (4.11) becomes Y_{Ieq}, which contains the equivalence of the simplified lines and loads in the study grid. The submatrix Y_{Ieq} is in return considered as the admittance matrix of the simplified grid. Based on Y_{Ieq}, the direct connection between the A-P nodes and the monitored bus is established as shown in Fig. 4.12. The coupling impedance between them is directly extracted from the corresponding element in the matrix Y_{Ieq}.

STEP 3: Modeling virtual active power flow from weak A-P node by a reactance and computing the Thevenin impedance

As expected, the direct connection between the A-P nodes and the monitored load bus by an impedance has been established. Utilization of this impedance is dependent on how the A-P nodes are categorized.

- For the strong A-P nodes, the coupling impedance between them and the monitored bus is used directly in the Thevenin impedance estimation. The reason is that this impedance is the factor that imposes the limit on maximum power transfer from the considered A-P node to the load.
- For the weak A-P nodes, the coupling impedance is not used directly. It is replaced by a modeling reactance determined by the following steps:
  - Compute virtual active power injected into the monitored load bus from the weak A-P node.
  - If the active power is positive, use (4.10) to obtain the modeling reactance for this flow.
  - If the active flow is negative, treat it as a resistive load connected to the monitored bus. The resistance is computed as

$$R = \frac{V_L^2}{P} \tag{4.12}$$

    where V_L is the magnitude of the load voltage and P is the virtual flow of active power.
- Finally, the Thevenin impedance seen at the monitored bus is the equivalent of all the parallel impedances obtained from above steps.

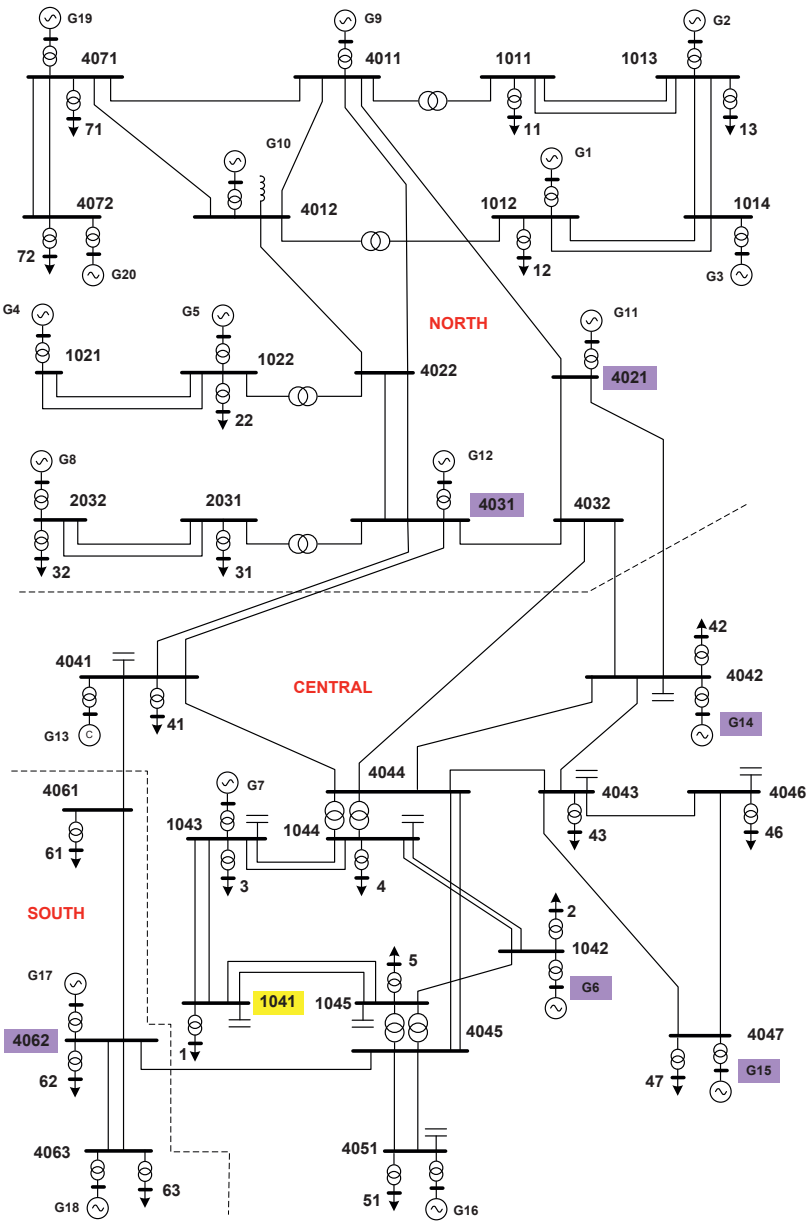

Figure 4.11: The Nordic32 test system [60].

4.4 Real time estimation of the post-contingency Thevenin impedance

Online voltage stability monitoring is a useful tool to determine the operational margin at the current operation point. However, it cannot assess potential risk under certain contingencies. As been observed by many voltage collapse incidents and blackouts in the

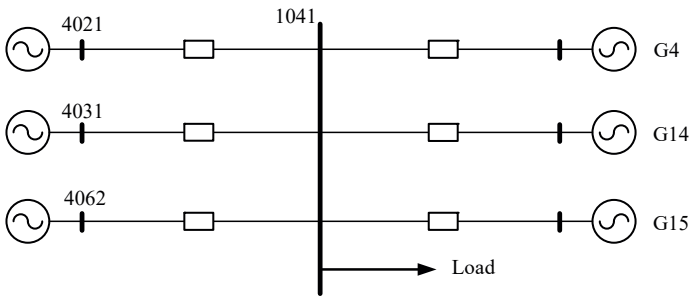

Figure 4.12: Direct connection between A-P nodes and the considered load bus after the simplification of the studied area.

past, critical disturbances have pushed the system out of its limits and led to the system collapse. In addition, to increase utilization, the grid is nowadays expected to operate closer to limits. It makes the system even more vulnerable to disturbances. The current operation point can be within the limits, but certain perturbations can push it beyond the constraints. As illustrated in Fig. 4.13, the load impedance in normal operation is far from the Thevenin impedance, but it can be quite close to the voltage stability limit under certain contingencies, indicating that the system can face the risk of voltage instability. Therefore, early detection of post-contingency voltage stability limits plays an important role in securing system operation. In modern power systems, power flow pattern can predictably change quickly due to high penetration of variable renewable generation. Therefore, the need for real time estimation of post-contingency Thevenin impedance becomes more and more important.

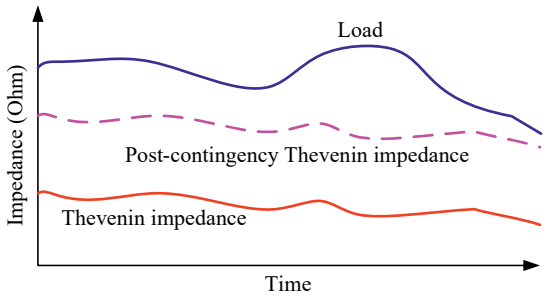

Figure 4.13: Illustration of the Thevenin impedance estimation under contingency.

For methods based on local PMU measurements, it is very challenging to approximate the post-contingency Thevenin impedance in real time, simply because of lack of post-contingency measurements. For topology-based methods, this issue is less challenging; combination of measurements and information about system topology contains clues about post-contingency estimate. In the VIP++ [62], only load behaviors in the studied area are taken into account to compute the distance to point of collapse. But this study has not considered the effect of outages of generators or lines on the Thevenin equivalent estimation.

As presented in Section 4.3.2, after limiting the size of the concerned area, the bounded

studied area, as depicted in Fig. 4.11, is just a small network, which comprises of some lines, A-P buses and loads. Therefore, it is possible to carry out the analysis on concerned contingencies, such as line or generator outages. The procedure is as follows:

- Determine the concerned contingencies, which can come from experience of system operators or from offline analysis or other means.
- Based on the concerned contingency, modify the admittance matrix accordingly. If the contingency is a line outage, just remove the line admittance in the corresponding elements in the matrix. If the contingency is a generator outage, the bus where this generator is connected is not treated as an A-P bus; it is, thus, not included in the Y_I submatrix.
- Follow Step 2 in Section 4.3.2 to obtain the simplified grid.
- In Step 3, use current measurements at A-P nodes and the monitored load to compute the modeling reactance between them.
- Compute the post-contingency Thevenin impedance seen at the concerned load bus. It is noted that several contingencies can be implemented; the one that results in the highest Thevenin impedance is ranked as the most critical contingency with respect to voltage stability assessment.

In order to illustrate the idea, a small system shown in Fig. 4.14 is taken as an example. In this simulation, a line between bus 1 and 3 is tripped at $t = 25$ s. As depicted in Fig. 4.15, before the disturbance, the load is within the voltage stability limit; the load impedance is 99.13 Ω and the currently estimated Thevenin impedance is 49.02 Ω. The estimated post-contingency Thevenin impedance under the disturbance contingency is 96.15 Ω, which is quite close to the current load impedance; it indicates the potential risk caused by the line outage. After the disturbance, the Thevenin impedance becomes 99.51 Ω. There is a small error of 3.36 Ω between the post-contingency and the actual Thevenin impedance. Since the load impedance is smaller than the Thevenin impedance after the outage, the load power cannot return to the initial value; it goes down during the load recovery period.

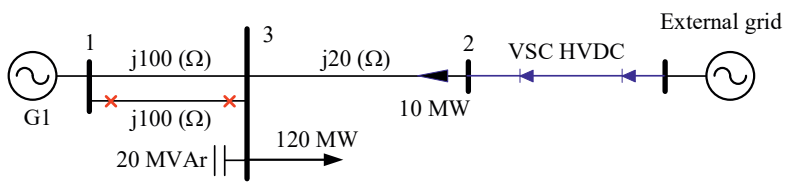

Figure 4.14: A small system to demonstrate the post-contingency Thevenin impedance.

4.5 Summary of the topology-based method

The method for online voltage stability monitoring in this chapter can be summarized by the flow chart shown in Fig. 4.16. For a given subsystem that is prone to voltage instability, first, the A-P buses are determined. This step is to reduce the size of the

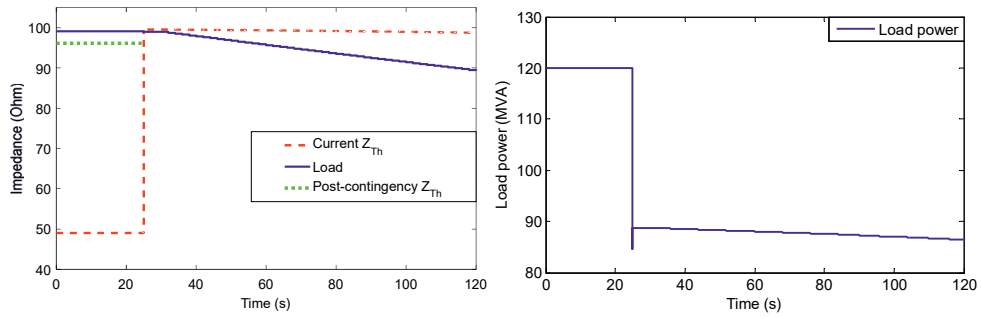

Figure 4.15: Performance of the post-contingency Thevenin impedance estimation.

concerned area and to make the algorithm suitable for online implementation. Moreover, it is necessary to install PMUs at the weak A-P nodes. These measurements are required to compute the coupling reactance between them and the monitored load bus.

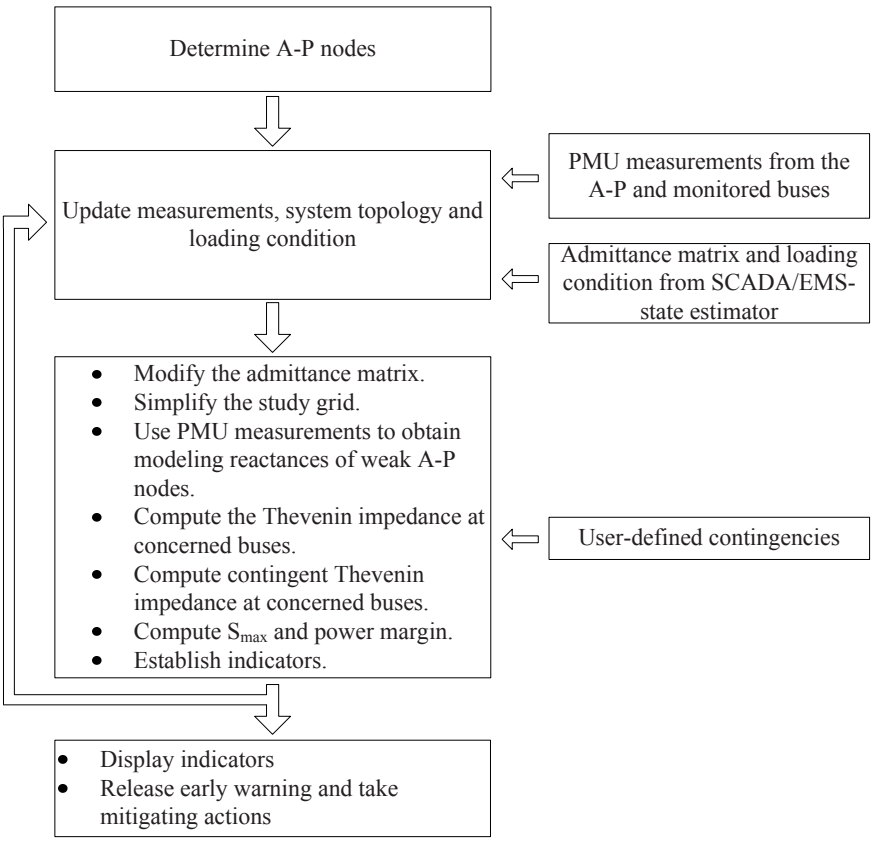

Figure 4.16: Flow chart of the proposed approach to online voltage stability monitoring based on system topology and PMU measurements.

In this algorithm, system topology plays an essential role; every change of the system

topology should be updated as soon as possible to secure accuracy of the method, preferably event-based. Additionally, the loading condition is also important in the approach; however, it does not necessarily require fast update. Variations of load impedances have small impact on the estimated Thevenin impedance. It is noted that both system topology and load power are available information; they can be extracted from existing state estimators or SCADA/EMS systems, which are widely implemented at the control centers of TSOs. So, the method does not demand further resources, except for PMU measurements at the A-P nodes and monitored buses.

After all the required data are collected, the Thevenin impedances seen at the monitored buses are computed. Depending on the specific system, the size of the study subsystem can vary. In the Norwegian transmission system, for example, the areas vulnerable to voltage instability can be bounded as a small one, whose total number of buses is less than 50. Therefore, there is no problem with computation time; the method is fast enough for online implementation. In addition, since the approach focuses on the long term voltage instability, it does not demand very fast update; probably once per second is quick enough.

Moreover, estimation of the post-contingency Thevenin impedances is possible in this approach. The number of contingencies is not limited, but it demands computation time. After the analysis, the highest post-contingency Thevenin impedance can be plotted together with the currently estimated Thevenin impedance and the load.

4.6 Remarks on impacts of shunt compensation

4.6.1 Effect of shunt compensation on the Thevenin impedance

It is widely acknowledged that the small Thevenin impedance represents a strong network, which has high transfer capacity to supply the load, and vice versa. This notion to some extent does not hold true when the system is highly compensated by capacitive shunt compensation. Take a simple grid shown in Fig. 4.17 as an example. Without the capacitor, the magnitude of Thevenin impedance seen by the load is

$$Z_{Th1} = X_L$$

With the capacitor connected, however, it will become

$$Z_{Th2} = \frac{X_L X_C}{X_C - X_L}$$

Obviously, $Z_{Th2} > Z_{Th1}$. In this case, the presence of the shunt compensation results in larger Thevenin impedance although the maximum power transfer is higher. In general, the Thevenin impedance is related to the strength of the grid, but when the assessment of voltage stability is conducted, it is more precise to compare this equivalent impedance with the load impedance to form the indicator ISI as presented in Chapter 2.

4.6.2 Relation between the maximum power transfer and the peak load power in highly overcompensated systems

The main principle of the methods for online voltage stability monitoring based on the Thevenin impedance is built on the two pillars: estimation of the Thevenin impedance

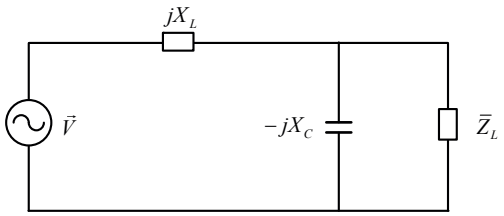

Figure 4.17: A simple system with shunt capacitor.

seen at a load bus and the maximum power transfer theorem. It is normally interpreted as: when the load reaches the peak power, the maximum power transfer condition occurs and the magnitude of the load impedance is equal to that of the Thevenin impedance. This condition is also used to validate the accuracy of the estimated Thevenin impedance. This paradigm works appropriately in many cases, but it is misleading when the system is highly overcompensated. Fig. 4.18 illustrates a simple system, in which an ideal voltage source is connected to bus 1 to supply the load at bus 2, which is represented as a resistance R. At this bus, the SVC is deployed to regulate the load voltage. The compensator is represented by a reactance X_c, which is computed as

$$X_c = \frac{U_2^2}{Q} \tag{4.13}$$

where Q is the reactive output power of the compensation system. According to the Thevenin theorem, the magnitude of Thevenin impedance seen at bus 2 is

$$Z_{Th} = \frac{XX_c}{X_c - X} \tag{4.14}$$

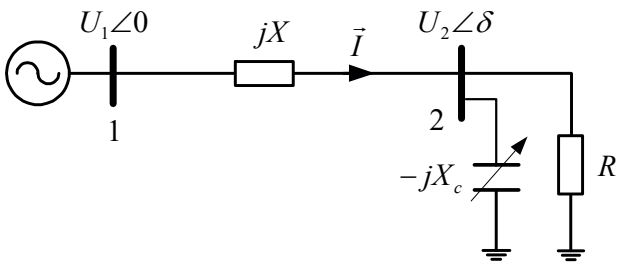

Figure 4.18: A 2-bus system with static VAr compensator.

To closely examine the system behavior, let $U_1 = 130$ kV and $X = 50\ \Omega$. The SVC and voltage source at bus 1 are modeled by the CSVGN5 and GENCLS models in the PSS/E standard library, respectively; voltage setpoint for the SVC is 1 pu. To demonstrate the relation between the Thevenin impedance and the maximum load power, the load originally equal to 50 MW is gradually increased until it exceeds the transfer capacity of the system as shown in Fig. 4.19b; meanwhile, the rated power of the SVC is set as 56 MVAr. At $t = 230$ s, the load power reaches its peak and starts falling. As can be seen in Fig. 4.19a, at this instant, the magnitude of the Thevenin impedance is equal to

that of the load impedance. In this case, the Thevenin impedance matches the maximum power transfer theorem. The load draws maximum power at the maximum power transfer condition.

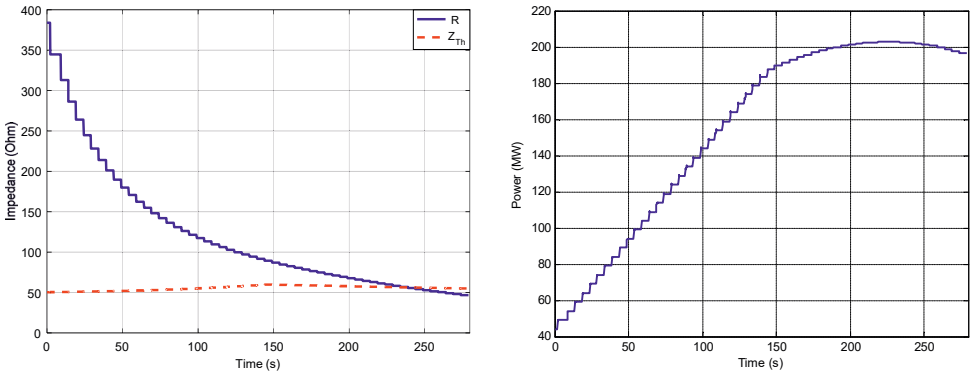

(a) The Thevenin and load impedance. **(b)** The load power.

Figure 4.19: The Thevenin impedance and load power when rated power of the SVC is 56 MVAr.

However, when the rated power of the SVC is adjusted from 56 MVAr to 169 MVAr, the situation changes. In Fig. 4.20b, it is seen that the peak power is reached at $t = 265$ s. At this instant, the magnitude of the Thevenin impedance is not equal to the load as seen in Fig. 4.20a. There is a mismatch between the instant when the maximum power transfer condition takes place and the time the load reaches the maximum power. Considering Fig. 4.18, the voltage source at bus 1 and the line reactance X are linear elements; therefore, the Thevenin theorem is applicable and consequently the Thevenin impedance seen at bus 2 is properly computed. So for this situation, the peak load power does not necessarily occur at the maximum power transfer condition, when the load impedance is equal to the Thevenin impedance. In this case, the rated power of the SVC and its controller are the main factors that drive the peak load power away from the maximum power transfer condition. As known, the main function of the SVC is to keep the controlled voltage at the desired value. When the two impedances are equal at $t = 220$ s, that is the instant of maximum power transfer condition. At this point, if the susceptance of the SVC is kept fixed, the load power will increase and starts decreasing. However, the SVC has not reached its limit yet; as the load continues rising, the SVC injects more and more reactive power to keep the voltage almost constant as can be seen in Fig. 4.21. As a result, the power demand is met until $t = 265$ s when the SVC has reached its limit. The process is graphically illustrated by the PV curves shown in Fig. 4.22. Initially, point A is the current operation point. As the demand increases, voltage is kept constant by the SVC. Gradually, the operation point is moving from point A to B and ends up at point C, where the SVC reaches its limit. As can be seen, at this point, the load power is maximum, but the operation point is located below the nose point, meaning that the maximum power transfer condition has been passed. In summary, for highly overcompensated areas in power systems, the peak load power can drift away from the maximum power transfer condition. Therefore, using the maximum load power to validate the accuracy of the estimated Thevenin impedance will lead to

improper assessment.

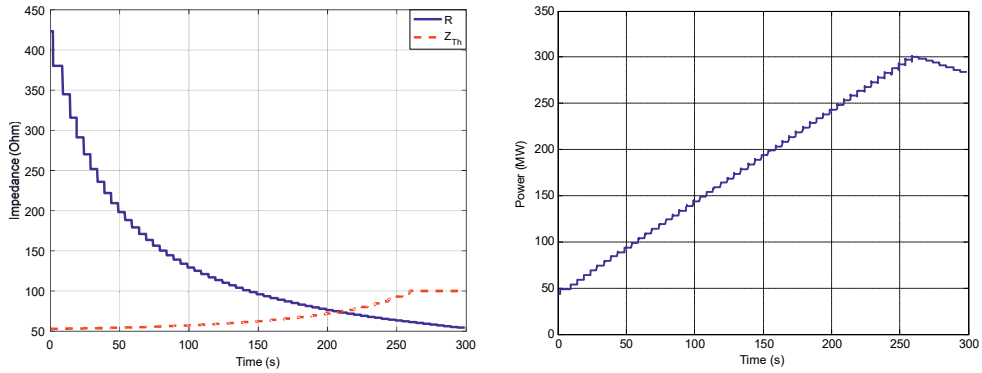

(a) The Thevenin and load impedance. **(b)** The load power.

Figure 4.20: The Thevenin impedance and load power when rated power of the SVC is 169 MVAr.

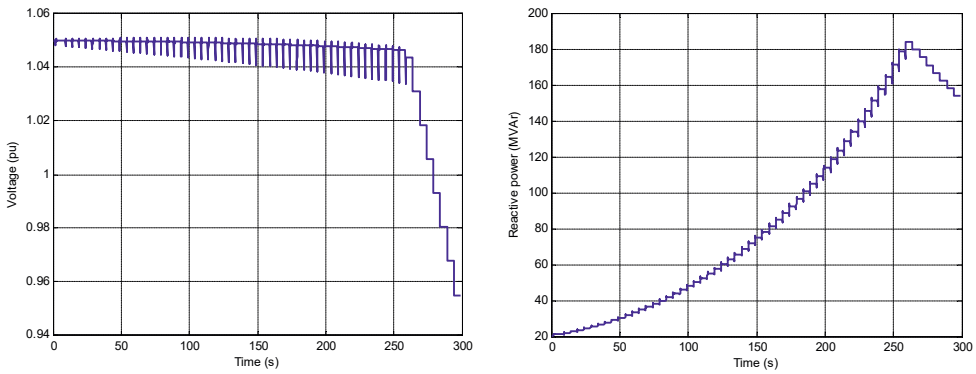

(a) Voltage at bus 2. **(b)** SVC's reactive power.

Figure 4.21: Load voltage and reactive output power when rated power of the SVC is 169 MVAr.

To determine the border, where the SVC can push the maximum load power away from the maximum power transfer condition, the system depicted in Fig. 4.18 is considered for further analysis. From the circuit, the magnitude of the load voltage is computed as

$$U_2 = \left|\vec{U}_1 - jX\vec{I}\right| = \frac{U_1 X_c R}{\sqrt{\left(X - X_c\right)^2 R^2 + X^2 X_c^2}} \tag{4.15}$$

Define P as the load active power. This gives

$$P = \frac{\left|\vec{U}_1 - jX\vec{I}\right|^2}{R} = \frac{U_1^2 X_c^2 R}{\left(X - X_c\right)^2 R^2 + X^2 X_c^2} \tag{4.16}$$

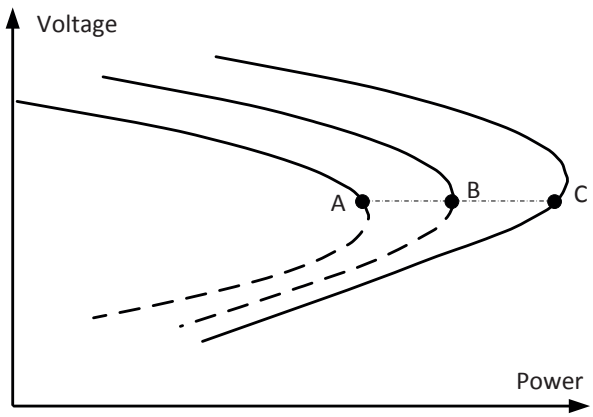

Figure 4.22: PV curves to illustrate the trajectory of the operation point when the system is highly overcompensated by the 169 MVAr SVC.

Based on the parameters of the system on page 73, the load power is plotted versus the X_c and R and shown in Fig. 4.23. As can be seen, at a given SVC capacity represented by X_c, when the load resistance decreases, the power increases until it reaches the maximum loadability; afterwards, the power cannot increase any more and starts to go down. Based on (4.16), the partial derivative of the load power with respect to the load resistance is

$$\frac{\partial P}{\partial R} = \frac{U_1^2 X_c^2 \left[(X - X_c)^2 R^2 + 2 (X - X_c)^2 R + X^2 X_c^2 \right]}{\left[(X - X_c)^2 R^2 + X^2 X_c^2 \right]^2} \tag{4.17}$$

With a given X_c, equating (4.17) to zero yields

$$R_{max} = \frac{X X_c}{X_c - X} \tag{4.18}$$

It is noted that R_{max} is in fact the load resistance at the maximum power transfer condition.

Assume that U_1 in (4.15) is known. The voltage U_2 as a function of R and X_c is the plane, which is plotted and shown in Fig. 4.24a. It is noted that when the load is projected to the peak power, the load voltage is kept constant by the SVC. Therefore, the load trajectory is the intersection of the two surfaces, which also can be seen in the top view shown in Fig. 4.24b.

Combining features from Fig. 4.23 and 4.24 gives an insight into the system's behavior when it is highly overcompensated. From (4.18), the trajectory of the maximum power transfer condition can be plotted as the red curve in the R-X_c plane shown in Fig. 4.25. On the right hand side of this curve, the load resistance is larger than R_{max}; that means the load has not reached the maximum power transfer condition. However, the left hand side of the curve represents the operation condition when the maximum power transfer has been crossed. In addition, in (4.15) U_2 is the load voltage, which is also the voltage setpoint for the SVC. Given a setting value of U_2, one can use (4.15) to plot a curve in the R-X_c plane; this curve is called the load trajectory. In effect, the blue and green curves in Fig. 4.25 are plotted based on (4.15) when the voltage setpoint is 0.95 pu and 1.05 pu, respectively. As can be seen, as the load increases, the load trajectory will cross

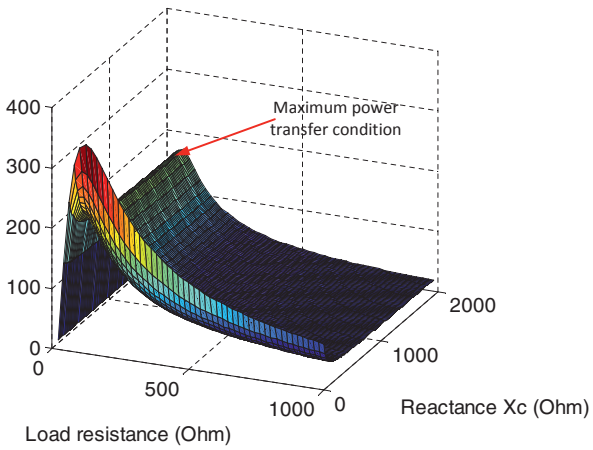

Figure 4.23: Load power versus R and X_c.

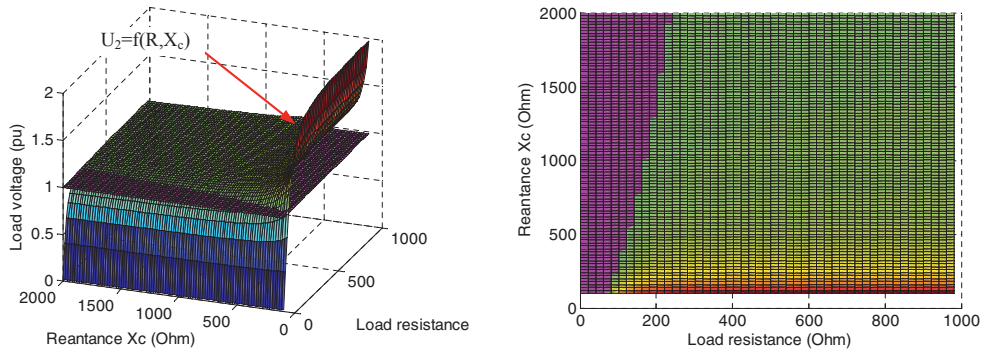

(a) Voltage plane as a function of R and X_c, plotted from (4.15).

(b) Top view of the load projection on the R-X_c plane.

Figure 4.24: Load trajectory on the R-X_c plane under SVC's constant voltage control.

the red curve at a certain X_c, say 200 Ω. If the SVC has $X_c > 200$ Ω (for example: 500 Ω), it does not have enough reactive power to drive the operation point beyond the maximum loadability border. This means the peak load power will occur at the maximum power transfer condition. In other words, the instant when the load and the Thevenin impedance are equal is the same as the time the load reaches its peak power. That is the case previously seen in Fig. 4.19 when the SVC has the rated power of 56 MVAr. If the SVC has higher capacity ($X_c < 200$ Ω), the load can draw more power from the grid although the maximum power transfer condition has been passed. In this case, the load does not obtain maximum power at the maximum loadability condition as stated in the maximum power transfer theorem. The demand can increase its power as long as the SVC does not reach its limit. This condition has been illustrated in Fig. 4.20 and 4.21. In addition, from Fig. 4.23 and 4.25, one can recognize that with the same SVC capacity, the higher the SVC voltage setpoint, the higher power the load can draw from the grid, assuming that the SVC has enough reactive power to drive the load beyond the maximum power transfer condition.

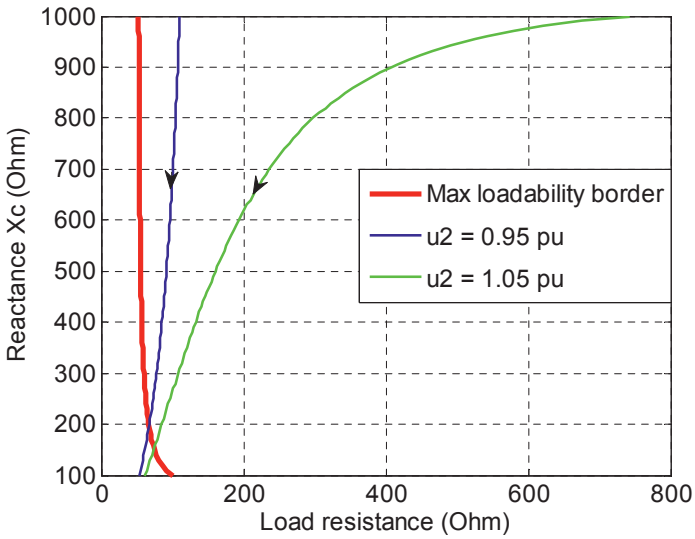

Figure 4.25: Maximum power transfer condition curve and load trajectory under constant voltage control.

Chapter 5

Case study for online voltage stability monitoring

This chapter presents results of a case study and assesses performance of the two proposed methods for online voltage stability monitoring, in comparison with the CT algorithm [47] in several test cases. The first study is conducted by a simulation on a 130 kV subsystem located in the northern part of Norway. It is followed by another test case at the Hasle corridor, the main 420 kV connection between the Norwegian and Swedish transmission systems. In the next section, a prototype for online voltage stability named V_{app} is introduced, and its performance with real PMU data at the Hasle corridor and a 130 kV substation in the Norwegian transmission system is presented. The chapter continues with a further case study on the Nordic32 test system and ends with performance of the proposed load shedding scheme implemented in this 32-bus benchmark.

5.1 Case study on a 130 kV subsystem in the northern Norway

The studied subsystem is a part of the Norwegian transmission grid that is vulnerable to voltage instability. Fig. 5.1 depicts a simplified single line diagram of the studied area. The modeled region consists of 21 buses and has the rated voltage at 130 kV. As can be seen, the area is supplied via a 420/130 kV substation at bus 1 and two large power plants connected to bus 2 and 3. In this area, the long 130 kV lines impose constraints on the transfer capacity, and consequently voltage instability. In this subsystem, bus 21 is the weakest bus, which has been exposed to voltage instability. Therefore, this node is selected as the monitored bus in the case study.

In order to estimate the Thevenin impedance seen at the considered node, the following configurations are used in the tested algorithms:

- In the topology-based method, only 21 buses in this area are taken into the admittance matrix. The rest of the system topology is not included. Since bus 1 is connected to a strong transmission system, and bus 2 and 3 have also connections to large generation, they are treated as strong A-P buses.

- In the S-Z method, the ratio X_{Th}/R_{Th} of the Thevenin impedance must be set in advance. In this 130 kV subsystem, a typical value of the ratio X/R of the power lines is 5.1774. Therefore, this number is assigned to the Thevenin impedance.

- As presented in Chapter 2, the factor k has a decisive role in the CT method. In this case study, $k = 0.008$ is selected because it produces a better estimation of the Thevenin impedance than the others.

To validate performance of the two proposed approaches, in comparison with that of the CT method, the load at bus 21 is increased until it crosses the maximum power transfer limit; meanwhile the rest of the loads in the area are modeled as constant power loads. The simulation in PSS/E is run based on the dynamic model of the whole Norwegian transmission system; the time step is 10ms. Fig. 5.2 shows voltage at the monitored bus and the PV curve of the load during the simulation period. As can be seen, the voltage gradually drops when the load increases. At $t = 41$ s, the voltage falls sharply when the maximum loadability is crossed. This event can also be seen in the PV curve in Fig 5.2b.

Fig. 5.3 depicts magnitudes of the load impedance ($ZLoad$) and the Thevenin impedances ($ZTopo$, $ZS\text{-}Z$ and ZCT) obtained from the topology-based, S-Z, and CT methods, respectively. As can be seen, the three methods produce similar estimations of the Thevenin impedance seen at bus 21. At $t = 41$ s, all the estimated impedances are equal to the load impedance. That is the instant when the load reaches its maximum loadability as can be seen in Fig. 5.4. In addition, the results from the S-Z and CT methods are almost the same during the load increase period. Meanwhile, the estimated Thevenin impedance obtained from the topology-based is slightly higher than the others, but the mismatch is quite small. Among others, the topology-based method shows a consistent performance during the simulation period; the estimated Thevenin impedance is almost unchanged. In addition, it is noted that during the initial period $t = 0 - 13$ s, the result from the CT method is initially high and quickly converges to an appropriate value. This is the one time initialization as an intrinsic characteristic of the method; it does not have any negative effects on performance of the method.

In Fig. 5.4, the load power and the estimated maximum power transfer are plotted. As can be seen, the topology-based method has a better estimation than the other approaches; the estimated value is consistent during the simulation time. At $t = 0$ s, the estimated power is 0.0815 pu, then it slightly drops to 0.076 pu and becomes equal to the load power at $t = 41$ s. Although the S-Z and CT methods have an optimistic estimation of the maximum loadability, the gap between the load power and the estimated maximum power transfer is significantly reduced as the load is approaching the voltage stability limit. At the instant of maximum power transfer condition, these two methods eventually provide a good estimation; the estimated maximum loadability falls and becomes equal to the peak load power.

Fig. 5.5 depicts performance of the S-Z sensitivity indicator (S-ZI) at the monitored bus. As can be seen in Fig. 5.5a, when the load is within the voltage stability limit, the S-ZI is negative. At $t = 41$ s, the load reaches the maximum loadability. This condition is timely reflected by the S-ZI. This indicator becomes positive from this instant to the end of the simulation. In addition, Fig. 5.5b shows a trajectory of the S-ZI versus magnitude of the load impedance. As expected, the S-ZI trajectory is in line with the pattern shown in Fig. 3.5. When the load is light (high load impedance), the S-ZI is negative. As the load increases (smaller load impedance), this sensitivity gradually goes down. The trend is unchanged until the load impedance falls to 10 pu, then the S-ZI reverses its direction. It starts rising and reaches zero when the load is crossing the maximum loadability; evidently, S-ZI is able to detect the maximum power transfer condition timely and successfully.

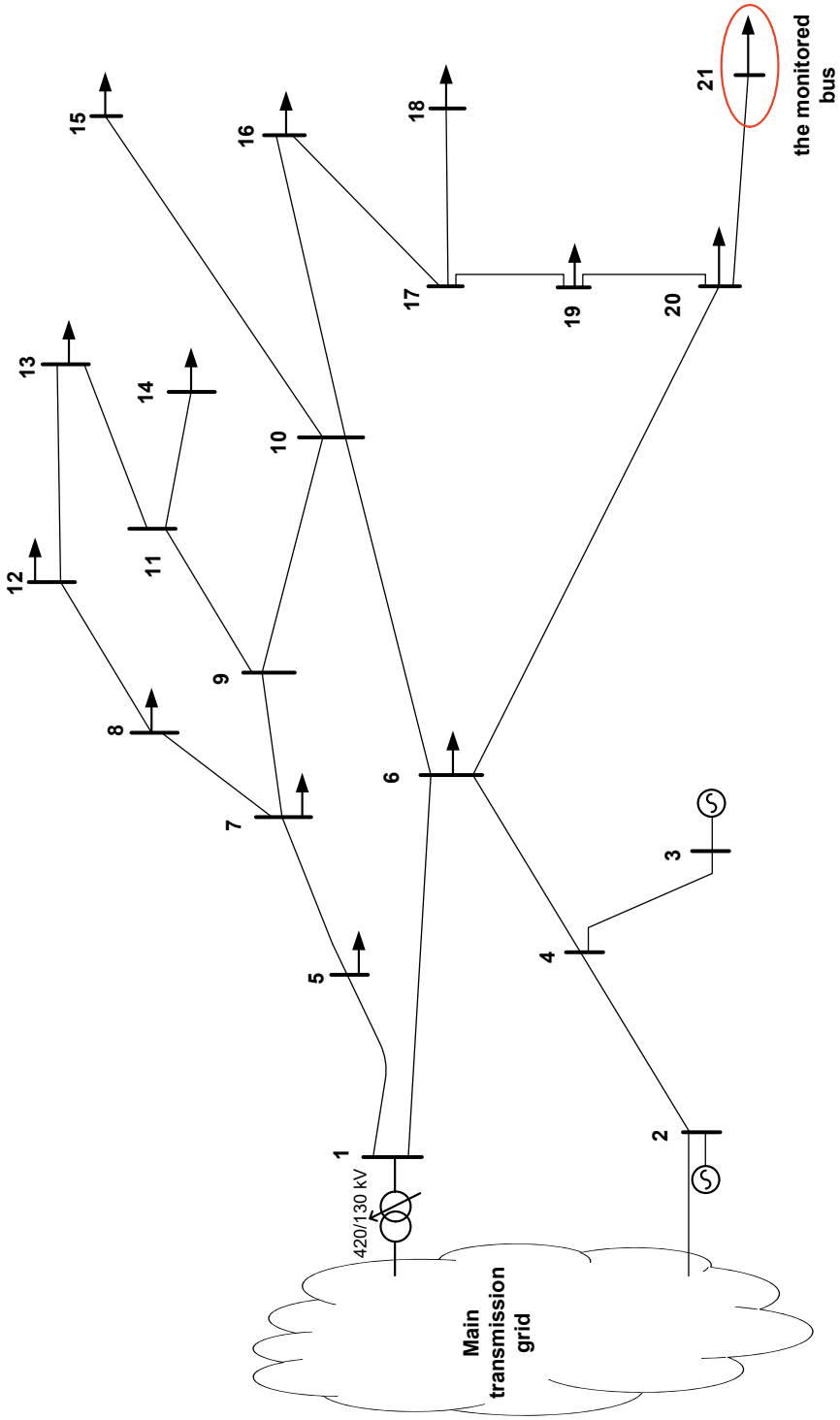

Figure 5.1: Simplified single line diagram of the studied 130 kV subsystem.

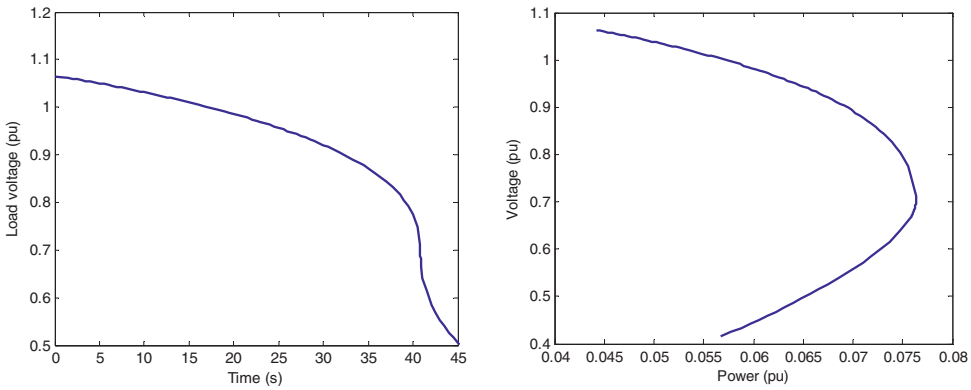

(a) Voltage at bus 21. **(b)** The PV curve at bus 21.

Figure 5.2: Voltage and the PV curve at bus 21 during the load increase period.

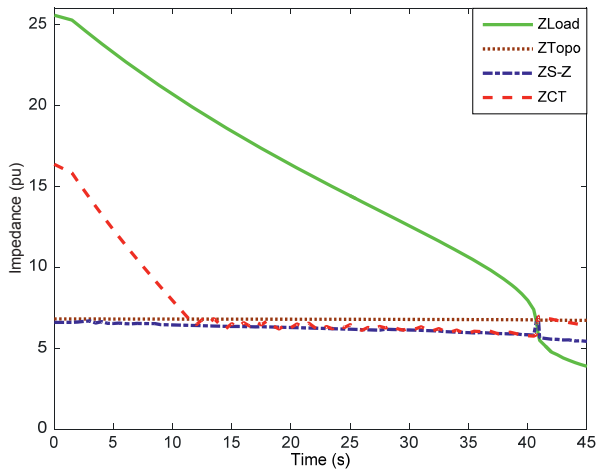

Figure 5.3: The Thevenin impedance seen at bus 21.

DISCUSSION

- In the studied subsystem, small generators do not exist. Therefore, the Thevenin impedance seen at the considered load bus is determined by the system topology and impedance of the other loads in the area. The load impedance at the other buses slightly varies during the time the load at bus 21 increases; consequently, the magnitude of the Thevenin impedance obtained from the topology-based method has a very small drop. This is an advantage of the topology-based method. The estimated value is normally smooth, consistent and highly resistant to noise or errors of the measurements. However, information on the system topology is vital to the method's performance. Changes of the system topology should be updated as soon as possible, preferably event-based.

- The power injected into bus 2 and 3 in this case study is large and comparable to the power drawn from the transmission system at bus 1; hence, these buses are

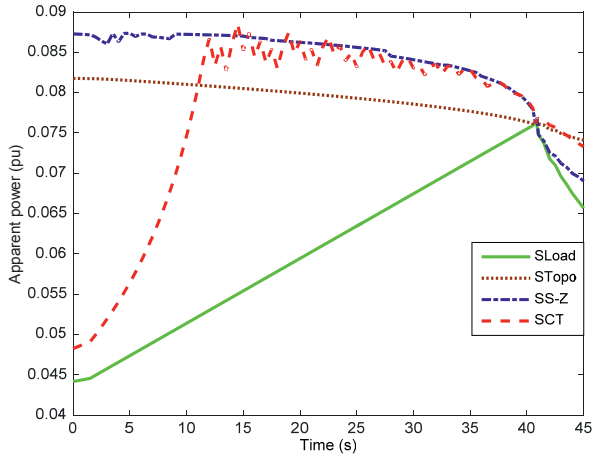

Figure 5.4: Estimated maximum loadability at bus 21.

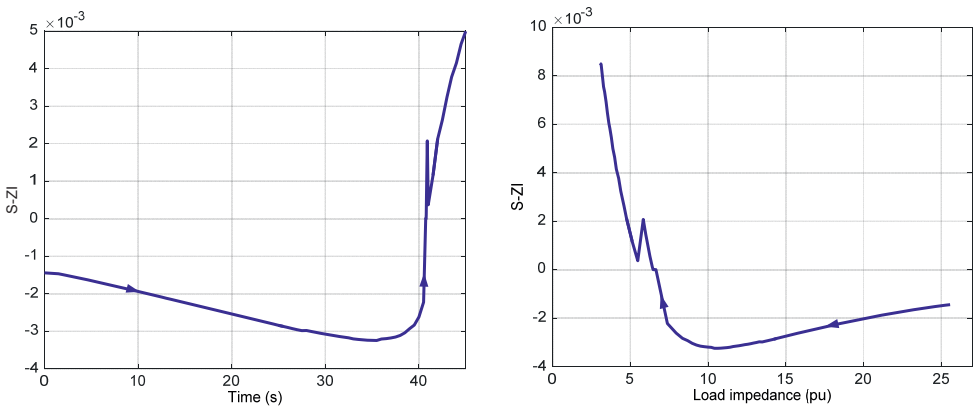

(a) S-ZI trajectory versus time **(b)** S-ZI trajectory versus load impedance.

Figure 5.5: Trajectory of the S-ZI during the load increase period.

treated as strong A-P nodes. In practice, they can be considered as weak A-P nodes because the generators can frequently change their active power, depending on the day-ahead and intraday markets. At a low power production level, they cannot be treated as the strong A-P buses since it will lead to smaller Thevenin impedance. In this case, PMUs need to be installed at these two buses to compute the virtual power flow between them and the monitored bus. This power is then used to compute the coupling reactance, which has a contribution to the Thevenin impedance seen at the monitored bus as presented in Chapter 4.

- The topology-based method does not require information about system topology of the entire Norwegian transmission system. Instead, only 21 buses in the studied area are needed. In general, the size of a concerned area that is vulnerable to voltage instability can be limited to a small number of boundary buses. Consequently, inversion of the modified admittance matrix incurs a very low computational cost.

This makes the method suitable for online implementation of voltage stability monitoring.

- The maximum loadability is sensitive to accuracy of the estimated Thevenin impedance, especially when the load is far from the voltage stability limit. In Fig. 5.3, the Thevenin impedances obtained from the S-Z and CT methods are slightly lower than the actual value, but this mismatch leads to a quite large disparity in the estimated maximum power transfer. Therefore, between the two indicators (the impedance index indicator ISI and power margin), the ISI should be used to assess voltage stability at the monitored load bus, and the power margin should be considered as extra information although it is more indicative for system operators.

- The proposed S-Z method is model-free; it requires only phasor measurements of voltage and current of the monitored load. In the test case, this algorithm performs very well and produces a good estimation of the Thevenin impedance. Compared to the topology-based approach, this methodology is obviously outstanding.

- Despite its simplicity, the S-Z sensitivity indicator (S-ZI) shows a good performance. The indicator is able to detect the voltage stability limit properly; its trajectory during the load increase period closely matches the expected pattern shown in Fig. 3.5. Undoubtedly, S-ZI is an appropriate indicator for online voltage stability assessment.

5.2 Case study at the Hasle corridor

5.2.1 Load increase

The Hasle corridor is located in the south-eastern Norway as can be seen in Fig. 5.6. This is the main corridor for power exchange between the Norwegian and Swedish transmission systems. Due to high power transfer from Norway to Sweden, online voltage stability monitoring at this location is of interest. The transmission system in this region comprises the 420 kV and 300 kV networks, transferring energy from large generation mainly located in the west to the load center, which is situated in the eastern part. At the Hasle corridor, there is a SVC used to regulate the 420 kV voltage and to increase the power transfer. There are also several SVCs and synchronous condensers in the area. These fast-acting components increase the degree of dynamic interactions in the grid. The case study in this section is to explore the maximum power transfer at the corridor and to validate the estimated Thevenin impedance of the Norwegian transmission system seen at the corridor. Therefore, the power transfer at the corridor is increased until it crosses the maximum loadability. It is noted that, in reality, there are many factors that limit the maximum power transfer at the Hasle corridor. These constraints are not considered in this work; only the maximum power transfer limit with respect to voltage stability is studied.

In order to estimate the Thevenin impedance seen at the corridor, the following settings are used in the tested algorithms:

- The topology-based method treats all the generation buses and 420 kV nodes that have connections to the 300 kV system as the weak A-P nodes. Consequently, the size of the studied system is limited to 20 buses.

- In the S-Z method, the ratio $X_{Th}/R_{Th} = 15$ is assigned to the Thevenin impedance. This is a typical value of the power lines in this 420 kV network.
- In the CT method, $k = 0.0003$ is selected because it gives better estimation of the Thevenin impedance than the others.
- In addition, there are two tie lines (Hasle - Borgvik and Hasle - Halden) at the Hasle corridor. The currents of these lines are summed up and considered as the load current. This current and the voltage at the 420 kV bus are used as the inputs of S-Z and CT methods.

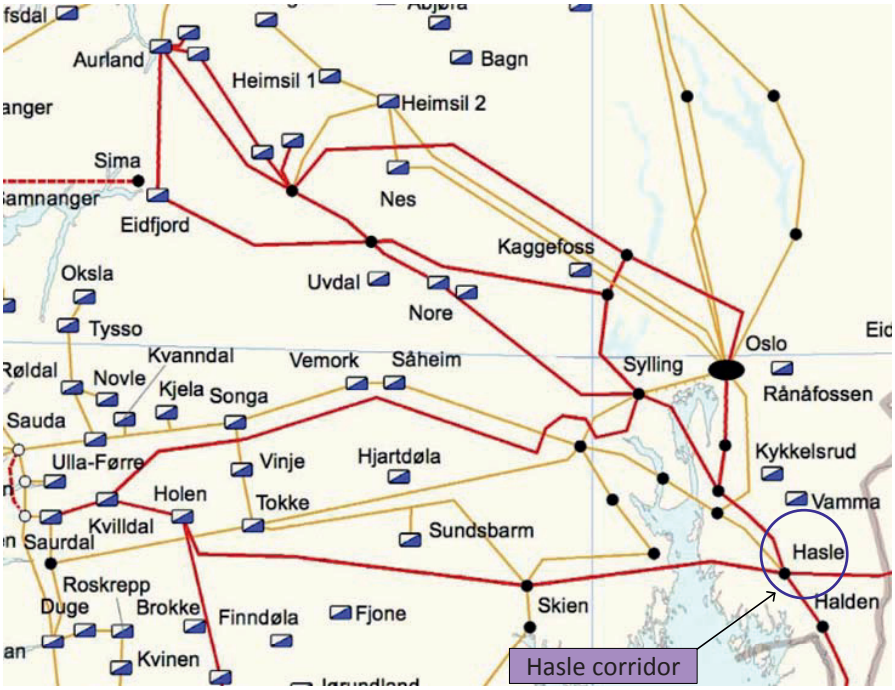

Figure 5.6: The transmission system in the southern Norway [63].

To validate performance of the two proposed algorithms, in comparison with that of the CT method, the power transfer on the tie lines in this simulation is increased until it goes beyond the transfer capacity. All the loads are modeled by a ZIP model that consists of 40% of constant power, 30% of constant current and 30% of constant impedance. The simulation in PSS/E is run based on the dynamic model of the whole Norwegian transmission system; the time step is 10ms. Fig. 5.7a shows voltage at the concerned bus and the PV curve during the simulation period. As can be seen, the voltage gradually drops when the load is increasing. At $t = 370$ s, the voltage falls more sharply when the maximum loadability is reached. This event can also be seen in the PV curve in Fig. 5.7b.

Fig. 5.8 shows the load impedance ($ZLoad$) and the Thevenin impedances ($ZTopo$, $ZS\text{-}Z$ and ZCT) obtained from the topology-based, S-Z, and CT methods, respectively. As can be seen, the three methods produce comparable estimations of the Thevenin

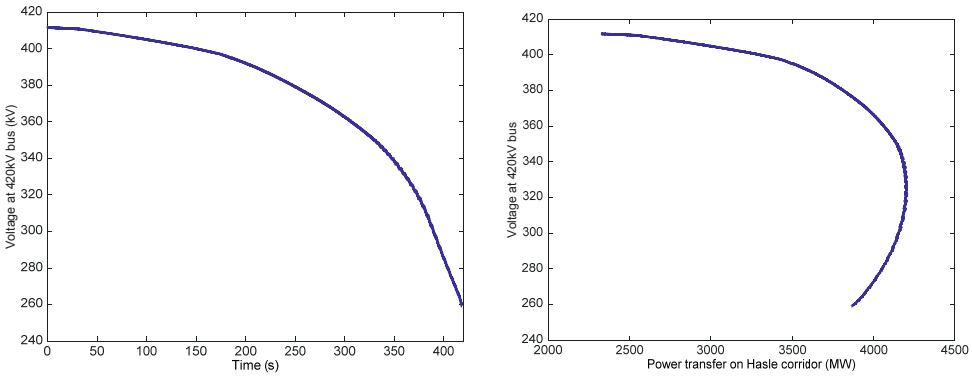

(a) Voltage at the 420 kV busbar. **(b)** The PV curve.

Figure 5.7: Voltage and the PV curve at the Hasle corridor when power transfer on the corridor is increased until it crosses the maximum loadability.

impedance. During the simulation period, the estimated Thevenin impedance obtained from the topology-based method varies from 25 Ω to 29 Ω; meanwhile, the estimated value from the S-Z method has a small variation and lies within the range from 26 Ω to 42 Ω. Except for the one time initialization period $t = 0 - 175$ s, the CT method also shows a comparable estimate, ranging from 26 Ω to 29 Ω. In comparison, the two local PMU measurement-based methods exhibit a very similar performance; the estimated Thevenin impedance is around 29 Ω, which is about 3 Ω higher than the value obtained from the topology-based approach. Consequently, the S-Z and CT methods detect the maximum power transfer condition at $t = 335$ s, when their estimates are equal to the load impedance. However, the topology-based approach identifies the maximum power transfer condition at $t = 365$ s. Nevertheless, this mismatch is insignificant. As can be seen in Fig. 5.9, during the period $t = 335 - 365$ s, the demand is almost unchanged and stays at the peak power.

It is noticeable that although the Thevenin impedance has a small variation in magnitude, the estimated maximum power transfer has a large variation. At $t = 0$ s, the load power is 2300 MVA; meanwhile, the maximum loadability is estimated at 3000 MVA by the topology-based method and 2700 MVA by the S-Z approach. The power margins produced by the two approaches are 700 MVA and 400 MVA, respectively. As the load power increases, the estimated maximum loadability also rises accordingly. However, power margin is continuously reduced until it becomes zero at $t = 357$ s. At this instant, the three methods provide the same maximum power transfer, which is about 4180 MVA. Compared to the actual peak power at 4200 MVA, the mismatch is insignificant.

Fig. 5.10 depicts the S-Z sensitivity indicator (S-ZI) at the corridor during the load increase period. As can be seen in Fig. 5.10a, when the load is within the voltage stability limit, S-ZI is negative. At $t = 338$ s, the S-ZI is equal to zero, meaning that the nose point is reached. However, from Fig. 5.9, the peak load power occurs at $t = 365$ s. In this case, the S-ZI detects the maximum power transfer condition slightly earlier than the actual condition. Nonetheless, from $t = 338$ s to $t = 365$ s, the load power increases by 36 MVA, which is very minor, compared to the load power at 4200 MVA. The error is obviously acceptable.

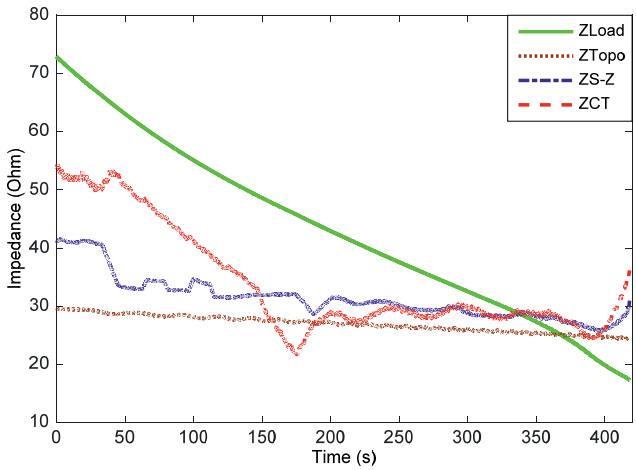

Figure 5.8: Thevenin impedance at the Hasle corridor when power transfer on the corridor is increased until it crosses the maximum loadability.

In addition, Fig. 5.10b shows a trajectory of the S-ZI versus magnitude of the load impedance. As expected, the S-ZI trajectory is in line with the pattern shown in Fig. 3.5. When the load is light (high load impedance), the S-ZI is negative. As the load increases (smaller load impedance), the S-Z sensitivity slightly goes down and then it reverses its direction. The sensitivity starts rising and becomes positive when the load impedance is equal to 28.64 Ω. This is the point, where the estimated Thevenin impedance obtained from the S-Z method is equal to the load impedance.

DISCUSSION

- In Fig. 5.8, the estimated Thevenin impedance from the topology-based method slightly drops when the load increases. It can be explained by the fact that the studied 420 kV network has several connections to the 300 kV grid. When the power transfer on the tie lines rises, more power is injected from the 300 kV side into the 420 kV network. As a result, the virtual reactances between the A-P nodes and the concerned bus (the Hasle corridor) is reduced. This makes the estimated Thevenin impedance slightly fall.

- There is a large variation of the estimated maximum loadability although the Thevenin impedance has small deviations. This can be explained by the following two reasons:

  – The estimated maximum loadability is largely influenced by the Thevenin impedance. Take the result of the topology-based method as an example. At $t = 0$ s, the estimated Thevenin impedance is 29 Ω and the maximum power transfer is estimated at 3000 MVA. When the load is at the peak power, the Thevenin impedance is 25 Ω and the maximum is 4180 MVA. The variation of the Thevenin impedance is just 4 Ω, but the estimated maximum loadability changes by 1500 MVA.

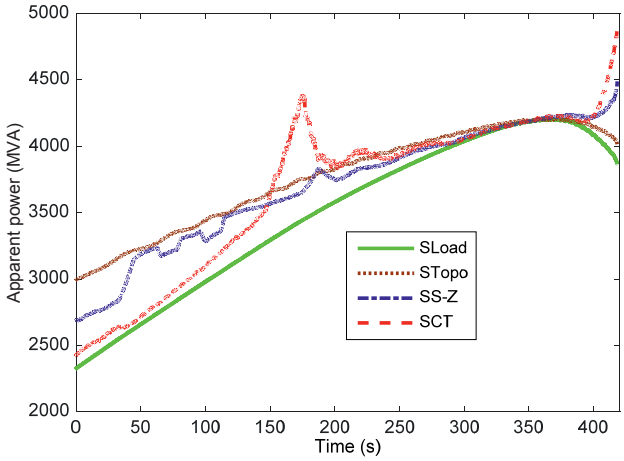

Figure 5.9: Estimated maximum loadability at the Hasle corridor when power transfer on the corridor is increased until it crosses the maximum loadability.

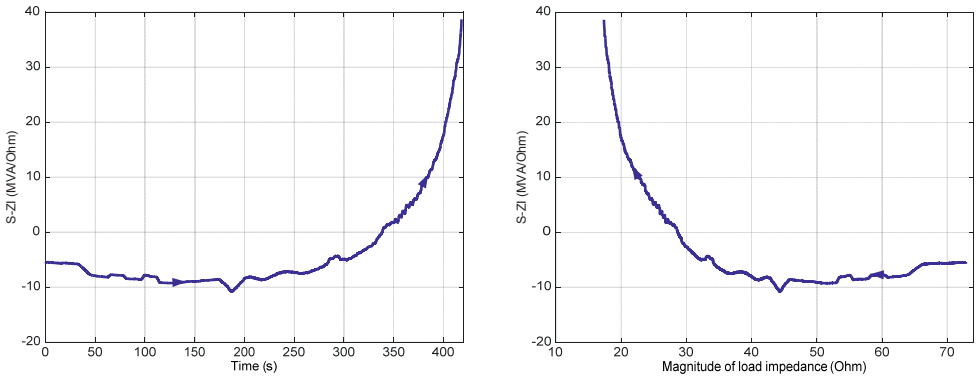

(a) S-ZI trajectory versus time. **(b)** S-Z trajectory versus load impedance.

Figure 5.10: Trajectory of S-ZI during load increase period at the Hasle corridor.

- In the studied area, there are several SVCs and synchronous condensers. At light load demand, these components inject a part of their VAr reserve. When the demand becomes higher and higher, these shunt compensators, in an effort to maintain the voltage at a desired value, gradually increase their reactive power until they reach the maximum power limit. As a result, transfer power of the system is increased.

It is, therefore, important to note that the Thevenin impedance and the maximum power transfer are measures of temporary strength of the network. Their value at a particular instant of time should not be used to evaluate the ultimate limit of the network. The system exposes its ultimate capacity only when the demand is approaching the voltage stability limit.

- Similar to the case study presented in Section 5.1, it is convincingly demonstrated

that S-ZI is a good indicator for online voltage stability monitoring. In both cases, the indicator successfully detects the voltage stability limit. Its trajectory is similar to the predefined pattern shown in Fig. 3.5.

5.2.2 Load recovery after a line outage

This case study simulates a scenario, in which voltage stability is caused by load recovery after a disturbance in the grid. In addition, the study also demonstrates a capability of the topology-based method to estimate of the Thevenin impedance subjected to contingencies, which is called the post-contingency Thevenin impedance. In this study, all the three algorithms use the same settings as presented in Section 5.2.1. In order to emulate voltage instability, the grid is heavily loaded. This loading condition is deliberately made to validate the methods; it is different from the actual loading level in the studied area.

Regarding the estimation of the Thevenin impedance under a particular contingency, Fig. 5.11 shows magnitudes of the load impedance, the Thevenin impedance (estimated in current operation condition) and the post-contingency Thevenin impedance on the assumption that one dedicated line is tripped. Before the disturbance at $t = 50$ s, the post-contingency Thevenin impedance is 41.3 Ω. This value is computed by: i) modifying the admittance matrix based on the contingency of tripping the line; and ii) using the current measurements at the A-P nodes and the monitored load bus as presented in Chapter 4. As can be seen, compared to the Thevenin impedance estimated after the disturbance, the mismatch between the post-contingency Thevenin impedance and the currently estimated impedance is just 1.67 Ω, which obviously is reasonably small compared to the Thevenin impedance (42.94 Ω) and the load impedance (61.73 Ω at $t = 50$ s).

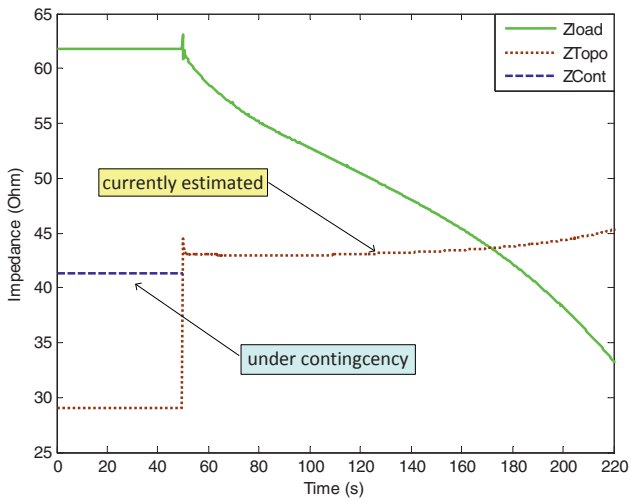

Figure 5.11: Estimation of the Thevenin impedance under contingency at the Hasle corridor, obtained from the topology-based method.

In the simulation, the load recovery is the main driver for voltage instability at the Hasle corridor. To emulate this phenomenon, the load model EXTLAL in PSS/E [64] is applied to all the loads in the grid. As can be seen in Fig. 5.13, after the disturbance,

the power demand ($SLoad$) tries to return to the pre-disturbance level. However, during the period $t = 90 - 160$ s, the load power is unchanged, and then it starts falling. Fig. 5.12 depicts magnitude of the load impedance and the Thevenin impedances obtained from the S-Z and CT methods (ZS-Z and ZCT, respectively). During the time $t = 0 - 60$ s, the S-Z method does not produce any output. The reason is that there are no load variations during the period $t = 0 - 50$ s at the corridor. Afterwards, from $t = 50 - 60$ s, the variations are distorted by transients, and they are, therefore, too small to reflect the actual response of the grid with respect to the Thevenin impedance.

Nonetheless, the S-Z and CT methods successfully detect the voltage stability limit despite a rather large mismatch between them before the load reaches the voltage stability limit. Roughly at $t = 170$ s, the estimated Thevenin impedances from these algorithms are equal to the load impedance. In addition, a similar result from the topology-based method is shown in Fig. 5.11. After the instant the Thevenin impedance is equal to the load impedance, the load power, as seen in Fig. 5.13, no longer stays at its peak and starts falling since it has passed the maximum loadability.

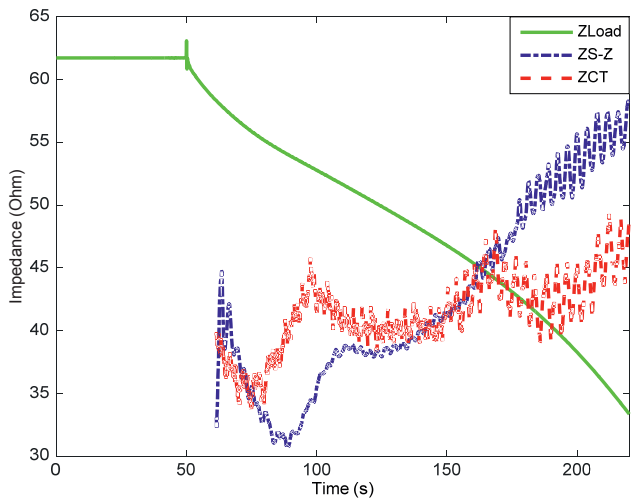

Figure 5.12: The Thevenin impedance at the Hasle corridor obtained from the S-Z and CT methods during the load recovery period.

Fig. 5.13 depicts the load power and the estimated maximum loadability obtained from the three methods. Among others, the topology-based approach shows the best performance. The result is very smooth and matches the peak power very well. The other methods perform rather well although they have quite large errors during a short period after the disturbance. In short, the three methods exhibit an appropriate performance; at $t = 170$ s, the estimated maximum power transfer is equal to the peak power as expected.

Alternatively, the voltage stability limit is also appropriately detected by the S-ZI as shown in Fig. 5.14. As can be seen in Fig. 5.14a, when the load is within the voltage stability limit, S-ZI is negative. From the instant $t = 160$ s, the S-ZI reaches zero and becomes positive during the rest of the simulation. This is in line with the load power as seen in Fig. 5.13. At this instant, the load power stays almost unchanged at the peak power. Alternatively, Fig. 5.14b shows trajectory of the S-ZI versus magnitude of the load impedance. As expected, the S-ZI trajectory matches the pattern shown in

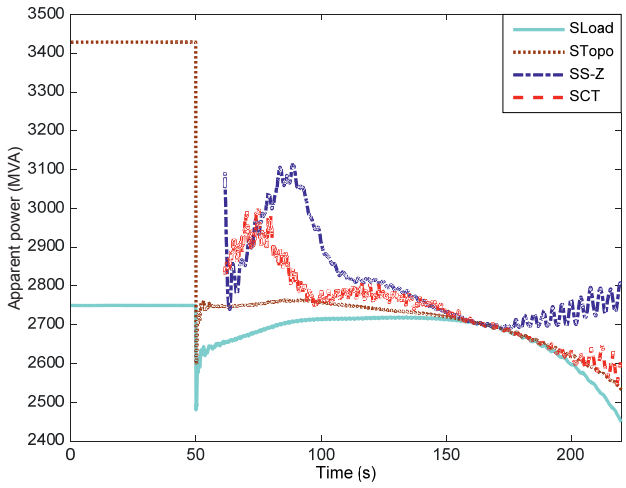

Figure 5.13: Estimated maximum loadability at the Hasle corridor obtained from the topology-based, S-Z and CT methods in the load recovery case study.

Fig. 3.5. When the load is light (high load impedance), the S-ZI is negative, but, as the load tries to restore the initial power demand (load impedance becomes smaller and smaller), S-ZI goes down and then reverses its direction when load impedance is 54 Ω. After that, the S-ZI starts rising and reaches zero when the load impedance is equal to 45 Ω. That is the instant the estimated Thevenin impedance is equal to the load impedance as can be seen in Fig. 5.11 and 5.12.

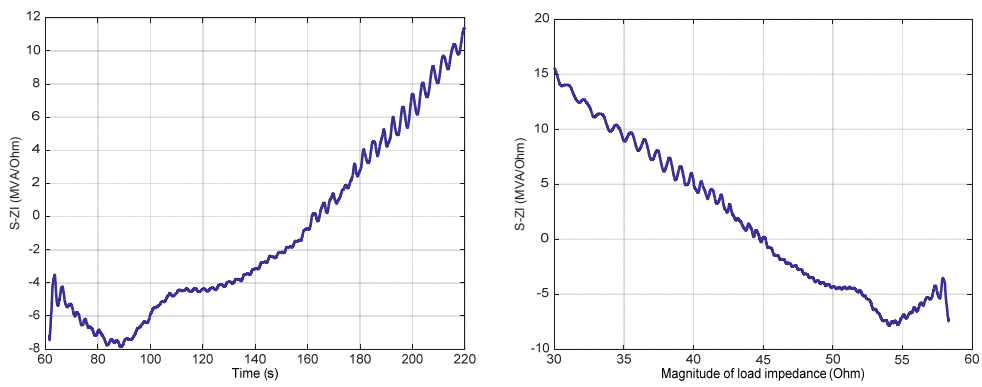

(a) S-ZI trajectory versus time. **(b)** S-ZI trajectory versus load impedance.

Figure 5.14: Trajectory of the S-ZI during the load recovery at the Hasle corridor.

DISCUSSION

- The capability to estimate the Thevenin impedance subjected to contingencies is an advantage of the topology-based approach. It reveals the potential risk of the current operating point under critical contingencies. The estimation does not require any simulation of the contingency as such; it solely utilizes measurements in the current operation condition and the system topology information. Therefore, it incurs a very low computational cost, and consequently it is suitable for online implementation. Fig. 5.11 has demonstrated the effectiveness of the proposed approach.

- The S-Z method estimates the Thevenin impedance based on variations of the local load and the corresponding response of the grid. In the period $t = 0 - 60$ s, the S-Z method cannot produce any output because of lack of load variations or too small variations. However, it is noted that this condition rarely occurs in practice. In the next section, a performance of a prototype that implements the S-Z method will be presented. This application has been tested in real time with real data from the PMU installed at the Hasle corridor since February 2014. During the testing period, conditions like lack of load variations or too small variations have not been observed yet. The monitored load constantly varies in time as seen in Fig. 5.15.

- It is observed in from Fig. 5.12 to Fig. 5.14 that the results from the two PMU measurement-based approaches contain some oscillations. In fact, the studied system is heavily loaded. Following the disturbance, transients in the system and fast load recovery at the Hasle corridor in short time have created power oscillations in the 420 kV network. The oscillations affect the voltage and current at the monitored bus, and that is why the S-Z and CT methods produce an oscillating performance.

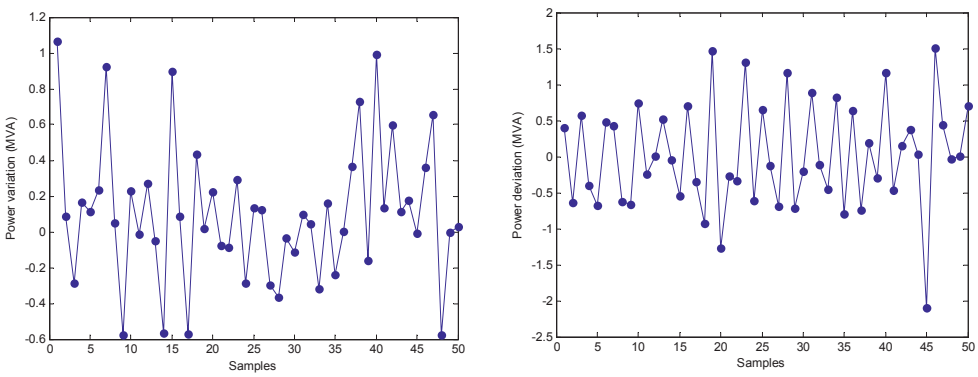

(a) Variations of apparent power between two consecutive measurements observed in a 1-second period on March 16, 2014.

(b) Variations of apparent power between two consecutive measurements observed in a 1-second period on October 20, 2014.

Figure 5.15: Variations of the apparent power between two consecutive measurements at the Hasle corridor.

5.3 Prototype of online voltage stability monitoring - V_{app}

Based on the proposed S-Z method for estimation of the Thevenin impedance and the new indicator S-ZI presented in Chapter 3, a prototype of online voltage stability monitoring, which is called V_{app}, has been built in Labview. As shown in Fig. 5.16, phasor of voltage at the 420 kV bus and currents of the two tie lines Hasle-Borgvik and Hasle-Halden at the Hasle substation are measured and sent to the phasor data concentrator (PDC). The reporting frequency is 50Hz, meaning that, in 1 second, 50 phasor measurements are taken by the PMU and sent to the PDC. The data is then concatenated into one stream and sent to a computer, where the application is developed. Here, a toolkit called PMU Recorder Light (PRL) [65] handles the communication with the PDC. This module, as shown in Fig. 5.17, is developed within the STRONg^2rid project; its function is to provide phasors and analog data extracted from the incoming streams. The toolkit frees researchers from handling the communication with the PDC and extracting data in the messages defined in the standard IEEE Std C37.118.1-2011 [66]. Therefore, developers can use the data directly from the PRL's outputs and consequently quickly build their own applications. A detailed description of the PRL is presented in [65].

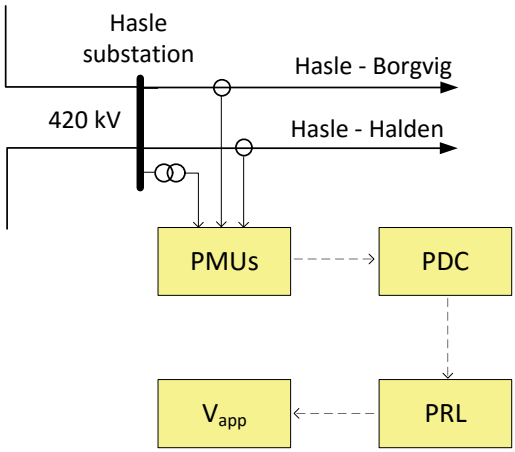

Figure 5.16: Online voltage stability monitoring application V_{app} at the Hasle corridor.

In the prototype, the Swedish transmission system is considered as a load; hence, the currents of the two tie lines are summed up and then treated as the load current. V_{app} is a real time application; it continuously receives phasor measurements from the PRL and then estimates the Thevenin equivalent (impedance and voltage) and computes the indicator S-ZI. Based on these parameters, it estimates the maximum loadability and plots the PV curve. Fig. 5.18 shows the interface of V_{app}, which has the following main features:

- *Estimation of the Thevenin impedance*: every second, V_{app} obtains phasor data and estimates the Thevenin impedance by (3.8). Then magnitudes of the Thevenin and the load impedance are then plotted in time as seen in graph 1. From this graph, one can observe directly variations of the two parameters and the gap between them.

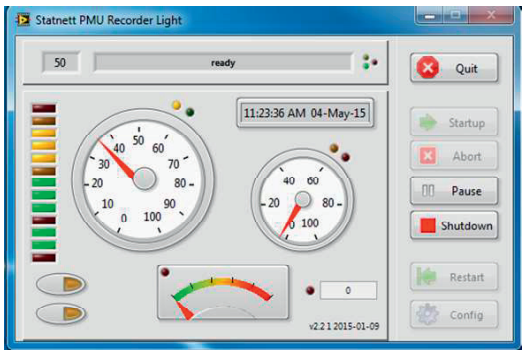

Figure 5.17: The PMU Recorder Light (PRL) developed for the STRONg^2rid project.

- *Estimation of the maximum loadability*: Based on the Thevenin equivalent and the load current and voltage, the maximum loadability is estimated by (2.49). As seen in graph 2, the power margin is clearly visualized when the estimated maximum loadability and apparent power of the load are plotted together.

- *The S-Z sensitivity indicator (S-ZI) and its trajectory*: as presented in Section 3.2, Z-SI is directly computed from local phasor measurements and plotted versus magnitude of the load impedance as the red dot in graph 3. With this indicator, response of the grid to the load variation is observed dynamically; the red dot is moving as the operation condition is constantly changing.
  At a particular load bus in the grid, a range of the Thevenin impedance can be roughly estimated (for example: by off-line simulations or observation of the online Thevenin equivalent estimation). Based on this approximation, one can plot trajectories of S-ZI versus magnitude of the load impedance in advance (by (3.6) in Section 3.1). In graph 3, six S-ZI trajectories, which correspond to six Thevenin impedances (25 Ω, 30 Ω, 40 Ω, 50 Ω and 60 Ω), are plotted. These curves, together with the current S-ZI (the red dot), show a vivid picture of location of the current operating point and its advance towards the voltage stability limit, which is the horizontal red bar in the graph.
  Additionally, the S-ZI trajectory obtained from the online estimated Thevenin impedance is also plotted; it is the thick blue curve in graph 3. If the Thevenin impedance is accurately estimated, this curve will pass the red dot. In this case, the curve represents a true trajectory of S-ZI under the current operating condition. If the Thevenin impedance estimation is inaccurate, the red dot will not be located on the blue curve. This feature is used as a measure to validate the estimation of the Thevenin impedance in real time.

- *The PV curve*: by assuming that the Thevenin impedance is a pure reactance X, the PV curve is computed by (2.7) in Section 2.3.2 and plotted in graph 4. It is the thick blue curve passing the red dot, which is determined by the load voltage and active power. Similar to graph 3, six PV curves corresponding to six Thevenin impedances (25 Ω, 30 Ω, 40 Ω, 50 Ω and 60 Ω) are plotted in this graph. Their function is to visualize power margin at the monitored load bus.

- *Indicators and warning*: as presented in Section 2.6, the impedance stability in-

dex (ISI) is the ratio of magnitude of the Thevenin impedance to that of the load impedance. In V_{app}, it is represented by the progress bar $Zth/Zload$. Similarly, the ratio of the load power to the maximum loadability is expressed by the progress bar $Sload/Smax$. Based on these indicators, warning LEDs are used to show the assessment of voltage stability at the considered load, which can be "Normal", "Close to limit" or "Beyond limit".

5.3.1 Results from the Hasle corridor

The V_{app} has been implemented to assess voltage stability at the Hasle corridor since February 2014. Over a long observation period, it has been observed that the proposed indicator S-ZI and the S-Z method have worked properly and consistently. Performance of the V_{app} is presented under the following conditions:

5.3.1.1 Under normal operation conditions:

- As seen in Fig. 5.18, a snapshot of V_{app} was taken on December 15, 2014, when power transfer at Hasle corridor was 2181 MW. During the time period from 10:08:15 to 10:11:48, the Thevenin impedance varied in a range from 26 Ω to 35 Ω; meanwhile the load impedance was around 76 Ω. In addition, as can be seen in graph 2, the power margin varied from about 700 MW to 1200 MW. It is worth noticing that although variation of the Thevenin impedance was small, it led to a large variation of the power margin.
  Further, graph 3 shows that the Thevenin impedance was properly estimated. As can be seen, the red dot S-ZI is located on the thick and blue curve, which was built based on the estimated Thevenin impedance.

- To make a thorough evaluation of the proposed approaches in the PhD work, several snapshots of V_{app} at different time and under different operation conditions are presented from Fig. 5.19 to Fig. 5.25. As can be seen, Fig. 5.19 depicts a snapshot of V_{app} on Feb. 18, 2014, when export power on both tie lines was about 1100 MVA. Under this condition, the Thevenin impedance was in a range from 50 Ω to 70 Ω; meanwhile, the load impedance stayed within a range from 157 Ω to 170 Ω. Obviously, the distance between the operating point and the voltage stability limit was large. This assessment is supported by the S-ZI in graph 3. This indicator shows that the operating point (the magenta dot on the graph) was quite far from the limit (the horizontal red bar).

  In Fig. 5.20, the power transfer on March 19, 2014 was around 1800 MVA. Compared to the estimated maximum loadability at 3000 MVA, the power margin under this operating condition was 1200 MVA. At this time, the Thevenin impedance was estimated at 30 Ω, much smaller than the load impedance, which was around 95 Ω. Compared to Fig. 5.19, the S-ZI (the red dot) in graph 3 closely followed the expected trajectory. This also confirms the accuracy of the estimated Thevenin impedance since the red dot is exactly located on the thick blue curve. Moreover, the PV curve in graph 4 shows a good performance. Overall, all the four graphs harmonize with each other.

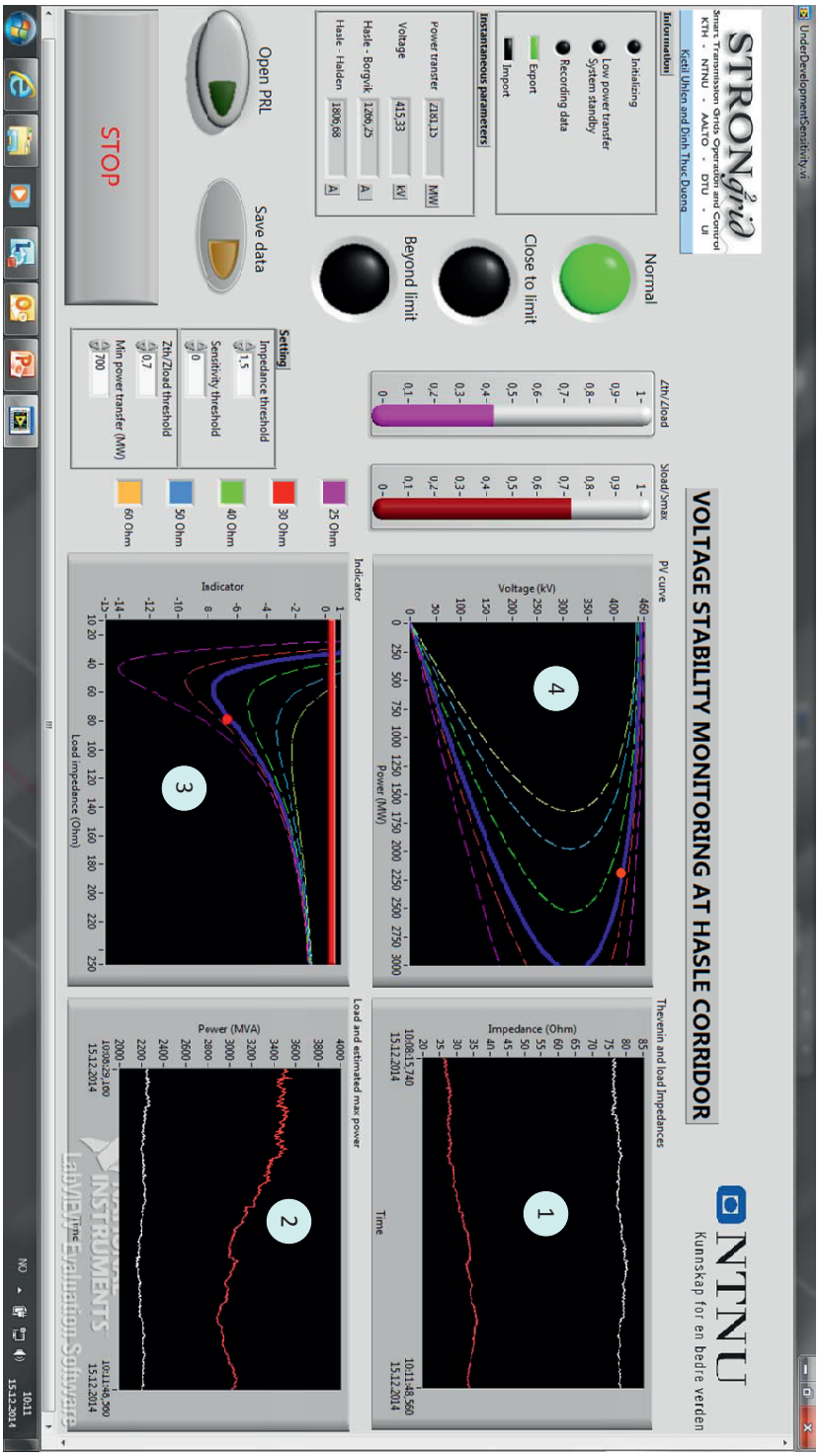

Figure 5.18: Prototype of the online voltage stability monitoring V_{app} at the Hasle corridor

Fig. 5.21 presents a case, in which the Thevenin impedance experienced a rather large variation when the export power was at a high level (around 2250 MVA). The estimated value was from 32 Ω to 40 Ω. It is seen that this impedance variation led to a large deviation among the estimated values of the maximum loadability. This maximum limit changed by about 400 MVA (from 2700 MVA to 3100 MVA). From this figure, it can be seen that the proposed methods are able to dynamically capture temporary strength of the network. This feature can also be observed from Fig. 5.22 to Fig. 5.25.

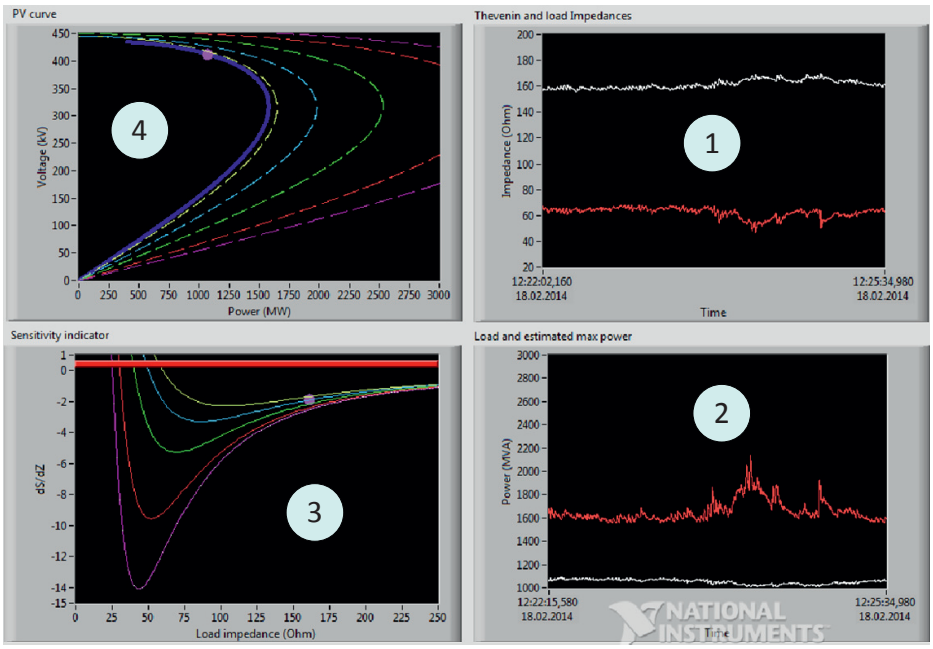

Figure 5.19: Snapshot of V_{app} at the Hasle corridor on Feb. 18, 2014.

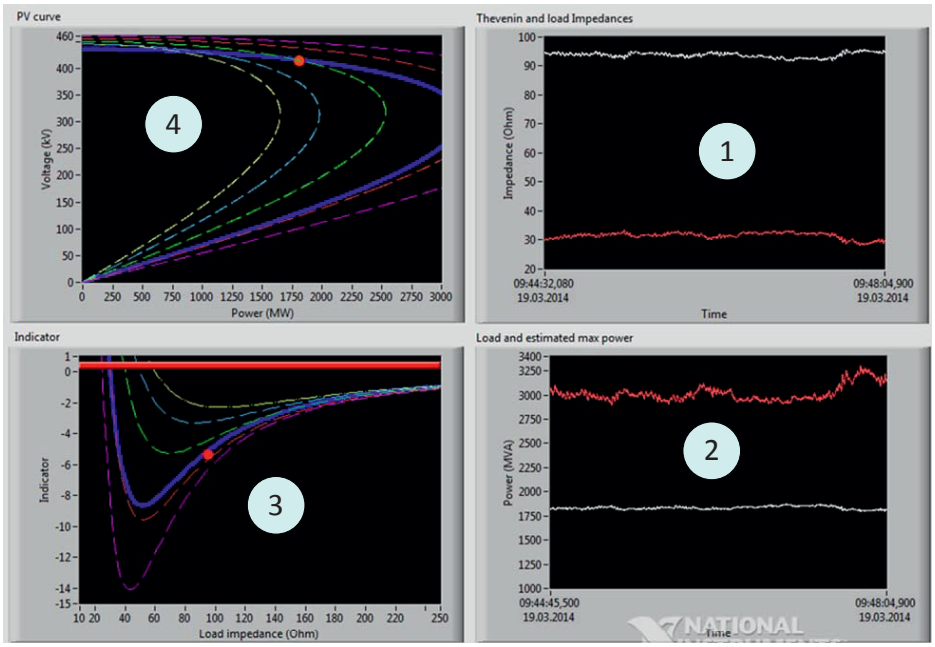

Figure 5.20: Snapshot of V_{app} at the Hasle corridor on Mar. 19, 2014.

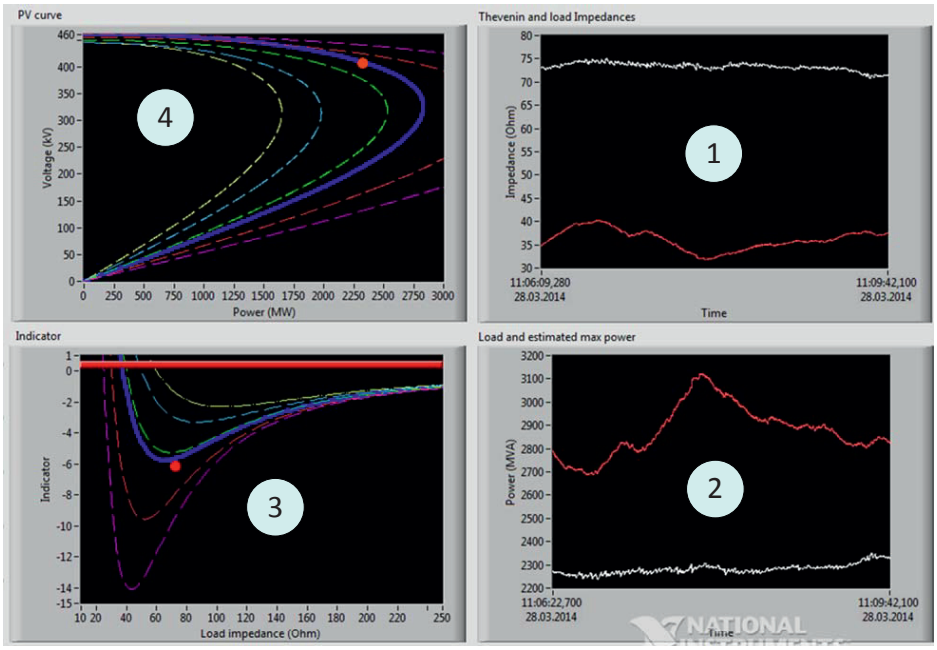

Figure 5.21: Snapshot of V_{app} at the Hasle corridor on Mar. 28, 2014.

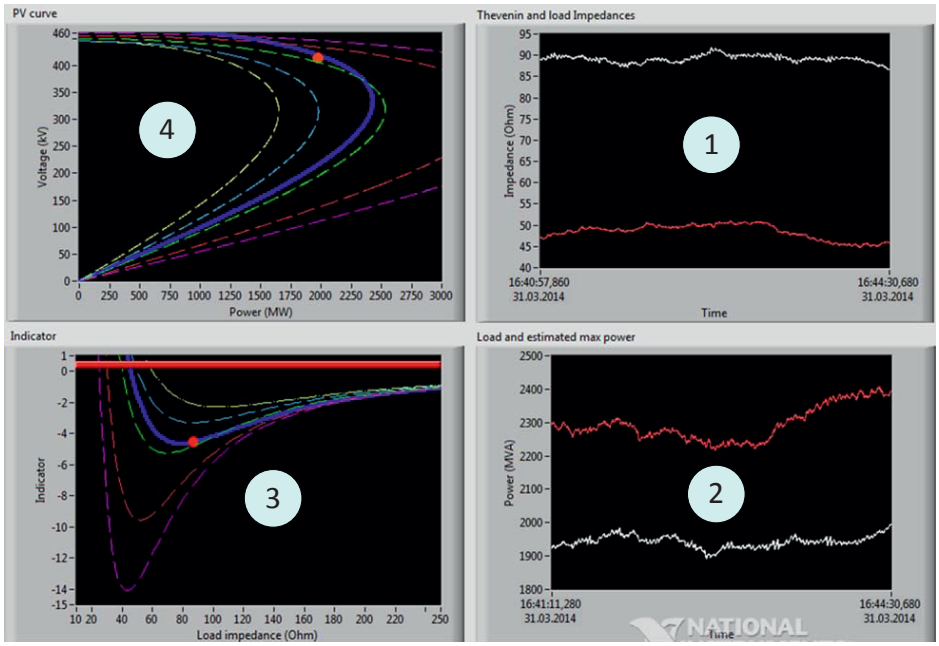

Figure 5.22: Snapshot of V_{app} at the Hasle corridor on Mar. 31, 2014.

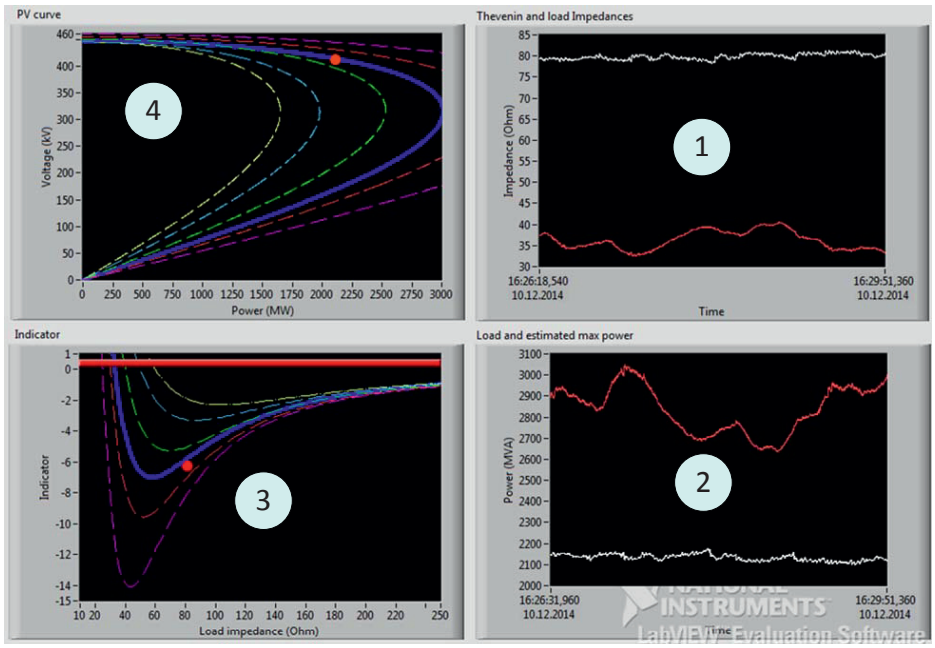

Figure 5.23: Snapshot of V_{app} at the Hasle corridor on Dec. 10, 2014.

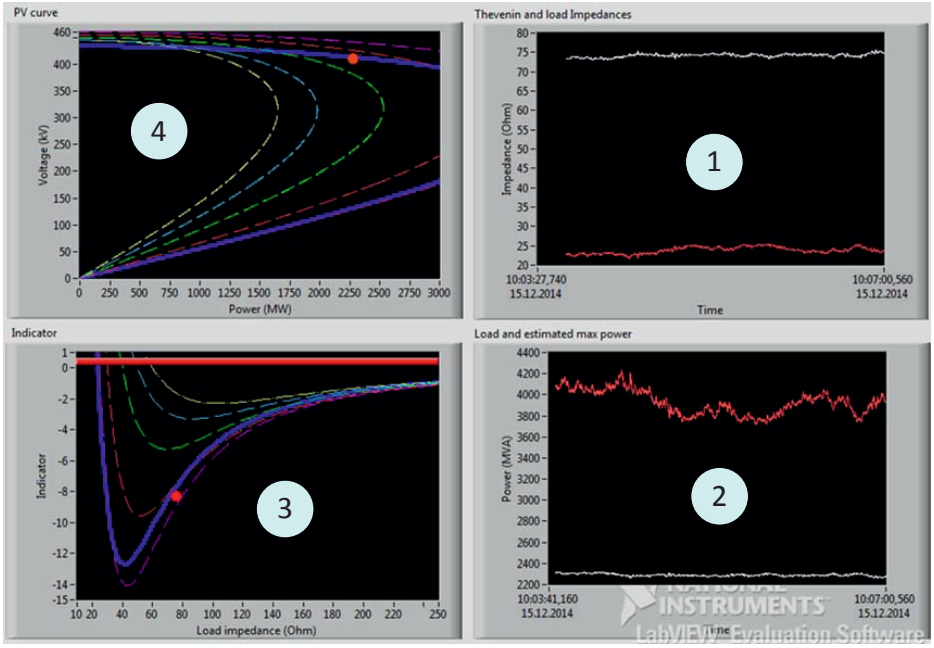

Figure 5.24: Snapshot of V_{app} at the Hasle corridor on Dec. 15, 2014.

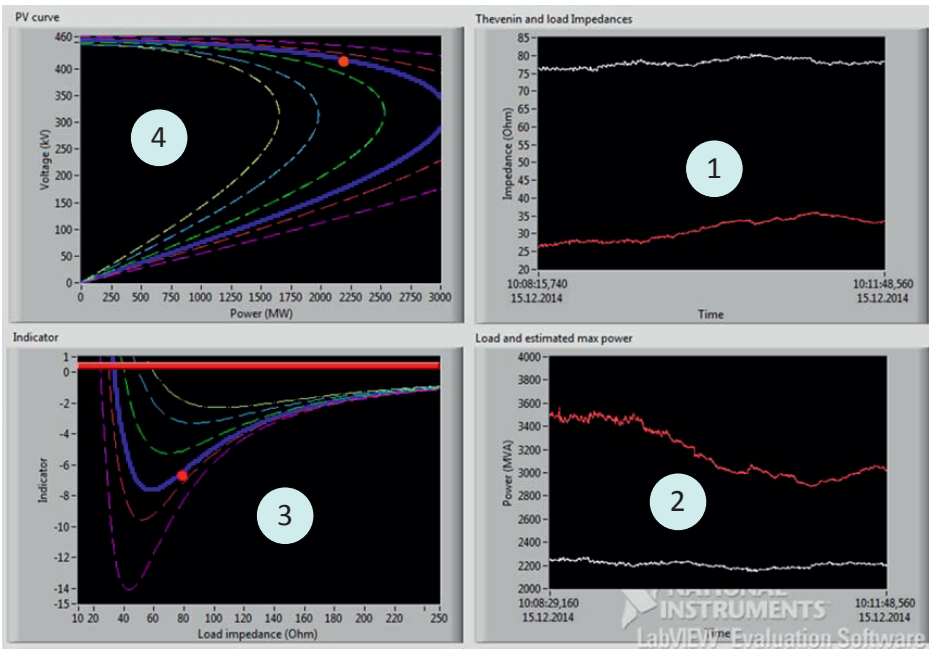

Figure 5.25: Snapshot of V_{app} at the Hasle corridor on Dec. 15, 2014.

5.3.1.2 Under disturbance conditions

The V_{app} works properly not only in normal operation conditions but also in other conditions with disturbances. Fig. 5.26 depicts a snapshot of the application on Feb. 11, 2014. During the observation time, there were two switching actions at the load side. These events were witnessed by the two steps of voltage increase at the 420 kV busbar as seen in graph 2. In graph 4, it shows that the Thevenin impedance was slightly affected by the switching; the impedance slightly dropped and returned to a normal value afterwards. It is noted that the power transfer was very high (2500 MVA) and close to the estimated maximum loadability; the power margin was around 500 MVA. In addition, the Thevenin impedance was between 32 Ω and 39 Ω, which was quite close to the load impedance, varying from 65 Ω and 70 Ω.

Later on the same day, robustness of V_{app} was observed in Fig. 5.27 when the export power was very high. As seen in graph 2, voltage at the 420 kV bus oscillated, probably caused by operation of the SVC installed at the corridor; meanwhile, the power transfer on the corridor showed a similar pattern. This transient condition, however, did not affect the performance of V_{app}. Graph 4 does not exhibit any abrupt changes of the estimated Thevenin impedance although a certain deviation of the maximum loadability is observed in graph 1.

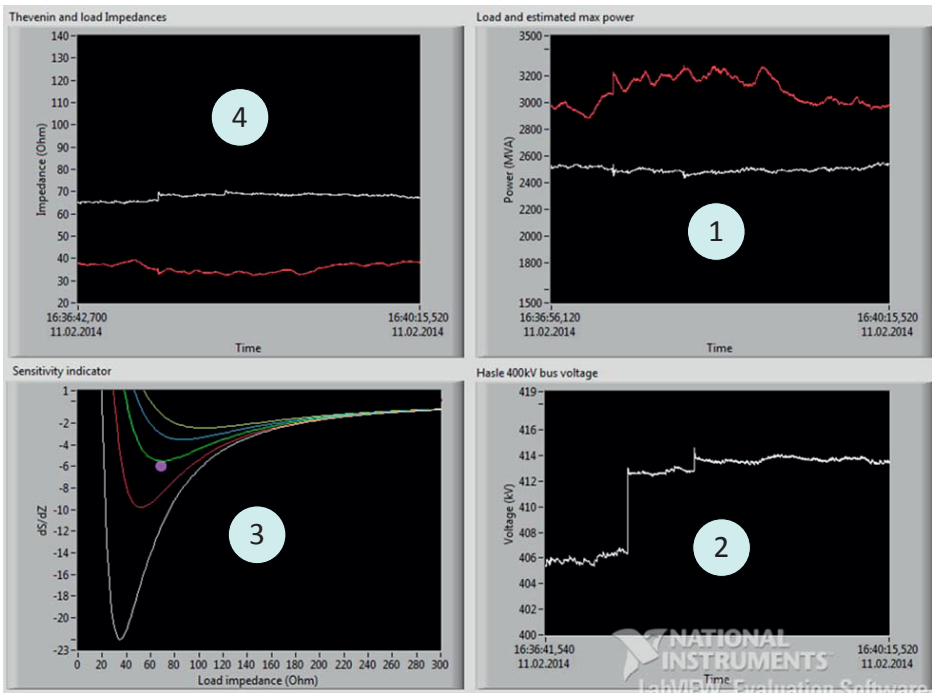

Figure 5.26: Snapshot of V_{app} at the Hasle corridor on Feb. 11, 2014.

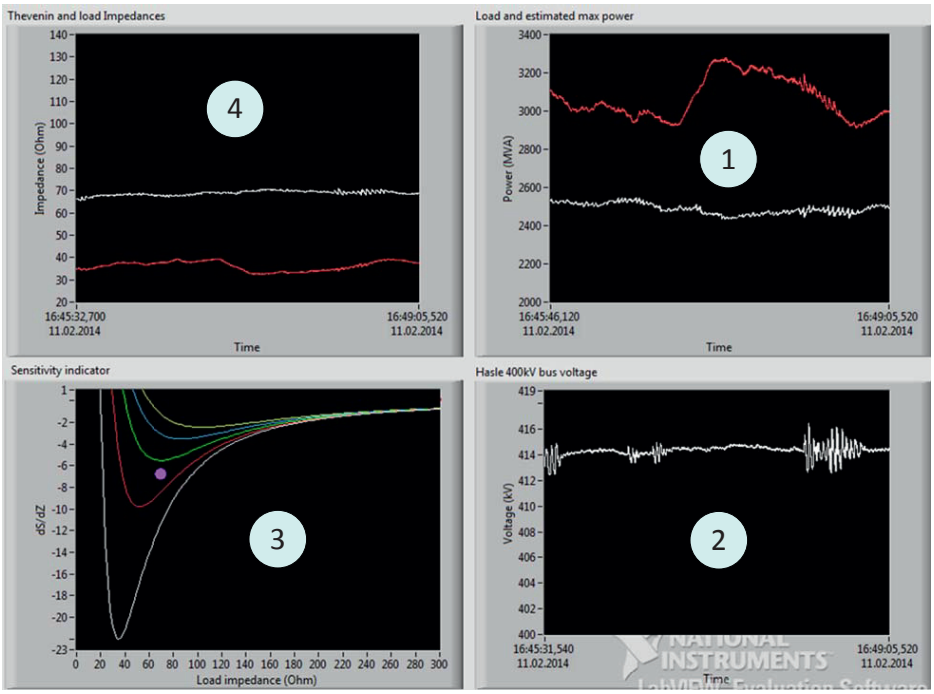

Figure 5.27: Snapshot of V_{app} at the Hasle corridor on Feb. 11, 2014.

5.3.1.3 Comparison with the CT method

As presented in Section 5.2, the CT method [47] shows a similar estimated Thevenin impedance compared to the S-Z and topology-based methods. Therefore, this method was implemented in the V_{app} for comparison purpose. To tune the CT algorithm properly, several values of the factor k have been tested to obtain the best estimation. Eventually, $k = 0.0015$ is selected since it results in a better performance than the other. Fig. 5.28 shows the Thevenin impedance estimated from the S-Z and CT methods. At a loading level around 900 MVA, the two algorithms produced comparable results although the Thevenin impedance from the CT method had less variation compared to the one obtained from the S-Z method. In graph 3, it is seen that when the load impedance is high (low power), the difference among the S-ZI trajectories is very small. Therefore, at this operating condition, it is difficult to use the S-Z sensitivity to verify the estimated Thevenin impedance. Moreover, a large variation of the Thevenin impedance estimated by the S-Z method is predictable. In other words, the Thevenin impedance estimated by the S-Z method under light load condition is less accurate. However, this drawback is minor because voltage instability does not occur when the load is light. Nevertheless, S-ZI is still a reliable indicator; the red dot always closely follows the expected trajectories.

In a similar loading condition, the snapshot in Fig. 5.29, however, shows a different picture of the two methods. The Thevenin impedance obtained from the S-Z method was smooth and stayed around 45 Ω. The CT method, on the contrary, exhibited an oscillating estimate; the estimated Thevenin impedance varied in a range of 20 Ω and 100 Ω. Using the S-ZI in graph 3 as a verifying tool, the result from the S-Z method was

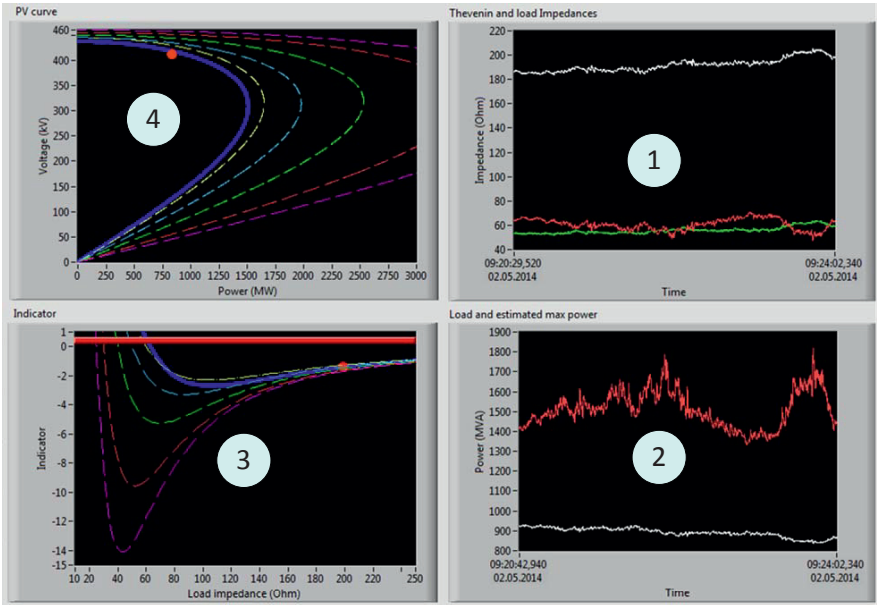

Figure 5.28: Snapshot of V_{app} at the Hasle corridor on May 2, 2014; the red curve is from the S-Z method, the green curve is from the CT method.

obviously more accurate and reliable than that of the CT approach.

In Fig. 5.30, the Thevenin impedance was estimated at a high loading level, the export power on the corridor was about 2200 MVA. Similar to the result shown in Fig. 5.29, the S-Z method had a better performance than the CT approach. The Thevenin impedance obtained from the S-Z algorithm in graph 1 was in line with the S-ZI in graph 3; meanwhile, the CT method produced a large variation of the Thevenin impedance, which did not match the indicator S-ZI, which is directly computed from local phasor measurements.

Moreover, Fig. 5.31 and 5.32 depict an abnormal performance of the CT approach, which has been frequently observed in the V_{app}. Generally, the result from the CT method falls into two categories:

- The algorithm does not produced a converged estimation. The estimated value is unstable; it varies very quickly as seen in Fig. 5.31. When validated by the S-ZI in graph 3, the estimated Thevenin impedance is obviously inaccurate.

- After a long period with oscillating estimation, the algorithm produces converged result as seen in Fig. 5.32 and 5.33. However, the estimated Thevenin impedance is almost unchanged. If one uses the S-ZI for verification, the result is again inaccurate.

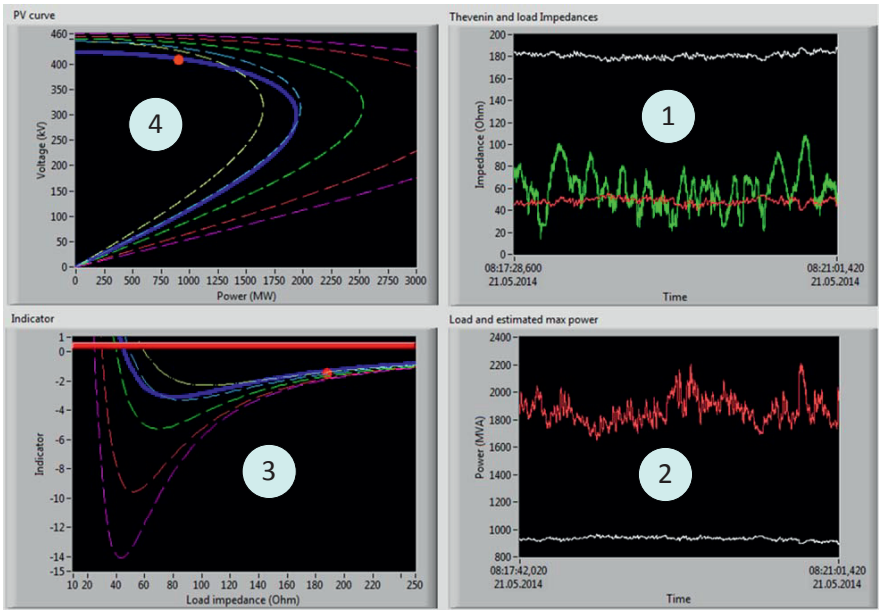

Figure 5.29: Snapshot of V_{app} at the Hasle corridor on May 21, 2014; the red curve is from the S-Z method, the green curve is from the CT method.

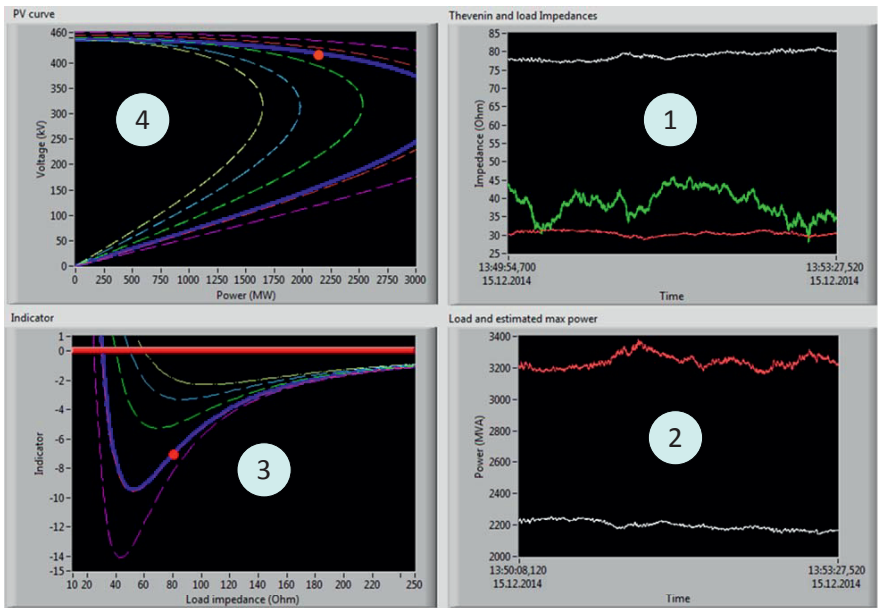

Figure 5.30: Snapshot of V_{app} at the Hasle corridor on Dec. 15, 2014; the red curve is from the S-Z method, the green curve is from the CT method.

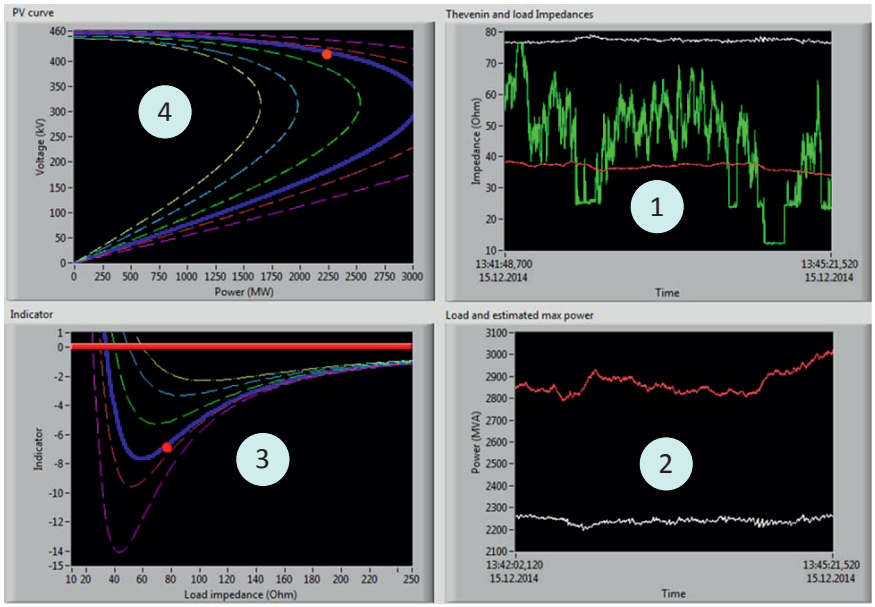

Figure 5.31: Snapshot of V_{app} at the Hasle corridor on Dec. 15, 2014; the red curve is from the S-Z method, the green curve is from the CT method.

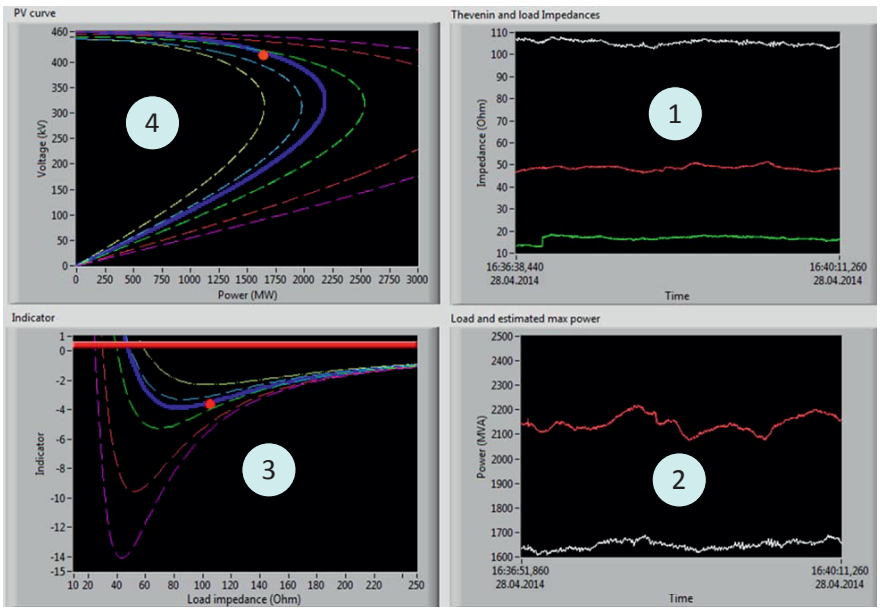

Figure 5.32: Snapshot of V_{app} at the Hasle corridor on Apr. 28, 2014; the red curve is from the S-Z method, the green curve is from the CT method.

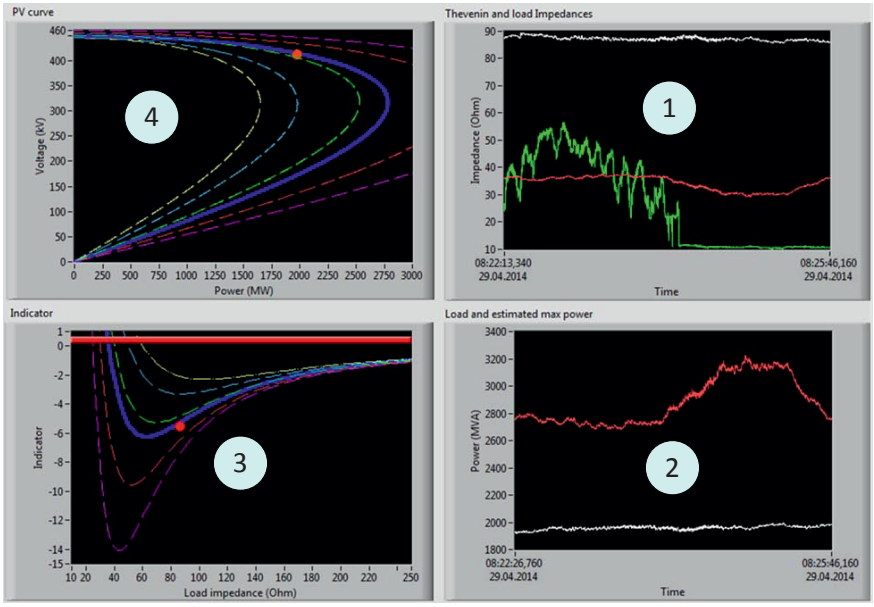

Figure 5.33: Snapshot of V_{app} at the Hasle corridor on Apr 29, 2014; the red curve is from the S-Z method, the green curve is from the CT method.

5.3.1.4 Discussion about V_{app} perpormance at the Hasle corridor

- The S-Z method proposed in this PhD project works properly with real PMU measurements. Over a long testing period, the result has been satisfactory; abnormal performances or unexpected results have not been observed. The proposed methods are robust and reliable; they produce appropriate estimation in both normal operation and disturbance conditions.

- The estimated Thevenin impedance from real PMU measurements is comparable with the result obtained from the simulation presented in Section 5.2. In high export power condition at the Hasle corridor (above 2000 MVA), the Thevenin impedance from V_{app} observed at different time instants is in a range from 23 Ω to 40 Ω. Compared to the variation of the Thevenin impedance between 25 Ω and 30 Ω from the topology-based method and a range from 30 Ω to 41 Ω obtained from the S-Z method with simulation data, the result from V_{app} shows a very good fit between the Thevenin impedances obtained from a dynamic model of the Norwegian transmission system in PSS/E and the real PMU measurements in the field.

- The S-ZI indicator has shown a very good performance. By comparing Fig. 5.28, Fig. 5.20 and Fig. 5.24, one can observe that, as the load increases, the red dot closely follows the trajectory shown in Fig. 3.5. It is noted that the S-ZI is computed directly from PMU measurements without any assumptions. Its performance in the V_{app} strongly substantiates the proposed algorithms in this PhD project.

- The S-Z method estimates the Thevenin impedance by (3.8) in Chapter 3. In this equation, the S-Z sensitivity has a large influence on the estimated Thevenin impedance. From Fig. 5.26, it is seen in graph 3 that the S-ZI trajectories corresponding to different Thevenin impedances are very close to each other when the load is light (large load impedance). This affects the estimation of the Thevenin impedance significantly; a small variation of S-ZI can lead to a large variation of the Thevenin impedance. In other words, the estimation is less accurate when the considered load impedance is much larger than the Thevenin impedance. This disadvantage is, however, minor because the operating point is far from the voltage stability limit.

- In case the voltage stability limit is imposed only by the strength of the network, estimation of the Thevenin impedance based on local PMU measurements can detect the actual Thevenin impedance of the grid even if the load is still far from the maximum loadability. The case study in Section 5.1 is a typical example to demonstrate this point. Fig. 5.3 and 5.4 show that the Thevenin impedance and the maximum loadability estimated when the load is light have a small deviation from the ultimate value, which is estimated at the peak load power.

  However, in meshed areas with a high number of dynamic components like generators and FACTS devices, algorithms for estimating the Thevenin impedance based on local PMU measurements are only able detect the temporary strength of the network, but it cannot reveal the ultimate limit of the grid except that the monitored load is really close to the voltage stability limit. For instance, the estimated maximum loadability is about 1500 MVA when the power transfer on the Hasle corridor is about 900 MVA, and the power margin is 600 MVA. However, when the

power transfer increases to 2200 MVA, it is still within the limit. The estimated maximum loadability at this loading level grows to about 3200 MVA, and the power margin is 1000 MVA. It cannot, therefore, be concluded that the ultimate power limit on this corridor with respect to voltage stability is 1500 MVA or 3200 MVA. The actual maximum loadability can be properly estimated when the load is close to the voltage stability limit.

5.3.2 Results from the Alta substation

The proposed methodologies work properly with PMU measurements taken not only in the transmission system but also in the sub-transmission network, where the ratio X/R of power lines is much lower than that in the transmission network. Compared to other methods, this is an advantage of the proposed algorithms. Indeed, the second test of V_{app} is carried out at a 130 kV substation called Alta located in the northern part of Norway. At this substation, there is a 130 kV line, which transports energy from the substation to a remote load. The current of this line is considered as the load current; meanwhile, voltage is measured at the 130 kV busbar. In this 130 kV area, the ratio X_{Th}/R_{Th} of the Thevenin impedance in the S-Z method is set equal to 5.1774, instead of 15 as used in the V_{app} at the Hasle corridor. This ratio is a typical ratio of the 130 kV lines in the studied grid.

Fig. 5.34 shows a snapshot of V_{app} implemented at this substation on March 26, 2015. As can be seen, although the load power was quite low (54.86 MW), V_{app} shows a good performance. The estimated Thevenin impedance in graph 1 was around 45 Ω. Meanwhile, the load impedance was 325 Ω. Obviously, the load was far from the voltage stability limit. This assessment is also supported by graph 2, displaying the load power and the estimated maximum loadability, which was around 200 MW. In addition, the PV curves in graph 4 also show the same picture; the current operating point was still far from the nose point. Since the load was light (large load impedance), there was a very small difference among S-ZI trajectories as seen in graph 3. Therefore, it is not possible to use the S-ZI to validate the estimated value of the Thevenin impedance.

Another snapshot of V_{app} on Dec. 18, 2014 is depicted in Fig. 5.35 when the load power was around 60 MW. Similar to the previous one, V_{app} still shows a good estimation of the Thevenin impedance.

At the Alta substation, the CT method was also implemented. But the result was not satisfactory. The estimated magnitude of X_{Th} obtained from this algorithm was a complex number, which does not have a physical meaning. As shown in Fig. 5.36, magnitude of the estimated number was first smaller than that of the load impedance, but it quickly increased and became equal to magnitude of the load impedance. Clearly, the estimated Thevenin impedance was not satisfactory because the system in reality was stable; it did not experience any voltage stability problems. Moreover, the green curve in graph 1, in Fig. 5.35, is actually the real part of the estimated value obtained from the CT method, which was plotted together with the result from the S-Z method. By coincidence, they were comparable. This interesting feature probably needs further explanation, which is left for future work.

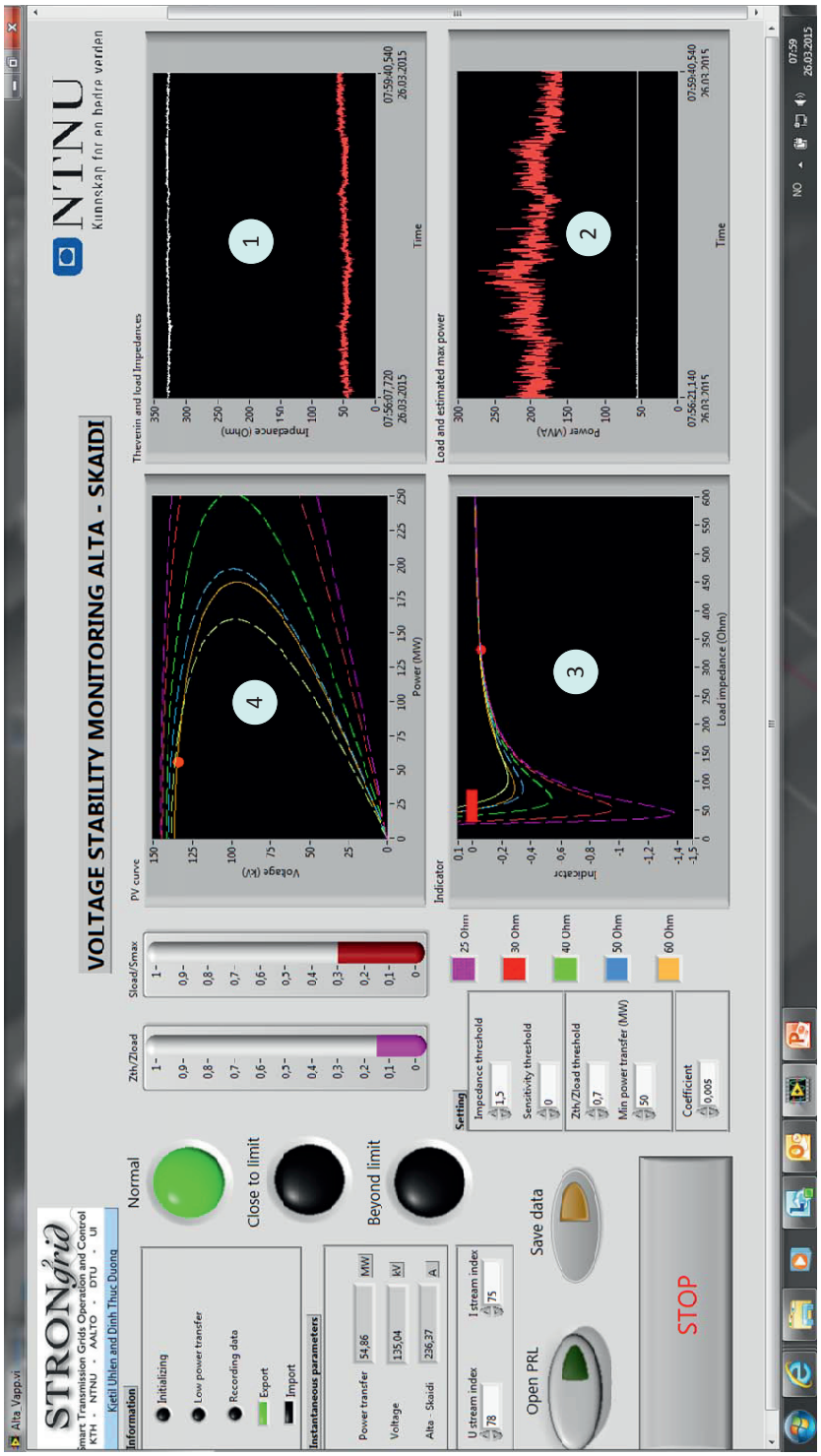

Figure 5.34: Online voltage stability monitoring at the 130 kV substation Alta

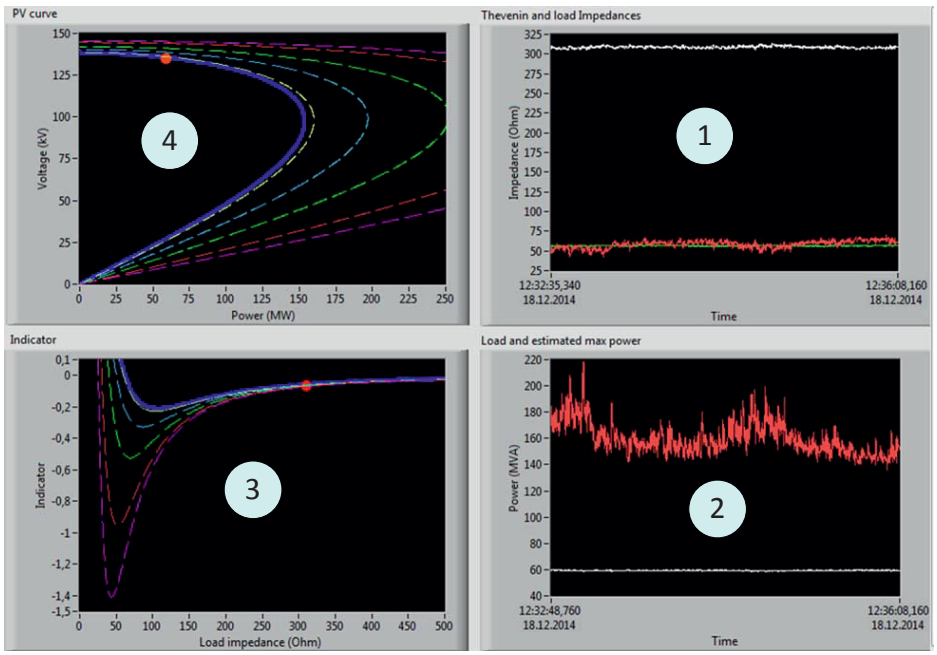

Figure 5.35: Snapshot of V_{app} at the 130 kV substation Alta on Dec. 18, 2014; the red curve in graph 1 is the result from the S-Z method.

DISCUSSION

- The V_{app} works properly not only in the 420 kV grid but also in the 130 kV network. At both locations, the Thevenin impedance is appropriately estimated. Moreover, it is noted that the shape of the S-ZI trajectories is independent from the voltage level. Comparing Fig. 5.24 and 5.35, for example, one can recognize that the trajectories have the same shapes. In the two figures, although the load impedances are different, the red dot (S-ZI) is nicely located on the blue curve as expected.

  It is also noted that the unit of the S-Z sensitivity is not important; one can multiply this parameter by a particular multiplier to obtain desired visualization. Whatever the unit is, the limit for the S-Z sensitivity is still zero. Therefore, adjusting the multiplier is similar to an action of zooming in or out the figure.

- As discussed in Section 5.3, the S-Z method does not result in smooth estimation when the load impedance is much large than the Thevenin impedance. This feature is seen again at the Alta substation. Probably, this location is not the best place to test the V_{app} in the 130 kV network; this node was not vulnerable to voltage instability under normal operation conditions, when the snapshots of V_{app} were captured.

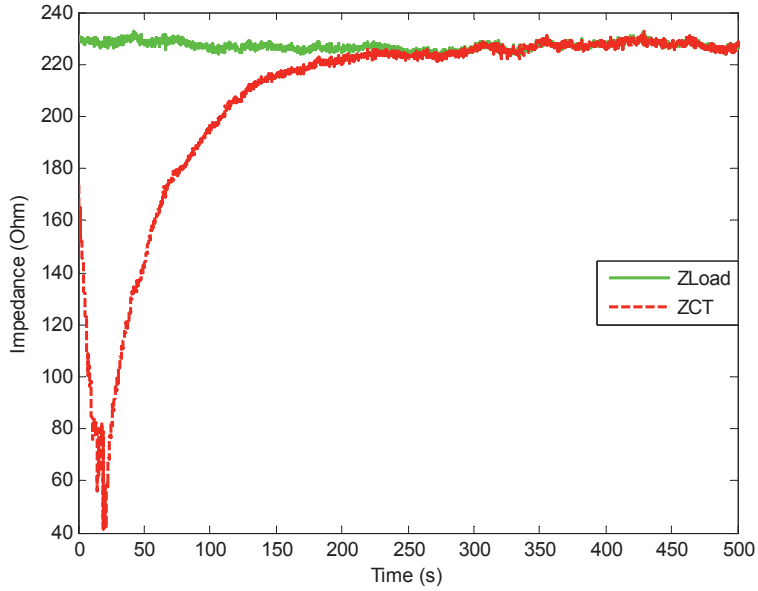

Figure 5.36: Estimated Thevenin impedance from the CT method at Alta substation.

5.4 Case study on the modified CIGRE Nordic32 test system

The modified CIGRE Nordic32 test system as shown in Fig. 5.37 is described in [60], and it is a variant of the system presented in [61]. The system has the same network parameters as the original one. However, load and dispatch of active power among generators are modified. As a result, the central area is exposed to the long-term voltage instability after an outage of the line between node 4032 and 4044. Compared to the system in [60], the grid used in this test case has the following variations:

- Dynamic models of AVRs, governors and OXLs used in [60] are replaced by standard models in PSS/E. Details of these models used in this test case are presented in Appendix A.
- Voltage instability in [60] is driven by the load recovery emulated by operation of OLTCs in the central area and the load dynamics (constant current for active power and constant impedance for reactive power). This produces too small variations of the load impedance, which are not sufficient for the S-Z method to estimate the Thevenin impedance. Therefore, to emulate the load recovery, the load model EXTL in PSS/E is applied to all the loads in the system.

In this study, the system is, first, disturbed by a tripping of the line between bus 4032 and 4044. After this disturbance, all the loads try to recover their initial power. As a result, the rising demand goes beyond the transfer capacity of the network and consequently leads to voltage collapse in the central region. To validate performance of the proposed algorithms, voltage stability at bus 1041 is analyzed because this node is the weakest bus in the central area. To estimate the Thevenin impedance properly, configurations of the tested algorithms are specified as follows:

- The S-Z method takes measurements of voltage and current from load 1 located at bus 1041 as its inputs. The ratio X_{Th}/R_{Th} of the Thevenin impedance is set equal to 8.
- Compared to the S-Z algorithm, the CT method has the same inputs. In this algorithm, the tuning parameter is set as $k = 0.00015$.
- As mentioned in Chapter 4, the topology-based method does not take the entire system into its calculation. Instead, the studied area is confined by some A-P nodes. In Fig. 5.37, these nodes are marked by the magenta rectangles. As can be seen, bus 4021 and 4031 have strong connections to the northern area, which is not exposed to voltage instability; hence these buses can be treated as the A-P nodes. As a result, the network in the north is not included in the calculation. Bus 4062 is also selected as the A-P bus because, at this location, active power of generator G17 and G18 is injected into the studied area. Similarly, the terminal buses of generator G6, G14 and G15 are also considered as A-P buses. At bus 1043 and 4051, active power from the generators is smaller than the load power; they are actually load buses, not A-P bus. In addition, all the A-P buses are considered as the weak A-P buses. Therefore, as presented in Chapter 4, the virtual coupling reactances between them and bus 1041 are computed based on the virtual power

injection into bus 1041. This makes the algorithm independent from the dispatch of active power among generators in the system.

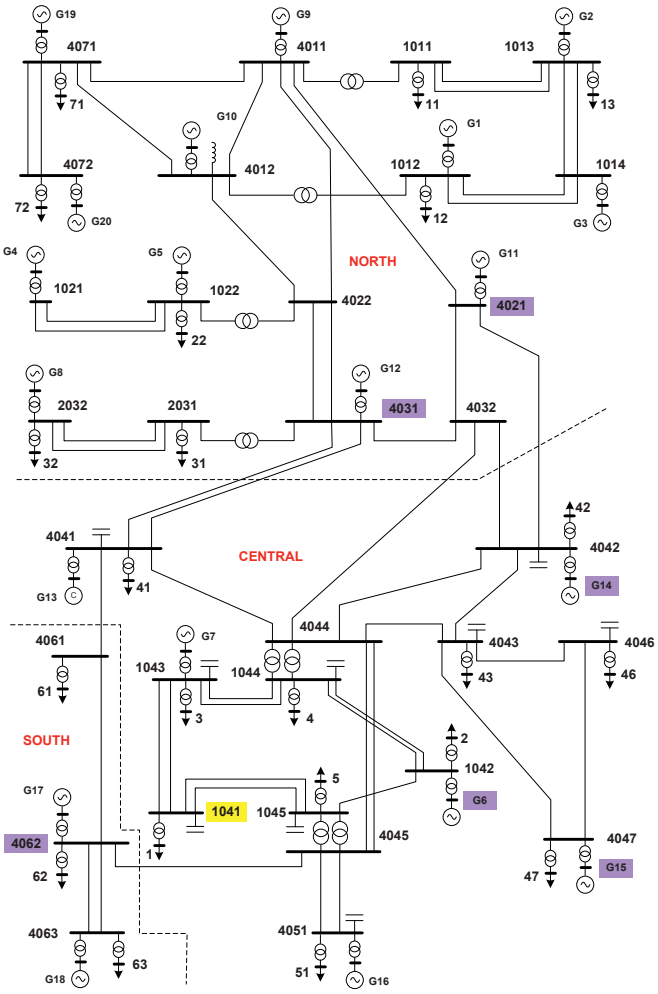

Figure 5.37: Single line diagram of the Nordic32 test system [60].

Fig. 5.38 shows the power of the loads in the central area. As can be seen, after the outage of the line between bus 4032 and 4044 at $t = 50$ s, the power demand becomes smaller than its initial value. Afterwards, all the loads simultaneously increase their power. However, at around $t = 300$ s, the load power no longer rises; the power remains almost unchanged until the voltage collapse occurs. This situation is clearly captured by the S-ZI as shown in Fig. 5.39. At the beginning, although all the S-ZIs are different from each other, they are smaller than zero, indicating that the loads stay inside the voltage stability limit. At $t = 280$ s, the S-ZIs of load 1 at bus 1041 and load 3 at bus 1043 are crossing the voltage stability limit. After that, other loads follow similar paths; they gradually become positive at different time instants. Clearly, the S-ZI in this case timely

and successfully detects the maximum power transfer condition of the loads in the studied area. Additionally, Fig. 5.40 depicts the load impedance and the Thevenin impedance

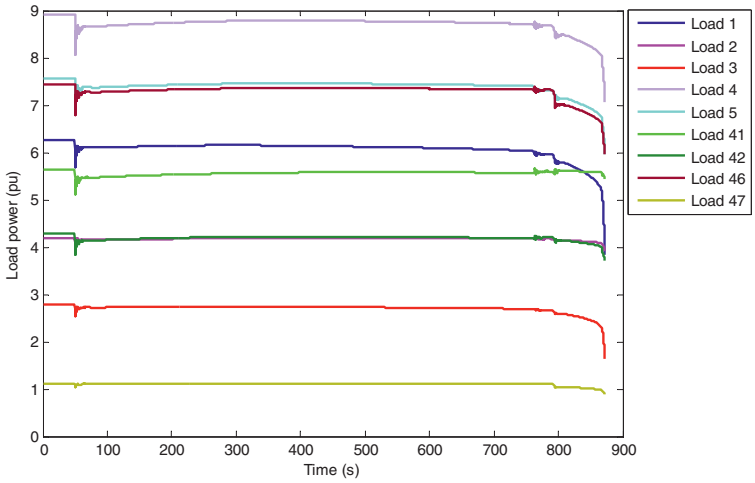

Figure 5.38: Load recovery in the central area.

obtained from the topology-based method. At the time the disturbance occurs, there is a small variation of the Thevenin impedance. After that, this impedance slightly increases; however, as the system is approaching voltage instability, the Thevenin impedance sharply rises; meanwhile, the load impedance quickly decreases. Finally, the two impedances are equal at $t = 867$ s, just before the instant of voltage collapse. Compared to the performance of the topology-based method, the S-Z and CT approaches show a rather different picture although they also successfully detect the voltage stability limit. After the line outage, the two algorithms start to produce converged estimation after $t = 120$ s. Their results are comparable with each other in most of the simulation time. First, the estimated impedances are smaller than the load impedance; afterward, they slightly drop before they make a sharp jump in the period $t = 250 - 300$ s and become higher than the load impedance during the rest of the simulation. Comparing Fig. 5.40 and 5.41, it is recognized that the two local PMU measurement-based algorithms detect voltage stability limit earlier than the topology-based approach.

DISCUSSION

- Unlike the previous test cases, in this case study, there is a rather large mismatch of Thevenin impedance between the topology-based method and the other two local phasor measurement-based approaches. The reason for this is the dramatic change of operation condition. After the disturbance, all the loads are in a race to recover the initial demand. As a result, the load impedance at load buses simultaneously and continuously becomes smaller and smaller. As presented in [67], the Thevenin impedance matching condition occurs after the considered load has passed the peak power. This explains why the topology-based method does not perform well in this simulation.

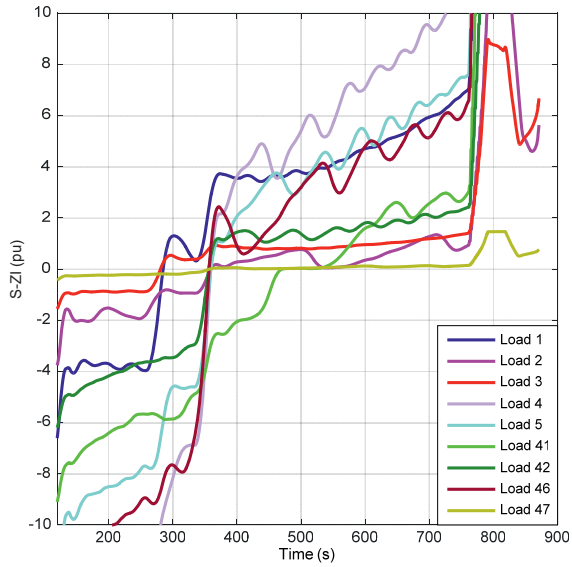

Figure 5.39: S-ZI of all the loads in the central area.

- The S-Z method, however, still shows a good performance. As presented in Chapter 3, the S-ZI is to track the instant when the considered load reaches the peak power; at this instant, the sensitivity is equal to zero. The S-ZI is then used to estimate the Thevenin impedance; therefore, the result corresponds to the maximum load power and is not affected by the rapidly changing operation condition. That explains why the magnitude of the estimated Thevenin impedance is equal to that of the load impedance when the load power is maximum.

- If the operation condition is unchanged, meaning that all the other load impedances are constant, the result from the topology-based method will be comparable to that of the S-Z method. To illustrate this, another simulation is conducted. This time, a load increase after the disturbance is only applied to the load at bus 1041. Other loads are modeled as constant impedances. In Fig. 5.42, it is seen that, after the disturbance, the load power at bus 1042 increases and reaches its peak at $t = 620$ s. At this instant, the Thevenin impedances obtained from the topology-based and the S-Z algorithms are equal to each other, and they are also equal to the load impedance at the maximum power transfer point as can be seen in Fig. 5.43. In this case, as expected, there is no mismatch between the Thevenin impedances estimated by the two algorithms.

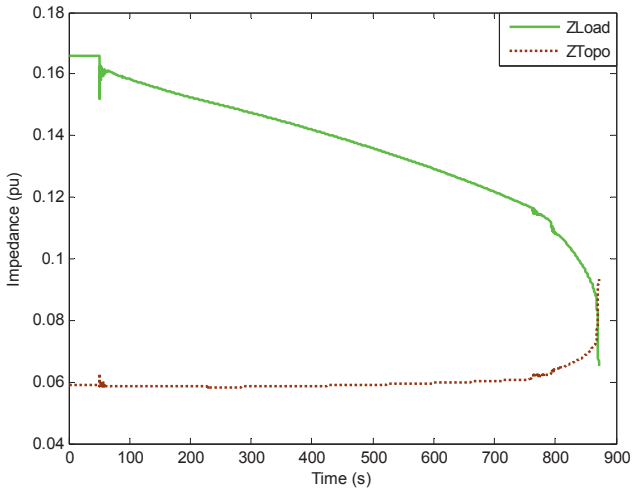

Figure 5.40: Thevenin impedance from the topology-based method as seen at bus 1041.

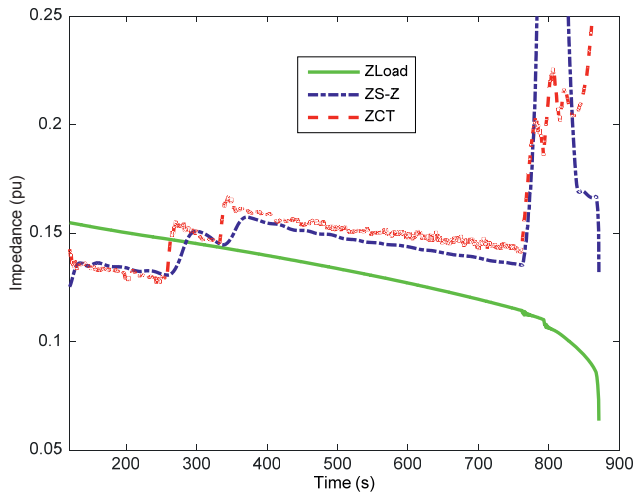

Figure 5.41: Thevenin impedances from the S-Z and CT methods seen at bus 1041.

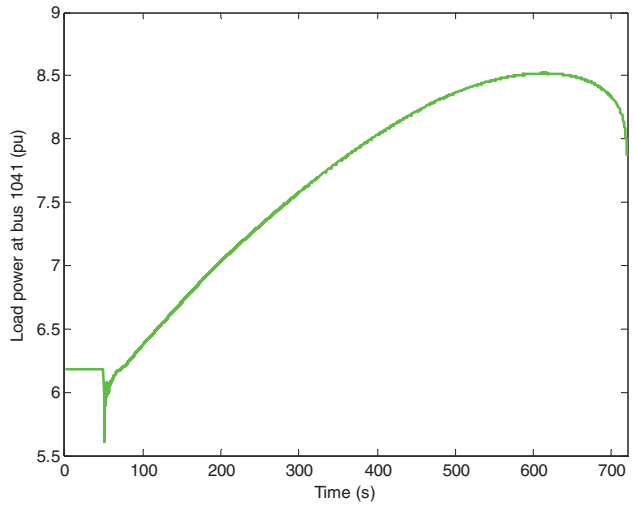

Figure 5.42: Load power at bus 1041 when there is only load recovery at the monitored bus.

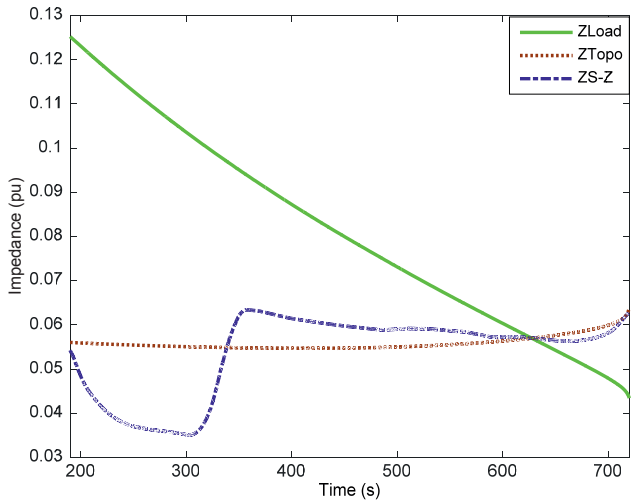

Figure 5.43: The Thevenin impedance and the load impedance at bus 1041 when there is only load recovery at the monitored bus.

5.5 Load curtailment based on online voltage stability indicators

Although load curtailment is not a favorable remedial action with regard to continuity of power supply, it is one of the most effective countermeasures against voltage collapse. The essence of voltage instability is that the network capacity cannot meet the excessive demand. Therefore, to maintain system stability, the load must be reduced, assuming that other remedial measures have already been taken. As presented in Section 2.8, in the recent major blackouts, it has been observed that there was an involvement of voltage instability. In the foreseeable future, when there will be a high penetration of variable renewable generation in power systems, operation conditions might quickly change from a normal state to a critical one. Under this circumstance, a fast load shedding scheme seems to be one of the effective measures to maintain resilience of the grid.

As proposed in Section 3.4, the S-ZI and the ratio of the Thevenin impedance to the load impedance are suitable criteria for a load shedding scheme since they fulfill requirements for selectivity and adequacy. Considering Fig. 5.39, it is seen that bus 1 and 3 are the weakest buses in the Nordic32 test system. At $t = 280$ s, these loads have crossed the maximum loadability limit. To secure operation of the system, excessive demand at these buses should be shed first; meanwhile, the other loads should stay untouched. Fig. 5.44 depicts the voltage and load power at these buses when 60 MVA at bus 1 and 20 MVA at bus 3 are shed at $t = 300$ s. As can be seen, the load shedding action is an effective measure; the system is stable for the rest of the simulation.

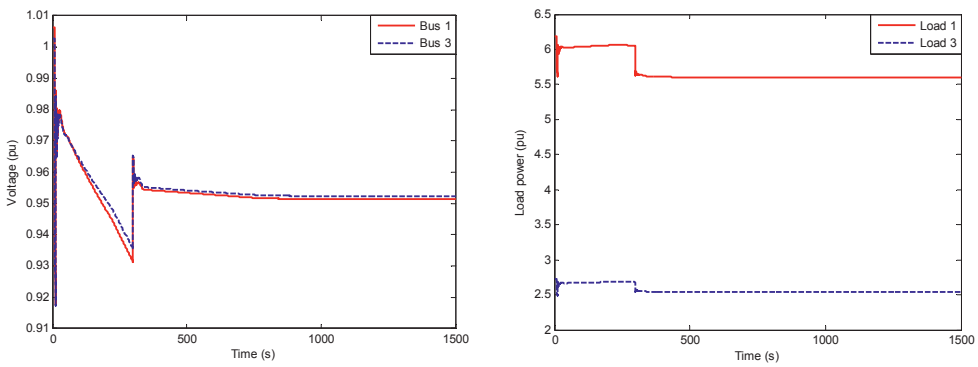

(a) Voltage excursion at bus 1 and 3. **(b)** Load power at bus 1 and 3.

Figure 5.44: System performance when load 1 and 3 are curtailed.

In addition, to validate the selectivity characteristic of the load shedding scheme, the loads at bus 1 and 3 are not curtailed. Instead, a curtailment of 80 MVA is allocated to bus 4, 5 and 43 in three separate simulations. Fig. 5.46 and Fig. 5.47 show that the system is still exposed to voltage collapse although the load has been shed. Since these buses are not the weakest nodes, the amount of loads, which needs to be shed, must be larger than the required quantity of load 1 and 3. Evidently, the load curtailment scheme based on S-ZI and the ratio of the Thevenin impedance to the load impedance is an effective and simple approach.

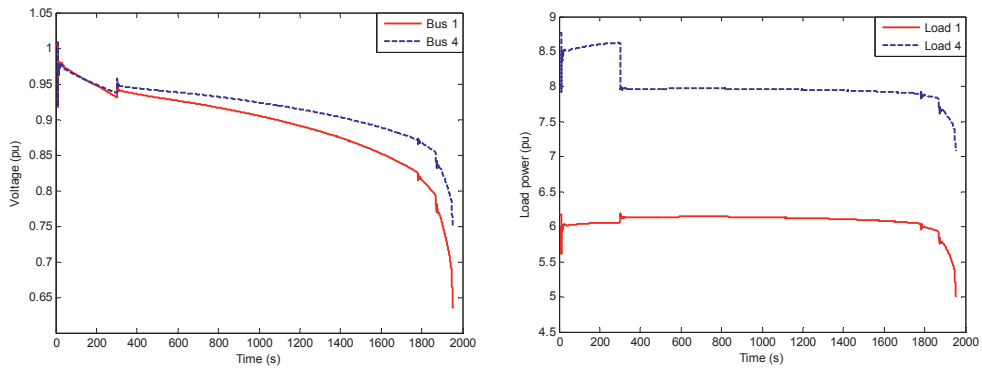

(a) Voltage excursion at bus 1 and 4. **(b)** Load power at bus 1 and 4.

Figure 5.45: System performance when load 4 is curtailed.

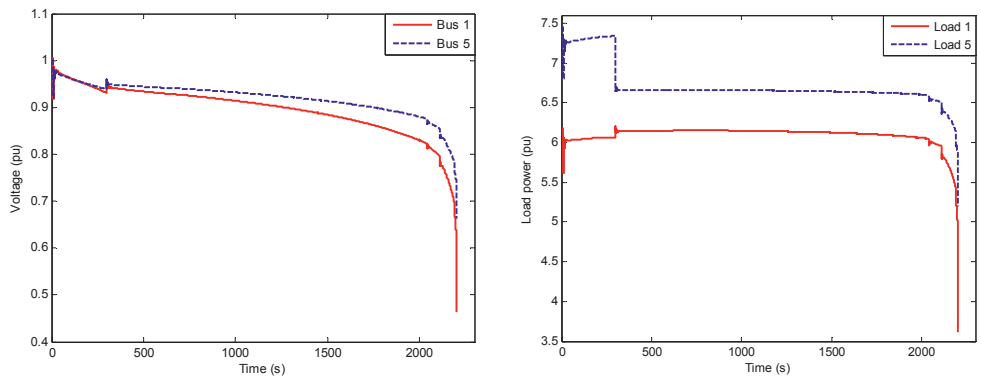

(a) Voltage excursion at bus 1 and 5. **(b)** Load power at bus 1 and 5.

Figure 5.46: System performance when load 5 is curtailed.

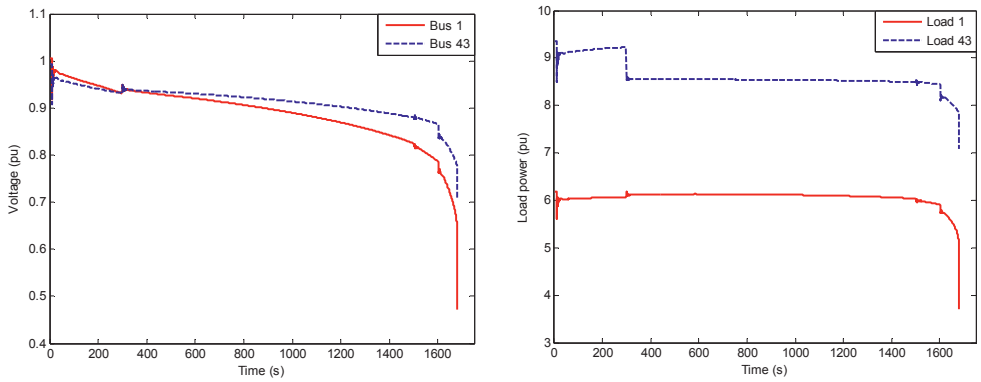

(a) Voltage excursion at bus 1 and 43. **(b)** Load power at bus 1 and 43.

Figure 5.47: System performance when load 43 is curtailed.

Chapter 6

Coordinated secondary voltage control

This chapter presents a voltage control scheme for coordinating reactive power reserves in power systems, which is inspired by the concept of multi-agent system. Similar to an agent, the proposed local controller takes on its own assigned tasks and contacts its neighbors for reactive power support when needed. The control structure incorporates not only controllable VAr sources but also mechanically switched capacitor banks and reactors, resulting in increased online reactive power reserves for critical contingencies. The approach is suitable for areas with high penetration of FACTS devices and distributed generation connected to power systems through voltage source converter (VSC), or VSC-HVDC systems. The control structure is simple and flexible in terms of coordinated, implementation and expansion.

The chapter starts with the review of the secondary voltage control in power systems. Then it continues with the proposed coordination control scheme. Finally, simulation results are presented.

6.1 Review of the secondary voltage control

6.1.1 Voltage control structure in power systems

Voltage control is an important issue in operation of power systems in order to comply with regulations on the quality of power supply. It is strictly regulated that voltage at all buses must be kept within an allowable band, despite load variations and disturbances in the grid. The accepted voltage variation is different from regulation to regulation, but it is normally in the range of $\pm 10\%$ of the nominal value at the consumer end [68].

Normally, voltage profile is scheduled in advance by offline analysis based on forecast of load and generation. However, there is uncertainty in the load forecast. With high penetration of renewable sources in the grid, the total generation becomes less predictable. On the other hand, disturbances also contribute to voltage deviations; they change system topology and operation condition. These factors can lead to deviations of the voltage from the scheduled level. Therefore, control actions are necessary to bring the voltage back to the desired value.

As voltage is highly related to reactive power; it is controlled by the following resources: excitation of generator (through AVR), capacitor, reactor, SVC, STATCOM and other

FACTS devices. Mechanically switched capacitor is mainly installed in the load areas and used as the base compensation in controlling the load voltage. It is not involved in dynamic voltage control because it cannot adjust reactive power continuously, but in a stepwise manner. At power plants, automatic voltage control is carried out by the AVR, which adjusts, smoothly, reactive power of generators to maintain the terminal voltage. Since the AVR considers only the local voltage, it is not guaranteed that the load voltage is always in the permissible band. In fact, voltage violation can occur due to voltage drop along power lines, disturbances and changes of operation conditions. Therefore, to obtain a good voltage profile throughout the network in real time, voltage control in power systems can be structurally divided into three categories: primary, secondary and tertiary control as illustrated in Fig. 6.1. These three control levels dictate the operation of the same machine. Therefore, they must be decoupled with respect to the time scale to avoid interactions among them. Otherwise, it can lead to oscillatory behaviors of the controlled component.

It is noted that SVC and STATCOM are not addressed in this "conventional" control

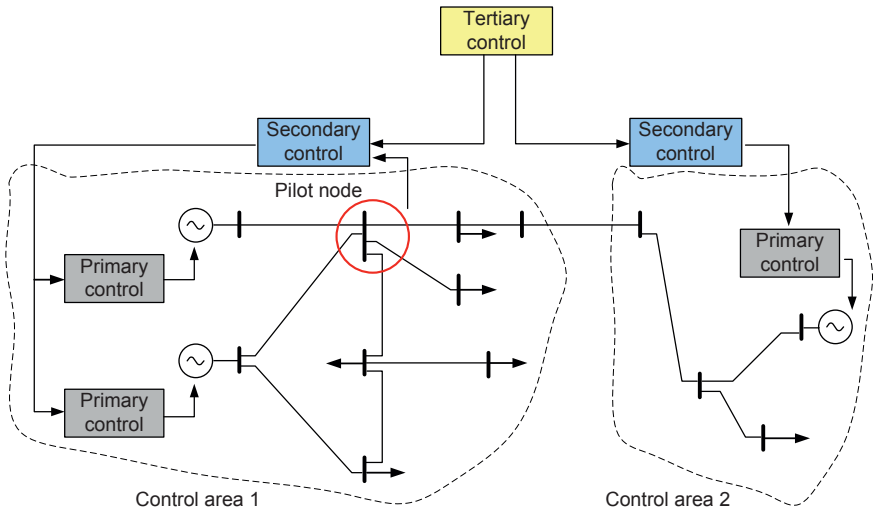

Figure 6.1: Structure of voltage control in power systems.

structure, probably because the installed capacity is small compared to other existing VArs sources. However, this situation is going to change thanks to developments in power electronics and its applications in power systems.

- **Primary control** is control actions automatically taken by the controller to regulate the local control variable (voltage or reactive power). As the deviation between the measured output and the setpoint arises, the controller will act to bring the voltage back to the reference. The time response of the primary control is different from one to another, but it ranges from 100ms to some seconds [16]. As listed in [16], equipment that has primary control is generator or synchronous condenser equipped with AVR, static VAr compensators like SVC, STATCOM, capacitors and reactors (if they are integrated into automatic voltage control scheme).

- **Secondary control** is a control scheme that involves generators in a particular

area to control the voltage at a special load bus called the pilot bus. To avoid interactions with the primary control, this scheme has the time scale between one and a few minutes [16]. Details of this scheme are presented in the next section.

- **Tertiary control** establishes a voltage map of the entire grid based on optimization of economic cost and system security under various constraints of equipment and voltage limits in the network. The output of this control is used as the setpoint for pilot nodes in the secondary control scheme. In automatic closed-loop operation, the time response of the tertiary control is from 5 to 15 minutes [16].

6.1.2 Secondary voltage control

The main task of the secondary control is to maintain the voltage at the pilot node following the setpoint by regulating reactive power of the involved generators. The secondary voltage control has been thoroughly studied and presented in several works [69–81]. The first secondary voltage control was implemented and went into operation in France in the early 1980s [72]. Later, in 1998, an improved scheme of this type of control (the coordinated secondary voltage control) was demonstrated in the western area of France [72]. Similar control structures have also been implemented in Italy [73, 74], and recently in Switzerland [78] and China [77]. A prototype of this coordinated control was also implemented in the Norwegian transmission system [16]. In Belgium, the coordinated voltage control scheme has been in place since 1998 [81], but the secondary control is not utilized. Instead, tertiary control is conducted to obtain the setpoints. Then it is up to the system operator to decide whether or not to send these references to the primary control of generators.

Although specific implementation of the secondary voltage control may be different, the main idea behind is almost the same. The control scheme can be characterized by the following main features:

- **Divide the system into control zones**: As reactive power cannot be transmitted over long distances, generators have only high controlability on the voltage of buses that are electrically close to them. For those nodes, which are electrically distant from generators, the influences are less significant. Hence, the grid, as shown in Fig. 6.1 can be divided into small control areas, which are electrically weakly coupled. In other words, voltage control in this area has little impact on the voltage in the other areas. In addition, another criterion to define the control zone is that generators in each control zone must have sufficient reactive power to regulate the voltage [69].

  The number of zones is different from system to system. For example, there were 27 control zones in the transmission system in France in 1985 [69]. In Italy, the number of zones was 18 [73], but there are only four controlled areas identified by the study on the Spanish power system presented in [76].

  After the control areas are defined, voltage profile in each zone is controlled independently by generators involved in the zone. From the system point of view, secondary voltage control is a distributed control; it simplifies the tasks of voltage control for the whole network. Therefore, there is no need for a complex control that takes care of all the load buses and generators in the grid.

- **Determine pilot nodes:** In complex systems, it is "unrealistic and uneconomical" [73] to control voltage of hundreds of transmission buses automatically in real time. Therefore, the solution is to find a bus, called the pilot node, that can represent the voltage profile of all buses in each control area, assuming that the voltage at the other nodes will follow closely the pilot node. Instead of controlling voltages throughout the network, the secondary control regulates only the voltage of the pilot node. In addition, to avoid interactions among control zones, pilot nodes should be electrically distant. This task is determined by the concept of electrical distance proposed in [70] or by the sensitivity matrix as presented in [73].

  The practice to select the pilot node is also different among approaches. In France and Italy, the pilot node is the node, which has high short circuit power [71, 73]. Reference [76], however, proposes an alternative approach. In this method, the pilot node is selected based on not only the short circuit capacity but also the minimization of voltage variations of other buses in the control area, which are caused by random disturbances of reactive power at load buses. However, in these three approaches, selection of the pilot node is done by offline analysis. For systems, which experience structural changes, expansion and fast growing loads, offline analysis has certain drawbacks. Therefore, [77] introduces an alternative approach, which can adaptively determine control zones and select the pilot nodes in real time based on system operation conditions.

- **Control loop:** Despite minor differences among specific applications, the control loop for the secondary voltage control is almost the same. The objective is to control the voltage at the pilot node by adjusting reactive power of the involved generators as basically illustrated by the sketch in Fig. 6.2, where V_{p_ref} is the setpoint and V_{pilot} is the measured voltage at the pilot node. The voltage at the pilot bus is measured and compared to the setpoint; if there is voltage deviation between them, the proportional-integrator controller will utilize this mismatch to compute output in order to correct the error. The output of this controller is reactive power, which generators in the control zone will adjust to bring the voltage at the pilot node back to the setpoint. This amount of power is shared by the involved generators, determined by the correspoding coefficients $K_1, K_2, ..., K_n$. The controller is tuned in the way that the time response of the secondary control is in the range of a few minutes.

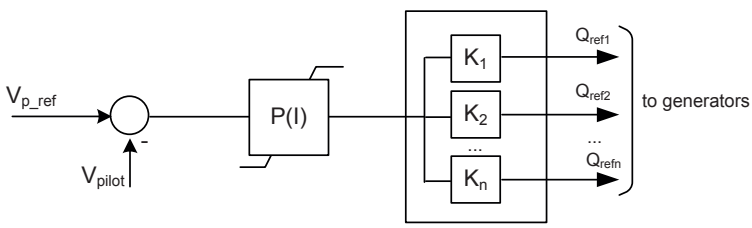

Figure 6.2: Sketch of block diagram of secondary voltage control.

6.1.3 Coordinated secondary voltage control

Although the secondary voltage control is a suitable control scheme and has performed appropriately in the transmission system in France; it has certain limitations [72]:

- One of the prerequisites of the secondary voltage control is that the system can be divided into non-interaction zones, which allows independent voltage control in each zone. As the system is growing and becomes more meshed, this assumption is not valid in some areas. This can worsen performance of the control scheme.
- The control scheme does not fully consider permissible voltage and reactive power limit of generators.
- Generators must follow the control's commands. They are not allowed to contribute more reactive power in case they have higher sensitivities to the pilot node.
- Parameters of the control loop is unchanged, which does not secure optimization under various operation conditions.
- Demand for rate of change of reactive power can go beyond the generators' response capability.

To overcome the above limitations, the coordinated control is structured as depicted in Fig. 6.3. Control zones, which have strong interactions with others, are merged into one control area. In this zone, the number of pilot nodes is not limited to one, but can be expanded to some buses. Within the merged control zone, involved generators are governed by the control vector ΔU_c, which is the variable of the optimization problem [72]:

$$\begin{aligned}\min\{\lambda_v\|\alpha\,(V_c - V_{pp}) - C_v\Delta U_c\|^2 + \lambda_q\|\alpha\,(Q_{ref} - Q) - C_q\Delta U_c\|^2 \\ +\lambda_u\|\alpha\,(U_{ref} - U) - \Delta U_c\|^2\}\end{aligned} \tag{6.1}$$

where:

α	:	control gain,
V_{pp}, V_c	:	measured and setpoint voltage values at the pilot node,
Q, Q_{ref}	:	measured and setpoint reactive power values at generating units,
U, U_{ref}	:	measured and setpoint stator voltage values,
ΔU_c	:	vector of stator voltage variation,
$\lambda_v, \lambda_q, \lambda_u$	:	weightings for terms in objective function: pilot point voltage, reactive power, and generator unit stator voltage,
C_v	:	sensitivity matrix relating variations in pilot point voltage to variations in stator voltage (network is modeled by sensitivity matrices for coordination between generating sites),
C_q	:	sensitivity matrices relating to variations in reactive power to variations in stator voltage.

under the following constraints:

$$\|\Delta U_c\| \leq \Delta U_{max}$$
$$a\,(Q + C_q \Delta U_c) + b\Delta U_c \leq c$$
$$V_{pp_{min}} \leq V_{pp} + C_v \Delta U_c \leq V_{pp_{max}}$$
$$V_{ps_{min}} \leq V_{ps} + C_{vs} \Delta U_c \leq V_{ps_{max}}$$
$$V_{EHV_{min}} \leq V_{EHV} + C_v \Delta U_c \leq V_{EHV_{max}}$$

where:

a, b, c	:	coefficients of straight lines representing operating diagrams for generator units (P, Q, U). These diagrams depend on the active power output by the generator unit,
$V_{pp}, V_{pp_{min}}, V_{pp_{max}}$	:	measured, minimum and maximum voltage at the pilot nodes,
$V_{ps}, V_{ps_{min}}, V_{ps_{max}}$	:	measured, minimum and maximum voltage at the sensitive nodes,
V_{EHV}	:	voltages computed at generator unit EHV output.

It is noted that sensitivity nodes are buses, which do not have voltage setpoint, but their voltage must be within the upper and lower limit. Based on the problem formulation, it

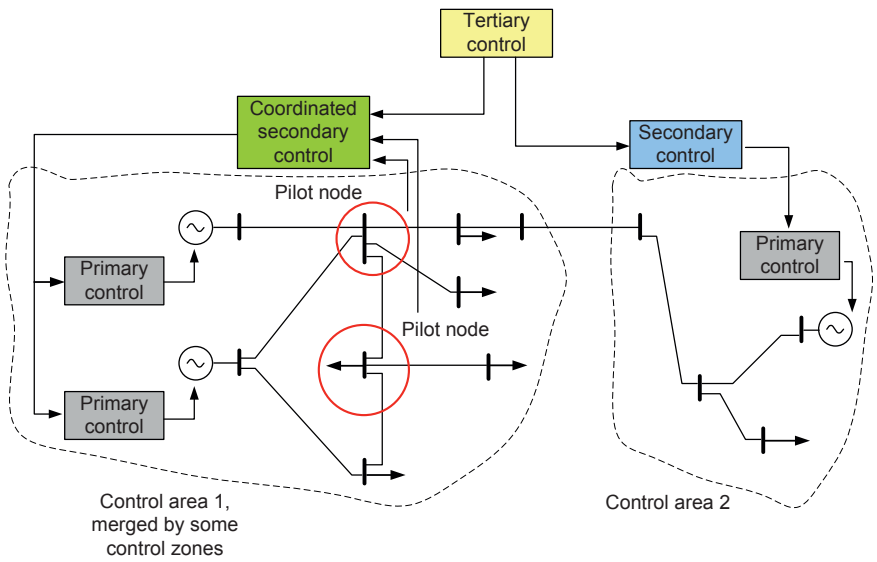

Figure 6.3: Structure of coordinated secondary voltage control in power systems.

can be elaborated that the control scheme tries to minimize not only voltage deviation of the pilot nodes but also voltage deviation at generators' terminal; meanwhile it also ensure that change of voltage of pilot nodes, sensitive bus and generators' terminals is within the permissible band. In addition, operational reactive power margins of generators are also considered in the control scheme. As the control output obtained from the optimization is used as the setpoint to regulate in real time reactive power sources, one of the concerns

is whether the approach always convergences. In [71], it is proven that this requirement is fulfilled; the algorithm for optimization of the quadratic problem using active constraint methods will converge after a finite number of iterations. Detailed information about the coordinated secondary voltage control is presented in [69, 71, 72].

6.2 A new scheme for coordinated secondary voltage control for systems with multiple VAr reserves

6.2.1 Motivation for the proposed control scheme

As presented in the secondary voltage control in the preceding section, it can be recognized that generators are the main resources, which are utilized to control the load voltage. The control scheme functions well as long as generators have enough controllability on the load voltage. However, the methods might have less effectiveness under these circumstances:

- In some areas, generation is electrically distant from the load; consequently, sensitivity of the load voltage with respect to the generators' reactive power is low. As a result, generators have little controllability on the voltage profile in the load area. In these sub-systems, the load voltage is normally regulated by local shunt compensation. The 420 kV network in the southern part of Norway is a typical example of this kind of system, where large generation is located in the west, but the load center lies in the eastern part. In this load area, several SVCs and synchronous condensers are installed to maintain a desired voltage profile.

- In the secondary voltage control, the pilot node is the controlled object. Its voltage reflects the voltage profile in the control area. However, the pilot node is not well defined in areas dominated by several controllable VAr sources like synchronous condenser, SVC and STATCOM. These components have very fast response and are able to keep the voltage close to the setpoint as long as they have enough capacity. As power systems are transforming, this kind of grid is more foreseeable in the near future with more and more renewable sources connected to the grid through voltage source converter, which is able to inject or absorb reactive power to control the local load voltage. In this scenario, the concept of pilot node is no longer relevant.

- STATCOMs and SVCs have become increasingly important as shunt compensation devices to regulate the voltage. Beside the main function, these components and possibly VSC-HVDC are utilized for damping low frequency inter-area oscillations. To be able to accomplish this task, the components must have sufficient reactive power reserve to regulate the voltage. However, it is not guaranteed that this requirement is always fulfilled since these compensators, in an effort to regulate the load voltage, can run out their capacity. Hence, it is necessary to coordinate them to obtain better utilization of the resources.

Addressing these issues, the proposed control scheme in this chapter is developed for areas with high penetration of VAr sources, especially SVC, STATCOM and VSC-HVDC. The method is considered as an alternative solution for voltage control in these special areas in the grid.

In recent years, smart grid has attracted enormous attention from researchers around the world. One of the outstanding features of this grid is the distributed generation, which consequently arouses interest of distributed control and coordination of controllers based on telecommunication. Among many new concepts and solutions, which have been created and applied in this field, multi-agent system is an attractive approach; it has potential applications in the power grid [82,83]. In this direction, [84] proposes a coordinated voltage control scheme based on the multi-agent system, in which an agent will send a request for help to its neighbors and decides which neighboring agent is selected to contribute to the support. Although the method is elegant, there is still room for further improvement. As we know, when an agent lacks reactive power, it is less effective if there is only one neighboring agent offering the support at one instant of time; simultaneous joint efforts of all neighboring agents are more effective. Moreover, it is not well defined in [84] how the multicast selects supporting agent when it receives multiple offers. The controller also requires training from offline simulation to act properly; this can reduce its effectiveness in various operation conditions of the real power systems. In addition, the requirement for predetermination of agents makes the coordination complex and inflexible in meshed power systems.

The proposed control scheme in this chapter embraces the concept of multi-agent; it considers each shunt compensator as an agent, which is responsible for regulating its own local voltage. However, the way the agent coordinate with other agents is totally different, which is presented in the next section.

6.2.2 Overview of the proposed control scheme

The control scheme is to coordinate VAr sources in power systems, e.g. SVCs, STATCOMs, generators (AVRs), VSC-HVDC systems, capacitors and reactors. The main objectives are:

- to avoid voltage violation, both in normal operation and under disturbances.
- to maintain sufficient reserve of fast-acting compensators for other functions and therefore to improve voltage stability in critical contingencies.
- to relieve system operators of trivial tasks of voltage control, especially after disturbances.

Consider a small system shown in Fig. 6.4, in which the high demand is allocated at bus 1. Here there is a tie line connected to an external system. The main tasks of the STATCOM are to maintain desired voltage and to damp oscillations on the corridor; meanwhile, the SVC, synchronous condenser, and voltage source converter of the wind farm have duty to keep the local voltage at the desired level. Obviously, the voltage at these buses represents the voltage profile of the considered area; their role is similar to that of the pilot node in the secondary control. Assume that the line from bus 2 to 3 is lost and the STATCOM no longer has enough capacity for its duty; consequently voltage at this bus drops below the lower limit. Since the generator at bus 3 is electrically distant from the load, it cannot inject more reactive power to increase the voltage at bus 1 if its voltage has reached the maximum voltage limit.

It is noted that when a node needs more injection of reactive power from other buses to increase its voltage, the most effective one is the electrically closest injection because

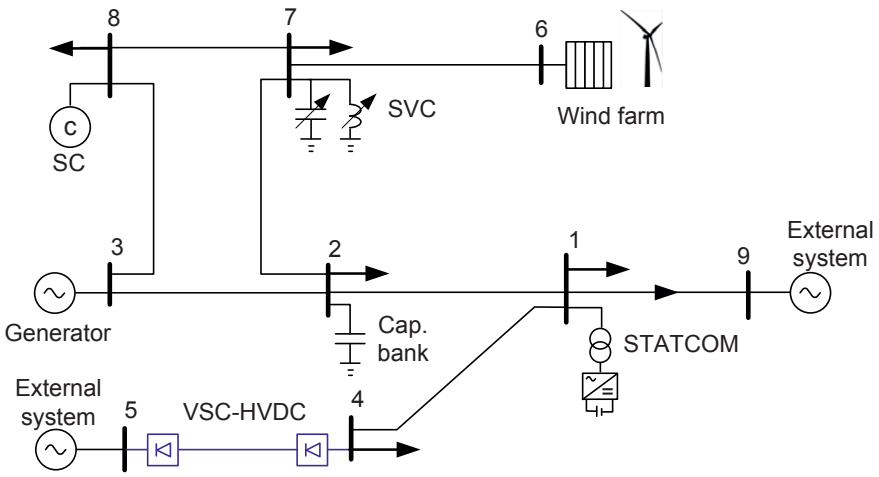

Figure 6.4: Example of a subsystem with shunt compensators.

the losses of reactive power on power lines are naturally minimized. Thus, without any calculation, it is obvious that more injection of reactive power from bus 2, 4 and 9 is the best support. Based on the this analysis, the main idea of the proposed control scheme is as follows:

- Build a secondary controller for each node, where VAr resource is located. There are two types of controllers: one for mechanically switched capacitor banks and reactor, and one for controllable VAr sources like SVC, STATCOM, synchronous condenser, generator and voltage source converter.

- The controller only cooperates with its neighbors. Here, "neighbors" are defined as the nodes that have direct or close electrical connections with the considered node.

- In normal condition, the controller controls the local voltage by itself. There is no communication between the controllers. The voltage setpoint can come from the tertiary voltage control or simply a certain value around the nominal value. When the local controller detects that the unit approaches its maximum capacity (or lack of reserve), it will first communicate to its neighbors to ask the neighboring mechanically switched capacitor/reactor to switch in. This step is to maximize the dynamic VAr reserves in the system. After that, if there is still a need for more reactive power, the controller will stepwise send out simultaneously a request to all of the neighboring nodes to increase reactive power injection until the reserve is recovered. During the process, if the neighbor controllers are out of limit, they will ask their neighbors for more support. Therefore, there will be more and more automatic contribution from other resources as needed, without any massive computation. Since each controller keeps its local voltage within the maximum limit, there is no risk of overvoltage.

- The controller will automatically ask the neighboring nodes to reduce their support when its reserve is restored. The process goes on as long as the controller still has sufficient reserve. Here, the criterion to determine whether the reserve is sufficient

or not is very important. Otherwise, the controller will lack its reserve again after its neighbors have reduced the reactive power support. In this case, the controller just swings between the two states of lack and surplus of support, meaning that the control scheme is unstable.

An example of the proposed scheme for the simple grid above is depicted in Fig. 6.5. The double headed arrow means that the two nodes support each other; the single headed arrow indicates that the support comes from only one side, here node 2 supports node 1 and 7. It is not necessary to integrate all the nodes into the control scheme. In the first stage, depending on available resources, the scheme can cover some nodes, e.g. 1, 7, and 4. The expansion can be done in the next stage when the resources are available. Note that the control scheme is not limited to a small system. With the same philosophy, it can be applied to the whole network.

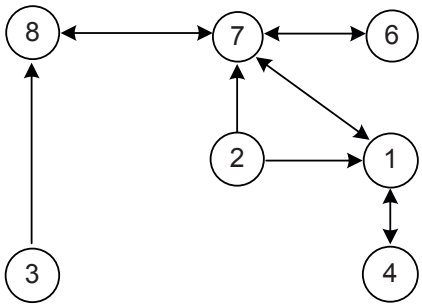

Figure 6.5: One of possible control schemes for the system in Fig. 6.4.

6.2.3 Detail of controller design for controllable VAr sources

Controllable VAr sources like STATCOM, SVC, VSC-HVDC have their own fast controller acting as an inner loop to regulate voltage or reactive power. The controller proposed in this chapter is an outer loop, sending supplementary reference to the inner loop. Take a simplified block diagram of a SVC controller depicted in Fig. 6.6 as an example, where U_{ref} is the reference voltage, U_{POD} is the supplementary signal from the oscillation damping function, and ΔU_{ref} is the output of the proposed control scheme. Without the requests for support from the neighboring controllers, ΔU_{ref} is zero. Thus, the proposed control scheme has no impact on the primary controller in normal operation.

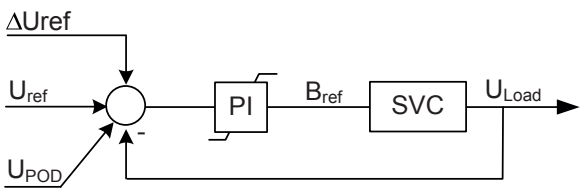

Figure 6.6: A simplified primary controller of SVC.

Fig. 6.7 depicts the structure for the proposed controller, which has two independent blocks, namely Outgoing Support Transmitter (OST) and Incoming Support Handler (ISH). The meaning of each input and output is explained as follows:

- *CapOn*: output command to ask the neighboring mechanically switched capacitor/reactor to switch in. There is no output to ask the neighbors to switch out. The controller at the capacitor/reactor node decides to take this action based on its own logic, which is presented in the next section.

- ΔU_{out}: This is the output sent to the neighboring controllers to ask them to increase or decrease their voltage or reactive power reference. It is considered as the input signal ΔU_{in} of the neighboring controllers. Each neighboring VAr reserve is assigned a separate ΔU_{out}, depending on the electrical distance to the bus, which needs the support. The smaller the distance is, the more reactive power the neighboring unit should increase, meaning that higher ΔU_{out}.

- *No more support*: this is a Boolean signal, indicating that the controller is out of its limit. In this case, its neighbors will stop increasing the demand for support (ΔU_{out}) sent to this controller. Instead, they will send the previous demand. This tactic is to reduce the time delay when the controller has restored its reserve and starts asking its neighbors to lower the support.

- *NeedSupport*: a Boolean signal sent to the neighboring controllers, indicating that the controller is running out its reserve and requires more reactive power support.

- Q_{SVC}, B_{SVC}: the current reactive power and susceptance of the local VAr resource. These quantities are used to determine whether there is sufficient reserve or not.

- U_{local}: local voltage.

- ΔU_{ref}: supplementary voltage reference sent to the inner loop.

6.2.3.1 Operation of the OST block

Fig. 6.8 describes the logic of the OST block, which is responsible for sending the support request to the neighbors when the condition $B_{SVC} > B_{upper}$ (and $U_{load} > U_{low}$) is fulfilled, where B_{upper} and U_{low} are the setting thresholds for the susceptance and voltage, respectively. The condition $U_{load} > U_{low}$ is optional; it is used when less interaction among controllers is needed. The controller requires reactive support when it lacks VAr reserve and the local voltage drops below the lower limit. After the susceptance B_{SVC} is above the threshold B_{upper} continuously in *T1* seconds, the controller first asks its neighboring mechanically switched capacitor/reactor banks to switch in/out. This action is necessary to save reactive power reserve of the dynamic VAr resources as much as possible. After the first action, if there is still a need for more reactive power, the controller will send the signal ΔU_{out} (or the demand for increase of reactive power ΔQ) to the neighboring controllers. Each neighboring controller receives its own ΔU_{out}, depending on the electrical distance to the considered node; the closer the controller, the larger ΔU_{out}. The ΔU_{out} is a design parameter; large ΔU_{out} means more reactive power injection for each step, and therefore smaller response time. But it can push the VAr reserve of the neighbors out of their limits by a few steps. The OST increases ΔU_{out} step by step until it restores the required reactive power reserve.
When the neighboring controllers are increasing reactive power, they can run out their reserve. If the OST detects that one of its neighboring controllers is out of limit, it does not

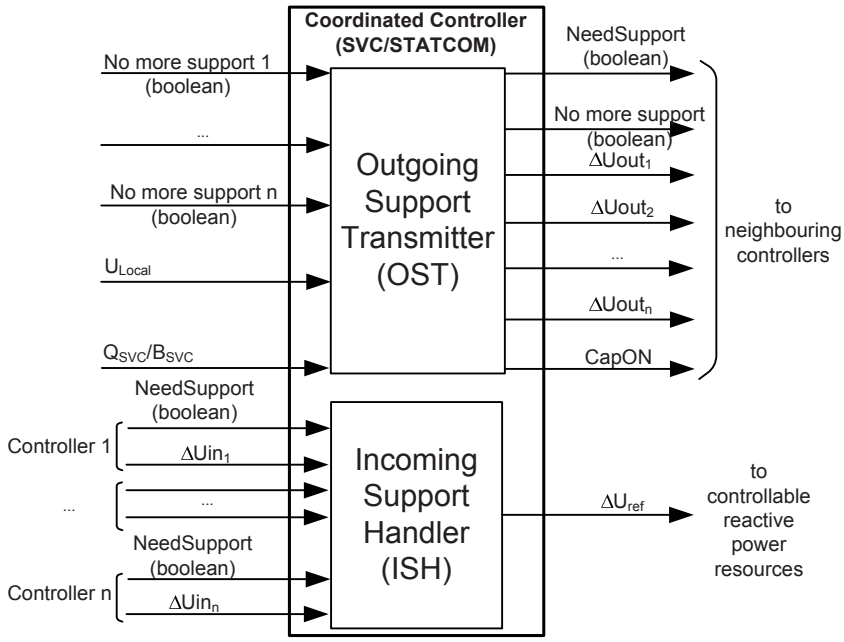

Figure 6.7: Control structure for controllable VAr reserves.

increase ΔU_{out} sent to that particular neighbor, but instead keeps sending the previous ΔU_{out}. This tactic reduces the time delay when the system reverts to normal operation condition; consequently the OST no longer needs support from the other. This is the starting point to reduce the demand for reactive power support.

Support of reactive power from the neighboring VAr reserves is only necessary when there is lack of reactive power in the system. In normal state, however, such interference among controllers should be avoided. Therefore, whenever the controller is able take its own responsibility, to some extent, the support from the neighboring controllers must be reduced. Otherwise, the control system would be tangled with the requests for voltage increase (ΔU_{out}) sent by controllers to each other. As illustrated in Fig. 6.9, as long as the susceptance B_{SVC} is smaller than the threshold B_{lower} continuously in $T4$ seconds, the OST block will lower the ΔU_{out} it has sent out in a stepwise manner. It is important that there must be a deadband between B_{upper} and B_{lower}, as shown in Fig. 6.10, to avoid oscillation between the two states: lack and surplus of the local reserve. When the susceptance is within the deadband, there is not any action from the OST block.

6.2.3.2 Operation of the ISH block

As shown in Fig. 6.11, the ISH simply receives all support requests from all of the neighbors (U_{in_1}, , U_{in_n}) and sends the supplementary voltage reference U_{ref}, which is the maximum of all the incoming requested voltage increase, to the inner loop. The voltage limit U_{max} (normally 5% of the nominal value) is considered in the loop to make sure that the control does not send excessive setpoint to the inner loop; Therefore, there is no risk of overvoltage caused by the ISH block. If the reserve is out of limit (the Boolean signal

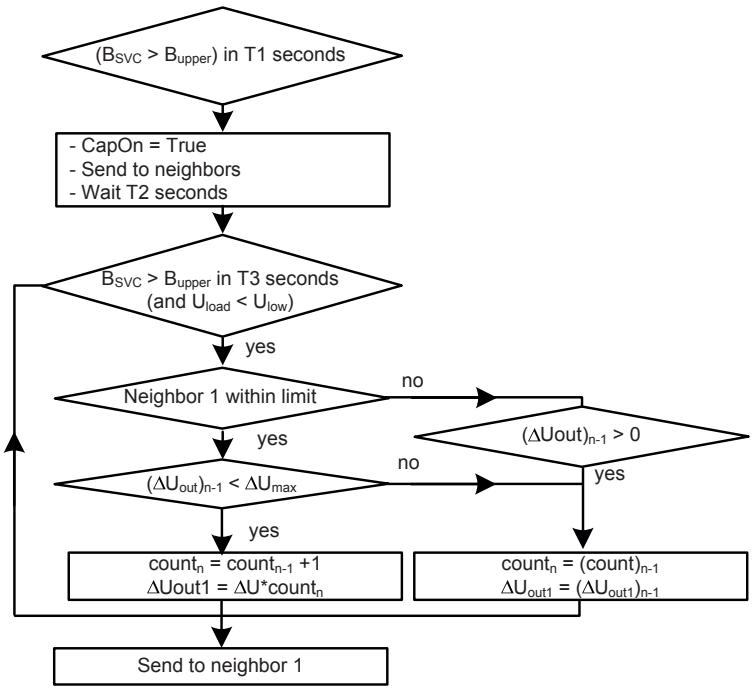

Figure 6.8: Logic to obtain support from the neighboring controllers.

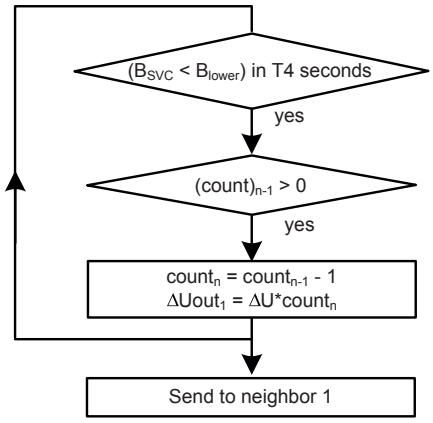

Figure 6.9: Logic to lower support from the neighboring controllers.

NoMoreSupport is true), the ISH does not increase the setpoint and uses the previous value.

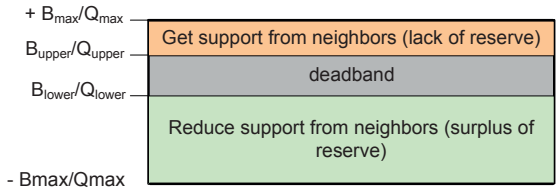

Figure 6.10: Criterion to decide the state of lack or surplus of reactive power reserve.

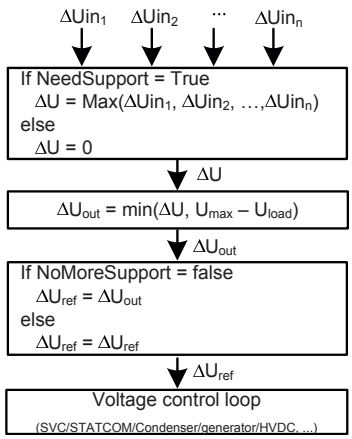

Figure 6.11: Algorithm of the Incoming Support Handler block (ISH).

6.2.4 Detail of controller design for mechanically switched shunt capacitor/reactor

Normally mechanically switched shunt capacitor and reactor are controlled manually by the system operators. They are switched in or out based on planning, operation conditions or system operators' experience. When the system requires more reactive power injection, the mechanically switched capacitor banks should be switched in and the reactor should be switched out in the first stage in order to maximize the dynamic reactive power reserves. Moreover, after disturbances, the operators can be busy with remedial actions. During this time, switching these components automatically can relieve them from trivial tasks.

In terms of reactive power compensation, the effect of a reactor is just opposite to that of a capacitor. Therefore, hereafter only operation of the controller for the capacitor is presented. When the neighboring controllers need reactive power support, the controller for capacitor banks will receive the command *CapOn* to switch in. As shown in Fig. 6.12, to make sure that the local voltage will not exceed the limit U_{max} after closing the capacitor bank, the controller checks the current local voltage U_{load} at its node. If the gap between U_{load} and U_{max} is larger than U_{inc}, it will switch in the bank as requested by its neighbors; here, U_{inc} is setting parameter - the estimated voltage rise if the capacitor is switched in. This value can be obtained from offline simulations or simply by historic data or the operator's experience. Probably machine learning can be applied to obtain U_{inc} automatically.

It is noted that the capacitor bank is not switched out by the command issued by the

neighboring controllers, but by the capacitor bank controller itself. For substations with capacitor banks, it is possible to coordinate this component with the OLTC and other equipment. The Substation Controller in [16] is one of good example for the coordination.

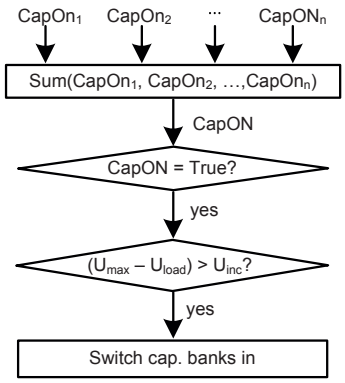

Figure 6.12: Control logic for capacitor bank.

6.2.5 Simulation results

6.2.5.1 Test on the 5-bus system

The first simulation is conducted on a simple 5-bus system shown in Fig. 6.13. There are two SVCs installed at bus 3 and 4. Since they are neighbors, the mutual support between them is established in the coordinated scheme. Moreover, the capacitor at bus 2 also supports SVC1 and generator G1 helps SVC2. To illustrate the performance of the control scheme, initially the capacitor bank at bus 2 is off. At $t = 7.5$ s, the load at bus 3 increases from 30 MVA to 75 MVA in 10 s and starts going down to the original level at $t = 97.5$ s. As can be seen in Fig. 6.14, after the load increases, SVC1 reaches its limit and the voltage U_3 drops. Due to the control scheme, the capacitor bank at node 2 is switched in at $t = 12$ s to support node 3. However, the support is not enough, the controller at node 3 consequently requests more reactive power injection from SVC2; thus the voltage U_4 gradually increases. However, SVC2 also reaches its limit at $t = 27.7$ s and starts asking the generator at node 5 to assist. The process goes on until $t = 72$ s when $U_5 = 1.05$ pu and G1 cannot contribute more support; the requested voltage increase sent by the controller at node 3 and 4 ($\Delta U_{out}B3$, $\Delta U_{out}B4$) are unchanged at 0.038 pu and 0.05 pu, respectively. It is noted that every time the SVC2 runs out its reserve, the controller at bus 3 stops asking for more support. Otherwise, SVC2 will continuously be pushed out of its limit while it is seeking support from the neighbor G1.

After the demand at node 3 falls, the reactive power reserve of the SVC1 and SVC2 increases. They start to reduce the support from their neighbors. It can be recognized by the stepwise reduction of the requested voltage support ($\Delta U_{out}B3, \Delta U_{out}B4$). As a result, voltage at node 3, 4 and 5 slowly return to the initial values.

Fig. 6.15 shows the voltage and susceptance of the SVCs at bus 3 and 4 when the coordinated control scheme is not applied. Compared to Fig. 6.14, voltage at bus 3 is lower during the heavy load condition. After the load increases, the voltage falls to 0.97

and remains unchanged until the load returns to its initial level. Without the coordinated control, the SVC at bus 4 does not increase its output to support the voltage at bus 3 although it still has reactive power reserve.

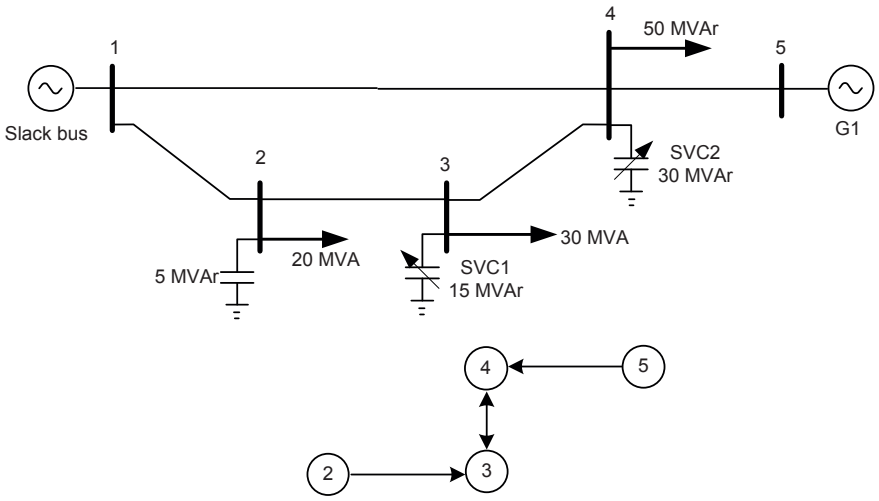

Figure 6.13: A 5-bus system and the coordinated control scheme.

6.2.5.2 Test on the simplified 420 kV system

The second test case is carried out with the simplified model of the 420 kV network in the southern part of Norway. As seen in Fig. 6.16, the system is characterized by large generation in the west, but the load center is located in the eastern side. Due to the large distance between generation and load, voltage control in the load area is heavily dependent on the SVCs and mechanically switched capacitor banks. Coordination of voltage control among these VAr reserves shown in Fig. 6.16 is necessary to obtain a flat voltage profile in this area as well as fast automatic voltage recovery after disturbances. To illustrate the effectiveness of the proposed control scheme, a disturbance at $t = 25$ s is created by tripping the line from bus 10 to 12, where the heaviest load is located. Consequently, voltages in the area drop (except at bus 10) and the SVCs at bus 12, 14 and 8 reach their limits. At $t = 30$ s, the controller at bus 8 starts sending the request for voltage increase to the controllers at bus 2 and 3. Therefore, voltage at these buses starts to go up. Since the SVC at bus 8 is beyond its limit, the controllers at bus 12 and 14 do not send the support request to this one until $t = 44.5$ s, after the controller at bus 8 has received support from bus 2 and 3 and recovered its reserve. At $t = 90.5$ s, all the SVCs have restored the required reserve and the voltage is slightly lower than the nominal thanks to the reactive power assistance from bus 2 and 3. Obviously, the lack of reactive power support in the load area is propagated and sensed by the western power plants and they get involved in the control scheme automatically. The control scheme is working well and all the relevant actors together contribute to the voltage recovery. At $t = 124$ s, the line between bus 10 and 12 is closed. Thus, all the SVCs restore enough reserve and start reducing the support from the neighbors. The system smoothly returns

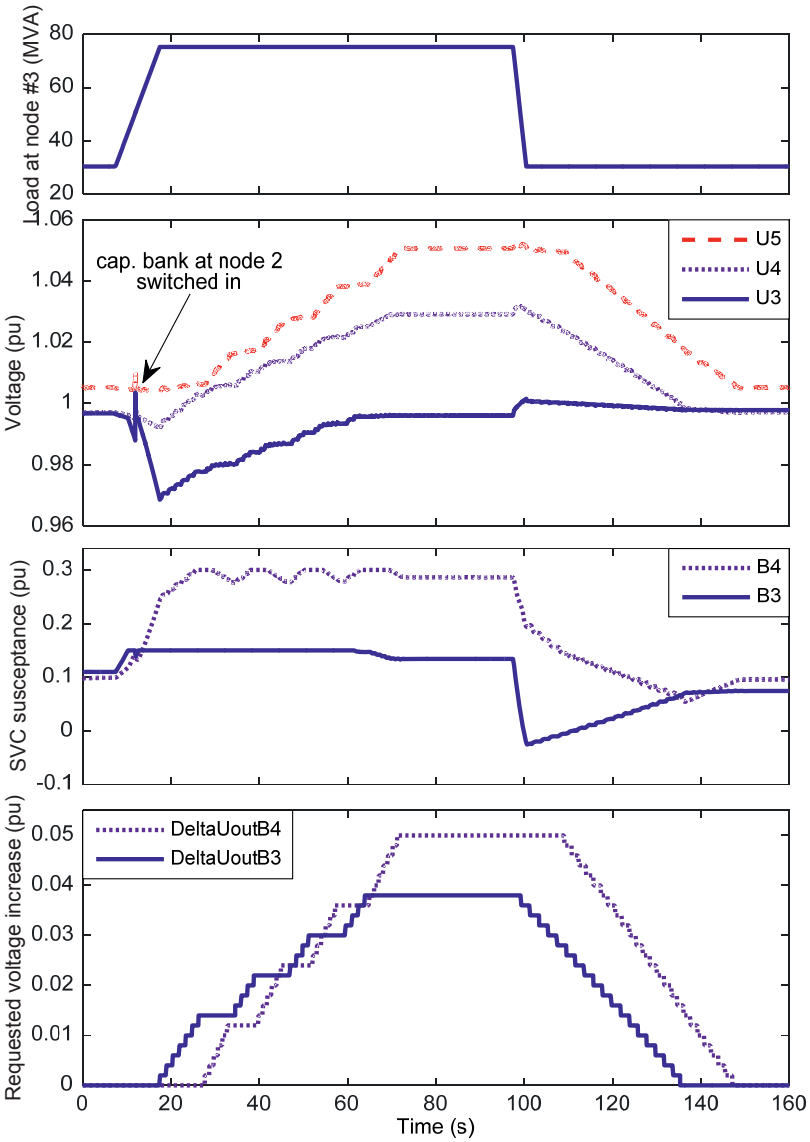

Figure 6.14: Five-bus system's performance during load variation.

to the initial condition. Thanks to the deadband shown in Fig. 6.10, there are no oscillatory behaviors of the control system. In this test, the condition to request reactive power support is $B_{SVC} > B_{upper}$; the voltage condition is not included. Thus the controllers ask for support from the neighbors even when the voltage is not critically low. To reduce the interactions among controllers, the low voltage condition can be applied to certain controllers as desired. In this test, the control scheme involves all possible VAr resources in the system, including generators that are not directly controlled by the TSO. It should be noted that the possible commercial/contractual issues are not discussed here, only the technical feasibility of the control scheme.

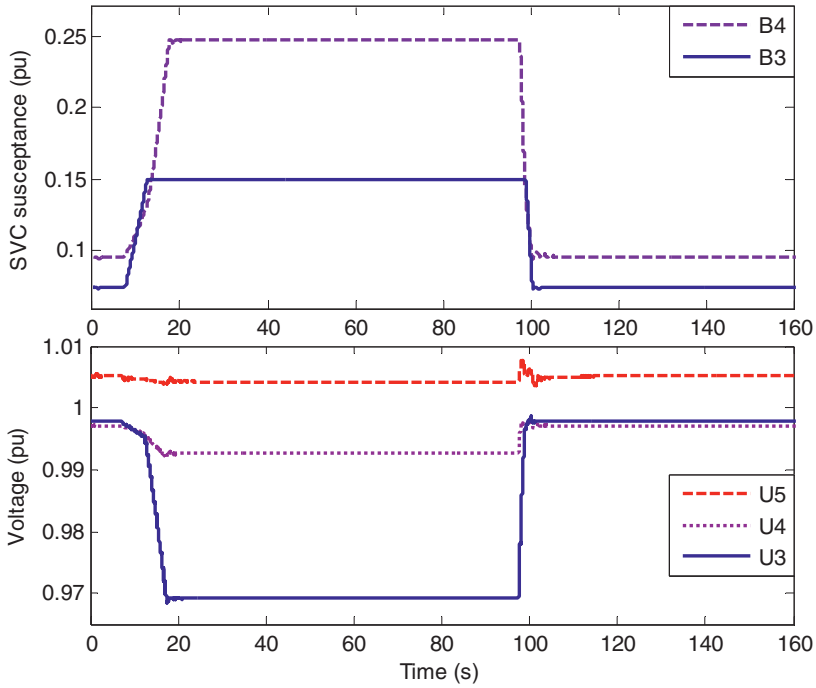

Figure 6.15: Voltage and SVC's susceptance in the five-bus system without coordinated control.

Fig. 6.18 depicts the voltage and susceptance of the SVCs in the studied area when the coordinated control scheme is not applied. As can be seen, voltage at bus 8, 12 and 14 drops below 1.0 pu during the line outage period, but not critical. However, the SVCs at these buses reach their limit; they do not have dynamic reserve to help the grid survive other disturbances or damp oscillations.

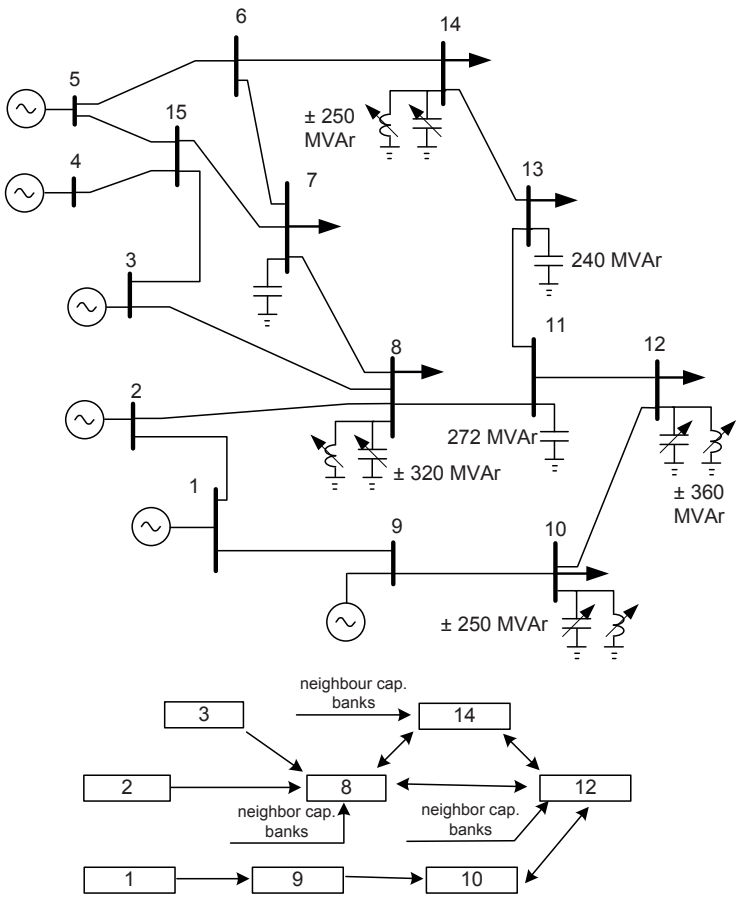

Figure 6.16: The simplified 420 kV system in the southern part of Norway and its coordinated control scheme.

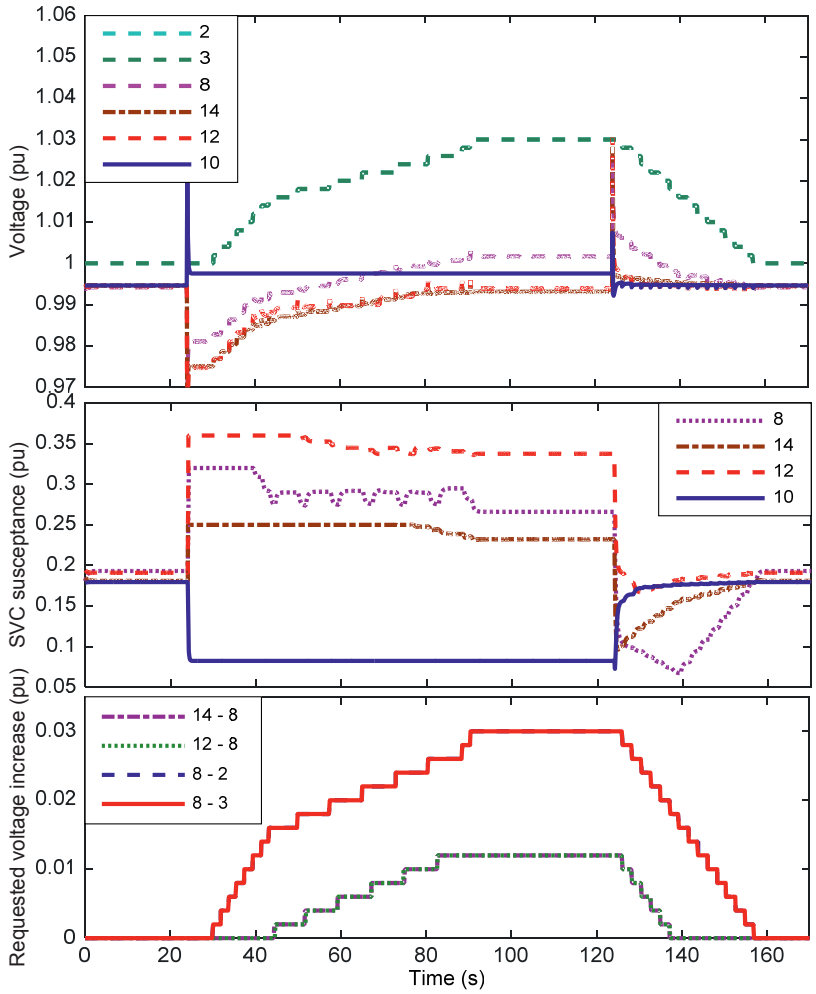

Figure 6.17: The 420 kV system performance during the test.

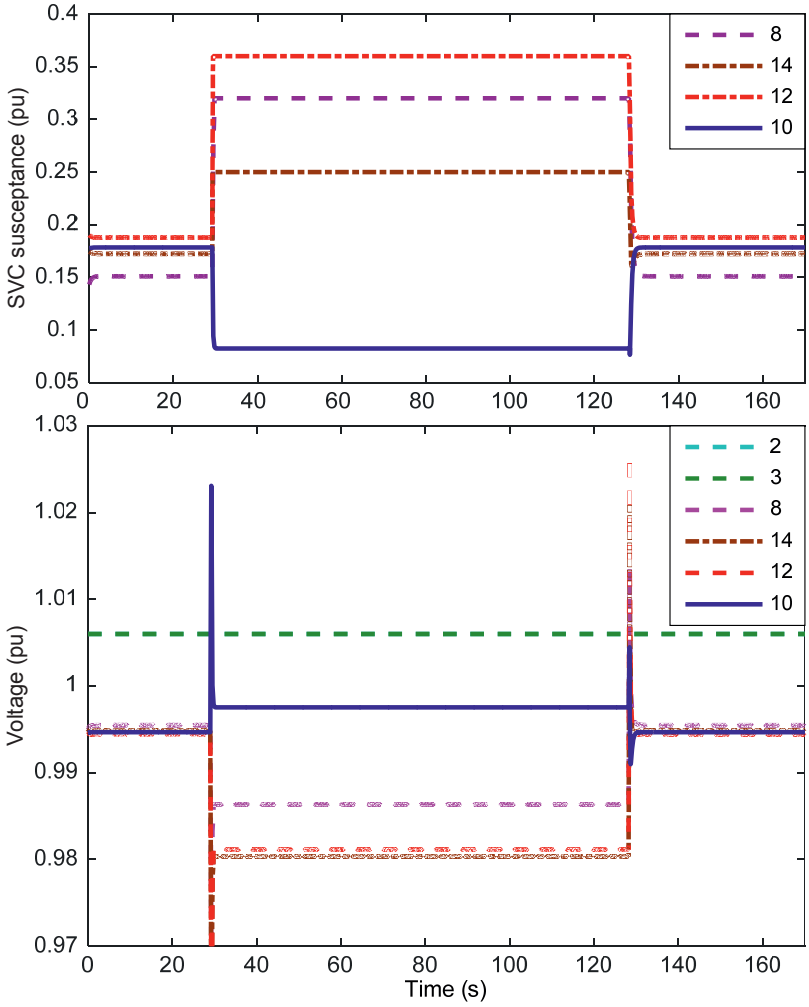

Figure 6.18: Voltage and SVC susceptance without the coordinated control.

Chapter 7

Conclusions and future work

This chapter presents main conclusions drawn from the findings and contributions of the PhD project, which have been presented in the preceding chapters of the thesis. In addition, some ideas for future work are also discussed.

7.1 Conclusions

In this PhD thesis, two algorithms for online voltage stability monitoring and a scheme for voltage control have been proposed, in which the S-Z algorithm is the main contribution. Initially, the main objective of the PhD work is to develop new tools for online voltage stability assessment, especially aiming at utilizing PMU measurements. The expected methods should be simple and have low computational cost, so it can be easily implemented in the control center to increase situational awareness of the system operators and help them determine appropriate remedial actions against voltage instability. Regarding this expectation, the S-Z method and its prototype V_{app} have achieved the initial goal of the PhD project. This algorithm requires only PMU measurements of the load current and voltage and has a very low computational demand. Besides, it works properly in both transmission and sub-transmission systems. There is great potential for large scale implementation of the method in power systems. Of course, this algorithm has its own shortcomings, which are left for the future work as being discussed in the next section.

Compared to the S-Z method, the topology-based approach is less attractive since it requires both information on system topology of the concerned area and PMU measurements. However, one of the advantages of this method is the possibility to estimate the post-contingency Thevenin impedance, which cannot be obtained from the measurement-based algorithm. During the PhD project, this algorithm was not tested with real-time information in the power grid. Access to available information from the SCADA/EMS and state estimator and lack of PMU measurements at the A-P nodes were the main obstacle. Nevertheless, the method is viable for practical implementation in power systems and should be tested with real data.

Unlike the comprehensive secondary voltage control systems in France and Italy, the proposed scheme for coordinated secondary voltage control targets a specific case in the 420 kV system in the southern Norway, where there are several reactive power compensation units in the load center, which is far from the generation. The idea is to have an algorithm, which requires little resources and low computational demand, but it is able to automate voltage control tasks of the system operators to coordinate the local

controllers in order to maintain a flat voltage profile and sufficient dynamic reserves of reactive power. In the future grid with a large number equipment that can inject reactive power into both transmission and distribution grids, voltage control schemes based on optimization would face many challenges caused by fast variations of operation conditions and big data management. In this case, the proposed scheme can be a solution, but it needs more study.

The main conclusions drawn from the PhD work are as follows:

- Online voltage stability monitoring based on estimation of the Thevenin impedance and the maximum power transfer theorem is a workable approach. At a load bus in power systems, it is viable to find an equivalent impedance, from which it is possible to detect an occurrence of the maximum power transfer condition. When the magnitude of the Thevenin impedance is equal to that of the load impedance, it is deemed that the load reaches its maximum loadability and the maximum power transfer condition occurs.

  However, the load can reach the peak power in an operation condition that is different from the maximum power transfer condition when the operation condition dramatically changes or when the load is highly overcompensated by a controllable reactive power compensation.

- The estimated maximum loadability is sensitive to the magnitude of the Thevenin impedance. A small error of the Thevenin impedance can lead to a large variation of the estimated power. Moreover, when the considered load is far from its maximum loadability, estimation of the maximum power transfer based on local phasor measurements cannot measure the ultimate limit of the system transfer capacity. The actual maximum loadability can be estimated properly when the load is in the vicinity of the voltage stability limit.

- It has been sufficiently verified that the proposed indicator S-ZI is a suitable indicator for online voltage stability assessment. Through simulations and real PMU data, the indicator closely follows the predefined curves, which are plotted based on the S-Z sensitivity and load impedance. As mentioned, the S-Z sensitivity is simply computed from phasor measurements of the load current and voltage; therefore, it does not have any problems with divergence during the calculation, which is often experienced by other approaches. In addition, the proposed indicator works properly at any loading level of the considered load. Whether the demand is low or high, the indicator is always located on the trajectories as expected.

- The S-ZI, moreover, has a unique capability to verify the estimated Thevenin impedance seen at a load bus. Given a Thevenin impedance, it is possible to draw a trajectory of the S-ZI versus magnitude of the load impedance. If the Thevenin impedance is properly estimated, the corresponding S-ZI trajectory must cross the S-ZI point, which is directly computed from phasor measurements of the load current and voltage. With this tool, the online estimated Thevenin impedance can be validated in normal operation condition.

- It is viable to estimate the Thevenin impedance seen at a load bus from local phasor measurements of the load current and voltage. The proposed method using local phasor measurements has successfully estimated the Thevenin impedance from both

simulation and real PMU data. In the V_{app}, despite influences of noise, disturbances and other factors in power systems, the Thevenin impedance has been estimated properly and robustly. This shows a real possibility for implementing the approach on a large scale in power systems.

- Alternatively, the Thevenin impedance can be estimated from information of the system topology and PMU measurements. Through simulations, the proposed topology-based method has shown a good performance. The results from this algorithm are comparable to that of other approaches. A major advantage of this method is that it is able to estimate the Thevenin impedance under contingency in real time. With this capability, it is possible to assess voltage stability of the current operating point under critical contingencies. This improves situational awareness of system operators and provides a useful input for planning preventive actions to enhance security of power system operation.

- The proposed voltage control scheme in Chapter 6 is developed for areas in power systems, where there is a high penetration of controllable VAr sources. The scheme has shown a good performance in coordinating reactive power compensation to obtain a flat voltage profile and sufficient dynamic reactive power reserves under conditions of disturbances and operational variations. The control structure is simple and effective; there is no need for massive computation. Moreover, this algorithm is easy to be implemented and flexibly adapted, which makes the method feasible for practical applications in real networks.

- The Thevenin impedance and the S-ZI are suitable tools for load shedding, which is an effective countermeasure to prevent voltage instability. Without massive calculation for optimization, the load shedding scheme based on these parameters is still able to secure selectivity and to minimize an amount of load which should be curtailed.

7.2 Future work

- The application V_{app} has been tested with real PMU data at two locations in the Norwegian transmission system. However, these two nodes are not vulnerable to voltage instability. Therefore, to have a better demonstration of the proposed methods, there should be more test cases at different locations in power systems, especially at buses prone to voltage instability. Probably, practical implementations might reveal hidden limitations of the algorithms, which are helpful to enhance the methods.

- The Thevenin impedance estimated by the S-Z sensitivity method has large variations when the load is light. The reason is that there is a very small difference among the S-Z sensitivity trajectories in this loading condition. The future work can focus on overcoming this limitation, exploring new possibilities to obtain the Thevenin impedance in real time at these light load buses.

- Blackouts are normally a complex process, consisting of different stability problems. With an increasing penetration of variable generation from renewable sources and use of power electronics, maintaining stability of the grid becomes more and more

challenging. To prevent blackouts, several actions should be taken quickly and timely. In this context, there are possibilities to integrate the proposed load shedding scheme based on the voltage stability indicators into a comprehensive protection system that is able to make the grid more resilient to disturbances under operation with higher uncertainty in the foreseeable future.

- As observed in Section 5.2, there is a mismatch between the post-contingency Thevenin impedance and the actual one estimated after the disturbance. This disparity is affected by many factors, such as types of the disturbance, system topology, operation condition, etc. In the thesis, this issue is not thoroughly examined. Further study is left for future work.

- More study on voltage control under condition of high penetration of renewable generation and power electronic devices in power systems. Fast variation of operation conditions and its impact on voltage in the grid should be thoroughly investigated.

References

[1] C. W. Taylor, *Power System Voltage Stability.* McGraw Hill, 1994.

[2] Final report on the August 14 2003 blackout in the United State and Canada: Causes and Recommendations. [Online]. Available: http://energy.gov/sites/prod/files/oeprod/DocumentsandMedia/BlackoutFinal-Web.pdf

[3] G. Andersson, P. Donalek, R. Farmer, N. Hatziargyriou, I. Kamwa, P. Kundur, N. Martins, J. Paserba, P. Pourbeik, J. Sanchez-Gasca, R. Schulz, A. Stankovic, C. Taylor, and V. Vittal, "Causes of the 2003 major grid blackouts in north america and europe, and recommended means to improve system dynamic performance," *Power Systems, IEEE Transactions on*, vol. 20, no. 4, pp. 1922–1928, Nov 2005.

[4] S. Larsson and A. Danell, "The black-out in southern sweden and eastern denmark, september 23, 2003." in *Power Systems Conference and Exposition, 2006. PSCE '06. 2006 IEEE PES*, Oct 2006, pp. 309–313.

[5] Final report of the Investigation Committee on the 28 September 2003 blackout in Italy. [Online]. Available: https://www.entsoe.eu/fileadmin/user_upload/_library/publications/ce/otherreports/20040427_UCTE_IC_Final_report.pdf

[6] S. Corsi and C. Sabelli, "General blackout in italy sunday september 28, 2003, h. 03:28:00," in *Power Engineering Society General Meeting, 2004. IEEE*, June 2004, pp. 1691–1702.

[7] A. Berizzi, "The italian 2003 blackout," in *Power Engineering Society General Meeting, 2004. IEEE*, June 2004, pp. 1673–1679 Vol.2.

[8] 2012 India blackouts. [Online]. Available: https://en.wikipedia.org/wiki/2012_India_blackouts

[9] Project Group Turkey. (2015, Sep.) Report on Blackout in Turkey on 31st March 2015. [Online]. Available: https://www.entsoe.eu/publications/system-operations-reports/continental-europe/Pages/default.aspx

[10] Webpage of the project "Smart transmission grid operation and control". [Online]. Available: http://www.nordicenergy.org/project/smart-transmission-grid-operation-and-control/

[11] Prabha Kundur, *Power System Stability and Control.* McGraw Hill, 1994.

[12] P. Kundur, J. Paserba, V. Ajjarapu, G. Andersson, A. Bose, C. Canizares, N. Hatziargyriou, D. Hill, A. Stankovic, C. Taylor, T. Van Cutsem, and V. Vittal, "Definition and classification of power system stability ieee/cigre joint task force on stability terms and definitions," *Power Systems, IEEE Transactions on*, vol. 19, no. 3, pp. 1387–1401, Aug 2004.

[13] W.R. Lachs, "Voltage collapse in EHV power systems," in *IEEE PES winter meeting (paper No. A78057-2)*, New York, Feb. 1978.

[14] Thierry Van Cutsem and Costas Vournas, *Voltage Stability of Electric Power Systems*. Springer, 2008.

[15] Cigre WG B4.37, "VSC transmission," Cigre, Technical Brochure 75, Apr. 1993.

[16] Cigre Task Force C4.602, "Coordinated voltage control in transmission networks," Cigre, Technical Brochure 310, Feb. 2007.

[17] "IEEE Standard for Cylindrical-Rotor 50 Hz and 60 Hz Synchronous Generators Rated 10 MVA and Above," *IEEE Std C50.13-2014 (Revision of IEEE Std C50.13-2005)*, pp. 1–63, May 2014.

[18] S. Johansson, "Mitigation of voltage collapse caused by armature current protection," *Power Systems, IEEE Transactions on*, vol. 14, no. 2, pp. 591–599, May 1999.

[19] J. Walker, "Operating characteristics of salient-pole machines," *Proceedings of the IEE - Part II: Power Engineering*, vol. 100, no. 73, pp. 13–24, February 1953.

[20] R. Bruck and H. Messerle, "The capability of alternators," *Proceedings of the IEE - Part A: Power Engineering*, vol. 102, no. 5, pp. 611–618, October 1955.

[21] Venkataramana Ajjarapu, *Computational Techniques for VoltageStability Assessment and Control*. Springer, 2006.

[22] Mats Larsson, "Coordinated voltage control in electric power systems," Ph.D. dissertation, Lund University , Lund, Dec. 2000. [Online]. Available: https://www.iea.lth.se/publications/Theses/LTH-IEA-1025.pdf

[23] C.-C. Liu and K. Vu, "Analysis of tap-changer dynamics and construction of voltage stability regions," *Circuits and Systems, IEEE Transactions on*, vol. 36, no. 4, pp. 575–590, Apr 1989.

[24] K. Vu and C.-C. Liu, "Shrinking stability regions and voltage collapse in power systems," *Circuits and Systems I: Fundamental Theory and Applications, IEEE Transactions on*, vol. 39, no. 4, pp. 271–289, Apr 1992.

[25] Cigre WG 38-01, "Static VAr compensators," Cigre, Technical report, 1986.

[26] K. R. Padiyar, *FACTS controllers in power transmission and distribution*. New Age, 2007.

[27] Cigre Task Force 38.02.10, "Modelling of voltage collapse including dynamic phenoma," Cigre, Technical Brochure 269, Apr. 2005.

[28] X. Zhang, C. Rehtanz, and B. Pal, *Flexible AC transmission systems: modelling and control*. Routledge, 2012.

[29] S. G Johansson, G. Asplund, E. Jansson and R. Rudervall, "Power system stability benefits with vsc dc-transmission systems," in *Cigre Section*, 2004, pp. 1–8.

[30] Cigre Task Force 38.02.12, "Criteria and countermeasures for voltage collapse," Cigre, Technical Brochure 101, Oct. 1995.

[31] B. Ingelsson, P.-O. Lindstrom, D. Karlsson, G. Runvik, and J.-O. Sjodin, "Wide-area protection against voltage collapse," *Computer Applications in Power, IEEE*, vol. 10, no. 4, pp. 30–35, Oct 1997.

[32] C. Taylor, "Concepts of undervoltage load shedding for voltage stability," *Power Delivery, IEEE Transactions on*, vol. 7, no. 2, pp. 480–488, Apr 1992.

[33] F. Capitanescu, T. Van Cutsem, and L. Wehenkel, "Coupling optimization and dynamic simulation for preventive-corrective control of voltage instability," *Power Systems, IEEE Transactions on*, vol. 24, no. 2, pp. 796–805, May 2009.

[34] B. Otomega and T. Van Cutsem, "Undervoltage load shedding using distributed controllers," *Power Systems, IEEE Transactions on*, vol. 22, no. 4, pp. 1898–1907, Nov 2007.

[35] D. Lefebvre, C. Moors, and T. Van Cutsem, "Design of an undervoltage load shedding scheme for the hydro-quebec system," in *Power Engineering Society General Meeting, 2003, IEEE*, vol. 4, July 2003, pp. –2036 Vol. 4.

[36] C. Moors, D. Lefebvre, and T. Van Cutsem, "Design of load shedding schemes against voltage instability," in *Power Engineering Society Winter Meeting, 2000. IEEE*, vol. 2, 2000, pp. 1495–1500 vol.2.

[37] V. Ajjarapu and C. Christy, "The continuation power flow: a tool for steady state voltage stability analysis," *Power Systems, IEEE Transactions on*, vol. 7, no. 1, pp. 416–423, Feb 1992.

[38] S. G. Ghiocel and J. H. Chow, "A power flow method using a new bus type for computing steady-state voltage stability margins," *IEEE Transactions on Power Systems*, vol. 29, no. 2, pp. 958–965, March 2014.

[39] B. Gao, G. Morison, and P. Kundur, "Voltage stability evaluation using modal analysis," *Power Systems, IEEE Transactions on*, vol. 7, no. 4, pp. 1529–1542, Nov 1992.

[40] K. Vu, M. Begovic, D. Novosel, and M. Saha, "Use of local measurements to estimate voltage-stability margin," in *Power Industry Computer Applications., 1997. 20th International Conference on*, May 1997, pp. 318–323.

[41] John Bird, *Electrical Circuit Theory and Technology*. Routledge, 2010.

[42] M. Begovic, B. Milosevic, and D. Novosel, "A novel method for voltage instability protection," in *System Sciences, 2002. HICSS. Proceedings of the 35th Annual Hawaii International Conference on*, Jan 2002, pp. 802–811.

[43] Y. Wang, I. Pordanjani, W. Li, W. Xu, T. Chen, E. Vaahedi, and J. Gurney, "Voltage stability monitoring based on the concept of coupled single-port circuit," *Power Systems, IEEE Transactions on*, vol. 26, no. 4, pp. 2154–2163, Nov 2011.

[44] D. Julian, R. Schulz, K. Vu, W. Quaintance, N. Bhatt, and D. Novosel, "Quantifying proximity to voltage collapse using the voltage instability predictor (vip)," in *Power Engineering Society Summer Meeting, 2000. IEEE*, vol. 2, 2000, pp. 931–936 vol. 2.

[45] K. Vu, M. Begovic, D. Novosel, and M. Saha, "Use of local measurements to estimate voltage-stability margin," *Power Systems, IEEE Transactions on*, vol. 14, no. 3, pp. 1029–1035, Aug 1999.

[46] T. K. Vu and D. Novosel, "Voltage instability predictor (VIP)–method and system for performing adaptive control to improve voltage stability in power systems," U.S. Patent US6 219 591B1, Apr. 17, 2001.

[47] S. Corsi and G. Taranto, "A real-time voltage instability identification algorithm based on local phasor measurements," *Power Systems, IEEE Transactions on*, vol. 23, no. 3, pp. 1271–1279, Aug 2008.

[48] G. Taranto, C. Oyarce, and S. Corsi, "Further investigations on a phasor measurement-based algorithm utilized for voltage instability awareness," in *Bulk Power System Dynamics and Control - IX Optimization, Security and Control of the Emerging Power Grid (IREP), 2013 IREP Symposium*, Aug 2013, pp. 1–8.

[49] Thales M. Papazoglou, T. Babnik, U. Bezerra, C. Cattaneo, S. Gasperic, J. Kostevc, R. Mihalic, U. Rudez, G. Taranto, M. Testori and J. Vieira, "On voltage and VAr support in electric power system operation," *ELECTRA*, vol. 272, pp. 4–17, Feb. 2014.

[50] S. Corsi and G. Taranto, "Voltage instability - the different shapes of the "nose"," in *Bulk Power System Dynamics and Control - VII. Revitalizing Operational Reliability, 2007 iREP Symposium*, Aug 2007, pp. 1–16.

[51] B. Milosevic and M. Begovic, "Voltage-stability protection and control using a wide-area network of phasor measurements," *Power Systems, IEEE Transactions on*, vol. 18, no. 1, pp. 121–127, Feb 2003.

[52] Root-finding algorithm. [Online]. Available: https://en.wikipedia.org/wiki/Root-finding_algorithm

[53] Find polynomial roots in Matlab. [Online]. Available: http://se.mathworks.com/help/matlab/ref/roots.html

[54] M. Larsson, C. Rehtanz, and J. Bertsch, "Monitoring and operation of transmission corridors," in *Power Tech Conference Proceedings, 2003 IEEE Bologna*, vol. 3, June 2003, pp. 8 pp. Vol.3–.

[55] S. Arefifar and W. Xu, "Online tracking of power system impedance parameters and field experiences," *Power Delivery, IEEE Transactions on*, vol. 24, no. 4, pp. 1781–1788, Oct 2009.

[56] M. Parniani, J. Chow, L. Vanfretti, B. Bhargava, and A. Salazar, "Voltage stability analysis of a multiple-infeed load center using phasor measurement data," in *Power Systems Conference and Exposition, 2006. PSCE '06. 2006 IEEE PES*, Oct 2006, pp. 1299–1305.

[57] D. Duong, K. Uhlen, and S. Lovlund, "A method for real time voltage stability monitoring in sub-transmission networks," in *Power Systems Computation Conference (PSCC), 2014*, Aug 2014, pp. 1–7.

[58] Jonh J. Grainger and William D. Stevenson, JR., *Power System Analysis*. McGraw Hill, 1994.

[59] Hadi Saadat, *Power System Analysis*. McGraw Hill, 1999.

[60] T. V. Cutsem and L. Papangelis. Description, modeling and simulation results of a test system for voltage stability analysis,. [Online]. Available: http://hdl.handle.net/2268/141234

[61] Cigre Task Force 38.02.08, "Long term dynamics phase II," Cigre, Technical Brochure 102, Mar. 1995.

[62] Leif Warland, "A voltage instability predictor using local area measurements VIP++," Ph.D. dissertation, Norwegian University of Science and Technology, Trondheim, Feb. 2002. [Online]. Available: http://www.diva-portal.org/smash/get/diva2:121795/FULLTEXT01.pdf

[63] ENTSO-E grid map. [Online]. Available: www.entsoe.eu

[64] *PSS/E User manual version 33*, Siemens, 2011.

[65] L. Vanfretti, V. Aarstrand, M. Almas, V. Peric, and J. Gjerde, "A software development toolkit for real-time synchrophasor applications," in *PowerTech (POWERTECH), 2013 IEEE Grenoble*, June 2013, pp. 1–6.

[66] "IEEE standard for synchrophasor measurements for power systems," *IEEE Std C37.118.1-2011 (Revision of IEEE Std C37.118-2005)*, pp. 1–61, Dec 2011.

[67] C. D. Vournas and N. G. Sakellaridis, "Tracking maximum loadability conditions in power systems," in *Bulk Power System Dynamics and Control - VII. Revitalizing Operational Reliability, 2007 iREP Symposium*, Aug 2007, pp. 1–12.

[68] *Voltage characteristics of electricity supplied by public distribution systems*, CENELEC Std. 50 160:11-1999, 1999.

[69] J. Paul, J. Leost, and J. Tesseron, "Survey of the secondary voltage control in france : Present realization and investigations," *Power Systems, IEEE Transactions on*, vol. 2, no. 2, pp. 505–511, May 1987.

[70] P. Lagonotte, J. Sabonnadiere, J. Leost, and J. Paul, "Structural analysis of the electrical system: application to secondary voltage control in france," *Power Systems, IEEE Transactions on*, vol. 4, no. 2, pp. 479–486, May 1989.

[71] H. Vu, P. Pruvot, C. Launay, and Y. Harmand, "An improved voltage control on large-scale power system," *Power Systems, IEEE Transactions on*, vol. 11, no. 3, pp. 1295–1303, Aug 1996.

[72] H. Lefebvre, D. Fragnier, J. Boussion, P. Mallet, and M. Bulot, "Secondary coordinated voltage control system: feedback of edf," in *Power Engineering Society Summer Meeting, 2000. IEEE*, vol. 1, 2000, pp. 290–295 vol. 1.

[73] S. Corsi, M. Pozzi, C. Sabelli, and A. Serrani, "The coordinated automatic voltage control of the italian transmission grid-part I: reasons of the choice and overview of the consolidated hierarchical system," *Power Systems, IEEE Transactions on*, vol. 19, no. 4, pp. 1723–1732, Nov 2004.

[74] S. Corsi, M. Pozzi, M. Sforna, and G. Dell'Olio, "The coordinated automatic voltage control of the italian transmission grid-part II: control apparatuses and field performance of the consolidated hierarchical system," *Power Systems, IEEE Transactions on*, vol. 19, no. 4, pp. 1733–1741, Nov 2004.

[75] M. Ilic, X. Liu, G. Leung, M. Athans, C. Vialas, and P. Pruvot, "Improved secondary and new tertiary voltage control," *Power Systems, IEEE Transactions on*, vol. 10, no. 4, pp. 1851–1862, Nov 1995.

[76] J. Sancha, J. Fernandez, A. Cortes, and J. Abarca, "Secondary voltage control: analysis, solutions and simulation results for the spanish transmission system," in *Power Industry Computer Application Conference, 1995. Conference Proceedings., 1995 IEEE*, May 1995, pp. 27–32.

[77] H. Sun, Q. Guo, B. Zhang, W. Wu, and B. Wang, "An adaptive zone-division-based automatic voltage control system with applications in china," *Power Systems, IEEE Transactions on*, vol. 28, no. 2, pp. 1816–1828, May 2013.

[78] M. Geidl, "Implementation of coordinated voltage control for the swiss transmission system," in *MELECON 2010 - 2010 15th IEEE Mediterranean Electrotechnical Conference*, April 2010, pp. 230–236.

[79] S. Corsi, F. De Villiers, and R. Vajeth, "Secondary voltage regulation applied to the south africa transmission grid," in *Power and Energy Society General Meeting, 2010 IEEE*, July 2010, pp. 1–8.

[80] G. Taranto, N. Martins, D. Falcao, A. Martins, and M. dos Santos, "Benefits of applying secondary voltage control schemes to the brazilian system," in *Power Engineering Society Summer Meeting, 2000. IEEE*, vol. 2, 2000, pp. 937–942 vol. 2.

[81] J. J. Van Hecke, N. Janssens and F. Promel, "Coordinated voltage control experience in Belgium," in *Cigre session 2000 Report 38-111*, 2000.

[82] S. McArthur, E. Davidson, V. Catterson, A. Dimeas, N. Hatziargyriou, F. Ponci, and T. Funabashi, "Multi-agent systems for power engineering applications-part I: Concepts, approaches, and technical challenges," *Power Systems, IEEE Transactions on*, vol. 22, no. 4, pp. 1743–1752, Nov 2007.

[83] S. McArthur, E. Davidson, V. Catterson, A. Dimeas, N. Hatziargyriou, F. Ponci, and T. Funabashi, "Multi-agent systems for power engineering applications-part II: Technologies, standards, and tools for building multi-agent systems," *Power Systems, IEEE Transactions on*, vol. 22, no. 4, pp. 1753–1759, Nov 2007.

[84] H. F. Wang, H. Li, and H. Chen, "Coordinated secondary voltage control to eliminate voltage violations in power system contingencies," *Power Systems, IEEE Transactions on*, vol. 18, no. 2, pp. 588–595, May 2003.

Appendix A

Dynamic models of the modified CIGRE Nordic32 test system

The modified CIGRE Nordic32 test system used in Section 5.4 is the same as the benchmark described in [60], except for the dynamic models. Since the simulation is carried out in PSS/E, dynamic models of governors, AVRs, power system stabilizers and OXLs are selected from the standard library of this power system simulation software. Parameters of all the dynamic models are presented in the next pages.

```
/IBUS   'GENROU'   I   T'do  T"do   T'qo  T"qo   H    D    Xd     Xq
X'd   X'q   X"d    Xl    S(1.0)     S(1.2)/
 404214 'GENROU'   1   7.0   0.05   1.5   0.05   6.   0.   2.20   2.00
0.30  0.40  0.20  0.15   0.0        0.0/
 404715 'GENROU'   1   7.0   0.05   1.5   0.05   6.   0.   2.20   2.00
0.30  0.40  0.20  0.15   0.0        0.0/
 405116 'GENROU'   1   7.0   0.05   1.5   0.05   6.   0.   2.20   2.00
0.30  0.40  0.20  0.15   0.0        0.0/
 406217 'GENROU'   1   7.0   0.05   1.5   0.05   6.   0.   2.20   2.00
0.30  0.40  0.20  0.15   0.0        0.0/
 406318 'GENROU'   1   7.0   0.05   1.5   0.05   6.   0.   2.20   2.00
0.30  0.40  0.20  0.15   0.0        0.0/
 10426  'GENROU'   1   7.0   0.05   1.5   0.05   6.   0.   2.20   2.00
0.30  0.40  0.20  0.15   0.0        0.0/
 10437  'GENROU'   1   7.0   0.05   1.5   0.05   6.   0.   2.20   2.00
0.30  0.40  0.20  0.15   0.0        0.0/
/IBUS   'GENSAE'   I   T'do  T"do   T"qo         H    D    Xd     Xq
X'd          X"d    Xl    S(1.0)    S(1.2)/
 40119      'GENSAL'   1   5.0  0.05    0.10      3.   0.   1.10   0.70
0.25         0.20   0.15  0.0       0.0 /
 401210     'GENSAL'   1   5.0  0.05    0.10      3.   0.   1.10   0.70
0.25         0.20   0.15  0.0       0.0 /
 402111     'GENSAL'   1   5.0  0.05    0.10      3.   0.   1.10   0.70
0.25         0.20   0.15  0.0       0.0 /
 403112     'GENSAL'   1   5.0  0.05    0.10      3.   0.   1.10   0.70
0.25         0.20   0.15  0.0       0.0 /
 404113     'GENSAL'   1   7.0  0.05    0.10      2.   0.   1.55   1.00
0.30         0.20   0.15  0.0       0.0 /
 407119     'GENSAL'   1   5.0  0.05    0.10      3.   0.   1.10   0.70
0.25         0.20   0.15  0.0       0.0 /
 407220     'GENSAL'   1   5.0  0.05    0.10      3.   0.   1.10   0.70
0.25         0.20   0.15  0.0       0.0 /
 10121      'GENSAL'   1   5.0  0.05    0.10      3.   0.   1.10   0.70
0.25         0.20   0.15  0.0       0.0 /
 10132      'GENSAL'   1   5.0  0.05    0.10      3.   0.   1.10   0.70
0.25         0.20   0.15  0.0       0.0 /
 10143      'GENSAL'   1   5.0  0.05    0.10      3.   0.   1.10   0.70
0.25         0.20   0.15  0.0       0.0 /
 10214      'GENSAL'   1   5.0  0.05    0.10      3.   0.   1.10   0.70
0.25         0.20   0.15  0.0       0.0 /
 10225      'GENSAL'   1   5.0  0.05    0.10      3.   0.   1.10   0.70
0.25         0.20   0.15  0.0       0.0 /
 20328      'GENSAL'   1   5.0  0.05    0.10      3.   0.   1.10   0.70
0.25         0.20   0.15  0.0       0.0 /
/Voltage regulators and exciters
/IBUS       'SEXS'      I     TA/TB       TB    K     TE          EMIN
EMAX/
 40119      'SEXS'      1     0.20        20.   50.   0.10        0.0   4.0/
 401210     'SEXS'      1     0.20        20.   50.   0.10        0.0   4.0/
 402111     'SEXS'      1     0.20        20.   50.   0.10        0.0   4.0/
 403112     'SEXS'      1     0.20        20.   50.   0.10        0.0   4.0/
 404113     'SEXS'      1     0.20        20.   50.   0.10        0.0   4.0/
 407119     'SEXS'      1     0.20        20.   50.   0.10        0.0   4.0/
 407220     'SEXS'      1     0.20        20.   50.   0.10        0.0   4.0/
 10121      'SEXS'      1     0.20        20.   50.   0.10        0.0   4.0/
 10132      'SEXS'      1     0.20        20.   50.   0.10        0.0   4.0/
 10143      'SEXS'      1     0.20        20.   50.   0.10        0.0   4.0/
 10214      'SEXS'      1     0.20        20.   50.   0.10        0.0   4.0/
 10225      'SEXS'      1     0.20        20.   50.   0.10        0.0   4.0/
 20328      'SEXS'      1     0.20        20.   50.   0.10        0.0   4.0/
```

```
 10426      'SEXS'      1     0.10        50.   120.  0.10        0.0   5.0/
 10437      'SEXS'      1     0.10        50.   120.  0.10        0.0   3.0/
 404214     'SEXS'      1     0.10        50.   120.  0.10        0.0
      3.27/
 404715     'SEXS'      1     0.10        50.   120.  0.10        0.0   5.0/
 405116     'SEXS'      1     0.10        50.   120.  0.10        0.0   5.0/
 406217     'SEXS'      1     0.10        50.   120.  0.10        0.0   5.0/
 406318     'SEXS'      1     0.10        50.   120.  0.10        0.0   5.0/
/Turbine regulators and water ways
 40119      'HYGOV'     1     0.04  0.80  5.0   0.05  0.20  0.10  0.95  0.00
1.00  1.00  0.  0./
 401210     'HYGOV'     1     0.04  0.80  5.0   0.05  0.20  0.10  0.95  0.00
1.00  1.00  0.  0./
 402111     'HYGOV'     1     0.04  0.80  5.0   0.05  0.20  0.10  0.95  0.00
1.00  1.00  0.  0./
 403112     'HYGOV'     1     0.04  0.80  5.0   0.05  0.20  0.10  0.95  0.00
1.00  1.00  0.  0./
 407119     'HYGOV'     1     0.08  1.60  5.0   0.05  0.20  0.10  0.95  0.00
1.00  1.00  0.  0./
 407220     'HYGOV'     1     0.08  1.60  5.0   0.05  0.20  0.10  0.95  0.00
1.00  1.00  0.  0./
 10121      'HYGOV'     1     0.04  0.80  5.0   0.05  0.20  0.10  0.95  0.00
1.00  1.00  0.  0./
 10132      'HYGOV'     1     0.04  0.80  5.0   0.05  0.20  0.10  0.95  0.00
1.00  1.00  0.  0./
 10143      'HYGOV'     1     0.04  0.80  5.0   0.05  0.20  0.10  0.95  0.00
1.00  1.00  0.  0./
 10214      'HYGOV'     1     0.04  0.80  5.0   0.05  0.20  0.10  0.95  0.00
1.00  1.00  0.  0./
 10225      'HYGOV'     1     0.04  0.80  5.0   0.05  0.20  0.10  0.95  0.00
1.00  1.00  0.  0./
 20328      'HYGOV'     1     0.04  0.80  5.0   0.05  0.20  0.10  0.95  0.00
1.00  1.00  0.  0./
/Power system stabilizers
 40119      'STAB2A'    1     1.0   4.0   1.    2.0   0.3   1.    0.05
      0.05  /
 401210     'STAB2A'    1     1.0   4.0   1.    2.0   0.3   1.    0.05
      0.05  /
 402111     'STAB2A'    1     1.0   4.0   1.    2.0   0.3   1.    0.05
      0.05  /
 403112     'STAB2A'    1     1.0   4.0   1.    2.0   0.3   1.    0.05
      0.05  /
 404113     'STAB2A'    1     1.0   4.0   1.    2.0   0.0   1.    0.05
      0.05  /
 407119     'STAB2A'    1     1.0   4.0   1.    2.0   0.3   1.    0.05
      0.05  /
 407220     'STAB2A'    1     1.0   4.0   1.    2.0   0.3   1.    0.05
      0.05  /
 10121      'STAB2A'    1     1.0   4.0   1.    2.0   0.3   1.    0.05
      0.05  /
 10132      'STAB2A'    1     1.0   4.0   1.    2.0   0.3   1.    0.05
      0.05  /
 10143      'STAB2A'    1     1.0   4.0   1.    2.0   0.3   1.    0.05
      0.05  /
 10214      'STAB2A'    1     1.0   4.0   1.    2.0   0.3   1.    0.05
      0.05  /
 10225      'STAB2A'    1     1.0   4.0   1.    2.0   0.3   1.    0.05
      0.05  /
 20328      'STAB2A'    1     1.0   4.0   1.    2.0   0.3   1.    0.05
      0.05  /
```

```
 406217     'STAB2A'    1     1.0   4.0   1.    2.0   0.3   1.    0.05
      0.05  /
 406318     'STAB2A'    1     1.0   4.0   1.    2.0   0.3   1.    0.05
      0.05  /
 405116     'STAB2A'    1     1.0   4.0   1.    2.0   0.3   1.    0.05
      0.05  /
 404715     'STAB2A'    1     1.0   4.0   1.    2.0   0.3   1.    0.05
      0.05  /
 404214     'STAB2A'    1     1.0   4.0   1.    2.0   0.3   1.    0.05
      0.05  /
 10426      'STAB2A'    1     1.0   4.0   1.    2.0   0.3   1.    0.05
      0.05  /
 10437      'STAB2A'    1     1.0   4.0   1.    2.0   0.3   1.    0.05
      0.05  /
/Current limiters
 404214     'MAXEX2'    1   1   3.1167  1.0500   60.000    1.200   20.000
1.500   10.000    1.000   1.0   -0.80 /
 404715     'MAXEX2'    1   1   3.0000  1.0500   60.000    1.200   20.000
1.500   10.000    1.000   1.0   -0.80 /
 405116     'MAXEX2'    1   1   3.0000  1.0500   60.000    1.200   20.000
1.500   10.000    1.000   1.0   -0.80 /
 406217     'MAXEX2'    1   1   3.1167  1.0500   60.000    1.200   20.000
1.500   10.000    1.000   1.0   -0.80 /
 406318     'MAXEX2'    1   1   3.1167  1.0500   60.000    1.200   20.000
1.500   10.000    1.000   1.0   -0.80 /
 10426      'MAXEX2'    1   1   3.1167  1.0500   60.000    1.200   20.000
1.500   10.000    1.000   1.0   -0.80 /
 10437      'MAXEX2'    1   1   3.1167  1.0500   60.000    1.200   20.000
1.500   10.000    1.000   1.0   -0.80 /
 404113     'MAXEX2'    1   1   2.51    1.0500   60.000    1.200   20.000
1.500   10.000    1.000   1.0   -0.80 /
 40119      'MAXEX2'    1   1   2.07    1.0500   60.000    1.200   20.000
1.500   10.000    1.000   1.0   -0.80 /
 401210     'MAXEX2'    1   1   2.07    1.0500   60.000    1.200   20.000
1.500   10.000    1.000   1.0   -0.80 /
 402111     'MAXEX2'    1 1.0   2.07    1.0500   60.000     1.200  20.000
1.500   10.000    1.000   1.0   -0.80 /
 403112     'MAXEX2'    1   1   2.07    1.0500   60.000    1.200   20.000
1.500   10.000    1.000   1.0   -0.80 /
 407119     'MAXEX2'    1   1   2.07    1.0500   60.000    1.200   20.000
1.500   10.000    1.000   1.0   -0.80 /
 407220     'MAXEX2'    1   1   2.07    1.0500   60.000    1.200   20.000
1.500   10.000    1.000   1.0   -0.80 /
 10121      'MAXEX2'    1   1   2.07    1.0500   60.000    1.200   20.000
1.500   10.000    1.000   1.0   -0.80 /
 10132      'MAXEX2'    1   1   2.07    1.0500   60.000    1.200   20.000
1.500   10.000    1.000   1.0   -0.80 /
 10143      'MAXEX2'    1   1   2.07    1.0500   60.000    1.200   20.000
1.500   10.000    1.000   1.0   -0.80 /
 10214      'MAXEX2'    1   1   2.07    1.0500   60.000    1.200   20.000
1.500   10.000    1.000   1.0   -0.80 /
 10225      'MAXEX2'    1   1   2.07    1.0500   60.000    1.200   20.000
1.500   10.000    1.000   1.0   -0.80 /
 20328      'MAXEX2'    1   1   2.07    1.0500   60.000    1.200   20.000
1.500   10.000    1.000   1.0   -0.80 /
/Load model
 1 'EXTLOW' 1 0.01 2 -2 0.01 2 -1/
 2 'EXTLOW' 1 0.02 2 -2 0.01 2 -1/
```